A dissertation submitted in partial satisfaction
of the requirements
for the Degree of Doctor of Philosophy in Chemistry

Università degli Studi dell'Insubria
Dipartimento di Scienza e Alta Tecnologia - Como

A Comprehensive Multi-Scale Modeling of Defective CdSe Colloidal Nanocrystals through Advanced X-ray Scattering Techniques

Daniele Moscheni

XXXI Ph. D. Cycle in Chemistry and Environmental Sciences

Supervisors:

Prof. Norberto Masciocchi Dr. Antonella Guagliardi

Acknowledgements

Taking part to a Ph.D. program is, for most of the students, an exciting and stimulating opportunity to improve their own scientific skills during a three-years course under the guide of an expert supervisor. I've been supervised by Prof. Norberto Masciocchi and Dr. Antonietta Guagliardi since the early stage of my bachelor's degree, so that they are more than a supervisor for me: they represent a "scientific family" that has been inspiring me for many years, thanks to their passion and expertise. For this reason, I wish to thank them for the great opportunity they gave me, for their hard work, without limits and with extreme patience for my personal and scientific growth. In these three years they always asked me to simply call them Norberto and Antonella; until today, despite the great moments spent together in many occasions, I desire to call them "Prof.", a term that I consider a word of gratitude for what they taught me and for the mini-scientist that now I am!

I would like to thank another young scientist, Dr. Federica Bertolotti, that has always been a scientific benchmark and a great friend. Working with her was (and actually is) not only a pleasure but a great privilege and source of continuous intellectual stimuli and curiosity.

I would like to thank the ETH team, leaded my Prof. Maksym Kovalenko, and in particular Dr. Loredana Protesescu, Laura Piveteau, Dr. Dmitry Dirin, Bogdan Benin, for their support during my abroad experience. Taking part to a research project with them was a great opportunity to discover the "world" of nanomaterial synthesis and surface characterization.

Special thanks are also addressed to Prof. Jan Skov Pedersen and Jeppe Lyngsø, for their support in SAXS measurement and analyses that were fundamental for this project.

I wish to thank Dr. Antonio Cervellino and the material science beamline staff of the Paul Scherrer Institut for their support in the WAXTS data collection and reduction.

I wish to express my gratitude to Prof. Simon Billinge, Dr. Maxwell Terban and the BNL staff for the PDF data collection performed on my samples.

Special thanks are for the rest of the "scientific family" called "To.Sca.Lab." and the other material scientists of the Department of Science and High Technology (among

these, Prof. Fabio Ferri, Dr. Jose Manuel Delgado Lopez, Dr. Gregorio Dal Sasso, Dr. Francisco Jesus Carmona Fernadez, Prof. Simona Galli, Rebecca Vismara) simply for making these 3 years so special!
I also want to extend my gratitude to two Ph.D. student of my cycle, Davide Spanu and Gilberto Binda, for the lively moments and reassurance during the day.
Special thanks go to my family for its unconditional support in every step of my life giving me the possibility to express my aptitude to scientific disciplines.
Another special thank goes to my girlfriend Gisella, that always supported me being, even in bad moments, by my side.

Last but not least, I want to thank you, reader for considering my work.

Table of contents

List of Abbreviations

1D	*Mono-dimensional*
2D	*Two- dimensional*
3D	*Three Dimensional*
AR	*Aspect ratio*
CB	*Conduction Band*
COSH	*Core-Shell*
cQDs	*Colloidal Quantum Dots*
CYL	*Cylinder*
d-PDF	*Differential Pair Distribution Function*
DDF	*Double Deformation Fault*
DF	*Deformation Fault*
DFA	*Debye Function analysis*
DNP	*Dynamic Nuclear Polarization*
DSE	*Debye Scattering Equation*
ESF	*Extrinsic Stacking Fault*
fcc	*Face centered cubic*
FF	*Form Factor*
FWHM	*Full Width at Half Maximum*
GF	*Growth Fault*
GoF	*Goodness of fit*
hcp	*Hexagonal closed pack*
HRTEM	*High Resolution Transmission Electron Microscopy*
IG	*Intergrowth*
IL	*Inorganic ligand*
ISF	*Intrinsic Stacking Fault*
LOC	*Localized*
MS	*Material Science*
NC	*Nanocluster*
NMR	*Nuclear Magnetic Resonance*
NP	*Nanoparticle*
nPL	*Nanoplatelet*
nRD	*Nanorod*
OA	*Oleic Acid*

ODE	*1-octadecene*
OL	*Organic Ligand*
PASS	*Phase Adjust Spinning Sidebands*
PD	*Planar Defect*
PDF	*Pair Distribution Function*
PIETA	*Incremented Echo Train Acquisition*
PL	*Photoluminescence*
PSI	*Paul Scherrer Institut*
QDs	*Quantum Dots*
QY	*Quantum Yield*
RND	*Random*
RT	*Room Temperature*
S/N	*Signal to Noise Ratio*
SAXS	*Small-Angle X-ray Scattering*
SF	*Stacking Fault*
SFE	*Stacking Fault Energy*
SID	*Sampled Interatomic Distances*
SLS	*Swiss Light Source*
s.o.f.	*Site Occupancy Factor*
SPH	*Sphere*
TEM	*Transmission Electron Microscopy*
TF	*Twin Fault*
uSFE	*Barrier Stacking Fault Energy*
UV	*Ultraviolet*
VB	*Valence Band*
Vis	*Visible*
WAXTS	*Wide-Angle X-ray Total Scattering*
WZ	*Wurtzite*
XRF	*X-ray Fluorescence*
XRPD	*X-ray Powder Diffraction*
ZB	*Zinc Blende*

1

Introduction to II-VI Semiconducting Nanomaterials

This Chapter introduces the reader to the entire work of the Ph. D. thesis and to its main topic of research, which is focused on structural and microstructural characterization of colloidal quantum-dots. Initially, colloidal syntheses and relevant applications of nanocrystalline semiconductors are briefly rationalized, highlighting the key points and the recent achievements of this global research activity, which has undergone a huge acceleration in the last decades, soon after the discovery of the quantum confinement effect. The most important synthetic approaches to II-VI semiconducting nanomaterials, that are the "hot-injection" and the "heat-up" protocols, are presented and discussed, with a brief section of mechanistic flavor and a critical view on their possible limits. A brief paragraph follows, dedicated to new characterization methods of II-VI semiconducting materials using the advanced X-ray diffraction techniques. On the basis of the themes here described, the final part of this Chapter intends to clarify the motivations for this thesis and to outline its objectives and its structure.

1.1 The Explosion of Research on Quantum Dots

In the last three decades, soon after the discovery of the quantum confinement effect by L. E. Brus in 1983,[1] the research on nanostructured or nanosized semiconducting materials has enormously increased. These efforts have pushed several branches of Science to study these amazing materials, from the synthetic aspects, to the development of new analytical and structural characterization methods, to computational work and to surface or core doping, with all efforts eventually targeted toward the understanding and optimization of the related opto-electronic properties.

A proof of this statement can be easily obtained by performing a search on the *topic* keyword within the Web of Science database (*webofknowledge.com*) that shows a total number of 122.958 manuscripts (as per September 1st, 2018), a value that has systematically increased since 1983 (see Figure 1.1). Also astonishing is the number of disciplines in which these materials were investigated and employed (more than 100), spanning from applied physics (16%), to materials science (multidisciplinary) (15%), nanoscience and nanotechnology (11%) and, for what is of interest for this Thesis, crystallography (1%) (see the pie charts in Figure 1.2). Indeed, the extreme versatility and tunability of these materials make them highly popular, mainly thanks to their attractive optical properties and consequent appeal, at both the academic and industrial levels. Quite obviously, investigation on these materials is of different nature depending on the field. For example, one of the most cited paper[2] on QDs reports on the cytoxicity (the quality of being toxic to cells of living a organism) of nanoparticles and their accumulation in the human body. Alternatively, biomimetic functionalization of the QD surface (as Lysine-ZnS@CdSe QDs) has been tested in order to exploit luminescence properties as a contrast medium for clinical imaging diagnostics.[2] In the engineering field, applications are manly focused on the implementation of QDs in high performance devices such as displays and solar cells.[3–5] Chemists mainly target they studies to the synthesis and functionalization of QDs, aiming at improving their optical properties and managing with the upscaling process fostering their introduction into the of market of high-tech goods.[6–8]

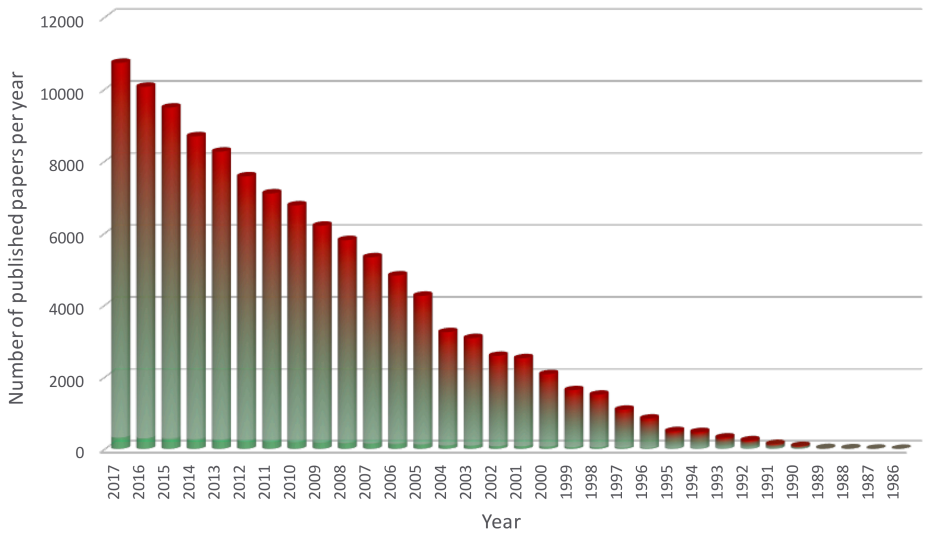

Figure 1.1. *The histogram represents the number of articles published every year according to a bibliographic research on webofknownledge.com based on the "Quantum-Dots" keyword (accessed September 1st, 2018).*

Physics-based works include experimental techniques, such as spectroscopic methods aiming at investigating the nature and the origin of photoluminescence, often supplemented by computational tools,[9–11] or nanomaterial fabrication by top-down processes (lithography) to structural characterization by X-ray diffraction methods and, to some extent, microscopies of the different kinds.

Starting from a quick glance on the scientific and patent literature, or simply analyzing the wide market of sensors, displays, batteries and other devices filling our world, it is fully clear that these materials have a high impact on our society and that chemistry and physics are the master disciplines offering the most effective characterization tools able to deeply investigate these materials. Needless to say, basic research and the understanding of still unknown fundamental features on QDs have the potential to promote, or increase, the usage of these materials in many technological fields, way beyond our present knowledge and expectations.

Best suited to my Thesis in Chemistry, the following paragraph is dedicated to providing an overview of the synthesis process and the most appealing applications of CdSe QDs, one of the most investigated II-VI semiconducting materials.

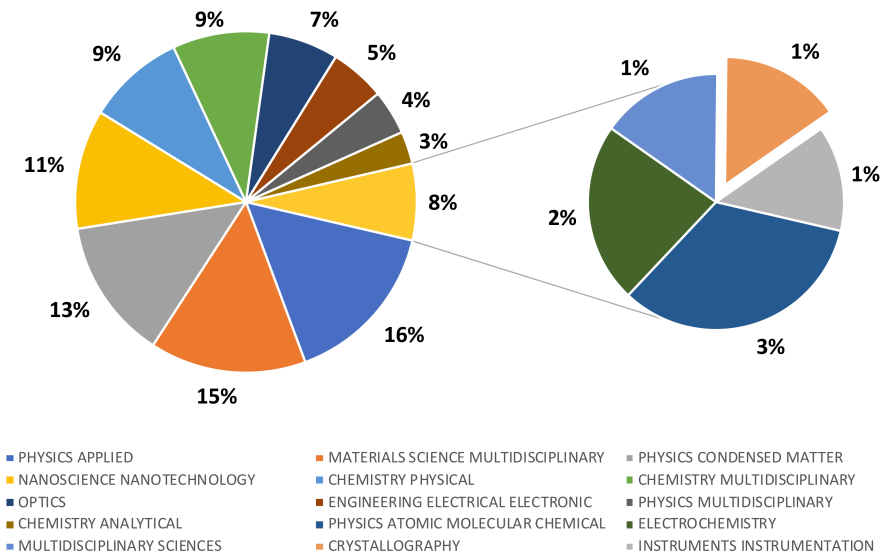

Figure 1.2. *The pie charts represent the percentage of published articles on "Quantum Dots" on different fields during the last thirty years. The crystallography slice (the pink sector in the right panel) corresponds to a mere 1% of the whole pie, revealing that most of the research efforts were dedicated to the synthesis, properties and applications, with a much lower focus on structural and microstructural characterization at the atomic and nano levels. Data were taken from a bibliographic research on webofknownledge.com (as per September 1st, 2018).*

1.2 CdSe Quantum-Dots: an Overview on Synthesis and Applications

The discovery of the so-called *quantum confinement effect* in 1983[1] widely raised the interest on semiconducting materials and on their tunable properties in the visible and infrared spectrum, achievable by an accurate size and shape control.[3,12–15] Understanding why this happens is facilitated by what inserted in Figure 1.3, which schematically shows the origin of the quantum confinement effect; briefly, the extreme downsizing of the crystalline domain of an intrinsic semiconductor modifies the conduction (CB) and valence (VB) bands by increasing the energy band

gap (E_g). This effect is particularly evident when the spatial extent of the electronic wave function becomes comparable with the (nano)particle size. In a quantitative description, quantum effects become very important when the particle size is lower than the Bohr excitation radius[1] of the bulk, forcing material's properties to be (extremely) size dependent. The presently available theory predicts that, for an electron-hole pair sitting in the lowest CB and the highest VB orbitals, respectively, the coulombic interaction model induces a size dependent band gap, the analytical formulation of which is shown in Equation 1.1.[1]

$$E_g \simeq E_{bulk} + \frac{\hbar^2 \pi^2}{2R^2}\left[\frac{1}{m_e} + \frac{1}{m_h}\right] - \frac{1.8e^2}{\epsilon R} \qquad Eq.1.1$$

where:

E_{bulk} : band gap energy of the bulk material(J)

R : particle radius (m)

ϵ : dielectric constant of the material ($C^2/(Nm^2)$)

m_e : electron effective mass (kg)

m_h : hole effective mass (kg)

e : electron charge (C)

$\hbar$: reduced Plank constant (J s)

Equation 1.1 shows that the band gap energy depends on the band gap of the bulk material, which is modified by two terms related to the size of the nanocrystal (as described by their *inverse* R dependence). Semiconductors having different E_{bulk} values (*e.g.* ZnS 3.6 eV, CdSe 1.74 eV, PbS 0.37 eV), falling already at, or near, the typical photon energies of the visible range, can then be used to tune the absorption and emission peak profiles at optical wavelengths, by simply controlling the size of the NCs.[13] Among these, CdSe QDs emerged for applications in displays, thanks to their wide tunability in the whole visible spectrum, from pale green (λ = 495 nm, D = 2.36 nm) to dark red (λ = 595 nm, D = 4.37 nm), as shown in Figure 1.4. Additionally, the high technological impact of CdSe-based QDs has enormously benefitted from other appealing properties, which include their high quantum yield emission and chemical stability and the easiness in obtaining extremely monodisperse materials. [4,16–19]

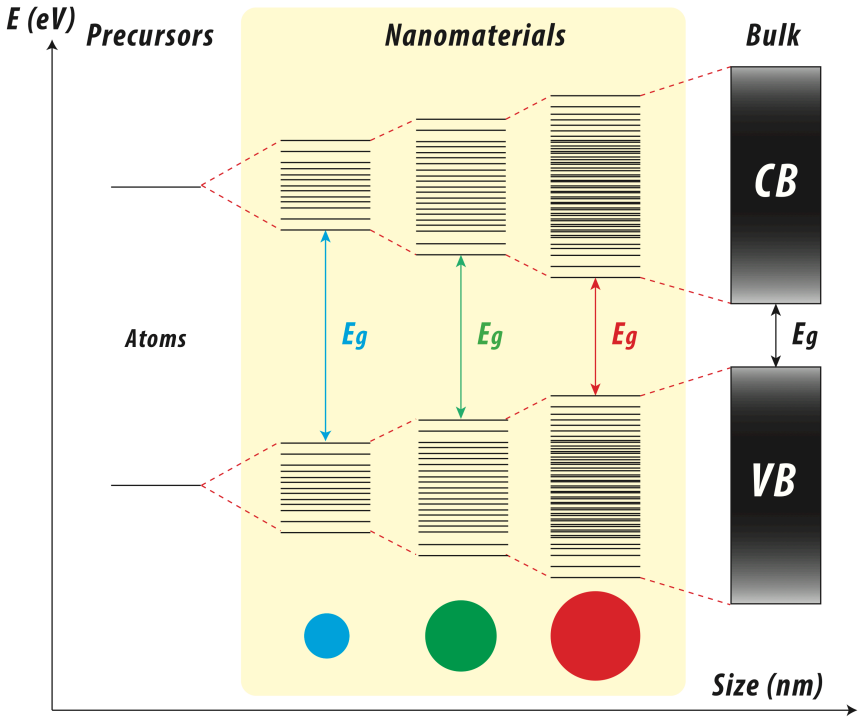

Figure 1.3. *Graphical representation of the quantum confinement effect and its impact on the energy band gap on nano and bulk materials. This figure intends to show that lowering the size of the NC (i.e. moving to the left) brings about an increase of the energy band gap, with radical consequences on the absorption and emission properties.*

Since NCs with different sizes may emit radiation with markedly different colors (photon energies or wavelengths), the control of the size dispersion (especially for ultra-small NCs) plays a predominant role in determining a narrow emission profile. Such a condition, in turns, means that a neat, precise and unblurred, color hue is generated. In this line, the first stable colloidal synthesis of CdE (E = S, Se, Te) NCs, proposed by Bawendi and co-workers in 1993,[20] enabled the isolation of high quality Cd-based cQDs (ranging from 2 to 6 nm) with an high degree of monodispersity within a single, and purportedly simple, reaction. This synthetic approach is nowadays known as the "*hot injection*" method, because the reaction promoting the formation of colloidal NCs starts with the direct injection of one or more precursor solutions (*i.e.* a Se source as [Se-ODE]) in a high boiling solvent (*e.g.* 1-

octadecene) where the other precursor (*e.g.* the Cd ions source) has been previously dissolved at high temperature.

The hot-injection synthesis and its crucial steps are graphically summarized in Figure 1.5. This method relies on the generation of an oversaturation condition of precursors at high temperature that promotes a single "burst nucleation" event where numerous nuclei simultaneously form and start to growth. In order to obtain highly monodisperse NCs, nucleation must indeed occur simultaneously in a single event, meaning that the largest fraction of nuclei need to form in a very short time-window of the early stage of the reaction. In such a way, no additional nucleation crystal growth occurs which would inevitably produce polydisperse samples.[21]

The thermodynamic description of the hot-injection colloidal synthesis requires the definition of the energy barrier profile for the homogeneous nucleation. Following ref [21], the Gibbs free energy term for the formation of a spherical NC of radius r in supersaturation conditions (ΔG) can be expressed as the sum of a surface

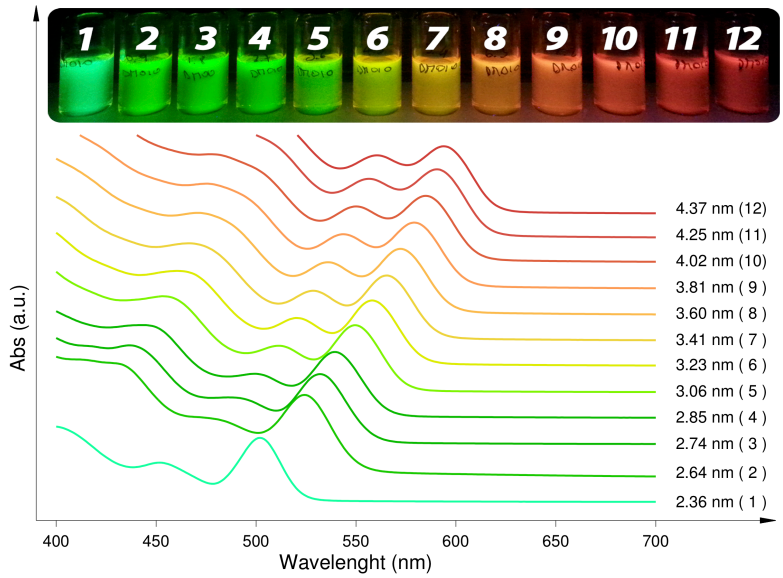

Figure 1.4. *A practical example of the size effect on optical properties of CdSe materials. Samples from 1 to 12 were synthetized according to ref[22] from the same reaction batch and extracted from the same mixtures at different times, restoring after each withdrawal extra Se-ODE suspension in order to continue the NCs growth. The picture on top represents high diluted samples under a UV light emitter. The plot on the bottom reports the absorption spectra of all 12 samples shifted upwards for a matter of clarity.*

contribution (r^2 − dependent) and the energy difference between the monomers and the bulk crystal (ΔG_v), as follows:

$$\Delta G = 4\pi r^2 \gamma + \frac{4}{3}\pi r^3 \Delta G_v$$

$Eq.\ 1.2$

Where:

γ : surface energy per unit area (J/m^2)

r : radius of a spherical particle (m)

$\Delta G_v = (-RT(\ln S)/V_m)$: monomer to bulk Gibbs energy change per unit volume (J/m^3), with:

S : supersaturation $S = [M]/[M_\infty]$ ($S > 1$ supersaturated solution)

$[M]$: monomer (precursor) concentration

$[M_\infty]$: monomer (precursor) concertation in saturation condition

V_m : molar volume of the bulk crystal (m^3/mol)

Since the surface tension γ of a naked particle is always positive and the ΔG_v contribution in supersaturation conditions ($S > 1$) is negative, the ΔG function is not monotonic and, typically, shows a maximum in r space. By simply differentiating Equation 1.2 with respect to r, it is possible to obtain the critical radius r_c (Equation 1.3),

$$r_c = -\frac{2\gamma}{\Delta G_v}$$

$Eq\ 1.3$

which expresses the radius corresponding to the maximum ΔG value, ΔG_{max}. Substituting Equation 1.3 into Equation 1.2, the Gibbs free energy needed to form a stable cluster of diameter $2r_c$ is obtained (Equation 1.4).

$$\Delta G_{max} = \frac{16\pi\gamma^3}{3(\Delta G_v)^2}$$

$Eq.\ 1.4$

From Equation 1.4, it is possible to understand the fundamental role in choosing the

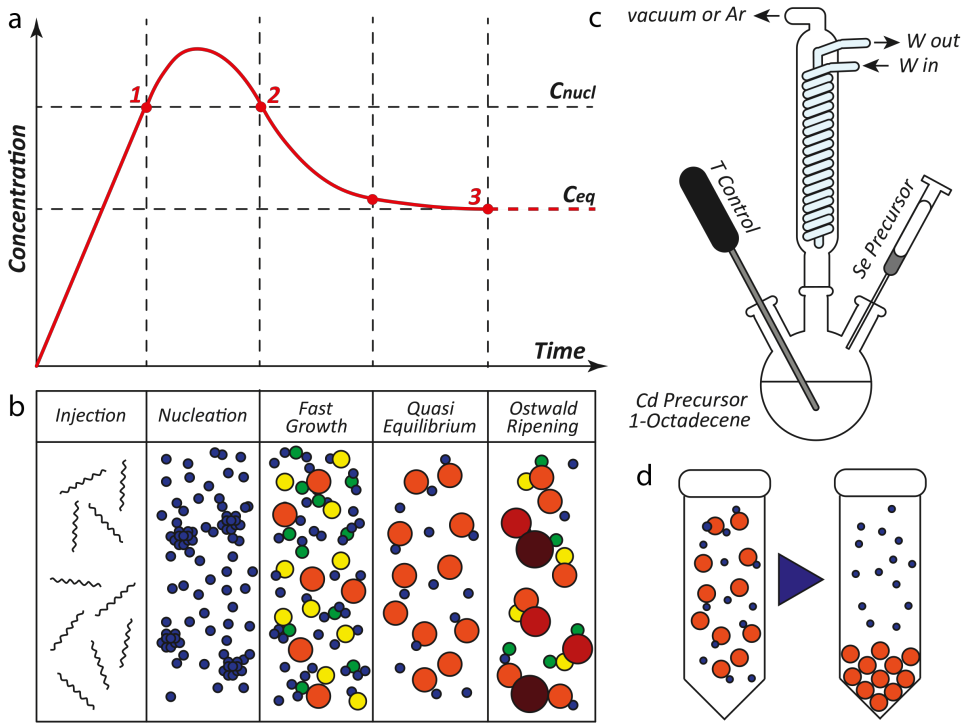

Figure 1.5. *General scheme of the hot-injection synthesis and nucleation process. In a and b, the precursor concentration plot and a pictorial sketch of the steps of "hot-injection" synthesis, respectively, are shown. In panel b, step 1 represents the* ***injection*** *of precursors (depicted as black wavy segments). Subsequently, oversaturation is reached and, in the* ***nucleation*** *step, the formation of nuclei (blue spheres in b) with critical radius* r_c *is activated. Once step 2 is over, the nucleation process stops and the extra precursor may only contribute to a* ***fast growth*** *of the particles (yellow to red spheres in b and d). The last steps in panel b refer to* ***quasi equilibrium*** *and final* ***ripening*** *towards the sought NCs dimension. At point 3 of panel a, the reaction is over. c: laboratory set-up for the "hot-injection" synthetic process. d: graphical representation of the solvent/antisolvent purification procedure of the raw reaction mixture; the strategy relies on the precipitation of the NC fraction permitting the elimination of the extra precursors in the mixture.*

correct amount of precursors (the supersaturation condition included in the ΔG_v term) at a well-defined and controlled temperature. Such a control would then trigger the nucleation process by maximizing its probability with subsequent (nano)crystal growth, which proceeds when the critical radius of the formed nuclei has been reached.

With reference to Figure 1.5, the description of the hot-injection method of CdSe colloidal QDs synthesis, is hereafter reported. The reaction starts with the fast injection of the Se source into a high boiling solvent where the Cd precursor is dispersed at high temperature (0-1 **injection** phase, T depends from the crystal phase and capping agents; 220 to 360 °C). The fast addition of the Se precursor provides the supersaturation condition, as previously described, and the beginning of the **nucleation** process (1-2). Once the supersaturation condition vanishes, the nuclei stop to form and the remaining precursors contribute to the growth of the nuclei generated in the nucleation step (2-3: **fast growth** phase in Figure 1.5). Since the growth kinetics depend on the concentration of the precursors, and on the reactivity of the exposed surface, the crystal growth rate right after the fall of the nucleation process is extremely high but tends to decrease over time.

The desired NC size is then obtained quenching the reaction (ideally instantly), by cooling down the crude suspension at RT with sand baths, water or compressed air after seconds or minutes, depending on the crystal phase and capping ligand used. Once the reaction stops, the NCs are washed through solvent/antisolvent precipitation cycles and re-dispersed in the host solvent.

During the synthesis, the crystal growth is strongly dominated by the temperature and the interaction of ligands with the surface. Recent reports on CdSe QDs show the fundamental role of the ligands in guiding the preferential formation of the specific crystalline ZB[23–25] or WZ[6,7,24–26] polymorphs in CdSe QDs. However, the hot-injection synthesis allows a high control at the lab scale only. Indeed, when upscaling of these reactions is required for industrial applications,[27] the hot injection synthesis, unfortunately, cannot be easily adopted because:

a) the increasing volume of the reactor dramatically affects the mixing time and does not enable a precise control the nucleation phenomenon;
b) large reaction volumes cannot be quickly (instantaneously) cooled down;
c) the injected solution volume represents 10 to 50% of the reaction mixture; therefore, managing a fast injection in large volumes and controlling their temperature becomes very problematic;
d) injection can produce effects on the batch-to-batch reproducibility, since the stint of injection can unpredictably vary, and may also depend on the skills and efforts of the different operators. Not to be forgotten, this is also

an issue at the lab scale.

For these reasons, in the last years, the so called *"heat-up"* approaches were studied and developed for optimizing the upscale process while limiting the above listed problems.[27,28] [*In addition, other synthetic approaches based on selenourea and cadmium nitrate precursors and triggered by the fast injection of a base have been reported in the literature*[29] *but are not described here since they are much less related to the synthetic methods adopted in this thesis.*]

The "heat-up" process relies on mixing the precursors at low temperature (RT) and subsequent heating up of the solution (to *ca*. 240 °C) to promote the nucleation, reducing complications related to the mixing time temperature control and to the overall reproducibility. However, since the heat-up synthesis cannot rely on a short "burst-like" event that controls the nucleation process, the reaction must be accurately designed, if the isolation of NCs with a comparable quality to the ones produced with the hot-injection synthesis is pursued. Hyeon *et al.* reported[28] that, for the hot-injection synthesis, the formation of the nuclei can be likewise described by Equations 1.2-1.4, confirming that the nucleation rate is strongly dependent on the temperature and on the surface tension (the latter, tuneable with the use, or addition, of suitable ligands). For an efficient synthetic procedure, the heat-up synthesis has to match two fundamental requirements (see Figure 1.6):

a) the nucleation rate ($d[N]/dt$) must be zero at RT; this is managed by controlling the surface tension, *e.g.* by selecting the nature of the capping ligands;
b) the nucleation rate has to be extremely temperature-sensitive up to a maximum T value, a condition at which nuclei start to grow (this is normally managed by the carefully controlling the concentration of the precursors – supersaturation) [27].

As a consequence of a strict control of reactants, concentrations, surfactants and temperature ramp, this new class of reactions reached a considerable success in the upscaling process, though further engineering improvements are still required.

The main success of II-VI colloidal suspensions of NCs, in particular of CdSe, can be certainly attributed to their excellent stability during the time. This feature is provided by the ligands, typically long-chain organics (oleate or oleamine) that

passivate the surface of the NCs impeding sintering and making the QDs soluble and stable in apolar solvents. However, some issues in having organic ligands at the surface are still present. Among the most relevant, the following ones can be highlighted:

a) they act as an insulating shell, impeding charge transfer processes, making ligand-covered QDs unsuitable for some applications;
b) capping ligands can produce surface strain and non-radiative trap states between the valence and conduction bands that drastically decrease the photoluminescence quantum yield (PLQY).

Accordingly, in the last decades, these findings pushed material chemists to investigate new solutions. One way out consists in replacing the organic ligands with inorganic ones,[8,30] aiming at solving the problem of limited charge transfer. Alternatively, surface passivation of QDs was obtained by epitaxially growing a

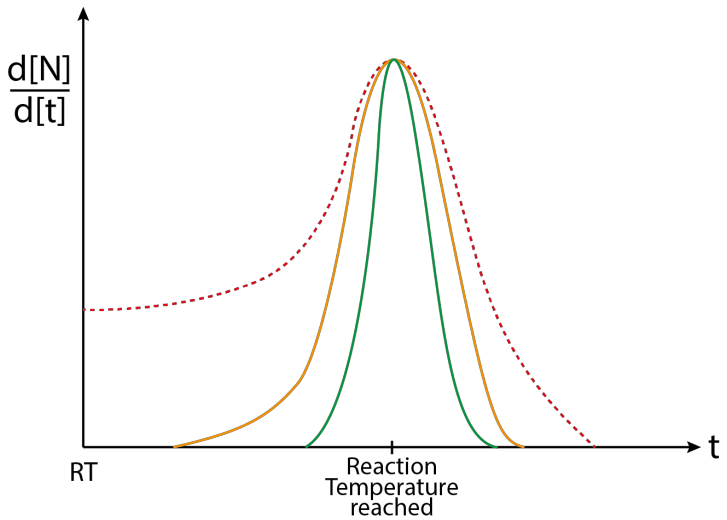

Figure 1.6. *Qualitative representation of three nucleation rate functions during a heat-up synthesis. The red dashed trace has non-zero nucleation rate at RT, meaning that the nucleation process starts right after the mixing of the precursors, and, therefore, should be avoided. The solid orange line presents a nucleation rate ideal for a heat-up synthesis at RT. However, since it is not extremely temperature sensitive, the nucleation rate is not able to provide a "burst nucleation" process producing a highly monodisperse population of NCs. The green solid line represents a close-to-ideal nucleation rate vs time curve, since it is able to reproduce a violent nucleation event comparable to that occurring in the hot-injection synthesis.*

crystalline shell of a different II-VI material, removing, at the same time, trap states that significantly reduce the PLQY.[31–35] Another fundamental problem related to CdSe QDs is the occasional occurrence of "blinking" dots.[9,36,37] This phenomenon drastically suppresses the PLQY, since a fraction of CdSe are "turned off". Starting from 2008, up to now, thanks to the contribution of Dubertret and co-workers[37] that demonstrated the control of blinking by the shell design and thickness, more complex solutions have been tested, reaching high performances in terms of PLQY improvement. These solutions include the following strategies:

a) in 2008: growing a thick shell of CdS on spherical CdSe cores obtaining core-shell heterostructures; [38]
b) in 2013: growing a shell on atomically thin nPLs (80% PLQY); [39]
c) in 2015: preparing CdSe/CdS core-shell heterostructures with a decreasing alloying ratio moving toward the surface (99% PLQY). [40]

All these efforts were addressed toward the minimization of the strain induced by the outer shell. It was clear indeed from these studies that the PLQY is not only dependent on the nature of the ligand but also on the strain generated by the passivating agent. Worth of note is that the upscale production of these high performance heterostructures is still a challenging and mostly unresolved task, since their syntheses are based on hot-injection methods, which, as we have seen, are not easily transferrable to large(r) volumes.

Today, the II-VI semiconductor NCs family is widely employed in modern displays.[41,42] Despite the fact that CdSe is considered highly toxic (Cd ions can be in principle released to the environment), its band gap makes this material ideal for applications in high quality displays, being CdSe NCs easily tunable to green and red light emission with extremely pure colors. Presently, many large TV-screen brands use a GaN blue backlight ($\lambda = 450$ nm) and make use of two different quantum dot sizes, green ($\lambda = 525$ nm) and red ($\lambda = 625$ nm). While absorbing the blue radiation, they emit bright radiation at their own wavelengths, making it possible to generate a large set of colors in RGB based displays. Figure 1.7 shows one of the most recent QLED displays marketed by Samsung.

The continuous evolution of the QDs engineering pushed this technology to surpass the pre-existent OLED technology; nonetheless, a wide margin of improvement is still present.[43]

Figure 1.7. *New generation 4K QLED tv (based on Q7 tech) that implements QDs technology. (www.samsung.com)*

Finally, II-VI semiconductor QDs have been finding application in several other fields such as:

a) infrared applications for photovoltaics;[5,44]
b) single dots devices (quantum computers);[45,46]
c) optical devices/Instruments (Lasers);[47]
d) in vivo imaging.[48]

Despite the impressive improvement in the synthesis and engineering of these systems, most of their physico-chemical characterization is performed by using conventional laboratory techniques such UV-Vis absorption spectroscopy, transmission electron microscopy and X-ray powder diffraction. In particular, conventional XRPD characterizations are typically addressed to phase identification and quantification, as more complex analyses are limited by the finite size of the crystalline domains[49] or by the presence of a high density of defects and strain at the core/surface interface.[50–52]

1.3 State of the Art of Structural and Microstructural Characterization of CdSe QDs

Several attempts in characterizing this class of materials have been made with advanced X-ray based diffraction techniques but a robust method able to describe these systems in terms of structure, density of defects, morphology and surface structure by a unique and unified approach is still missing. A first attempt in performing structural characterization of nanosized CdSe systems was done by Bawendi and co-workers in 1989 using the Debye Scattering formula (for simulation only), without including corrections for anomalous scattering factors and Compton scattering.[53] Despite this method relied only on simulations of equally sized spherical nanocrystals with different probability of stacking disorder, this pioneering study unveiled that ZB powder diffraction patterns do not necessarily reflect an underlying ZB structure. The high impact of these materials joined to the high potentiality of Wide Angle X-ray Total Scattering Techniques (WAXTS) and the improved performance of modern processors pushed chemists and physicists to develop new experimental and modelling methods for semiconductor characterization. In 2005, Neder and co-workers proposed a method based on the DSE for stacking fault characterization in CdS and ZnS NPs. Their model aimed at the introduction of multiple phases (ZB and WZ structures) within a cluster with a defined size and shape and variable volume fractions of Zincblende and Wurtzite phases. Despite the great potential of the analysis, the authors admitted, in their work, the limits of the proposed model: only a single nanocrystal was considered, and not a population of structurally related nanoparticles. They also highlighted the need to produce stochastic growth models for a more statistically robust treatment of the stacking fault probability and generation.[54] Few years later, several attempts in characterizing CdSe materials with the *real space* Pair Distribution Function (PDF) method have been proposed by Billinge and co-workers. In 2007, a first try in fitting CdSe QDs PDF data with atomistic models was proposed through the synergic use of the DISCUS and PDFgui computational analyses.[51] Despite such convincing method, the inability to refine the SF probability, together with the large CPU time required, favoured, in early 2013, the development of a fast(er) method for SF quantification using a biphasic model in the direct space using PDFgui.[52] Despite

being physically far from reality, this crude approach gave sensible indication on the presence, if not on the quantification, of stacking faults. Since PDFgui makes extensive use of periodic lattices and the local structure of the WZ or ZB crystal phases can be defined within a distance corresponding to the stacking of three "atomic" planes, a PDF refinement was performed on the *very* low-*r* portion of the G(r) function, enabling the *rough* estimation of the SF percentage for nanoparticles with 2 nm (or slightly larger) diameters. In the same year, the need to increase the accuracy and the robustness of nanomaterial analysis fostered the evolution of the modelling towards a "complex" modelling coupling Small Angle X-ray Scattering and atomic pair distribution function data available from separate experimental set-ups.[55] This study revealed the high value of using a "complex modelling" in testing the reliability of physical parameters, granted by the simultaneous use of multiple data sources. Despite this finding, the presence of a model able to extract, and refine, structural information on II-VI semiconductor materials with the use of a population of atomistic models within an affordable computational time is still missing and here is where this thesis intends to give its significant contribution.

1.4 Motivation and Goals of this Thesis

Despite the lack of advanced models and data analysis protocols for the characterization of very small II-IV NCs, Wide Angle X-ray Total Scattering techniques (WAXTS), coupled to the Debye Scattering Equation (DSE) approach (not restricted to ideally periodic and ordered materials), can be used to deeply investigate structural and microstructural features of cQDs. The use of these models, ideally matching X-ray diffraction traces on both the small angle and the wide-angle regions, represents a great opportunity to investigate simultaneously morphological, structural and microstructural features of quantum dots, with atomic scale precision. The development of such a complex model is intended to:

a) unveil and understand optical, chemical and functional properties related to the core and/or surface structure;
b) provide fundamental information for further improvement and upscaling

of the synthetic procedures and engineering of these materials. [56]

Starting from these considerations, this Ph.D. project is based on:

1) The understanding of CdSe nanomaterials, ranging from synthesis to conventional characterization, up to X-ray scattering data collection at large scale facilities (synchrotrons), followed by preliminary data reduction preceding for the complete DSE analysis (Chapters 1-4);
2) The development of an original and flexible model and of a stable protocol that enables, with the use of the DSE, the characterizing, with atomic precision, of structural, microstructural and surface features (down to the pm scale) of materials affected by planar defects with affordable CPU times (Chapter 5);
3) The application of this complex model to real systems (Organic ligand-capped CdSe cQDs and Pt NPs), discovering new features and opening the way to improving the upscaling of their synthesis and the engineering of their performances, with a special care toward their impact on future technologies (Chapters 6-7).

This introductory Chapter, which contains a brief introduction on CdSe-based nanomaterials, is followed by Chapter 2, dedicated to the description of conventional and unconventional characterization methods at the nanoscale, discussing their limits and potentiality in characterizing real nano-systems. Chapter 3 serves as a mathematical description of the DSE, and its implementation in the DebUsSy suite for the characterization of real ensembles of nanosized samples. Therein, the data collection and reduction procedures are also reported, together with a brief section in which the DSE to PDF approaches are compared. The need of introducing strains and defects in the complex atomistic model of CdSe nanocrystals makes it necessary to describe these defects, with a brief state of the art of their characterization methods (Chapter 4). Chapter 5 is completely dedicated to describing the computational model used for the characterization of cQDs and its use as a part of the overall data analysis strategy. The final Chapters focus on the application of the model to real systems in which its potentiality and sensitivity are tested on different materials, disclosing new size-dependent fault driven relaxation and faceting features in CdSe cQDs. An additional section presents an alternative method for the characterization of metallic NPs with larger sizes, but (much) lower

stacking fault probabilities. Finally, at the end of the manuscript, the list of publications produced in this doctoral path are collected for the interested reader.

References

(1) Brus, L. Electronic Wave Functions in Semiconductor Clusters: Experiment and Theory. *J. Phys. Chem.* **1986**, *90* (12), 2555–2560.

(2) Lewinski, N.; Colvin, V.; Drezek, R. Cytotoxicity of Nanoparticles. *Small* **2008**, *4* (1), 26–49.

(3) Carey, G. H.; Abdelhady, A. L.; Ning, Z.; Thon, S. M.; Bakr, O. M.; Sargent, E. H. Colloidal Quantum Dot Solar Cells. *Chem. Rev.* **2015**, *115* (23), 12732–12763.

(4) Tang, J.; Kemp, K. W.; Hoogland, S.; Jeong, K. S.; Liu, H.; Levina, L.; Furukawa, M.; Wang, X.; Debnath, R.; Cha, D.; et al. Colloidal-Quantum-Dot Photovoltaics Using Atomic-Ligand Passivation. *Nat. Mater.* **2011**, *10* (10), 765–771.

(5) Li, H.; Wu, K.; Lim, J.; Song, H.-J.; Klimov, V. I. Doctor-Blade Deposition of Quantum Dots onto Standard Window Glass for Low-Loss Large-Area Luminescent Solar Concentrators. *Nature Ener.* **2016**, *1* (12). https://doi.org/10.1038/nenergy.2016.157.

(6) B. O. Dabbousi; J. Rodriguez-Viejo; F. V. Mikulec; J. R. Heine; H. Mattoussi; R. Ober; K. F. Jensen; M. G. Bawendi. (CdSe)ZnS Core-Shell Quantum Dots: Synthesis and Characterization of a Size Series of Highly Luminescent Nanocrystallites. *J. Phys. Chem. B* **1997**, *101*, 9463–9475.

(7) Drijvers, E.; De Roo, J.; Geiregat, P.; Fehér, K.; Hens, Z.; Aubert, T. Revisited Wurtzite CdSe Synthesis: A Gateway for the Versatile Flash Synthesis of Multishell Quantum Dots and Rods. *Chem. Mater.* **2016**, *28* (20), 7311–7323.

(8) Protesescu, L.; Nachtegaal, M.; Voznyy, O.; Borovinskaya, O.; Rossini, A. J.; Emsley, L.; Copéret, C.; Günther, D.; Sargent, E. H.; Kovalenko, M. V. Atomistic Description of Thiostannate-Capped CdSe Nanocrystals: Retention of Four-Coordinate SnS4 Motif and Preservation of Cd-Rich Stoichiometry. *J. Am. Chem. Soc.* **2015**, *137* (5), 1862–1874.

(9) Chen, O.; Zhao, J.; Chauhan, V. P.; Cui, J.; Wong, C.; Harris, D. K.; Wei, H.; Han, H. S.; Fukumura, D.; Jain, R. K.; et al. Compact High-Quality CdSe-CdS Core-Shell Nanocrystals with Narrow Emission Linewidths and Suppressed Blinking. *Nat. Mater.* **2013**, *12* (5), 445–451.

(10) Juhás, P.; Cherba, D. M.; Duxbury, P. M.; Punch, W. F.; Billinge, S. J. L. Ab Initio Determination of Solid-State Nanostructure. *Nature* **2006**, *440* (7084), 655–658.

(11) Li, R.; Lu, S.; Kim, D.; Schönecker, S.; Zhao, J.; Kwon, S. K.; Vitos, L. Stacking Fault Energy of Face-Centered Cubic Metals: Thermodynamic and *Ab Initio* Approaches. *J. Phys. Condens. Mat.* **2016**, *28* (39), 395001.

(12) Kelestemur, Y.; Guzelturk, B.; Erdem, O.; Olutas, M.; Erdem, T.; Usanmaz, C. F.; Gungor, K.; Demir, H. V. CdSe/CdSe1–XTex Core/Crown Heteronanoplatelets: Tuning the Excitonic Properties without Changing the Thickness. *J. Phys. Chem. C* **2017**, *121* (8), 4650–4658.

(13) Pietryga, J. M.; Park, Y.-S.; Lim, J.; Fidler, A. F.; Bae, W. K.; Brovelli, S.; Klimov, V. I. Spectroscopic and Device Aspects of Nanocrystal Quantum Dots. *Chem. Rev.* **2016**, *116* (18), 10513–10622.

(14) Nasilowski, M.; Mahler, B.; Lhuillier, E.; Ithurria, S.; Dubertret, B. Two-Dimensional Colloidal Nanocrystals. *Chem. Rev.* **2016**, *116* (18), 10934–10982.

(15) Fedin, I.; Talapin, D. V. Colloidal CdSe Quantum Rings. *J. Am. Chem. Soc.* **2016**, *138* (31), 9771–9774.

(16) Azpiroz, J. M.; De Angelis, F. Ligand Induced Spectral Changes in CdSe Quantum Dots. *ACS Appl. Mater. Interfaces* **2015**, *7* (35), 19736–19745.

(17) Ip, A. H.; Thon, S. M.; Hoogland, S.; Voznyy, O.; Zhitomirsky, D.; Debnath, R.; Levina, L.; Rollny, L. R.; Carey, G. H.; Fischer, A.; et al. Hybrid Passivated Colloidal Quantum Dot Solids. *Nat. Nanotechnol.* **2012**, *7* (9), 577–582.

(18) Li, X.; Zhao, Y.-B.; Fan, F.; Levina, L.; Liu, M.; Quintero-Bermudez, R.; Gong, X.; Quan, L. N.; Fan, J.; Yang, Z.; et al. Bright Colloidal Quantum Dot Light-Emitting Diodes Enabled by Efficient Chlorination. *Nature Photonics* **2018**, *12* (3), 159–164.

(19) Pan, J.; Shang, Y.; Yin, J.; De Bastiani, M.; Peng, W.; Dursun, I.; Sinatra, L.; El-Zohry, A. M.; Hedhili, M. N.; Emwas, A.-H.; et al. Bidentate Ligand-Passivated $CsPbI_3$ Perovskite Nanocrystals for Stable Near-Unity Photoluminescence Quantum Yield and Efficient Red Light-Emitting Diodes. *J. Am. Chem. Soc.* **2018**, *140* (2), 562–565.

(20) C. B. Murray; D. J. Noms; M. G. Bawendi. Synthesis and Characterization of Nearly Monodisperse CdE (E = S, Se, Te) Semiconductor Nanocrystallites. *J. Am. Chem. Soc.* **1993**, *115*, 8706–8715.

(21) Park, J.; Joo, J.; Kwon, S. G.; Jang, Y.; Hyeon, T. Synthesis of Monodisperse Spherical Nanocrystals. *Angew. Chem.* **2007**, *46* (25), 4630–4660.

(22) Gao, Y.; Peng, X. Crystal Structure Control of CdSe Nanocrystals in Growth and Nucleation: Dominating Effects of Surface versus Interior Structure. *J. Am. Chem. Soc.* **2014**, *136* (18), 6724–6732.

(23) Chen, O.; Chen, X.; Yang, Y.; Lynch, J.; Wu, H.; Zhuang, J.; Cao, Y. C. Synthesis of Metal-Selenide Nanocrystals Using Selenium Dioxide as the Selenium Precursor. *Angew. Chem.* **2008**, *47* (45), 8638–8641.

(24) Qu, L.; Peng, X. Control of Photoluminescence Properties of CdSe Nanocrystals in

Growth. *J. Am. Chem. Soc.* **2002**, *124* (9), 2049–2055.

(25) Huang, J.; Kovalenko, M. V.; Talapin, D. V. Alkyl Chains of Surface Ligands Affect Polytypism of CdSe Nanocrystals and Play an Important Role in the Synthesis of Anisotropic Nanoheterostructures. *J. Am. Chem. Soc.* **2010**, *132* (45), 15866–15868.

(26) C. B. Murray; C. R. Kagan. Synthesis and Characterization of Monodisperse Nanocrystals and Close-Packed Nanocrystals Assemblies. *Annu. Rev. Mater. Sci.* **2000**, *30*, 545–610.

(27) van Embden, J.; Chesman, A. S. R.; Jasieniak, J. J. The Heat-Up Synthesis of Colloidal Nanocrystals. *Chem. Mater.* **2015**, *27* (7), 2246–2285.

(28) Kwon, S. G.; Hyeon, T. Formation Mechanisms of Uniform Nanocrystals via Hot-Injection and Heat-Up Methods. *Small* **2011**, *7* (19), 2685–2702.

(29) Campos, M. P.; Hendricks, M. P.; Beecher, A. N.; Walravens, W.; Swain, R. A.; Cleveland, G. T.; Hens, Z.; Sfeir, M. Y.; Owen, J. S. A Library of Selenourea Precursors to PbSe Nanocrystals with Size Distributions near the Homogeneous Limit. *J. Am. Chem. Soc.* **2017**, *139* (6), 2296–2305.

(30) Gaponik, N.; Talapin, D. V.; Rogach, A. L.; Eychmüller, A.; Weller, H. Efficient Phase Transfer of Luminescent Thiol-Capped Nanocrystals: From Water to Nonpolar Organic Solvents. *Nano Lett.* **2002**, *2* (8), 803–806.

(31) Voznyy, O.; Thon, S. M.; Ip, A. H.; Sargent, E. H. Dynamic Trap Formation and Elimination in Colloidal Quantum Dots. *J. Phys. Chem. Lett.* **2013**, *4* (6), 987–992.

(32) Jang, Y.; Shapiro, A.; Isarov, M.; Rubin-Brusilovski, A.; Safran, A.; Budniak, A. K.; Horani, F.; Dehnel, J.; Sashchiuk, A.; Lifshitz, E. Interface Control of Electronic and Optical Properties in IV-VI and II-VI Core/Shell Colloidal Quantum Dots: A Review. *Chem. Comm.* **2017**, *53* (6), 1002–1024.

(33) Giansante, C.; Infante, I. Surface Traps in Colloidal Quantum Dots: A Combined Experimental and Theoretical Perspective. *J. Phys. Chem. Lett.* **2017**, *8* (20), 5209–5215.

(34) Utterback, J. K.; Grennell, A. N.; Wilker, M. B.; Pearce, O. M.; Eaves, J. D.; Dukovic, G. Observation of Trapped-Hole Diffusion on the Surfaces of CdS Nanorods. *Nat. Chem.* **2016**, *8* (11), 1061–1066.

(35) Jain, A.; Voznyy, O.; Hoogland, S.; Korkusinski, M.; Hawrylak, P.; Sargent, E. H. Atomistic Design of CdSe/CdS Core-Shell Quantum Dots with Suppressed Auger Recombination. *Nano Lett.* **2016**, *16* (10), 6491–6496.

(36) Kuno, M.; Fromm, D. P.; Hamann, H. F.; Gallagher, A.; Nesbitt, D. J. Nonexponential "Blinking" Kinetics of Single CdSe Quantum Dots: A Universal Power Law Behavior. *J. Chem. Phys.* **2000**, *112* (7), 3117–3120.

(37) Mahler, B.; Spinicelli, P.; Buil, S.; Quelin, X.; Hermier, J.-P.; Dubertret, B. Towards Non-Blinking Colloidal Quantum Dots. *Nat. Mater.* **2008**, *7* (8), 659–664.

(38) Pu, C.; Peng, X. To Battle Surface Traps on CdSe/CdS Core/Shell Nanocrystals: Shell Isolation versus Surface Treatment. *J. Am. Chem. Soc.* **2016**, *138* (26), 8134–8142.

(39) Bae, W. K.; Park, Y.-S.; Lim, J.; Lee, D.; Padilha, L. A.; McDaniel, H.; Robel, I.; Lee, C.; Pietryga, J. M.; Klimov, V. I. Controlling the Influence of Auger Recombination on the Performance of Quantum-Dot Light-Emitting Diodes. *Nat. Commun.* **2013**, *4* (1).

(40) Jun, S.; Jang, E. Bright and Stable Alloy Core/Multishell Quantum Dots. *Angew. Chem.* **2013**, *52* (2), 679–682.

(41) Jang, E.; Jun, S.; Jang, H.; Lim, J.; Kim, B.; Kim, Y. White-Light-Emitting Diodes with Quantum Dot Color Converters for Display Backlights. *Adv. Mater.* **2010**, *22* (28), 3076–3080.

(42) Altintas, Y.; Genc, S.; Talpur, M. Y.; Mutlugun, E. CdSe/ZnS Quantum Dot Films for High Performance Flexible Lighting and Display Applications. *Nanotechnology* **2016**, *27* (29), 295604.

(43) Zhu, R.; Luo, Z.; Chen, H.; Dong, Y.; Wu, S.-T. Realizing Rec. 2020 Color Gamut with Quantum Dot Displays. **2015**, 14.

(44) Bronstein, N. D.; Yao, Y.; Xu, L.; O'Brien, E.; Powers, A. S.; Ferry, V. E.; Alivisatos, A. P.; Nuzzo, R. G. Quantum Dot Luminescent Concentrator Cavity Exhibiting 30-Fold Concentration. *ACS Photonics* **2015**, *2* (11), 1576–1583.

(45) Greve, K. D.; Press, D.; McMahon, P. L.; Yamamoto, Y. Ultrafast Optical Control of Individual Quantum Dot Spin Qubits. *Rep. Prog. Phys.* **2013**, *76* (9), 092501.

(46) Buckley, S.; Rivoire, K.; Vučković, J. Engineered Quantum Dot Single-Photon Sources. *Rep. Prog. Phys.* **2012**, *75* (12), 126503.

(47) Shirasaki, Y.; Supran, G. J.; Bawendi, M. G.; Bulović, V. Emergence of Colloidal Quantum-Dot Light-Emitting Technologies. *Nat. Photonics* **2013**, *7* (1), 13–23.

(48) Bruns, O. T.; Bischof, T. S.; Harris, D. K.; Franke, D.; Shi, Y.; Riedemann, L.; Bartelt, A.; Jaworski, F. B.; Carr, J. A.; Rowlands, C. J.; et al. Next-Generation in Vivo Optical Imaging with Short-Wave Infrared Quantum Dots. *Nat. Biomed. Eng.* **2017**, *1* (4), 0056.

(49) Billinge, S. The Nanostructure Problem. *Physics* **2010**, *3, 25*.

(50) Billinge, S. J. L.; Levin, I. The Problem with Determining Atomic Structure at the Nanoscale. *Science* **2007**, *316* (5824), 561–565.

(51) Masadeh, A. S.; Bozin, E.; Farrow, C. L.; Paglia, G.; Juhas, P.; Karkamkar, A.; Kanatzidis,

M. G.; Billinge, S. J. L. Quantitative Size-Dependent Structure and Strain Determination of CdSe Nanoparticles Using Atomic Pair Distribution Function Analysis. *Phys. Rev. B* **2007**, *76* (11).

(52) Yang, X.; Masadeh, A. S.; McBride, J. R.; Božin, E. S.; Rosenthal, S. J.; Billinge, S. J. L. Confirmation of Disordered Structure of Ultrasmall CdSe Nanoparticles from X-Ray Atomic Pair Distribution Function Analysis. *Phys. Chem.* **2013**, *15* (22), 8480.

(53) Bawendi, M. G.; Kortan, A. R.; Steigerwald, M. L.; Brus, L. E. X-ray Structural Characterization of Larger CdSe Semiconductor Clusters. *J. Chem. Phys.* **1989**, *91* (11), 7282–7290.

(54) Kumpf, C.; Neder, R. B.; Niederdraenk, F.; Luczak, P.; Stahl, A.; Scheuermann, M.; Joshi, S.; Kulkarni, S. K.; Barglik-Chory, C.; Heske, C.; et al. Structure Determination of CdS and ZnS Nanoparticles: Direct Modeling of Synchrotron-Radiation Diffraction Data. *J. Chem. Phys.* **2005**, *123* (22), 224707.

(55) Farrow, C. L.; Shi, C.; Juhás, P.; Peng, X.; Billinge, S. J. L. Robust Structure and Morphology Parameters for CdS Nanoparticles by Combining Small-Angle X-Ray Scattering and Atomic Pair Distribution Function Data in a Complex Modeling Framework. *J. Appl. Cryst.* **2014**, *47* (2), 561–565.

(56) Owen, J.; Brus, L. Chemical Synthesis and Luminescence Applications of Colloidal Semiconductor Quantum Dots. *J. Am. Chem. Soc.* **2017**, *139* (32), 10939–10943.

2

Characterization Methods at the Nanoscale

As presented in the previous Chapter, the functional properties of nanosized materials are deeply influenced not only by their atomic-scale structure, but also by additional properties, such as the crystal size and morphology, composition and surface reconstruction or by the presence of various kind of defectiveness. More relevantly, the impact of structural defects on the properties of semiconducting nanocrystals are still not fully understood. This aspect underlines the need of increasing both the knowledge about defects in nanoparticles and the power of experimental and computational tools for their investigation. This Chapter briefly introduces a number of conventional and advanced methods of physico-chemical characterization which have been used in this Ph.D. project and discusses their potentiality and limits in investigating materials at the nanoscale (in particular for II-VI semiconducting nanocrystals). Conventional laboratory methods used in this project include: Transmission Electron Microscopy (TEM), also in High Resolution (HRTEM) mode, Absorption/Emission Spectroscopy and X-ray Powder Diffractometry (XRPD). Advanced methods of characterization include: Wide Angle X-ray Total Scattering (WAXTS), Small Angle X-ray Scattering (SAXS) and Nuclear Magnetic Resonance (NMR), the latter as an innovative mode, hereafter presented.
This section further addresses the importance of a multiple scale characterization, built upon the combination of several and complementary techniques and the need of a robust strategy for characterizing complex, highly defective, CdSe-based colloidal QDs.

2.1 Conventional (Laboratory) Methods of Nanocrystal Characterization

2.1.1 (High Resolution) Transmission Electron Microscopy

Transmission Electron Microscopy is by far the most used imaging technique for studying materials at the nanoscale. The reason for the incredible success of TEM is due to its ability to produce pictures of nanoparticles at atomic-resolution (in real space) for "direct" observation (not requiring a complex modeling or information retrieval). The image is obtained using a high voltage electron beam (100-300 kV) passing through the sample and creating a high-resolution image. Today, TEM is a versatile tool for the direct investigation of a single particle or of a limited number of them, enabling an immediate interpretation. However, TEM may be not extremely informative if the particle is too small,[1] too sensitive to the electron beam[2] or highly defective.

Important aspects to be taken into account about microscopies in general is that they do not bear a high statistical relevance: the extracted information comes from counting single particles from a small portion of the sample, making this approach less-than-ideal for large-scale implementation.[3]

In TEM, the conventional sample preparation consists in dropping few μl droplets of a diluted nanocrystal dispersion in a non-polar solvent onto a carbon-coated copper-grid. The analysis is performed in high vacuum and can only provide 2D-information on 3D-objects. Despite the fact that TEM is the most used technique for studying QD size, size-dispersion and morphology, a major problem related to TEM and HRTEM emerges when dealing with colloidal suspensions of semiconductor nanocrystals. For example, in the case of CdSe and, more in general, of nanosized metal chalcogenides, several issues arise due to the intrinsic properties of these samples. Indeed, a "chemically stable", non-coalescing, nanoparticle is typically coated with a thick shell of organic/inorganic ligands that avoids particle sinterization/aggregation and provides a high stability to the sample. In order to be well investigated, the nanocrystals need to be washed properly several times to reduce the residual precursors and the excess of organic matter on the carbon-

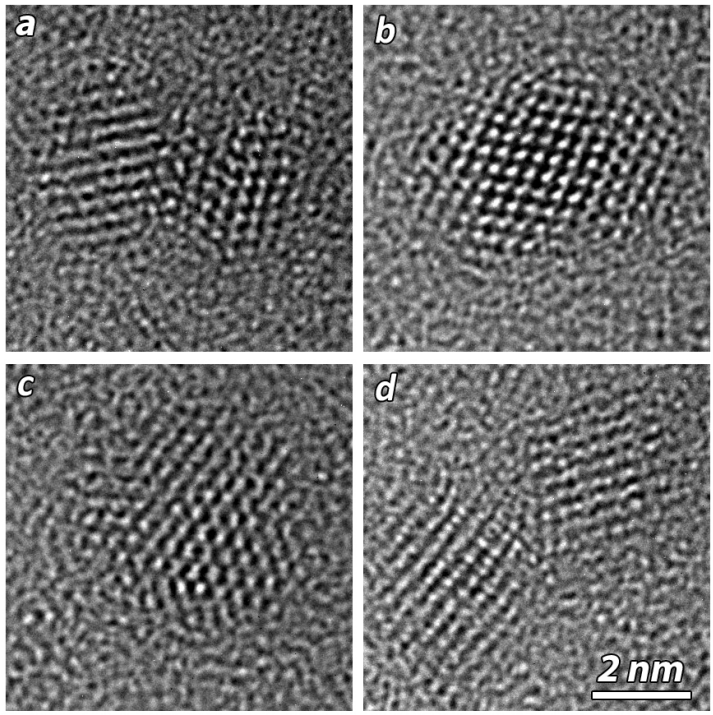

Figure 2.1. *TEM pictures of CdSe nanoparticles from highly monodisperse samples with average diameter of 3.8 nm. The single pictures show the main problems related to TEM and HR-TEM analysis such as: crystal coalescence due to the washing process (a), badly defined surface due to the presence of SF (b), blurry pictures due to excess of ligands (c) and poorly defined structure due to less than ideal particle orientations (d).*

coated copper-grid, which typically provides additional blurring effects on the final image. The standard washing process requires cycles of precipitation and re-dispersion of the nanoparticles (by a solvent/anti-solvent treatment), playing on the particles solubility. Every time a cycle is completed, a small fraction of particles is selectively erased (generally the smallest fraction remains in the waste solution), changing the average size, size-dispersion of the sample and sometimes causing unwanted alterations, such as coalescence, if some ligands are removed from the nanoparticle surface. Another problem related to CdSe is the presence of stacking faults (treated in depth in Chapter 4) that brake the periodicity of the crystal and tend to produce irregular surfaces, disfavoring a correct orientation of the nanocrystal for (HR)TEM analysis[4] (see Figure 2.1). Despite these limitations, the

technique is able to provide "easy to interpret" 2D pictures of faulted CdSe NCs, and important information about the nature of the crystalline phase can be retrieved therefrom.

In this Ph.D. thesis, TEM pictures of CdSe NPs were obtained using a JEOL JEM-2200FS electron microscope operating at 200 kV, located at the Inorganic Chemistry Department of ETH Zurich, in collaboration with Prof. Maksym Kovalenko's group. In Chapter 7, TEM pictures acquired on Pt NPs are also shown, which were provided by Dr. Andrea Migliori of the Institute of Micro Technology and Microsystems of CNR (Bologna, Italy), and measured on a FEI TECNAI F20 electron microscope operating at 200 kV.

2.1.2 Absorption/Emission Spectroscopy in the Visible Range

As explained in Chapter 1, II-VI semiconductors are very appealing materials, some of which already filling the market of high-tech devices, mostly thanks to their optical properties tunable with size.[5] Using this criterion, and considering that a real sample is made by several particles represented by an average size, a size-dispersion and a concentration, one can ideally calculate an absorption profile as being shaped by the sum of the contributions from all the particles which constitute the sample. The *experimental* absorption peak height, position and FWHM are indeed related to the NPs average size, their size-dispersion, sample concentration and QD extinction coefficient. Thanks to this dependence, with the simple measurement of an absorbance spectrum, it is theoretically possible to obtain a series of valuable information about size, size-dispersion and concentration of a colloidal sample of II-VI semiconducting QDs. Using this approach, Yu et al.[6] and Jasieniak et al.[7] calculated the molar extinction coefficient, ε, and the UV-Vis spectral dependence in highly monodisperse CdSe samples with sizes ranging from 1.5 to 8.0 nm, combining Absorption spectroscopy, Inductively Coupled Plasma-Optical Emission Spectroscopy (ICP-OES) and TEM evidences. The used strategy requires, for each CdSe sample:

- the measurement of the full absorption spectrum;

- the quantitative analysis of Cd^{2+} ions concentration, after the digestion of a known quantity of colloidal suspension in aqua regia and using calibration standards of known $Cd(NO_3)_2$ concentration;
- the calculation of the particle volumes using TEM sizing curves;
- the calculation of [QDs](M) in the original solution, using the density of WZ crystal structure (5.81 g/cm^3) and the Cd/Se stoichiometric ratio (1.15:1) reported in the literature.

The molar-extinction coefficient at the peak maximum ε $(M^{-1}cm^{-1})$ was obtained from the absorbance spectrum using the Lambert-Beer law, as follows:

$$\varepsilon = \frac{[QD]}{Abs} l$$

$Eq.2.1$

where l is the optical path length and Abs is the value of maximum absorbance.
In the original paper,[7] the observables were fitted using an empirical function, a fourth order polynomial in λ, thus obtaining phenomenological expressions able to predict microstructural parameters such as average size (D) and material concentration ($[CdSe]_{NPs}$). These equations follow:

$$D(nm) = 59.60816 - 0.54736\lambda + 1.8873 \times 10^{-3}\lambda^2 - 2.85743 \times 10^{-6}\lambda^3 + 1.62974 \times 10^{-9}\lambda^4$$

$Eq.2.2$

$$[CdSe]_{NPs}(M) = \frac{Abs}{l\varepsilon_{1s}} \times \frac{\Delta E_{1S,HWHF}}{0.06}$$

$Eq.2.3$

where:

$\varepsilon_{1S}(M^{-1}cm^{-1}) = 155507 + 6.67054 \times 10^{13} e^{\left(-\frac{E_{1S}}{0.10551}\right)}$

$\Delta E_{1S,HWHF}$: Half-width-half-maximum of the first absorption peak on the low energy side.

Thanks to these two equations, one can rapidly identify the average size and size-dispersion (from Equation 2.2) and the concentration (from Equation 2.3) of the as-

prepared sample. Information about size and concentration is particularly important for the synthetic chemist and the material engineer, since it enables to:

- test applications by precisely knowing the nanoparticles size and the amount of nanoparticles used;
- use the newly synthetized sample for successive synthesis steps (such as ligand/cation exchange or shell growth) and calibrating the stoichiometry of the reaction.

Assuming that all the particles contained in the colloidal suspension are spherical and the number-based size-distribution follows known (say, *log-normal*) law $\xi_N(D)$, a step forward in estimating the average diameter ($< D >$) and diameter dispersion (σ) from the absorption curve has been developed in Como by the To.Sca.Lab group.[8]

Given $< D >$ and σ, by numerically calculating Equations 2.1 and 2.2 to obtain $E_{1S}(eV)$ and $\varepsilon_{1S}(M^{-1}cm^{-1})$ as a function of the crystal diameter from the curve proposed by Jasieniak et. al,[7] we found it possible to compute the absorption curves by convoluting the log-normal number-based distribution $\xi_N(D)$ with $\varepsilon_{1S}(D)$, taking into account the full $E_{1S}(D)$ dependence, and adding a physically-sound broadening term $g(E, D)$, as follows:

$$Abs(E) \propto \int_0^{\infty} g(E,D)\, \xi_N(D) \varepsilon_{1S}(D) dD \qquad Eq.\,2.4$$

where:

$$g(E,D) = e^{\left(-\frac{E-E_{1S}(D)}{\sigma_R}\right)^2} \qquad Eq.\,2.5$$

$$E_{1S}(eV) = 1022.1 - 1627.6D + 979.34D^2 - 262.87D^3 + 26.514D^4 \qquad Eq.\,2.6a$$

$$\lambda(nm) = 4.8806 - 1.7959D + 0.4426D^2 - 0.0499D^3 + 0.0021D^4 \qquad Eq.\,2.6b$$

$$\xi_N(D) = e^{-\frac{1}{2}\frac{\left(log(D)-log(<D>)\right)^2}{\sigma^2}} \qquad Eq.\,2.6c$$

$$\varepsilon_{1S}(M^{-1}cm^{-1}) = 300773 - 140906D + 33478D^2$$

$Eq. 2.6d$

with $\sigma_R = 0.0255\ eV$ (as derived from the frequency of the lowest infrared Raman active mode from the bulk,[9] corresponding to the most populated vibrational level at room temperature). The application of this model to the cases studied in this Ph.D. thesis will appear in Chapter 6.

Since optical, electronic and structural properties also depend from the actual crystal phase, in recent years, Lim and coworkers,[10] extending the absorption measurement range to NUV (Near UV) and MUV (Medium UV), revealed interesting absorption profile differences in MUV region for ZB and WZ CdSe cQDs. The goal of this recently reported study relies on the use of the absorption spectroscopy for the crystal phase identification, enabling, through a fast measurement, to simultaneously extract information about the predominant crystal phase and the average size of the NPs constituting the sample.

In spite of its limitation on morphological and structural characterization, absorption, in combination with the emission spectroscopy, is the mother technique for *absolute* PL quantum yield (QY) measurement.[11] The standard procedure adopted by many consists in a separate PL measurement of a certified dye molecule taken as a standard,[12] and performing the following calculations:[11]

$$\frac{QY_S \times Abs_S \times n_{sol(s)}^2}{I_S} = \frac{QY_D \times Abs_D \times n_{sol(D)}^2}{I_D}$$

$Eq. 2.7$

$$QY_S = QY_D \times \frac{Abs_D}{Abs_S} \times \frac{I_S}{I_D} \times \frac{n_{sol(D)}^2}{n_{sol(s)}^2}$$

$Eq. 2.8$

where:

I_x : Integrated intensity of the Photoluminescence spectra

Abs_x : Absorbance at the excitation wavelength

$n_{sol(x)}$: Solvent refractive index

x : specie; $x = D$ dye and $x = S$ sample

In this Ph.D. thesis work, UV/VIS absorption spectra were collected on colloidal suspensions of CdSe QDs using a JASCO V670 spectrometer and PL profiles using a Fluorolog iHR 320 Horiba Jobin Yvon spectrofluorometer at the Inorganic Chemistry Department of ETH Zurich, in collaboration with Prof. Maksym Kovalenko's group.

2.1.3 Conventional X-Ray Powder Diffraction (XRPD)

As for bulk materials, XRPD is the most popular structural characterization technique for (poly)crystalline powders. In microcrystalline samples, this technique has reached a high degree of maturity; the methods of analysis rely on the hypothesis of a long-range order of the atomic arrangement in the crystal structure. In this case, the X-ray diffraction trace potentially contains a lot of information such as crystal phase, crystallite size (coherent domain), shape and lattice strain, interpretable through the classical whole pattern profile fitting procedures (*e.g.,* the structureless Le Bail[13] or Pawley[14] approaches or the commonly used Rietveld method[15]). As for most experimental techniques which rely on instruments with finite resolution broadening, it is also important to outline that any XRPD pattern $H(2\vartheta)$, is always the convolution of two independent contributions, F and G:

$$H(2\vartheta) = \int_0^{\pi} F(2\vartheta')G(2\vartheta - 2\vartheta')d2\vartheta' \qquad Eq.\,2.9$$

$F(2\vartheta)$ originates from the instrument and $G(2\vartheta)$ originates from the sample. As a consequence of this fact, the broadening of diffraction peaks has two main different sources, which normally include sample-dependent and sample-independent contributions.

- Peak broadening originating from the sample:
  - finite size effects;
  - crystal lattice distortion;
  - structural defects (*e.g.* point, linear or planar);

- Broadening originating from the instrument:
  - not perfectly monochromatic X-ray source;
  - axial divergence of the incident/diffracted beam;
  - size of slits and detector type;
  - diffractometer misalignment;
  - sample transparency and size;
  - and more…

When dealing with nanomaterials, the magnitude of the crystalline domains is drastically reduced, making the instrumental broadening contributions, in many cases of extreme downsizing, negligible. For this reason, many papers in the field report the simple and direct use of Scherrer's Equation[16] (reported in Equation 2.10) for the determination of the crystal size, apparently, and arbitrarily, completely disregarding the contribution of lattice distortions and other structural defects to peak widths and shapes.

$$< D >= \frac{K\lambda}{\beta \cos \vartheta} \qquad Eq.\,2.10$$

where:

β : Full-Width-Half-Maximum (or, more precisely, the integral breadth – *rarely used*)

K : Shape factor, 0.94 for spherical particles

λ : Operational wavelength [Å]

2ϑ : Diffraction angle

Recently, several papers presented and discussed the highly defective nature of very small nanoparticles, attributed to the high fraction of surface atoms. In particular, nanoscale II-VI semiconductors, such as CdS, CdSe, CdTe, ZnO, ZnS, etc., due to the presence of stacking defects that strongly contribute to peak broadening,[17–19] discredited the use of this equation making it only a rough approximation, providing, if taken in a more critical way, a lower limit for the average crystal size. For this reason, in this thesis, laboratory XRPD data on CdSe were used only for rough phase

identification, restricting the analysis to the simple peak indexing and to a qualitative ranking of nanomaterial sizes.
Even if Scherrer's equation is considered a too rough approximation, also Rietveld refinement methods may fail in reproducing the correct mass-based average nanoparticle size. The main reasons that turn Rietveld methods (*sensu lato*) unsuitable for nanomaterials are: i) the vanishing of the assumption of the infinite periodicity of the crystal lattice along all the crystallographic directions; and ii) neglecting, by definition, the contribution of diffuse (non-Bragg) scattering generated by the finite crystal size and its distribution, crystal shape and defectiveness and other kind of static or dynamic disorder, which Bragg theory alone cannot cope with. For these reasons, innovative diffraction/scattering routes to the investigation of nanomaterials are required which, as later reported are central to this work.

In this Ph.D. thesis, laboratory XRPD measurements of dry CdSe QDs were performed on a STOE STADI P powder diffractometer, operating in transmission mode (capillary mounting) at the Inorganic Chemistry department of ETH Zurich, in collaboration with Maksym Kovalenko's group and on a RIGAKU MINIFLEX powder diffractometer, operating in reflection mode (flat plate mounting) at the Department of Science and High technology of the University of Insubria, Como, Italy.

2.2 Advanced Characterization Methods

2.2.1 Wide Angle X-Ray Total Scattering Techniques (WAXTS)

Dealing with nanomaterials, lowering the size of the coherent domains down to few nanometers can be naively considered as constructing a *defective* replica of the corresponding bulk material; nevertheless, the information from the XRPD experimental data is generally highly degraded, while the complexity of the structure is much greater.[20] The failure of the conventional crystallographic methods in determining with high precision the atomic arrangement in

nanostructured materials (including defects) is known as the *nanostructure problem*.[21] Finite size effects significantly broaden the *Bragg* peaks and increase their overlap; a *diffuse* scattering appears between and below them. Additionally, anisotropic shapes of the nanoparticles affect the width and shape of Bragg peaks and the distribution of the scattered intensity. The substantial portion of atoms belonging to the surface (due to the higher surface/volume ratio, upon lowering the sizes) gives importance to phenomena that are usually neglected at the bulk scale; in particular, surface relaxation effects, as a consequence of the minimization of the surface energy that induces surface strains, can also modify the core structure and the nature of stable extended defects.[22] In colloidal synthesis, the surface structure of the nanoparticles is also strongly influenced by the chemical environment and by the nature of the passivating surfactant agents.[23,24] Many other structural defects may occur, depending on the type of the nanocrystal (e.g. stacking faults in *fcc* and *hcp* structures),[3] resulting in additional diffuse scattering in the diffraction patterns and less predictable peak broadening and shifts, no longer interpretable by the conventional crystallographic laws of ideally periodic systems.

According to these considerations, there is an urgent need of developing advanced characterization techniques to tackle the complex problem of fully characterizing *nanoscale* materials, in terms of structure, composition, size, shape, and their distribution. Starting from WAXTS data collection, two complementary methods for nanoparticle characterization are presently used, and are based on the:

- Debye Scattering Equation (DSE);
- Pair (or Radial) Distribution Function (PDF).

Since the effects of the presence of *structural distortions* and *disorder* on the X-ray powder diffraction pattern induces additional peak broadening and an increase of the diffuse scattering beyond and below the *Bragg* peaks, disentangling those from *size effects* is not a trivial task.

Significantly, in the DSE and PDF approaches, which are not restricted to the presence of long-range order, it is possible to simultaneously reproduce, or deal with, both Bragg and diffuse scattering, where the structural and defects information are simultaneously encoded. For this reason, DSE and PDF are called Total Scattering Methods.

For both DSE and PDF approaches, the physically-based theory behind the two methods, their use, and details on data collection and treatment, are presented in more details in the next Chapter.

In this thesis, WAXTS diffraction profiles for DSE analysis were collected at the Swiss Light Source (SLS) of the Paul Scherrer Institut (PSI), at the Material Science Beamline MS-X04SA, and WAXTS diffraction profiles for PDF analysis were collected at the Brookhaven National Laboratory (BNL) at the 28-ID-1 XPD beamline of the NSLS II synchrotron by Dr. Federica Bertolotti (Aarhus University & To.Sca.Lab).

2.2.2 Small Angle X-Ray Scattering (SAXS)

SAXS is an X-Ray-based structural and analytical method for the characterization of particles in terms of supramolecular structure, average size, size-dispersion and shape, and is best suited for systems lying at 1 to 100 nm length scale. This technique is presently used for the characterization of a large variety of biological systems, colloids, minerals, etc. and it is here presented with particular reference to nanocrystalline materials of few nanometers in size.
As for many other scattering methods, measurements performed at a given Q enable the investigation the "density" variability (inhomogeneity) in a sample on a distance regime inversely proportional to Q (see Equation 2.11 and Figure 2.2).

$$D_{SAXS} = \frac{2\pi}{Q} \qquad Eq.\,2.11$$

where:
$Q = (4\pi \sin\vartheta)/\lambda$: scattering vector [Å^{-1}]

Using this relationship, it is therefore possible to envisage which kind of features can be studied at different experimentally accessible Q values, depending on the analyzed sample.

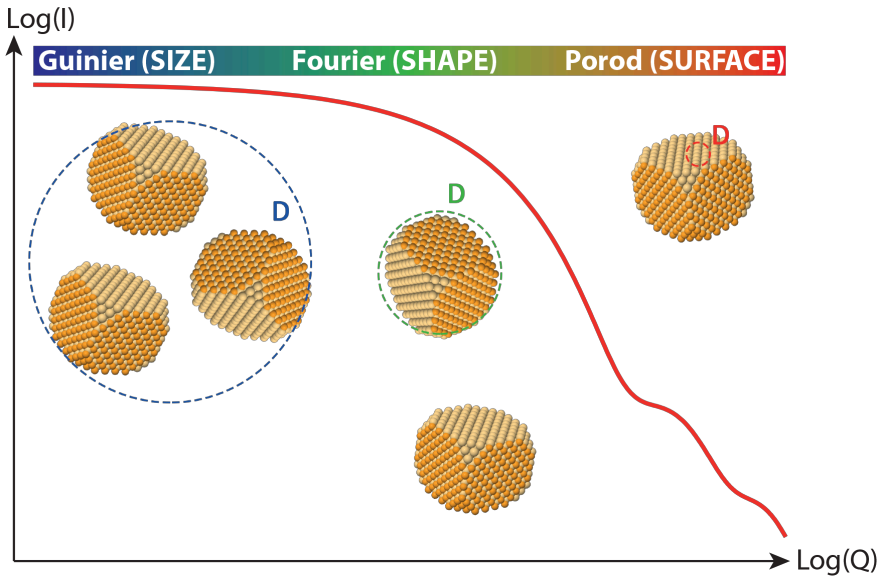

Figure 2.2. *Graphical representation of probed sample length scale in SAXS experiments. Large Q values (i.e. small D's as in red circle) promote the study of small "windows" giving information about the particle surface while, decreasing Q (i.e. at larger D's, see green to blue circles), larger lengths are explored, providing information on size, shape and particles aggregation.*

The SAXS pattern can be then divided in three regions:

- High Q or *Porod* domain (small D): gives information about the surface properties and faceting;
- Intermediate Q (or *Fourier*) domain: gives information about the NPs size and shape (*form factor*);
- Low Q (or *Guinier*) domain (large D): gives information about the interactions in the system (*structure factor*).

How much signal is measured in a SAXS experiment, and how spread in space, depend on the radiation-matter interaction at such small Q values (which are orders of magnitude smaller than in WAXTS ones). Specifically, if an X-ray beam hits a nanoparticle embedded in a matrix of different electron density, its electron cloud will scatter the X-ray wave, producing an interference pattern at the detector position which, though appearing featureless at first glance, may indeed provide important structural, or, best said, morphological, information. This trace is

distinctive of a specific shape and it is called *form factor*. When a particle with an electron density of ρ_1 is surrounded by a matrix of electron density ρ_2, the intensity measured by a SAXS experiment can be expressed as shown in Equation 2.12:

$$I_p(Q) = I_0(\Delta\rho)^2 V_p^2 P(Q) \qquad Eq.\,2.12$$

Where:
$I_p(Q)$: scattered intensity
I_0: intensity of the incoming beam
$\Delta\rho$: electron density difference between the material and the matrix
V_p: volume of the particle
$P(Q)$: form factor

For real cases, a sample is composed by a large number of particles that are simultaneously irradiated by the same radiation, producing a more complex signal, which than depends on the entire sample features. Simple cases can be however identified and summarized by:

- monodisperse and diluted samples of NPs;
- monodisperse and concentrated sample of NPs;
- size- and shape-polydisperse samples.

In monodisperse diluted samples, where the distance of each single particles with its neighbor is significantly larger than the operational wavelength, the scattering profile virtually corresponds to the form factor. For this reason, Equation 2.12 can be rewritten into Equation 2.13, valid an ensemble of particles of equal size, shape and composition (that is, sharing an identical electron density).

$$I(Q) = N \cdot I_p(Q) \qquad Eq.\,2.13$$

Where:
I_p: intensity scattering contribution of a particle
N: number of rigorously equal but non-interacting particles

In monodisperse, but concentrated (*e.g.* packed) samples, the scattering profile contains the contribution of multiple interference processes. Despite in some

analysis one prefers to avoid such multiple scattering process, in other cases this scattering contribution, originating from the juxtaposed particles (that, in combination with the form factor, produce the *structure factor*), becomes a highly valuable source of information about the nanoparticle packing or, in other words, provides information about the relative position of a single particle with respect to the others. Therefore, Equation 2.13 can to be re-written into Equation 2.14.

$$I(Q) = N \cdot I_p(Q) \cdot S(Q) \qquad Eq.\,2.14$$

Where:
I_p: intensity scattering contribution of a particle
N: number of equal particles
$S(Q)$: structure factor

In real samples of non-interacting particles (*i.e.,* when $S(Q)$=1), where a finite, though small, nanoparticle size distribution is present, the scattering curves can be obtained by summing up all the individual form factors, weighted by the relative contrast and volume of each *i*-th particle.[25]

$$I(Q) = I_0 \cdot \sum_{i=1}^{N} (\Delta\rho)_i^2 V_i^2 P_i(Q) \qquad Eq.\,2.15$$

Where:
I_0: intensity of the incoming beam
N: number of nanoparticles
$(\Delta\rho)_i$: electron density difference between the matrix and the *i*-th particle
V_i: volume of the *i*-th particle
$P_i(Q)$: form factor of the *i*-th particle

The small set of equations presented above is, therefore, sufficient to make us aware that, in the low Q section, a lot of "structural" information is encoded, which can fruitfully be extracted by a careful control of both the experimental data collection process and the subsequent data analysis step.

Notwithstanding, SAXS modeling is not a simple "push-button" procedure of immediate and safe use, as it requires the introduction, and control, of separate physically-based descriptors (including complex analytical formulae even for simple convex polyhedral shapes), not discussed here. Thus, SAXS can provide additional, and independent, information on sample morphology, average size and size dispersion. As anticipated, this technique is completely blind to atomic-scale structural defects, which are absolutely not visible in the low Q-range. Though this appears as a limitation, this feature is also a power of the technique, which, by definition, sees morphology, rather than "structure", making it possible to disentangle, in joint SAXS/WAXTS analyses, their relative contribution to the peak broadening in WAXTS experiments.

Additionally, the information about the *morphology* (as mentioned, sometimes blurred by nanocrystal defectiveness in *WAXTS* data) can be used to determine the nature and size of the exposed facets (particularly if monodisperse samples are studied). This can be an extremely important finding in investigating (nano)crystals growth and their interactions with the chemical environment (particularly in the presence of capping agents, that induce surface reconstruction phenomena).[26,27] Worth of note is that the experimental SAXS pattern can be also fitted using atomistic model through the innovative use of DSE developed in the course of this Ph.D. thesis project. Aspects of this assertion are explained in more details in Chapters 4 and 6.

In this work, SAXS experiments and data modeling were performed at Aarhus University, in collaboration with Prof. Jan Skov Pedersen and Dr. Federica Bertolotti. SAXS data were collected on colloidal CdSe QDs using a Bruker AXS NanoSTAR instrument, equipped with a liquid metal (Gallium) jet source from Excillum AB, Sweden, and homebuilt scatterless slits.[28] This experimental set-up provided very clean SAXS signals, later analyzed by locally available software. In a much more recent experimental session, further CdSe-based nanocrystalline samples (of the CdSe nanoplatelets and CdS@CdSe core-shell type) were measured on the same experimental set up, but they are still awaiting a complete analysis.

2.2.3 Dynamic Nuclear Polarization (DNP), Phase Adjust Spinning Sidebands (PASS) with Incremented Echo-Train Acquisition (PIETA), Nuclear Magnetic Resonance (NMR)

The complete characterization of a nanomaterial and of its properties requires a full understanding of its core structure and of its surface structure-chemistry. The non-periodic structure and the different chemistry of surfaces are fundamental aspects to be investigated to better understand how they can influence the nanomaterial properties. Today, characterizing the surface and its surrounding is an essential step to control and tune properties of nanomaterials, toward their useful incorporation in many fields of technology. NMR is an analytical method affording all specific and detailed information about the connectivity, oxidation state, distribution and symmetry one might desire in the study of NCs surface. In order to investigate these fundamental aspects, solid-state and solution NMR have been extensively used in materials science[29–34] but its wide application, particularly to inorganic materials, suffers from intrinsically low sensitivity. For the specific CdSe case under study, this problem is mainly attributable to:

- low gyromagnetic ratio (^{113}Cd = 56.9x10^{6} rad/(s T));
- low natural abundance of NMR active isotopes (^{113}Cd = 12.26%);
- inhomogeneous nanocrystal surface.

Thanks to many developments in the field, a signal enhancement protocol was recently reported using a Dynamic Nuclear Polarization (DNP) approach.[35] A detailed description on the method is out of the scope of this project thesis and can be found in specialized text.[35,36] However, a short, perhaps naive summary, follows.

DNP makes use of the large polarization of unpaired electrons of radicals (*e.g.*, TEKPol, see Figure 2.3) generated by a flux of microwaves, at the vicinity of their Larmor frequencies, and rapidly transferred to the protons of the solvent (*e.g.,* 1,1,2,2-tetrachloroethane, TCE). Spin diffusion spreads polarization throughout the whole pool of strongly coupled proton spins, from where the polarization transfer is realized to the Cd nuclei in NPs via cross polarization (CP) by irradiating with additional radiofrequencies.

DNP experiments must be run at low temperature (100K) in order to limit the electron and nuclear relaxation, but, in such conditions, the colloidal NCs inevitably

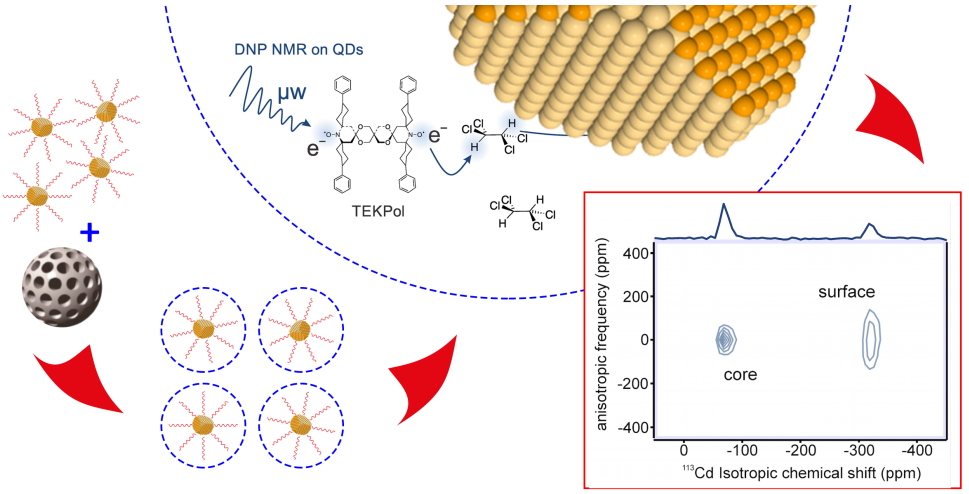

Figure 2.3. *Schematics of the DNP-PASS-PIETA-NMR experiment on colloidal QDs. The use of mesoporous silica limits the aggregation of the particles, producing an enhanced signal due to the efficiency of the polarization transfer on Cd atoms.*

aggregate and precipitate, thus becoming inaccessible to the polarization source. In order to reduce this phenomenon, a large fraction of porous-silica with nanosized pores is impregnated with the nanoparticles sample, acting like a cage and avoiding NCs aggregation.

Despite the enormous DNP-NMR signal enhancement, the defective nature of nanoparticles (due to their reduced domain size and high surface to volume ratio that cause a large environment spin anisotropy for every single spin) makes the interpretation of the broad 1D signal still troublesome. A different approach, which exploits DNP enhancement, has been developed at ETH Zurich in order to separate the information of the Chemical Shift Anisotropy (CSA) from the isotropic components using a Phase Adjust Spinning Sidebands (PASS) in combination with a Phase Incremented Echo Train Acquisition (PIETA).[31] In this very innovative way, it is possible to discriminate the isotropic chemical shift of ^{113}Cd species and evaluate its anisotropy in different CdSe-based cQDs samples. This approach was used in order to capture information about the core and surface order and, at the same time, on faceting and surface chemistry of different types CdSe NPs. The pertinent results are discussed in Chapter 6.

In this work, DNP NMR spectra were acquired using a Bruker Advance III NMR spectrometer equipped with a 395 GHz gyrotron microwave source at the Inorganic Chemistry Department of ETH Zurich, in collaboration with Maksym Kovalenko's group.

Conclusions

As discussed above, the complete and exhaustive characterization of complex nano-systems cannot be accomplished with a single technique. In this thesis, conventional characterization methods, of more general usage, have been supplemented by the advanced methods here briefly described. In particular, dealing with very small and highly defective materials such as CdSe cQDs, disentangling size and shape from defects-induced effects on the position, width and shape of the WAXTS peaks using a DSE-based approach alone, is not a trivial task and makes it necessary resorting to complementary, "atomic structure insensitive", techniques, such as Small Angle X-ray Scattering (SAXS). This analysis is described in Chapter 6. In order to complete the picture, an additional DNP-based NMR method has been here presented and used as an ancillary technique, providing primarily NMR signals originating from cadmium ions populating the nanoparticles surface.

At variance, the elemental Pt nanoparticles embedded in a mesoporous silica matrix discussed in the last part of the thesis (Chapter 7) could not take advantage from any complementary characterization technique, leaving our Wide Angle X-Ray Total Scattering analysis as the dominant source of information for this complex nanocomposite system.

References

(1) McBride, J. R.; Dukes, A. D.; Schreuder, M. A.; Rosenthal, S. J. On Ultrasmall Nanocrystals. *Chem. Phys. Lett.* **2010**, *498* (1–3), 1–9.

(2) Pennycook, T. J.; McBride, J. R.; Rosenthal, S. J.; Pennycook, S. J.; Pantelides, S. T. Dynamic Fluctuations in Ultrasmall Nanocrystals Induce White Light Emission. *Nano Lett.* **2012**, *12* (6), 3038–3042.

(3) Mangel, S.; Houben, L.; Bar-Sadan, M. Revealing Growth Schemes of Nanoparticles in Atomic Resolution: Mapping Stacking Fault Formation and Distribution. *Cryst. Growth Des.* **2015**, *15* (7), 3114–3118.

(4) Wang, Z. L. Transmission Electron Microscopy of Shape-Controlled Nanocrystals and Their Assemblies. *J. Phys. Chem. B* **2000**, *104* (6), 1153–1175.

(5) Pietryga, J. M.; Park, Y.-S.; Lim, J.; Fidler, A. F.; Bae, W. K.; Brovelli, S.; Klimov, V. I. Spectroscopic and Device Aspects of Nanocrystal Quantum Dots. *Chem. Rev.* **2016**, *116* (18), 10513–10622.

(6) Yu, W. W.; Qu, L.; Guo, W.; Peng, X. Experimental Determination of the Extinction Coefficient of CdTe, CdSe, and CdS Nanocrystals. *Chem. Mater.* **2003**, *15* (14), 2854–2860.

(7) Jasieniak, J.; Smith, L.; van Embden, J.; Mulvaney, P.; Califano, M. Re-Examination of the Size-Dependent Absorption Properties of CdSe Quantum Dots. *J. Phys. Chem. C* **2009**, *113* (45), 19468–19474.

(8) Bertolotti, F.; Dirin, D. N.; Ibáñez, M.; Krumeich, F.; Cervellino, A.; Frison, R.; Voznyy, O.; Sargent, E. H.; Kovalenko, M. V.; Guagliardi, A.; et al. Crystal Symmetry Breaking and Vacancies in Colloidal Lead Chalcogenide Quantum Dots. *Nat. Mater.* **2016**, *15* (9), 987–994.

(9) Kelley, A. M.; Dai, Q.; Jiang, Z.; Baker, J. A.; Kelley, D. F. Resonance Raman Spectra of Wurtzite and Zincblende CdSe Nanocrystals. *Chem. Phys.* **2013**, *422*, 272–276.

(10) Lim, S. J.; Schleife, A.; Smith, A. M. Optical Determination of Crystal Phase in Semiconductor Nanocrystals. *Nat. Commun.* **2017**, *8*, 14849.

(11) Grabolle, M.; Spieles, M.; Lesnyak, V.; Gaponik, N.; Eychmüller, A.; Resch-Genger, U. Determination of the Fluorescence Quantum Yield of Quantum Dots: Suitable Procedures and Achievable Uncertainties. *Anal. Chem.* **2009**, *81* (15), 6285–6294.

(12) Brouwer, A. M. Standards for Photoluminescence Quantum Yield Measurements in Solution (IUPAC Technical Report). *Pure Appl. Chem.* **2011**, *83* (12), 2213–2228.

(13) Le Bail, A. Whole Powder Pattern Decomposition Methods and Applications: A Retrospection. *Powder Diff.* **2005**, *20* (04), 316–326.

(14) Pawley, G. S. Unit-Cell Refinement from Powder Diffraction Scans. *J. Appl. Cryst.* **1981**, *14* (6), 357–361.

(15) Rietveld, H. M. A Profile Refinement Method for Nuclear and Magnetic Structures. *J. Appl. Cryst.* **1969**, *2* (2), 65–71.

(16) Scherrer, P. Bestimmung der inneren Struktur und der Größe von Kolloidteilchen mittels Röntgenstrahlen. In *Kolloidchemie Ein Lehrbuch*; Springer Berlin Heidelberg: Berlin, Heidelberg, 1912; pp 387–409.

(17) Masadeh, A. S.; Bozin, E.; Farrow, C. L.; Paglia, G.; Juhas, P.; Karkamkar, A.; Kanatzidis, M. G.; Billinge, S. J. L. Quantitative Size-Dependent Structure and Strain Determination of CdSe Nanoparticles Using Atomic Pair Distribution Function Analysis. *Phys. Rev. B* **2007**, *76* (11).

(18) Yang, X.; Masadeh, A. S.; McBride, J. R.; Božin, E. S.; Rosenthal, S. J.; Billinge, S. J. L. Confirmation of Disordered Structure of Ultrasmall CdSe Nanoparticles from X-Ray Atomic Pair Distribution Function Analysis. *Phys. Chem.* **2013**, *15* (22), 8480.

(19) Kumpf, C.; Neder, R. B.; Niederdraenk, F.; Luczak, P.; Stahl, A.; Scheuermann, M.; Joshi, S.; Kulkarni, S. K.; Barglik-Chory, C.; Heske, C.; et al. Structure Determination of CdS and ZnS Nanoparticles: Direct Modeling of Synchrotron-Radiation Diffraction Data. *J. Chem. Phys.* **2005**, *123* (22), 224707.

(20) Billinge, S. J. L.; Levin, I. The Problem with Determining Atomic Structure at the Nanoscale. *Science* **2007**, *316* (5824), 561–565.

(21) Billinge, S. The Nanostructure Problem. *Physics* **2010**, *3, 25*.

(22) Soni, U.; Arora, V.; Sapra, S. Wurtzite or Zinc Blende? Surface Decides the Crystal Structure of Nanocrystals. *Cryst. Eng. Comm.* **2013**, *15* (27), 5458.

(23) Saniepay, M.; Mi, C.; Liu, Z.; Abel, E. P.; Beaulac, R. Insights into the Structural Complexity of Colloidal CdSe Nanocrystal Surfaces: Correlating the Efficiency of Nonradiative Excited-State Processes to Specific Defects. *J. Am. Chem. Soc.* **2018**, *140* (5), 1725–1736.

(24) Drijvers, E.; De Roo, J.; Martins, J. C.; Infante, I.; Hens, Z. Ligand Displacement Exposes Binding Site Heterogeneity on CdSe Nanocrystal Surfaces. *Chem. Mater.* **2018**, *30* (3), 1178–1186.

(25) Schnablegger, H.; Singh, Y. Getting Acquainted with the Principles 3rd Edition. **2013**, 124.

(26) Gordon, T. R.; Diroll, B. T.; Paik, T.; Doan-Nguyen, V. V. T.; Gaulding, E. A.; Murray, C. B. Characterization of Shape and Monodispersity of Anisotropic Nanocrystals through Atomistic X-Ray Scattering Simulation. *Chem. Mater.* **2015**, *27* (7), 2502–2506.

(27) Becker, J.; Bremholm, M.; Tyrsted, C.; Pauw, B.; Jensen, K. M. Ø.; Eltzholt, J.; Christensen, M.; Iversen, B. B. Experimental Setup for *in Situ* X-Ray SAXS/WAXS/PDF Studies of the Formation and Growth of Nanoparticles in near- and Supercritical Fluids. *J. Appl. Cryst.* **2010**, *43* (4), 729–736.

(28) Li, Y.; Beck, R.; Huang, T.; Choi, M. C.; Divinagracia, M. Scatterless Hybrid Metal–Single-Crystal Slit for Small-Angle X-Ray Scattering and High-Resolution X-Ray Diffraction. *J. Appl. Cryst.* **2008**, *41* (6), 1134–1139.

(29) Protesescu, L.; Nachtegaal, M.; Voznyy, O.; Borovinskaya, O.; Rossini, A. J.; Emsley, L.; Copéret, C.; Günther, D.; Sargent, E. H.; Kovalenko, M. V. Atomistic Description of Thiostannate-Capped CdSe Nanocrystals: Retention of Four-Coordinate SnS4 Motif and Preservation of Cd-Rich Stoichiometry. *J. Am. Chem. Soc.* **2015**, *137* (5), 1862–1874.

(30) Gomes, R.; Hassinen, A.; Szczygiel, A.; Zhao, Q.; Vantomme, A.; Martins, J. C.; Hens, Z. Binding of Phosphonic Acids to CdSe Quantum Dots: A Solution NMR Study. *J. Phys. Chem. Lett.* **2011**, *2* (3), 145–152.

(31) Hassinen, A.; Moreels, I.; de Mello Donegá, C.; Martins, J. C.; Hens, Z. Nuclear Magnetic Resonance Spectroscopy Demonstrating Dynamic Stabilization of CdSe Quantum Dots by Alkylamines. *J. Phys. Chem. Lett.* **2010**, *1* (17), 2577–2581.

(32) Hens, Z.; Martins, J. C. A Solution NMR Toolbox for Characterizing the Surface Chemistry of Colloidal Nanocrystals. *Chem. Mater.* **2013**, *25* (8), 1211–1221.

(33) Fiurasek, P.; Reven, L. Phosphonic and Sulfonic Acid-Functionalized Gold Nanoparticles: A Solid-State NMR Study. *Langmuir* **2007**, *23* (5), 2857–2866.

(34) Sachleben, J. R.; Wooten, E. W.; Emsley, L.; Pines, A.; Colvin, V. L.; Alivisatos, A. P. NMR Studies of the Surface Structure and Dynamics of Semiconductor Nanocrystals. *Chem. Phys. Lett.* **1992**, *198* (5), 431–436.

(35) Piveteau, L.; Ong, T.-C.; Rossini, A. J.; Emsley, L.; Copéret, C.; Kovalenko, M. V. Structure of Colloidal Quantum Dots from Dynamic Nuclear Polarization Surface Enhanced NMR Spectroscopy. *J. Am. Chem. Soc.* **2015**, *137* (43), 13964–13971.

(36) Piveteau, L.; Ong, T.-C.; Walder, B. J.; Dirin, D. N.; Moscheni, D.; Schneider, B.; Bär, J.; Protesescu, L.; Masciocchi, N.; Guagliardi, A.; et al. Resolving the Core and the Surface of CdSe Quantum Dots and Nanoplatelets Using Dynamic Nuclear Polarization Enhanced PASS–PIETA NMR Spectroscopy. *ACS Cent. Sci.* **2018** 4, 1113-1125.

3

Theoretical and Experimental Aspects of the Debye Scattering Equation Method

The limited size of the crystalline domains and the presence of various kinds of defectiveness make the conventional crystallographic techniques not ideal for a full, and accurate, characterization of the nanosized materials. At variance, Wide-Angle X-Ray Total Scattering techniques, not being restricted by the crystalline long-range order, can simultaneously model both Bragg and Diffuse scattering, providing more precise atomic-scale information of the analyzed systems. The intrinsic potential of this approach requires careful and well-designed data collection and data reduction strategies, which, in Wide Angle Total Scattering analyses, entail a rigorous control of all experimental and numerical treatment steps. In this Chapter, fundamentals on the derivation of the Debye scattering equation are presented, in addition to data collection and data reduction aspects; significantly, a robust procedure for measuring scattering data from concentrated colloidal samples is also discussed. Since Wide Angle Total Scattering data can be analyzed both by fitting them directly in the reciprocal-space via the Debye Scattering Equation (DSE) and in direct-space via the Pair Distribution Function (PDF) methods, a brief comparison of these two approaches will be shown, highlighting their complementarity.

3.1 The Debye Scattering Equation

The analysis of a Wide Angle X-Ray diffraction trace of a nanocrystalline sample in reciprocal space, enabling the contribution of Bragg and diffuse scattering to be treated, is called Debye Function Analysis (DFA). This technique makes use of the Debye Scattering Equation originally proposed by Peter Debye more than a century ago, in 1915,[1] initially developed for liquids. The DSE reproduces the *elastic* and *coherent* scattering from a randomly orientated collection of isotropic materials, such as randomly oriented nanocrystals, in the solid state and in colloidal suspension. Here, a brief derivation of this equation, based on the kinematic approximation of the radiation-matter interaction, is reported and discussed adopting the treatment and formalisms from the book "*Crystallography for Health and Bioscience*"[2] edited in 2012 by A. Guagliardi and N. Masciocchi, Co-Supervisors of this Ph.D. thesis.

Let us consider a parallel and spatially uniform X-ray beam that hits a single point-like atom and being diffused. The intensity (I_0) of the incoming beam is given by the number of incident photons on the sample per unit time and unit area, while its diffusion can be associated to the elastic scattering cross section (σ); therefore, the total number of photons per unit time diffused by a single point-like atom in the entire solid angle (4π) is $I = I_0\sigma$.
However, the information gained from diffraction is mostly contained in the angular distribution of the diffused photons within an infinitesimal portion of a solid angle ($\delta\Omega$) around the wave vector (**k'** in Figure 3.1, which is the direction of deflection of the photons, coinciding with the direction of observation). The diffused intensity can then be expressed as follows (Equation 3.1):

$$I = I_0 \left(\frac{\delta\sigma}{\delta\Omega}\right) d\Omega$$

$Eq.\,3.1$

Of the highest importance, the differential cross section ($\delta\sigma/\delta\Omega$) is what is actually measured in a diffraction experiment.

If we consider an incident beam represented by a plane wave as shown in Equation 3.2:

$$A_0(\boldsymbol{r}) = \sqrt{I_0} e^{2\pi i \boldsymbol{k}\boldsymbol{r}} \qquad Eq.\,3.2$$

where:

$\sqrt{I_0}$: amplitude of the wave

$2\pi\boldsymbol{k}\boldsymbol{r}$: phase of the wave

$\boldsymbol{k}$: propagation vector of the wave (its length is λ^{-1}).

once the plane wave hits a "diffusion center" in position $\boldsymbol{r_1}$, the radiation is elastically diffused and can be represented by a spherical wave. At the detector position, located at $|\boldsymbol{R} - \boldsymbol{r_1}|$ distance, far away from the diffusion center along the direction of observation $\boldsymbol{k}'$, the resulting spherical wave $A(\boldsymbol{r})$ is represented by Equation 3.3.

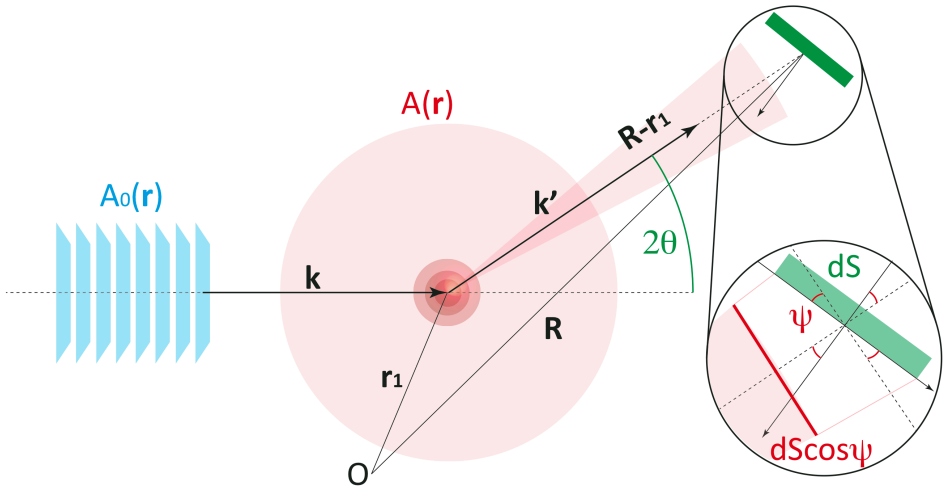

Figure 3.1. *Graphical schematization of the scattering process of a point-like atom. In light blue, the incoming planar wave described by Equation 3.2 in line with its propagation vector k; in pale red, the spherical wave described by the Equation 3.3 generated by the scattering of the point-like atom in position r_1; In green, a portion of the detector dS in position R that received the scattered spherical wave as a planar wave with a propagation vector k'. The magnification shows the need to consider that the detector can collect only a projection of the area inscribed in the solid angle described by Equation 3.4.*

$$A(\boldsymbol{r}) = -\sqrt{I_0}e^{2\pi i \boldsymbol{k} r_1}\frac{b}{|\boldsymbol{R}-\boldsymbol{r_1}|}e^{2\pi i \boldsymbol{k'}|\boldsymbol{R}-\boldsymbol{r_1}|} \qquad Eq.\,3.3$$

where:

b : scattering length of the point-like atom

$\boldsymbol{k}'$: propagation vector of the diffused wave (since the scattering is elastic, $|\boldsymbol{k}'| = |\boldsymbol{k}|$)

$2\pi\boldsymbol{k}'|\boldsymbol{R}-\boldsymbol{r_1}|$: phase of the diffused wave

Since the scattering is coherent, there is a precise phase relation between the incident and scattered beams. The negative sign in Equation 3.3 indicates a π phase offset among the two, a well-known feature of Thomson scattering.

Considering that the distance of the detector, ***R***, is very large compared to the operational wavelength (***R*** = 760 mm at the X04SA-MS of the SLS, see later – but this holds for every experimental setup, also in the laboratory), the spherical wave entering the detector and propagating along the propagation vector $\boldsymbol{k}'$ can be treated as a plane wave. This wave $A(\boldsymbol{r})$ hits the detector element of area dS (not perfectly or necessarily perpendicular to the propagation vector $\boldsymbol{k}'$), enabling the collection by the detector of *only the projection* of the plane wave on that area, $dS\cos\psi$ (as schematized in Figure 3.1). The resulting solid angle of the measurement is, therefore, represented by Equation 3.4:

$$d\Omega = \frac{dS\cos\psi}{|\boldsymbol{R}-\boldsymbol{r_1}|^2} \qquad Eq.\,3.4$$

The number of photons per unit time measured by the detector within the solid angle $d\Omega$ is then obtained by taking the squared modulus of Equation 3.3, $|A(\boldsymbol{r})|^2$, and multiplying it by the projection on the detector element dS, finally obtaining Equation 3.5.

$$|A(\boldsymbol{r})|^2 dS\cos\psi = I_0 b^2 \frac{dS\cos\psi}{|\boldsymbol{R}-\boldsymbol{r_1}|^2} \qquad Eq.\,3.5$$

By combining Equations 3.1, 3.4 and 3.5, the differential cross section is obtained:

$$\frac{\partial\sigma}{\partial\Omega} = b^2$$

$Eq.3.6$

Equation 3.6 tells us that, in case of a point-like atom, the differential cross section is the square of its form factor and is independent of the scattering angle.
If a target with more than one scattering point is considered, such as a molecule or an entire nanoparticle, each point atom produces a spherical wave, and Equation 3.3 turns into a sum of waves, es expressed by Equation 3.7.

$$A(\boldsymbol{r}) = -\sqrt{I_0}\sum_{j=1}^{N}\frac{b_j}{|\boldsymbol{R}-\boldsymbol{r_j}|}e^{2\pi i\boldsymbol{k}\boldsymbol{r_j}}e^{2\pi i\boldsymbol{k'}(\boldsymbol{R}-\boldsymbol{r_j})}$$

$Eq.3.7$

Like in the previous case, the distance of the sample from the detector is much larger than the distances $\boldsymbol{r_j}$ among atoms, and the term $|\boldsymbol{R}-\boldsymbol{r_j}|$ can be reasonably approximated by $|\boldsymbol{R}|$, permitting to rewrite Equation 3.7 as follows (Equation 3.8):

$$A(\boldsymbol{r}) \approx -\sqrt{I_0}\frac{e^{2\pi i\boldsymbol{k'}\boldsymbol{R}}}{|\boldsymbol{R}|}\sum_{j=1}^{N} b_j\, e^{2\pi i(\boldsymbol{k}-\boldsymbol{k'})\boldsymbol{r_j}}$$

$Eq.3.8$

Defining $\boldsymbol{q} = \boldsymbol{k} - \boldsymbol{k}'$ as the scattering vector ($q = 2\sin\vartheta/\lambda$), it is possible to calculate the intensity measured at the detector and deriving the differential cross section, again "squaring" Equation 3.8 and multiplying both members by $dS\cos\psi$, as shown in Equation 3.9:

$$|A(\boldsymbol{r})|^2 dS\cos\psi = I_0\frac{dS\cos\psi}{|\boldsymbol{R}|^2}\left|\sum_{j=1}^{N} b_j\, e^{2\pi i(\boldsymbol{k}-\boldsymbol{k'})\boldsymbol{r_j}}\right|^2$$

$Eq.3.9$

from which Equation 3.10 can be obtained:

$$\frac{\partial\sigma}{\partial\Omega} = \frac{|A(\boldsymbol{r})|^2 dS\cos\psi}{I_0 d\Omega} = \left|\sum_{j=1}^{N} b_j\, e^{2\pi i(\boldsymbol{k}-\boldsymbol{k'})\boldsymbol{r_j}}\right|^2$$

$Eq.\,3.10$

Using algebra and Eulero's formulae ($e^{ix} + e^{-ix} = 2\cos x$), and separating *i = j* and *i ≠ j* terms, it is possible to obtain Equation 3.11.

$$\frac{\partial\sigma}{\partial\Omega} = \sum_{j=1}^{N} b_j^2 + \sum_{j>i=1}^{N} b_j b_i\left(2\pi\cos\boldsymbol{q}\left(\boldsymbol{r_i} - \boldsymbol{r_j}\right)\right)$$

$Eq.\,3.11$

Within Equation 3.11, one can appreciate that the differential cross section (the term on the left) depends *on the entire set of interatomic* ***vectors*** of the system under analysis and on *the direction and amplitude of the scattering* ***vector***.

Let us now consider a system composed by millions/billions of particles (or molecules) with ideally *random* orientations. As explained in Chapter 2 (for the SAXS analysis discussed in Paragraph 2.2.2), the interference effects among the different particles contributing to the experimental signal is appreciable only at very low diffraction angles. For this reason, in the wide-angle regime, or even in the Porod section of the small-angle scattering section, the particles can be considered non-interacting one to each other.

Under such assumptions, the spherical average of the differential cross section can be performed by integrating along all the orientations (*i.e.*, over the $\beta \in [0,2\pi]$ and $\phi \in [0,\pi]$ angles), ending up into Equation 3.12:

$$\left\langle\frac{\partial\sigma}{\partial\Omega}\right\rangle = \frac{1}{4\pi}\int_0^{2\pi} d\beta \int_0^{\pi} \sin(\phi)\frac{\partial\sigma}{\partial\Omega}d\phi$$

$$= \frac{1}{4\pi}\int_0^{2\pi} d\beta \int_0^{\pi} \sin(\phi)\, d\phi \left[\sum_{j=1}^{N} b_j^2 + \sum_{j>i=1}^{N} b_j b_i\left(2\pi\cos\boldsymbol{q}\left(\boldsymbol{r_i} - \boldsymbol{r_j}\right)\right)\right]$$

$$= \sum_{j=1}^{N} b_j^2 + \frac{1}{2\pi} \sum_{j>i=1}^{N} b_j b_i \int_0^{2\pi} d\beta \int_{-1}^{1} d(\cos(\phi)) \cos\left(2\pi q d_{ij} \cos(\phi)\right)$$

$$= \sum_{j=1}^{N} b_j^2 + 2 \sum_{j>i=1}^{N} b_j b_i \frac{\sin\left(2\pi q d_{ij}\right)}{2\pi q d_{ij}}$$

$Eq.\,3.12$

Here, β and ϕ are the azimuthal and polar angles of a spherical coordinates reference system.

Equation 3.12 represents the DSE for a powder diffraction pattern ideally made of identical (single sized) NPs containing point-like atoms *only.* However, DSE reported in Equation 3.12, is still a crude approximation to reality, and, in this formulation, it is not suitable to model the scattering trace of real samples and to refine their relevant structural and microstructural parameters. Specifically, corrections for several physically-based features of real single atoms / molecules / nanocrystals need to be introduced. This point can be easily understood by considering that:

a) X-rays interact with the entire, and spatially diffuse, atomic electron-cloud, making atoms very different from the ideal point-like scatterer model assumed above;
b) Atoms are *never* at rest, that is they are not fixed at their equilibrium positions, due to their inherent, often complex, thermal motion;
c) Real nanocrystals can present a statistical or correlated set of missing atoms or ions, *i.e.* vacant sites.

Point a) is clearly related to the spread in space, typically limited to a few Å, of the electronic cloud around the atomic nucleus. This makes the constant scattering length b_j totally inappropriate for X-rays experiments (but not for elastic neutron scattering, where the scattering centers are the nuclei, the size of which is orders of magnitude smaller than their de Broglie wavelength); therefore, for real sample, a more realistic angle- (or *q*-) dependent atomic form factor $f_j(q)$, known with high precision,[3,4] is used instead of b_j.

As for point b), since the position and the spatial distribution of the scattering centers is of fundamental importance in calculating the scattered intensity of a real sample (which depends on the entire set of interatomic distances), the atomic

oscillations around their equilibrium position need to be considered as well. By considering the time scale of these motions (occurring at the femto-second scale) with that of the diffraction experiments (seconds to hours), only a statistical average of atomic displacements becomes accessible. Since these motions can be considered (in most cases) harmonic and uncorrelated, Debye Waller Factors $T_j(q)$ [5,6] (*i.e.* a Gaussian damping correction in *q* space) can be used, modifying the form factors of atoms at rest.

Finally, point c) addresses the necessity of modifying atomic site occupancy factors (*s.o.f.*) to values lower than 1.0. Indeed, *s.o.f.*s represent the probability of finding an atom in its site, an approximation which is fully valid if a randomly distributed disorder *only* occurs.

For all these reasons, the scattering form factor $f_j(q)$ is further modulated as $f_j(q)T_j(q)o_j$ obtaining an expanded version of the DSE, shown in Equation 3.13:

$$\langle\frac{\partial\sigma}{\partial\Omega}\rangle_{or.} = I(q) = \sum_{j=1}^{N} f_j(q)^2 {o_j}^2 + 2\sum_{j>i=1}^{N} f_j(q)^2 T_j(q)^2 {o_j}^2 f_i(q)^2 T_i(q)^2 {o_i}^2 \frac{\sin\left(2\pi q d_{ij}\right)}{2\pi q d_{ij}} \qquad Eq.\,3.13$$

where:

$f_i(q)$: atomic form factors

$T_i(q)$: atomic thermal motions

o_i: atomic site occupancy factor

A careful analysis of Equation 3.13 shows that it contains two distinct terms:

a) The "*self*" term (the first summation) represents the summation of the *zero* distances between an atom and itself (summation of the main diagonal elements of a $n \times n$ matrix where n is the number of atoms of the nanoparticle), that normally acts as a smoothly changing "background" term. This term is related to **stoichiometry**, rather than to structure.

b) The "interference" term (the second summation), representing the summation of the off-diagonal $n \times (n-1)$ terms, provides the **structural** information.

Equation 3.13 can now be used to reproduce the Wide Angle intensity pattern of an X-ray scattering experiment from a population of *real clusters of the same size and randomly oriented*, not necessarily possessing translational symmetry.

Significantly, DSE can also be used for the analysis of a population of nanocrystals with different size and even in the presence of multiple populations, each defined by a specific law. These aspects will be presented in Paragraph 3.4, in which the software used (the *Debussy Suite* of programs) and its versatile and highly performing features will be introduced. However, the coherent and elastic scattering measured during an X-ray diffraction experiment is not the only contribution to the overall intensity collected in the XRPD trace. Section 3.2 will focus on these extra contributions, with the goal of understanding, and quantifying, these additional phenomena and enabling their correct numerical treatment, which can precede (in the data reduction process) the entire DSE analysis or occur simultaneously with the DSE calculation while performing a reciprocal-space total scattering study.

3.2 Experimental Aspects and Corrections in DSE

The Debye scarring equation provides a function able to model the elastic and coherent scattering of a powder-like ensemble of particles of equal size. It is therefore necessary obtaining an XRPD trace from a real sample representative of the coherent end elastic scattering of the nanoparticle in it only. Several physical phenomena (absorption, polarization effects, XRF, inelastic Compton scattering, etc.) and extra scattering (air, sample holder, etc.) occur during a conventional XRPD acquisition but, the DSE is inherently not able to model these "extra" contributions encoded in raw XRD data. Since it is not possible to separate most of these effects during the data correction, a specific setting and type of the instrumentation (detector, X-ray source, etc.) and a protocol of data acquisition is recommended in

order to avoid or minimize these contributions, that will be introduced in Paragraph 3.3. Subsequently to the description of the experimental issues, a protocol for data collection and data reduction recently developed at the X04SA-MS beamline from the group of my supervisors, in collaboration with the beamline scientist, is presented.

3.2.1 Compton Scattering

Inelastic scattering was originally presented by Arthur Holly Compton in 1922,[7] and describes the decrease in energy of the scattered photon immediately after the interaction with a free electron, and its relation with the deflection angle.
Generally speaking, the inelastic interaction of these particles depends of the state of the electron that interacts with the photon.[8] For a completely free electron, a simplified description using the conservation laws of energy and linear momentum can be used. Considering λ and λ' as the incoming and outgoing wavelengths and 2ϑ the angle of deflection of the photon, the variation of λ, $\Delta\lambda$, can be expressed as in Equation 3.14. Such a value can be easily associated to an energy variation term between the two (incoming and outgoing) photons, ΔE_C.

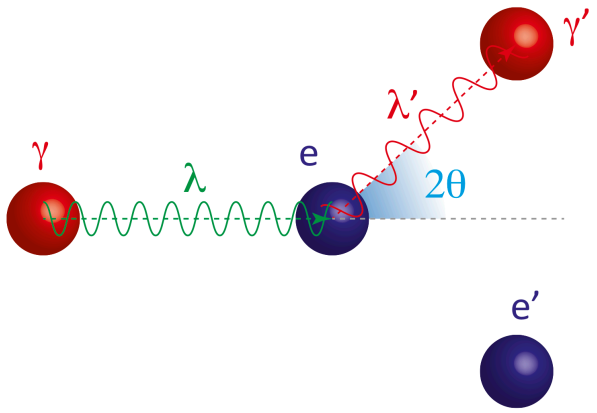

Figure 3.2. *Graphical representation of the Compton scattering phenomenon. The incoming photon (red sphere) hits a stationary free electron (blues sphere) loosing part of its energy by recoil.*

$$\Delta\lambda = \lambda' - \lambda = \left(\frac{h}{m_e c}\right)(1 - \cos 2\vartheta) = \lambda_c(1 - \cos 2\vartheta)$$

$Eq.3.14$

where:

$\lambda_c = 0.02426\text{Å}$: Compton wavelength

In real samples, the primary radiation hits electrons bonded to the nucleus within each atom; in these cases, the balance between the elastic (Thomson) and inelastic (Compton) scattering depends on the electron bonding energy E_b. If $\Delta E_C > E_b$, then the inelastic component prevails over the elastic one and vice versa. *This means that, if the electron is strongly bonded, the elastic scattering prevails*. For this reason, the main origin of the Compton scattering is associated to the external and less bounded electrons. In the context of quantum-mechanics, since the scattering intensity is defined by the scattering factor f (the Fourier transform of the electron density), the intensity of "diffraction" generated by a single electron (in electronic units) is given by Equation 3.15, where the Thomson and Compton scattering terms are suitably partitioned.

$$I_{e,tot}(\boldsymbol{Q}) = I_{e,T}(\boldsymbol{Q}) + I_{e,C}(\boldsymbol{Q}) = f_e^2(\boldsymbol{Q}) + [1 - f_e^2(\boldsymbol{Q})] = 1$$

$Eq.3.15$

where:

$I_{e,tot}(\boldsymbol{Q})$: total intensity scattered from one electron

$I_{e,T}(\boldsymbol{Q})$: intensity generated by Thomson scattering

$I_{e,C}(\boldsymbol{Q})$: intensity generated by Compton scattering

$f_e(\boldsymbol{Q})$: electronic scattering factor

Despite for a single electron the elastic and inelastic scattering are anticorrelated and $I_{e,C}(\boldsymbol{Q}) = \left[1 - f_e^2(\boldsymbol{Q})\right]$, when considering an atom with Z electrons, the contributions of all "single electrons" has to be summed-up. The summation of the coherent scattering produces positive interference and generates the well-known atomic *scattering* factor $f_0(\boldsymbol{Q})$ that, once it is squared, produces a scattering intensity that is maximized for $Q \to 0$ and is equal to Z^2. On the other side, the summation of incoherent scattering contributions produces a smooth function that increases with Q up to a maximum value of Z when Q is large (ideally, for $Q \to \infty$).

Thanks to these considerations, it is evident how the increase of the atomic number Z implies a relative reduction of inelastic scattering effects, which, at variance, is large for light elements, and in organic materials. In total scattering analyses, this contribution acts as a background that can be calculated taking into account the tabulated incoherent diffusion factors[4,5] and then added, after suitable scaling, to the DSE pattern model (as done by Debussy) or previously subtracted from the experimental pattern, as normally done when performing PDF analyses.

3.2.2 X-ray Fluorescence

In total scattering analyses, fluorescence is a phenomenon that appears when a photon possesses enough energy to remove an electron from core levels, causing atomic ionization and subsequent emission of less energetic radiation from the sample (see Figure 3.3). The energies of the emitted photons area characteristic of the material composition, and the probability of such process to occur is heavily dependent on the incident beam energy, in λ^3 fashion curves, separated by several (material-dependent) absorption edges. The emission is caused by the relaxation of the atom to its original state and generates extra signal at the detector.

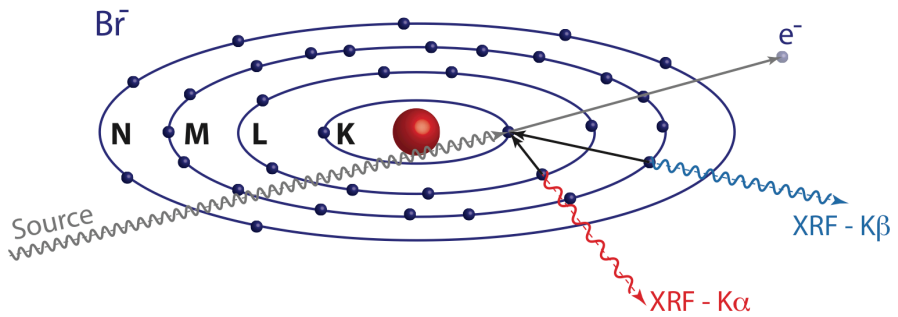

Figure 3.3. *Graphical representation of the XRF effect. The X-ray source promotes the removal of an electron of the inner orbital of an atom, causing the appearance of characteristic radiations (here labelled as Kα and Kβ, but many other are possible), generated by the relaxation of the external electrons while restoring the stable electronic configuration.*

It is however possible to manage these annoying effects using:

a) an appropriate wavelength which minimizes XRF emission (if possible);
b) a detector able to apply a cut-off energy threshold, a few keV away from the operational photon energy.

Needless to say, the deliberate choice of the incoming beam wavelength for a specific scattering experiment is viable only at synchrotron facilities. However, as it depends on several experimental requirements making the option a) not always applicable, this careful energy selection may require an appropriate experimental set-up, which includes detector optimization by recording long overnight flatfield calibration files, one per each different energy threshold.

3.2.3 Lorentz-Polarization Correction

In conventional crystallographic modeling, the Lorentz correction factor is necessary to obtain the differential elastic cross-section from Bragg intensity. In DSE, its computation does not need; the Debye equation approach calculates directly the differential cross section, *i.e.* the "observed" intensity value. At variance, a polarization correction must be fully considered and applied, depending on the experimental geometry and on the polarization state of the incident beam. In synchrotrons, since the electric field is (practically) 100% polarized in the orbital σ plane (which, at the SLS Material Science beamline, is perpendicular to the scattering plane), a polarization correction is not needed. At variance, in the laboratory, where the X-ray sources are rotating anodes or X-ray tubes, the radiation is completely unpolarized and the scattered intensity is modulated by an angular dependent factor $P(2\vartheta)$[9] (additional polarization effects might be introduced by primary or diffracted beam monochromators, but not by filters, but are not considered here).

Let us consider two extreme cases:

a) when the polarization is perpendicular to the plane of scattering, $P = 1$
b) when the polarization is in the plane of scattering, $P(2\vartheta) = \cos^2(2\vartheta)$

In *100% unpolarized* radiations (rotating anodes and X-ray tubes), a weighted mixture of the two cases should be considered (as in Equation 3.16).

$$P(2\vartheta) = \frac{1 + \cos^2(2\vartheta)}{2}$$

$Eq.3.16$

and applied, as a multiplicative correction factor, to the DSE calculated trace.

3.2.4 Absorption Correction

Very similarly to what already presented in Paragraph 2.1.2 for the UV-Vis absorption spectroscopy of CdSe materials or suspensions, also X-ray beams, passing through a sample of thickness L_{sc}, can be significantly attenuated by their inelastic interaction with the electronic clouds. The attenuation normally follows an exponential decay (as present in the common the Lambert-Beer Law), shown by Equation 3.17:

$$I = I_0 e^{[-\mu(E,C,x)L_{sc}]}$$

$Eq.3.17$

where:
I_0: intensity of the incoming beam
$\mu(E, C, x)$: attenuation coefficient [M^{-1} cm^{-1}]
E: beam energy
C: concentration or packing of particles [M]
x: particles composition
L_{sc}: optical path inside the sample (sample thickness) [cm]

In this Ph.D. thesis all measurements performed at the SLS synchrotron were performed on inorganic compounds and/or metallic nanoparticles with operational energies in the 20 - 22keV range, resulting in non-negligible sample absorption effects. To make the story slightly more complex, the beam passes through different materials (with different $\mu(E)$), such as the capillary walls, the sample and, in principle, the air surrounding the sample holder. The attenuation coefficient of the capillary can be calculated using the NIST table for sample-holders (typically of

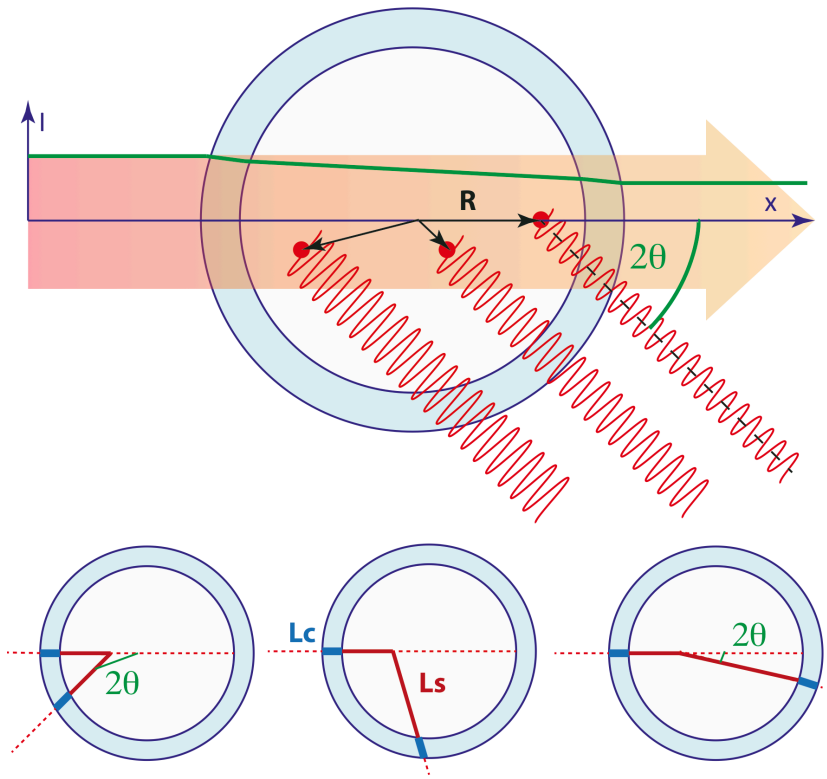

Figure 3.4. *Graphical representation of the beam attenuation passing through a capillary filled with an absorbing sample. The green line represents the decay of the intensity of the incoming beam passing through the sample. In X-Ray tracing approaches a large number (generally 1000) of scattering points of coordinates R, 2θ are considered in order to calculate their paths inside the capillary and as consequence their attenuation effects on the incident beam.*

nominal and known **Glass 50** composition) and known wall thickness of 0.01 mm, using the data freely accessible on https://www.nist.gov/.[4]

In the case of the sample, its $\mu(E, C, x)$ depends of the powder packing (or colloidal suspension concentration, C) and on the composition *x*, which are not always well-known for each sample; for these reasons, the direct experimental estimation of the attenuation coefficient via transmission (*radiographic*) measurement turns to be more accurate. Once the linear attenuation coefficient is obtained therefrom, starting from the Lambert-Beer law and using a complex ray-tracing procedure,[10,11] it is possible to calculate:

a) the angular dependent attenuation corrections $t(2\vartheta)$;

b) the angular dependent absorption curves $a(2\vartheta)$;

for the empty capillary, the ideally free-standing sample and capillary filled with the sample.

3.3 Data Collection and Data Reduction

In Paragraph 3.2 the general aspects to be considered when performing accurate WAXTS data collections were discussed, aiming at understanding and explaining the choice of a specific experimental set up. Table 3.1 summarizes possible solutions for the several effects discussed above.

Problem/Effect	Solution
Compton scattering	NOT AVOIDABLE Calculated and added to the Debye-based model
XRF	(NOT) AVOIDABLE Use of advanced detectors with energy cut-off threshold
LP correction	AVOIDABLE Use of a synchrotron source and DSE-based analysis
Absorption	NOT AVOIDABLE Calculated and subtracted from the experimental pattern

Table 3.1. *This table summarizes possible experimental problems and their most accessible solutions related "scattered-beam contamination" effects and other issues, illustrated above in Paragraph 3.2.*

Worth of note is the geometry of the diffraction setting chosen for the analysis. The control of experimental effects and their correction, not to mention the physical state of the sample (*e.g.*, a colloidal suspension), strongly suggest, if not force, the use of the Debye Scherrer geometry (in *transmission* mode) instead of the Bragg-

Brentano geometry (in *reflection* mode). Therefore, despite DSE experiments can be performed also with laboratory instruments (since very high-Q resolution is not-strictly mandatory), the WAXTS data acquisition of all samples treated in this thesis were performed at the material science beamline MS-X04SA of the Swiss Light Source (SLS) of the Paul Scherrer Institut (PSI).[12,13] The experimental setup available therein uses a horizontal mounting for capillaries, which is often found to be optimal for a number of reasons (size, shape and polarization of the beam; type of detector, etc.). The data collection and their data reduction processes were performed in collaboration with the beamline staff with locally developed program, portable on UNIX and MAC platforms. [It should be however noted that other beamlines at different synchrotrons (ESRF, APS, BNL, etc.) use different specimen mounting and positioning of 2D detectors, optimized for PDF studies and less prone to reciprocal-space DSE analyses].

The MS-X04SA beamline works in Debye-Scherrer transmission geometry and it is equipped with a high efficient 1-D single photon-counting solid-state silicon microstrip detector called MYTHEN (Microstrip sYstem for Time-rEsolved experimeNts, sketched in Figure 3.5).[14]

Its peculiar properties are:

a) the angular resolution of 0.0036° with a sample-to-detector distance of 760 mm (thus contributing in a negligible way to the instrumental broadening) and fast acquisition times (from few seconds up to 1 hour). It can collect simultaneously diffraction data over a 120° 2θ range; this wide-angle region is covered by 24 distinct modules of 1280 silicon microstrip sensor each, for a total of 30720 simultaneously active detectors;
b) the absence of dark noise;
c) the possibility of setting an electronic energy cut-off, *i.e.* a threshold eliminating low-energy XRF signals and undesired inelastic scattering contribution in the measured trace.

Before starting data collection procedure on the actual samples, a microcrystalline silicon powder (NIST SRM 640d, with certified cell parameter)[4] is measured in the same experimental conditions and used as standardized reference to accurately determine the operational wavelength and possibly correct minor capillary offsets (axial mis-centering).

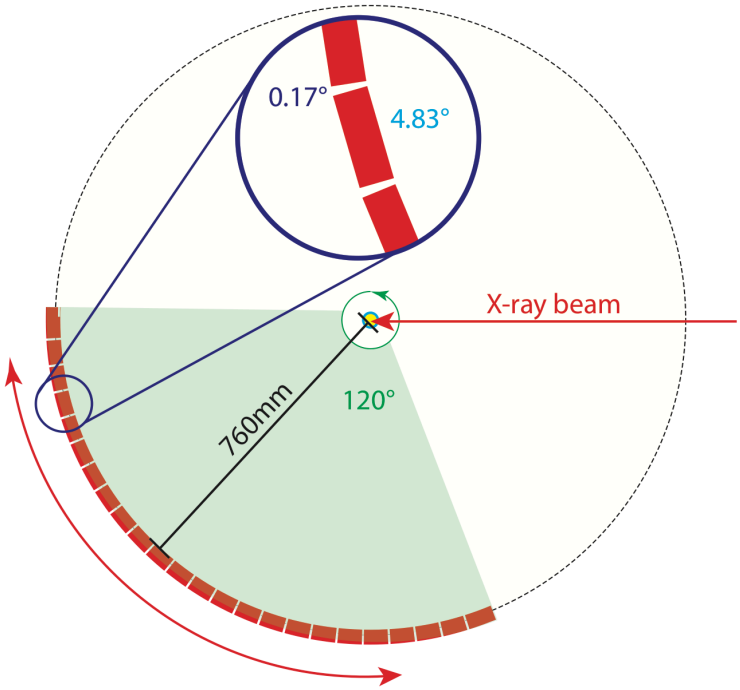

Figure 3.5. *The Debye-Scherrer diffraction geometry is here presented with a general scheme of the MYTHEN 2.0 detector. In red, all the 24 elements of the detector are presented, highlighting in the magnified insert, the inability of this detector to cover the* ***entire*** *range of 120°. For this reason, the elements are slightly shifted in four different positions (rotating the whole detector about the goniometer axis by fractions of a degree) in order to collect the scattered X-rays also on the gap region and providing individual datasets to be managed by an additional merging process, with outlier rejection.*

Once the instrument becomes calibrated, depending on the sample nature and on its scattering power (related to concentration, size and composition of the nanocrystals), several repetitions (generally from 4 up to 16) with a desired acquisition time (20 to 60 seconds each) are performed. Since MYTHEN II is built by modules able to cover 4.83° each, a systematically blind portion between modules (0.17° wide) produces a discontinuous XRPD trace. In order to obtain a complete and manageable diffraction trace, modules are rotated in four different position, enabling the data collection even in gap regions (after outlier rejection and dataset merging, see Figure 3.6).

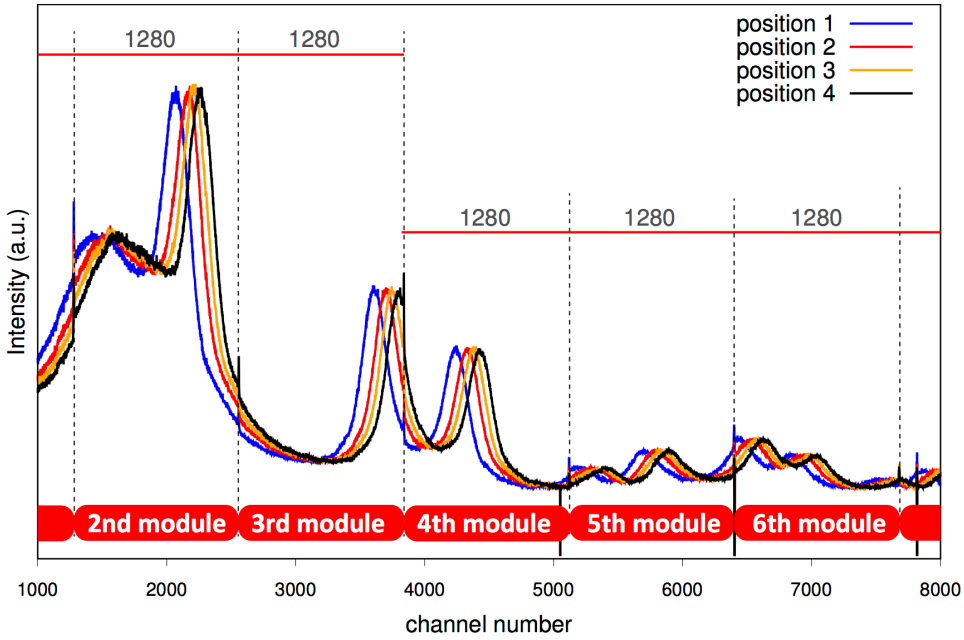

Figure 3.6. *Experimental patterns (Intensity vs Channel number) of CdSe QDs acquired with the MYTHEN 2.0 in different positions. From the plot one can appreciate that "blind sections" fall at multiples of 1280 (the number of Si stripes per element) and can be healed by collecting the same X-ray scattering trace in four different detector positions, offset by less than 1° each.*

For a single data collection, the exposure time can be approximatively calculated as follows:

$$t_m(s) = n_p n_r t_a \qquad Eq.\,3.18$$

where

n_p: number of MYTHEN positions (generally 4)

n_r: number of repetitions

t_a: seconds per single acquisition

The number of acquisitions permits to increase the signal to noise ratio and, at the same time, to monitor the diffraction experiment and check the sample under irradiation. Since the goal of data collection and data reduction is obtaining the scattering pattern of the sample only (S_s), devoid of capillary contributions, and

corrected for absorption ($S = S_s a_s$), a series of independent measurements, listed below, are performed (and schematically collected in Figure 3.7).[15]

The experimental scattering pattern (S_{exp}) collected on the sample (filled capillary) contains different contributions:

a) S_s: scattering from the sample with absorption effects;
b) S_c: scattering from the capillary attenuated by the sample;
c) S_e: scattering from air/He attenuated by the sample and the capillary.

In order to isolate and separate these contributions, three scattering measurements are performed (Figure 3.7, panel b):

1) $S_{e,exp}$: environmental (air/He) scattering (red trace in Figure 3.7, panel a);
2) $S_{c,exp}$: empty capillary in its environment (air/He) scattering (blue trace in Figure 3.7, panel a);
3) $S_{s,exp}$: capillary filled with the sample in its environment (air/He) scattering (yellow or black traces in Figure 3.7, panel a).

All these contributions are affected by angle-dependent beam attenuation (sample and capillary absorption), which we numerically calculate by X-ray tracing methods (as briefly explained in Paragraph 3.2). As packing density and sample stoichiometry are not easily known, two further transmission measurements are required in order to experimentally derive the "effective" linear absorption coefficient of the sample:

4) direct beam footprint (*i.e.* beam travelling in the air/He, grey trace in Figure 3.7, panel a)
5) transmitted beam footprint after passing through the sample-filled capillary in its environment (air/He) (green trace in Figure 3.7, panel a).

Resulting from a complex analytical treatment, the various attenuation functions $t(2\vartheta)$ are calculated as follows (Equations 3.19 to 3.24):

$$t_c(2\vartheta) = e^{-\mu_c L_c(R,2\vartheta)} \; ; \; a_c(2\vartheta) = \frac{N_c}{t_c} \qquad Eq.\,3.19; 3.20$$

$$t_s(2\vartheta) = e^{-\mu_s L_s(R,2\vartheta) - \mu_c L_c(R,2\vartheta)} \; ; \; a_s(2\vartheta) = \frac{N_s}{t_s} \qquad Eq.\,3.21; 3.22$$

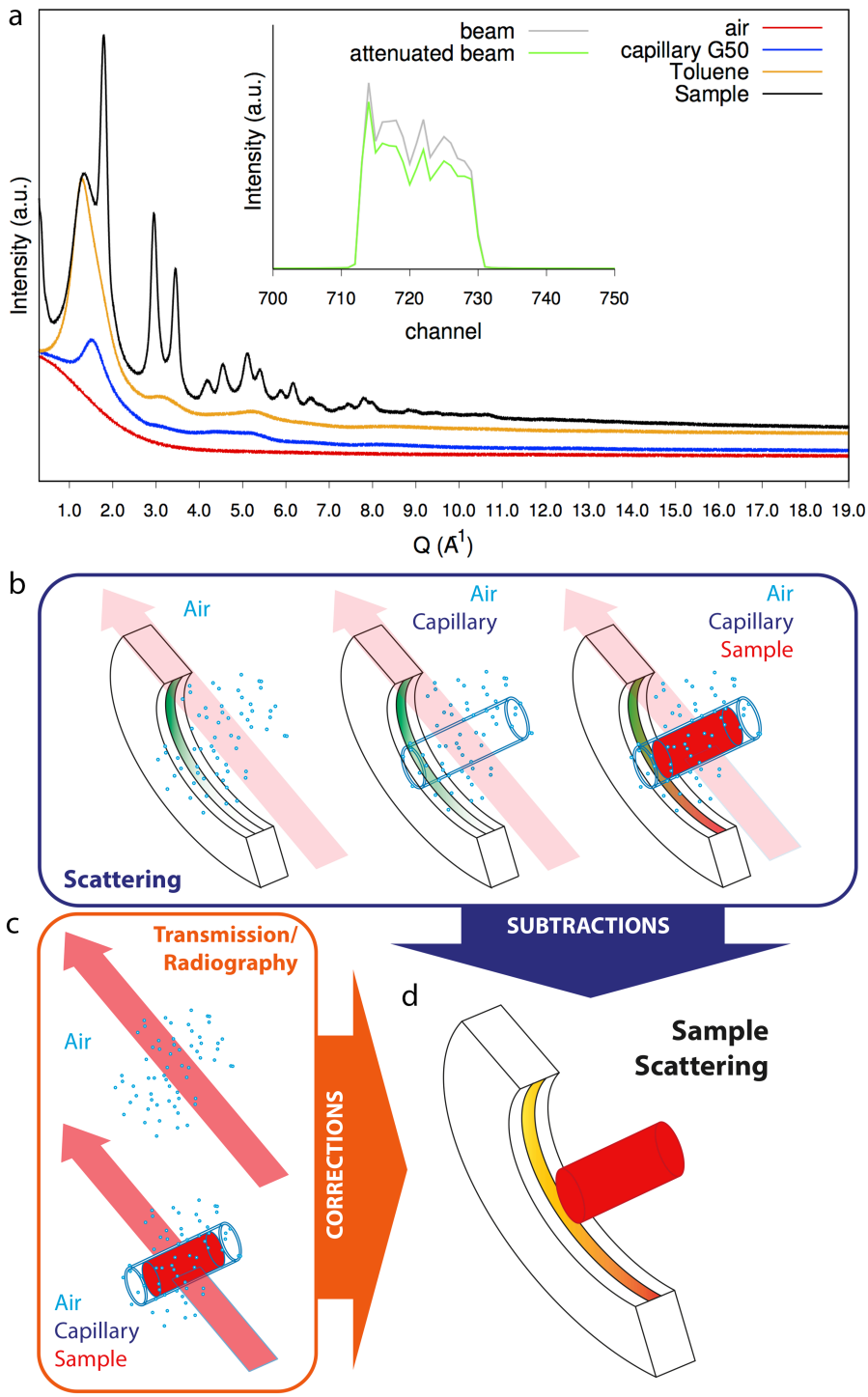
a
Intensity (a.u.)
beam
attenuated beam
Intensity (a.u.)
700 710 720 730 740 750
channel
air
capillary G50
Toluene
Sample
1.0 2.0 3.0 4.0 5.0 6.0 7.0 8.0 9.0 10.0 11.0 12.0 13.0 14.0 15.0 16.0 17.0 18.0 19.0
Q (A1)
b
Air
Air
Capillary
Air
Capillary
Sample
Scattering
SUBTRACTIONS
c
Transmission/
Radiography
Air
Air
Capillary
Sample
CORRECTIONS
d
Sample
Scattering

Figure 3.7. *a) merged experimental patterns and transmission plots needed for the data reduction; the reported traces belong to a real case of colloidal CdSe QDs. b, c and d) graphical representation of the measurement sequence enabling a correct and complete data reduction. This procedure ideally provides the scattering contribution from the sample only, as if it was freely floating in vacuum and 100% transparent to the X-ray beam.*

$$t_{cs}(2\vartheta) = e^{-\mu_s L_s(R,2\vartheta)-\mu_c L_c(R,2\vartheta)} \; ; \; a_{cs}(2\vartheta) = \frac{N_{cs}}{t_{cs}}$$

$Eq.\,3.23; 3.24$

N_c, N_s, N_{cs}: number of scattering points during the X-ray tracing procedure falling within the capillary walls, in the sample and in the capillary walls ($N_{cs} = N_c + N_s$), and sample respectively.

The scattering from the environment is obtained starting from the experimental air scattering pattern, taking in to account the attenuation coefficient of the filled capillary and the empty capillary as follows (Equation 3.25):

$$S_e = S_{e,exp} t_{cs}$$

$Eq.\,3.25$

The scattering from the capillary is obtained from *i)* the experimental pattern collected on the empty sample-holder and *ii)* the scattering of the air attenuated by the empty capillary and corrected for the absorption functions a_{cs} and a_c.

$$S_c = (S_{c,exp} - S_{e,exp} t_c) \frac{a_c}{a_{cs}}$$

$Eq.\,3.26$

Finally, using Equation 3.27, it is possible to obtain the scattering contribution of the sample **only**, corrected for absorption. This is the **main** ingredient of the total-scattering study, as it is this S dataset which is ready to be modeled with a DSE-based method.

$$S = S_s a_s = a_s \left[S_{exp} - \left(S_{c,exp} - S_{e,exp} t_c \right) \frac{a_c}{a_{cs}} - S_{e,exp} t_{cs} \right]$$

$Eq.\,3.27$

3.4 The DebUsSy Suite of Programs

As demonstrated in Paragraph 3.1, using the Debye scattering equation it is possible to reproduce the elastic and coherent scattering of an ideal ensemble of atoms/molecules/crystals with random orientations. Despite its enormous potential, the DSE shown in Equation 3.13 is not able, *as it is,* to extract strong information on real samples, since it is limited to the ideal case of equal replicas of a single entity, valid only for ideally monodisperse samples. Another issue of the DSE approach, and perhaps the main reason of its limited use, is represented by the computational time required for complex simulations, of for large enough nanocrystals. Indeed, in order to reproduce the entire Total Scattering pattern, a set of interatomic distances must be calculated from atomistic models of NPs, a problem which, in recent years, has been partially solved. It was indeed proved that, for truly periodic and not disordered systems, the number of terms to be calculated before they are summed up in the DSE shows a D^2 dependence (*D* being the diameter of a spherical NP), but rises up to D^6 for amorphous materials.[15]

An open source suite of programs, released in 2010[16] and recently improved in 2015,[17] is able to manage all these major aspects of DSE calculation and, at the same time, to reduce CPU usage by orders of magnitude. An overview of the suite and its strategy is given in Paragraph 3.4.1. In this thesis, since non-periodic systems can be easily inserted in the DSE strategy, this suite of programs has been used and expanded in order to:

a) manage and characterize planar defects (in metal chalcogenides NPs and metallic NPs, using different, but motivated, approaches) using mostly the Wide-Angle scattering region;
b) deal with subtle morphological properties (here, NC faceting) using the Small Angle scattering region.

In doing this, we resorted to many computational tricks and optimization strategies encoded in the main suite and linked our original treatment of planar faults into the database construction, one of the preliminary steps required by Debussy.

3.4.1 The Debye User System Suite (DebUsSy)

The Debye User System is an open source suite of programs downloadable at https://sourceforge.net/projects/debussy/. It makes use of fast calculation algorithm taking advantage, whenever possible, from the crystal symmetry and the implementation of a Gaussian sampling[18] of the interatomic distances. This last step is crucial to "rapidly" perform a complete DFA analysis with structural and microstructural parameter refinement. A series of papers and the detailed manuals supplied with the programs[16–18] explain the mathematical tricks used to speed up the calculations.

Hereafter, the core structure of the suite is briefly presented. This section is thus intended to clarify how the program works, as the development of a new advanced models for defects characterization, one of the major focus of this Ph.D. thesis, must cope with the general framework of the entire suite.

The *Debussy Suite* is composed by two separate units, labelled Claude and Debussy, and some ancillary utilities (the latter are not described here):

1) *Claude* deals with the generation of databases of sampled interatomic distances, starting from a minimal set of (easily accessible) crystallographic information;
2) *Debussy* deals with the DFA actively using the databases calculated by Claude.

Claude

Claude is the suite of modules that aims at generating the sampled interatomic distances of a population of NCs of selected shape and progressively increasing size, which are then stored in a suitable database, to be later be used in the DSE for the calculation of total-scattering patterns. The database generation requires a list of

basic information that varies as a function of the "cluster type", *i.e.* a morphological descriptor of the nanoparticles. According to the suite strategy, it is possible to build isotropic or anisotropically-shaped NCs, starting from the set of fractional coordinates and other metrical or symmetry data, stored, for example, in conventional Crystallographic Information Files. The cell parameters, the content of the asymmetric unit and information about the space group (and cell origin) are used to generate the entire unit cell content, which is then used as a building block for the progressive construction of the atomic list of each NC. Partially disordered or amorphous NPs can also be managed but, in this case, since the translational symmetry is broken, the starting building block (a unit cell) does not exist. Therefore, the user is asked to provide externally generated ascii files, each containing the complete list of the atoms (with label and cartesian coordinates) present in the desired nanoparticle, with suitable size, shape and defectiveness, to be directly used in the database calculation step.

Debussy

Debussy performs the DFA of the experimental pattern using the sampled interatomic distances previously calculated by *Claude*. In this step, initial parameters about the structure (Debye-Waller factors, *s.o.f.*s) and a starting microstructural hypothesis of the size distribution and of lattice strains are necessary to start the analysis. These parameters can be optimized by minimizing the difference between the calculated and the experimental pattern, using different minimization algorithms (named: simplex, bound optimization by quadratic approximation or simulated annealing).[19,20] As mentioned in Paragraph 3.3, high quality and suitably corrected data are recommended.

As anticipated, Equation 3.13 enables the user to calculate the XRPD pattern of a system of particles of equal size with a well-defined stoichiometry and Debye-Waller parameters. Despite this flexibility, the DSE, in the formulation set within Equation 3.13, it is not able to reproduce the pattern of a population of differently sized, and shaped, nanoparticles, which is the normal case for all real samples. A solution to this problem is found by considering that each nanoparticle contributes individually to the total X-ray diffraction pattern. For this reason, if the sample is constituted by

n_p particles with different size, shape or composition, the experimental X-ray scattering trace can be reproduced using a linear combination of DSE-calculated patterns, one for each particle and weighted by its fraction χ_i, as reported in Equation 3.28:

$$I_{cal}(q) = \sum_{i=1}^{n_p} \chi_i I_i(q)$$

$Eq.3.28$

In *Debussy*, the fraction χ_i is normally obtained from a discrete distribution function with its own average value and dispersion. Nanocrystalline materials, and, for what matters in this thesis, semiconducting QDs are often deliberately produced with different shapes, spanning from nearly isotropic (spherical or cubic) NPs to those with a high shape anisotropy (nanorods, nanoplatelets, *etc*.). Therefore, *Debussy* is able to manage the most common polyhedral shapes, jointly to *log-normal* size distribution laws for single (size) or double (size and shape) growth parameters. The analytical description of these functions is reported in Equations 3.29 and 3.30.

Monovariate log-normal size distribution

$$\chi_i(D_i) = N \frac{e^{-\frac{(\ln D_i - \ln\langle D\rangle)^2}{2\sigma^2_{\langle D\rangle}}}}{D_i}$$

$Eq.3.29$

where:
N : normalization factor ensuring $\sum_i \chi_i = 1$
D_i : operating diameter
$\langle D\rangle$: average diameter of the population
$\sigma_{\langle D\rangle}$: standard deviation

The refinable parameters, $\langle D\rangle$ and $\sigma_{\langle D\rangle}$, address the average diameter of the particles in the sample and the variance of the distribution.

Bivariate log-normal size distribution

$$\chi_{ij}(D_i, L_j) = N \frac{e^{-(\boldsymbol{UTAT'U'})}}{D_i L_j} \qquad Eq.\,3.30$$

$$\boldsymbol{U} = \left(\ln D_i - \ln\langle D\rangle\,, \ln L_j - \ln\langle L\rangle\right)$$

$$A = \begin{pmatrix} \sigma_{\langle D\rangle}^{-2} & 0 \\ 0 & \sigma_{\langle L\rangle}^{-2} \end{pmatrix} \qquad T = \begin{pmatrix} \cos\phi & -\sin\phi \\ \sin\phi & \cos\phi \end{pmatrix}$$

where:

D_i and L_j: diameter and length of the NCs in the ab plane and along the c-axis of the unit cell

T' and U': transposed matrix

$\langle D\rangle$: average diameter

$\langle L\rangle$: average length

$\sigma_{\langle D\rangle}$ and $\sigma_{\langle L\rangle}$: standard deviations

ϕ: correlation angle between the two growth directions

The five refinable parameters, $\langle D\rangle$, $\sigma_{\langle D\rangle}$, $\langle L\rangle$, $\sigma_{\langle L\rangle}$ and ϕ address the average size in the two perpendicular growth directions, the variances of the two "separate" distributions and the correlation between them. An average Aspect Ratio (AR) can be numerically derived therefrom. In particular, the refinement of the correlation angle ϕ enables to investigate if the two growth directions are independent one of the other or positively/negatively correlated. This coefficient, which in monodisperse sample is nearly undefined, is particularly important for polydisperse samples, where a much more robust information can be extracted thanks to the larger number of different "populated" NP sizes.

Additionally, the *Debussy Suite* makes it possible to refine phenomenological parameters of size-dependent laws using smoothly varying or stepped functions describing:

1) homogeneous contraction/expansion of the interatomic distances;
2) atomic site occupancy factors (*s.o.f.*s, toward extracting the correct size-dependent NP stoichiometry);

3) atomic isotropic Debye –Waller factors.

This is normally achieved by the DSE calculation, which contains size-dependent features, different for each NP in the database.

Last but not least, the DSE modelling can be extended to polyphasic samples, by a linear combination of the total WAXTS pattern of each phase and using a suitable weighting scheme. Very simply, to address the different phase fractions, an additional scaling factor, ω_k factor is introduced, as shown in Equation 3.31:

$$I_{cal}(q) = \sum_{k=1}^{n_{ph}} \omega_k \sum_{i=1}^{n_p} \chi_{i;k} I_{i;k}(q) \qquad Eq.3.31$$

where:

n_p : number of particles per population

n_{ph} : number of phases

ω_k: refinable scale factor

A method for the calculation of the standard errors of the above-listed optimized parameters is implemented as an optional feature of the Debussy program suite (version 2.0) using numerical first and second derivatives of the χ^2 function at the refined minimum to evaluate the variance-covariance matrix, based on a robust pseudo-inversion algorithm that takes into account possible parameter correlations. This enables also the propagation of the errors to derived quantities, which are evaluated starting from the refined parameters. Furthermore, the minimization of a large number of structural and microstructural parameters that correlate, inevitably produce shallow minima.

In conclusion, *Debussy* is able to compute a full DFA producing a calculated XRPD pattern of a powder-like ensemble of nanoparticles, extracting otherwise inaccessible information, thanks to the use of many computational tricks (not discussed here in detail) that drastically reduce the CPU time. Given such flexibility, in this Ph.D. thesis we found it possible to use the entire suite as starting tool, in which newly developed models and protocols for studying highly defective materials could be inserted.

3.5 Pair Distribution Function (PDF) Analysis

As introduced in Chapter 2, DFA is not the only available total scattering approach able to extract information from an X-ray diffraction experiment. In line with the Patterson approach[21] for crystalline materials, that provides a discrete map of interatomic vectors by Fourier transforming the integrated intensities of Bragg peaks, the 1D Pair (or Radial) distribution function (PDF) is a continuous function obtained by Fourier transforming the whole 1D X-ray diffraction total scattering pattern (see Figure 3.8).[22] In PDF approach, before the Fourier transform, a series of operations/considerations have to be taken into account in order to obtain a high quality G(r) function which is fully representative of the sample.

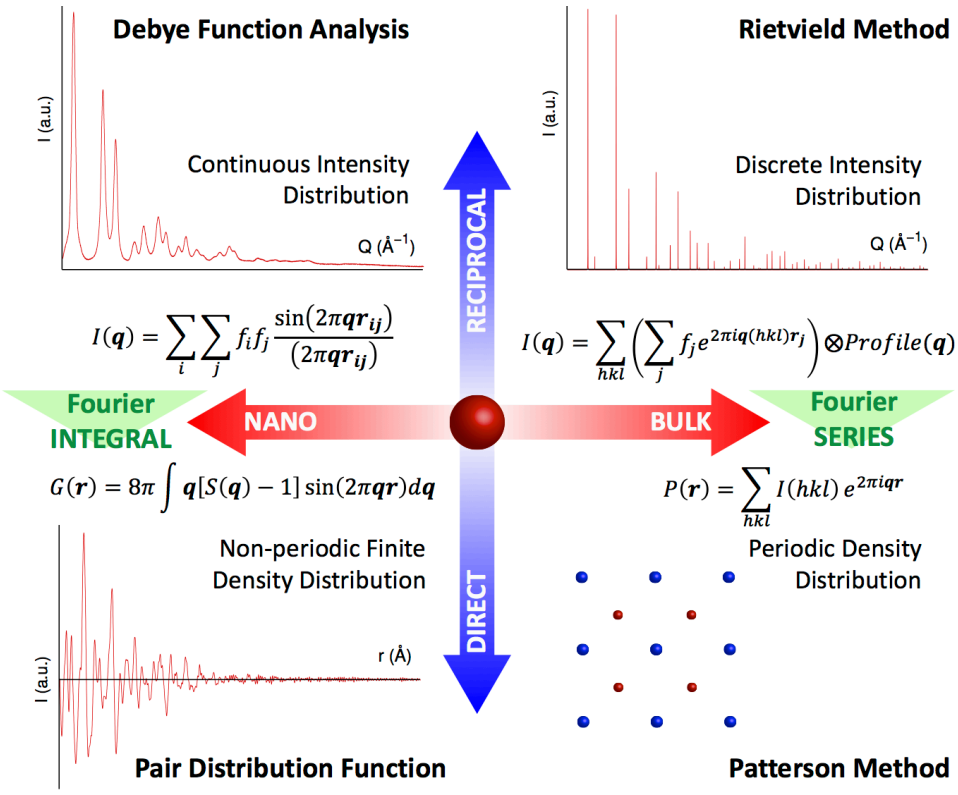

Figure 3.8. *Graphical representation of different XRD characterization methods, their range of application and their mathematic relation.*

These are listed hereafter:

1. The WAXTS trace has to be collected with an appropriate experimental set-up and very high energy photons, enabling the collection of intense enough radiation up to Q = 30 $Å^{-1}$ or more. Such a large Q value limits truncation errors and other numerical effects in the "numerically dangerous" sin-Fourier transform described below.
2. The experimental (raw) X-ray diffraction patterns need to be suitably corrected (with the same criteria described in Paragraph 3.3), aiming at obtaining only the *coherent* diffraction signal of the sample. Thus, Compton scattering must be pre-evaluated, and cannot be added to the final model.
3. The reduced experimental pattern must be normalized over the average scattering factors (as per Equation 3.32), according to the sample composition. Here, a pre-evaluation step, or an arbitrary assumption, is made. Fortunately, the final PDF trace is only marginally sensitive to a slightly wrong pre-determined sample composition. On the same line, uncertainties of similar magnitudes are also included when averaging atomic scattering factors in a non-elemental sample as, in the X-ray case, this is a crude, but unavoidable, approximation.

$$S(Q) = \frac{I(Q) - \sum_i c_i |f_i(Q)|^2}{|\sum_i c_i \, f_i(Q)|^2} + 1 \qquad Eq\ 3.32$$

where:

$Q = 2\pi q$

c_i : elemental fractions of the atomic species i

$f_i(Q)$: form factor of the atomic species i

$I(Q)$: total scattered intensity in the reciprocal space

S(Q) represents the intensity deviation from that of an ideal monoatomic gas of the same composition and reflects the changes of I(Q) due to an overall positive/negative interference of waves scattered by each atom, with an amplitude scaled to electron units.

Since, at high Q, S(Q) tends to 1, a so-called *reduced total scattering function* F(Q)

(defined in Equation 3.33) that oscillates around zero, is often used.

$$F(Q) = Q[S(Q) - 1]$$

$Eq.\,3.33$

Only when the three conditions listed above in points 1-3) are satisfied, and the F(Q) function calculated (in the widest Q range), the experimental G(r) function can be obtained by Fourier transforming F(Q), as shown by Equation 3.34:

$$G(r) = \frac{2}{\pi} \int_{Q_{min}}^{Q_{max}} Q[S(Q) - 1] \sin(Qr)\, dQ$$

$Eq\ 3.34$

Worth of note, the integration limits of the Equation 3.34 (which ideally require the usage of the entire [0,∞) range), are restricted to the measured Q interval (Q_{max} - Q_{min}). Indeed, neither the lower nor the upper "ideal" Fourier transform limits can be experimentally accessed. While the minimum Q value available in the dataset has little consequences on the final G(r) function, severe truncation effects are seen if Q_{max} (generally to 25-30 $Å^{-1}$) is too low. These truncation effects produce periodic ripples in G(r) which, in the worst cases, can be attributed to (manifestly non-existing) interatomic distances. Additionally, the choice of the Q_{max} should be balanced with the need of reaching high Q values and the counting statistics of the collected data. Indeed, since the X-ray scattering factors decrease with Q, very poor data with high S/N at high Q are often collected. Thus, the usage of large 2D detectors (set in close proximity to the sample) are a good compromise to measure meaningful scattering data for PDF analyses.

In the experimental G(r), the structural information of the particles analyzed is encoded; it represents the interatomic distances probability density as function of the distance r. Every peak of the G(r) profile, within a range r_2 - r_1, contains information about a specific bond distance, its distribution and coordination number of an atomic specie. To obtain this information, each peak of the G(r) function can be interpreted by a *direct analysis* evaluating the peak center, width

and area by fitting the PDF peaks with Gaussian functions. Since Gauss' curve is symmetric with respect to its maximum, the peak center is attributable to a definite average bond length while, its width is interpreted as a distribution of the interatomic distances of a specific "atom to atom" distance around its average bond length. The area of the gaussian represents the density of the interatomic distances within the range r_2 - r_1 of a specified atom pair. Therefore, normalizing the intensity against the scattering length and knowing which elements are involved, it is possible to calculate the coordination number (or the number of neighbors) of an atom around another one.

One of the main advantages of PDF approach is the possibility to perform the analysis separately onto different portions of the real-space, *r*, enabling the study of the local structure ("small box modelling" – a low *r* investigation, on which Rietveld is completely blind) and/or of the long-range order using an atomistic description represented by the Equation 3.35.

$$G(r) + 4\pi r\rho_0 = \frac{1}{r}\sum_i \sum_j \frac{f(0)_i f(0)_j}{\langle f(0)\rangle^2}\delta(r - r_{ij}) \qquad Eq.\,3.35$$

The idea of working in the direct space has been attractive since many years; accordingly, several PDF-programs have been released such as PDFgui[23] and its successor DiffpyCMI.[24] However, PDFs require well defined experimental conditions and (as for DSE analyses) scattering data are typically acquired only at specialized beamlines, optimized for very high-energy photons, up to 100 keV (with extremely reduced absorption by the sample) and often equipped with special sample environments.

Since G(r) represents the "continuous" multiplicity histogram of interatomic distances of a crystal (weighted by the scattering power of the atoms), other important information can be sometimes extracted when dealing with nanocrystalline materials. Indeed, a small crystal contains a large number of short distances (low *r* range), but, for larger *r* values, the multiplicity of these interatomic distances tends to decrease. Beyond a limiting value, defined by the size of the nanoparticle, no interatomic distances are possible (while they would be present in

the bulk. Thus, the fading away of the G(r) in *r*-space should be indicative of the nanocrystal size.[25] Unfortunately, in real samples, this information is partially blurred by the presence of polydisperse sizes and, more importantly, masked by the low sampling resolution (ΔQ) of the instrumental setups, tailored toward high Q's, high intensity without carefully managing the inherent DQ values, known to heavily affect the experimentally derived PDF curve of even standard microcrystalline samples, such as elemental nickel, widely used as a standard.

Conclusions

DSE is a powerful tool for characterizing real materials in their post-synthetic environment. The Debussy Suite of programs, making an extensive use of computational tricks, is able to speed up the sometimes prohibitive computational time of the Debye Scattering Equation, and performs the DFA of WAXTS data using populations of nanocrystals with a high level of flexibility. Integrating the open source suite with appropriate complex atomistic models enables the characterization of any type of compositional or structural defects at the nanoscale. The use of the DSE approach is linked to high quality data collection and data reduction procedures that must take into account different experimental aspects. In the next Chapters, the construction of atomistic models of NCs having planar defects of the stacking fault type will be presented, along with the strategy for implementing these calculations in Debussy. The model has been tested and used for the characterization of faulted CdSe QDs and, with some modifications, on larger elemental nanoparticles with low(er) stacking fault probabilities.

References

(1) Debye, P. Zerstreuung von Röntgenstrahlen. *Ann. Phys.* **1915**, *351* (6), 809–823.

(2) Debye Function Analysis: Theoretical and Experimental Aspects. In *Crystallography for Health and Biosciences*; A. Cervellino, A. Guagliardi, R. Frison, G. Cernuto, Eds.; Insubria University Press, **2012**; pp 177–186.

(3) Waasmaier, D.; Kirfel, A. New Analytical Scattering-Factor Functions for Free Atoms and Ions. *Acta Crystallogr. A* **1995**, *51* (3), 416–431.

(4) Seltzer, S. X-Ray Form Factor, Attenuation and Scattering Tables, NIST Standard Reference Database 66, **1995**.

(5) *International Tables of Crystallography*; IUCr's Commission on International Tables., Series Ed.

(6) Peng, L.-M.; Ren, G.; Dudarev, S. L.; Whelan, M. J. Debye–Waller Factors and Absorptive Scattering Factors of Elemental Crystals. *Acta Crystallogr. A* **1996**, *52* (3), 456–470.

(7) Compton, A. H. A Quantum Theory of the Scattering of X-Rays by Light Elements. *Phys. Rev.* **1923**, *21* (5), 483–502.

(8) P. Fornasini. Basics on Matter-Radiation Interaction. In *Crystallography for health and bioscience*; Insubria University Press, **2012**; pp 1–20.

(9) A. Coda. Tecniche Sprimentali: Intensitá Integrata e Sua Riduzione. In *Introduzione alla cristallografia moderna*; pp 268–272.

(10) Paalman, H. H.; Pings, C. J. Numerical Evaluation of X-Ray Absorption Factors for Cylindrical Samples and Annular Sample Cells. *J. Appl. Phys.* **1962**, *33* (8), 2635–2639.

(11) Bowden, M.; Ryan, M. Absorption Correction for Cylindrical and Annular Specimens and Their Containers or Supports. *J. Appl. Cryst.* **2010**, *43* (4), 693–698.

(12) Patterson, B. D.; Abela, R.; Auderset, H.; Chen, Q.; Fauth, F.; Gozzo, F.; Ingold, G.; Kühne, H.; Lange, M.; Maden, D.; et al. The Materials Science Beamline at the Swiss Light Source: Design and Realization. *Nucl. Instrum. Methods Phys. Res.* **2005**, *540* (1), 42–67.

(13) Willmott, P. R.; Meister, D.; Leake, S. J.; Lange, M.; Bergamaschi, A.; Böge, M.; Calvi, M.; Cancellieri, C.; Casati, N.; Cervellino, A.; et al. The Materials Science Beamline Upgrade at the Swiss Light Source. *J. Synchrotron Radiat.* **2013**, *20* (5), 667–682.

(14) Bergamaschi, A.; Cervellino, A.; Dinapoli, R.; Gozzo, F.; Henrich, B.; Johnson, I.; Kraft,

P.; Mozzanica, A.; Schmitt, B.; Shi, X. The MYTHEN Detector for X-Ray Powder Diffraction Experiments at the Swiss Light Source. *J. Synchrotron Rad.* **2010**, *17* (5), 653–668.

(15) A. Guagliardi. Experimental and Computational Aspects of the Debye Function Analysis. In *Structure-Property investigations of Nanomaterials by Debye Function Analysis*; **2015**.

(16) Cervellino, A.; Giannini, C.; Guagliardi, A. DEBUSSY: A Debye User System for Nanocrystalline Materials. *J. Appl. Cryst.* **2010**, *43* (6), 1543–1547.

(17) Cervellino, A.; Frison, R.; Bertolotti, F.; Guagliardi, A. DEBUSSY 2.0: The New Release of a Debye User System for Nanocrystalline and/or Disordered Materials. *J. Appl. Cryst.* **2015**, *48* (6), 2026–2032.

(18) Cervellino, A.; Giannini, C.; Guagliardi, A. On the Efficient Evaluation of Fourier Patterns for Nanoparticles and Clusters. *J. Comput. Chem.* **2006**, *27* (9), 995–1008.

(19) J. A. Nelder; R. Mead. A Simplex Method for Function Minimization. *Comput. J.* **1965**, *27*, 308–313.

(20) M. J.D. Powell. *The BOBYQA Algorithm for Bound Constrained Optimization without Derivatives*; Cambridge NA Report NA2009/06; Cambridge: University of Cambridge, **2009**; pp 1–39.

(21) Patterson, A. L. A Fourier Series Method for the Determination of the Components of Interatomic Distances in Crystals. *Phys. Rev.* **1934**, *46* (5), 372–376.

(22) Neder, R. B.; Korsunskiy, V. I. Structure of Nanoparticles from Powder Diffraction Data Using the Pair Distribution Function. *J. Phys. Condens. Mat.* **2005**, *17* (5), S125–S134.

(23) Farrow, C. L.; Juhas, P.; Liu, J. W.; Bryndin, D.; Božin, E. S.; Bloch, J.; Proffen, T.; Billinge, S. J. L. PDFfit2 and PDFgui: Computer Programs for Studying Nanostructure in Crystals. *J. Phys. Condens. Mat.* **2007**, *19* (33), 335219.

(24) Juhás, P.; Farrow, C. L.; Yang, X.; Knox, K. R.; Billinge, S. J. L. Complex Modeling: A Strategy and Software Program for Combining Multiple Information Sources to Solve Ill Posed Structure and Nanostructure Inverse Problems. *Acta Crystallogr. A* **2015**, *71* (6), 562–568.

(25) Kodama, K.; Iikubo, S.; Taguchi, T.; Shamoto, S. Finite Size Effects of Nanoparticles on the Atomic Pair Distribution Functions. *Acta Crystallogr. A* **2006**, *62* (6), 444–453.

4

Defects in CdSe: from the Bulk to the Nanoscale

The reduced size and the presence of various kinds of "core" defectiveness or surface reconstruction effects can have a strong direct or indirect influence on material (optical, magnetic, etc.) properties. The understanding of surface energy contribution in inducing structural defects is therefore a key-point in nanomaterials science, being it absent, or nearly negligible, in the bulk. This Chapter will be dedicated to the description and comprehension of defects in Cadmium Selenide, with a special focus on planar defects (stacking faults, SF), their origin and their impact on the XRPD trace. This Chapter serves as an introduction to the complex SF models elaborated during this PhD project; here, the origin of peak broadening and peak shifts is presented following the principles of classical diffraction theories and the pioneering data treatment and fault probability estimates originally presented by Warren. The limits of the classical theories in the identification and quantification of planar defects at the nanoscale will be highlighted, along with the need to elaborate new theoretical and numerical approaches for nanoscaled systems. Other microstructural features, such as surface and core strain and ion vacancies, are discussed, highlighting their relevance in deriving correct estimates of morphological parameters from X-ray diffraction traces.

4.1 Stacking Faults

4.1.1 Polymorphism and Classical Theory

When chemical species crystallize in two (or more) distinct crystal phases, polymorphs are formed. In the field of II-VI semiconductors, two stable crystal forms, zinc blende (ZB) and wurtzite (WZ) may be isolated RT (obviously, one of them as a metastable phase, but which one is still under debate), but periodic or random intergrowths may also exist (possibly generating polytypic structures).[1–3] As shown in the previous Chapters for nanostructured CdSe, by playing on thermodynamic and kinetic aspects during the nucleation, growth and, eventually, the isolation of QDs, it is apparently possible to obtain only (or, better, *preferentially*) one phase over the other.[1,4,5]

From a structural point of view, the existence of the two polymorphs, as pure end-members, can be explained by the simple 3D crystal building procedure, starting from a 2D lattice of nodes with hexagonal symmetry, where each node can equally be dressed by a noble gas atom, a metallic atom or, as discussed hereafter, a CdSe unit (normal to the plane). Extending this dense 2D packing along the third direction and targeting to the formation of a dense 3D lattices, parallel stacking of hexagonal planes requires the minimization of "empty" space (attributed to the volume of the interstitial cavity between ideally spherical atoms), a process which is governed by simple geometrical rules.

Using the nomenclature introduced in 1949 by Jagodinzski,[6] the first layer (A, used as a reference) is adjacent, in the third direction, to planes of the B and C type (not eclipsed with respect to A), *but not to A-type ones*. By periodically stacking layers of nodes or spheres with a $(ABC)_n$ sequence, an *fcc* cell of Fm-3m symmetry is generated, while the $(AB)_n$ sequence leads to an *hcp* cell of $P6_3/mmc$ symmetry (see Figure 4.1). If, instead, the slightly more complex heteronuclear AB unit is used to dress the nodes (as in CdSe), lowering of the space group symmetry down to F-43m or $P6_3mc$ space group symmetry is observed.

The small, chemistry-dependent, difference of the lattice energy of these two phases and their possibility to coexist in the same crystallite without introducing

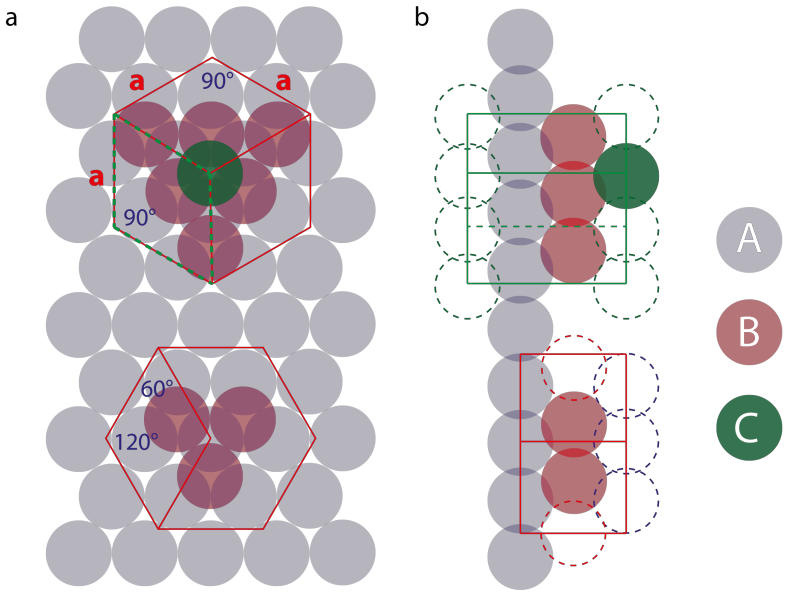

Figure 4.1. *Different types of stacking of closed packed layers with hexagonal symmetry. On the left (a), the top view of the stacking and on the right (b) the side view. For both stacking, two different unit cells with the same a and b vector can be found that are representative of two systems with different symmetry. The green cell with trigonal setting can be used to reproduce a ZB form, while the red cell, with hexagonal symmetry, can be used as building block to reproduce a WZ form.*

massive distortions make the control of phase purity during synthesis and isolation a challenging task. In the following, in order to use a common crystallographic reference system, the cubic unit cell will be described in the trigonal setting, as shown in Figure 4.2. The transformation reported therein provides a lattice with **a** and **b** cell parameters coinciding, in length and direction, with those of the hexagonal unit cell, making all considerations on stacking sequences and on their effects on the XRD pattern much easier.

During the crystallization process, it is however possible that hybrid defective structures (with planar defects known as stacking faults, SF) are formed. For bulk materials, and especially in metals, the presence of SF is strongly influenced by the thermal and mechanical history; at variance, in the (colloidal) synthesis of nanocrystals, which are not normally exposed to mechanical stress, the formation of stacking faults may be strongly influenced by the rapid quenching of the

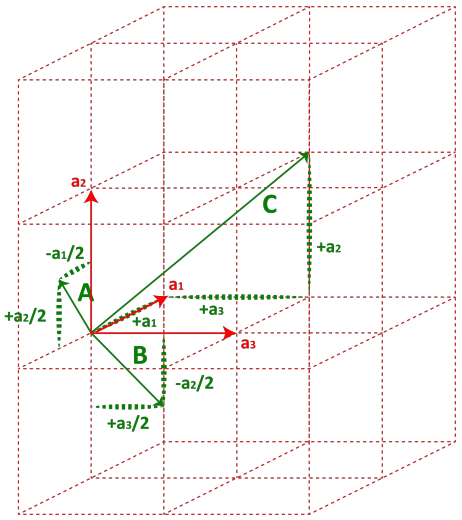

$$\boldsymbol{A} = -\boldsymbol{a_1}/2 + \boldsymbol{a_2}/2 + 0$$
$$\boldsymbol{B} = 0 - \boldsymbol{a_2}/2 + \boldsymbol{a_3}/2$$
$$\boldsymbol{C} = \boldsymbol{a_1} + \boldsymbol{a_2} + \boldsymbol{a_3}$$

$$H = -h/2 + k/2 + 0$$
$$K = 0 - k/2 + l/2$$
$$L = h + k + l$$

Figure 4.2. *Vectorial representation of the cubic cell transformation from the cubic setting to the trigonal (hexagonal) one. On the right, the new vectors of the trigonal cell are defined. During the transformation process, the hkl indices are transformed into HKL, in order to apply the selection rules for the estimation of the SF effects discussed in Paragraph 4.1.2.*

temperature of the suspension, as well as by surface energy contributions.

Neglecting entropic contributions, the occurrence of SF into an ideal "defect free" crystalline structure can be associated to an increment of the system energy.[7–9] This energy term, typically called Stacking Fault Energy (SFE), is generally measured in mJ/m^2 and represents the energy required to introduce a single planar defect (of a specific type, *vide infra*) in the thermodynamically stable structure, normalized to unit area. Obviously, the SF probability is anti-correlated with the SFE, in that low SFEs promote a high density of displaced layers. In Table 4.1, the SFEs of *fcc* metals are reported,[10] showing that they span well beyond one order of magnitude.

Stacking fault energies have be estimated by studying the difference in lattice energy stabilization within the two "pure" polymorphs. This energy term is the result of three different contributions:[9,11]

- Bond energy (BE)
- Electrostatic (Coulomb Energy) (CE)
- Band Structure Energy (BSE)

Metal	structure	SFE (ISF) (mJ/m^2)
Rh	*fcc*	320
Ir	*fcc*	499
Ni	*fcc*	187
Pd	*fcc*	225
Pt	*fcc*	393
Cu	*fcc*	56
Ag	*fcc*	34
Au	*fcc*	59
Co	*hcp*	27
Al	*fcc*	295

Table 4.1. *The table includes the thermodynamically stable crystal phases (column two) and their relative stacking fault energies (column three) for different metals. This table intends to show the high variability of the SFE (from 27 to 499 mJ/m^2) as function of the element. The reported values are taken from Ref* [10] *(N.M Rosengard and H. L. Skriver, Physical Review B, Volume 47, Number 19, 1993, 12870).*

In elemental crystals, the CE contribution is zero, while it becomes the leading term in crystals with high(er) ionicity. Since II-VI semiconductors generally possess non-zero ionic charges (Philips' ionicity values fall above 0.6),[12] some geometrical, though naïve, considerations may help in assessing which of the two polymorphs, WZ and ZB, is the thermodynamically stable one. As anticipated, the crystals are composed by two different atomic species and the nodes previously used to describe the stacking sequences (as in *fcc* or *hcp* metals) can now be dressed by A-B units (*e.g.*: CdSe), oriented normally to the **ab** plane.

As the small difference in the lattice energy of the two polymorphs is attributable to the contribution of the three terms, it becomes highly relevant to assess which of them differ the most. Likely, the coulombic contribution overwhelms the other terms: indeed, since the third nearest neighbor of an atom A is in an eclipsed or staggered configuration (with respect to atom B) in the WZ and ZB structures,

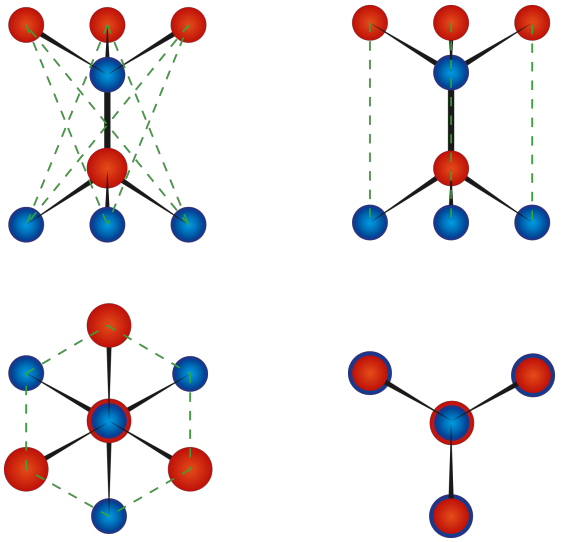

Figure 4.3. *Atomistic representation of a CdSe crystal portion in ZB (left) and in WZ phase (right). For each model, two projections are showed in order to well appreciate the differences in terms of stacking and interatomic distances. In this ideal model, the distances of the first and second nearest neighbor, don't change contrary to the third one. The staggered atomic configuration (ZB) favor a larger distance between Cd and Se atoms and minimize their ionic interaction. On the other side, the eclipsed (WZ) configuration tends to minimize the interatomic distances of the third nearest neighbor in order to maximize the ionic interaction that can be increased contracting the c axis.*

respectively (see Figure 4.3), a coulombic energy stabilization in WZ is expected. Starting from an ideal WZ *c/a* axial ratio of 1.633, contracting the lattice along the **c** crystallographic direction [0001] makes the coulombic interaction stronger and vice versa.[11] Thus, one expects highly ionic materials to prefer the eclipsed (hexagonal) *vs.* the staggered (cubic) structure. Table 4.2 collects examples of some of the most investigated II-VI semiconductors (data refer to the bulk phase structure):[11]
Following the above reasoning, it should not surprise that ZnO, having a significantly shrunk **c**-axis, crystallizes as a WZ phase thanks to a significant Coulombic stabilization. Here, the electrostatic component is highly predominant and the SFE is relatively high; accordingly, the pure ZB phase of ZnO has never been isolated in the bulk (though reports on its occurrence in thin films have appeared).[13] For the other cases shown in Table 4.2, both ZB and WZ structures are reported in literature,

Composition	Phase	SFE (mJ/m^2)	WZ c/a
ZnO	WZ	100±20	1.603
ZnS	ZB	≤6	1.637
ZnSe	ZB	13±1	1.634
ZnTe	ZB	16±2	1.645
CdS	WZ	8.7±1.5	1.632
CdSe	**WZ**	**14±5**	**1.635**
CdTe	ZB	9±1	1.637

Table 4.2. *The table includes: the thermodynamically stable crystal phases (column two), the stacking fault energies (column three) and the literature c/a ratios for WZ polymorphs (column four) of II-VI semiconductor compounds with different composition. The table intends to show the low SFE values of these binary compounds compared to the metallic ones. Additionally, column four highlights the deviations from the ideal 1.633 value (up to 1.8%) corroborating the fundamental role of the internal electrostatic interaction in defining the thermodynamically stable crystal phase and the stacking fault energy. The SFE and c/a values are taken from S. Takuechi et al. Physica Statu Solidi A 171, 99 (1999).*

in line with the lower SFE values and less-distorted *c/a* ratios. Worth of note, these materials are more prone to the formation of SF, if compared to metals, for their much lower SFEs.

However, the SFE represents the difference in energy between two stable configurations, both being minima in the transformation path of the faulted-to-unfaulted crystal conversion; thus, this energy difference *does not* refer to the energy required to heal the SF, turning into a defect-free structure. Indeed, in order to restore the periodic crystal (here taken as the thermodynamically stable phase, or the absolute minimum in energy), the faulted plane has to be strained or "lifted", overcoming an absolute activation energy barrier, the unstable stacking fault energy, or uSFE. Recent findings on metallic NPs revealed[14,15] that, contrary to SFE values that strongly depend on the elemental composition, the uSFE seems to be nearly independent from it. This concept will be reconsidered in Chapter 6 to explain

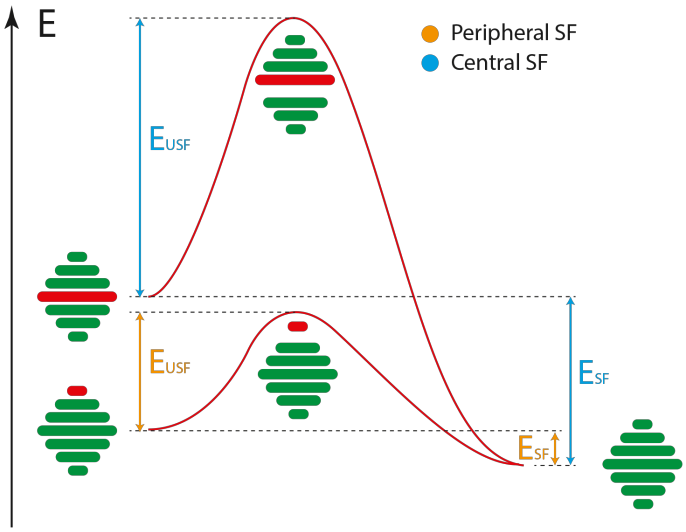

Figure 4.4. *A qualitative representation of the* ***actual*** *uSFE and SFE relationship for nanoparticles with a single defect localized in a different portion of a QD and, consequently, with a different faulted area.*

our results on CdSe cQDs, the main object of this project. Worth of note, the *actual* uSFE barrier depends on the lateral extension of the faulted plane, *i.e.* by the size of the section of the nanocrystal at the fault position, which can be markedly different in different portions of a QD (see Figure 4.4).

4.1.2 Stacking Fault Classification and Estimation of their Probability

After the introduction on the SFE energetics and on their influence of the crystal stability, this paragraph is dedicated to the enumeration of different types of stacking faults and the description of a common strategy for their quantification, based on the classical theory of Warren.[16] Historical developments in SF theory and their XRD data analysis will be presented in a next Chapter, when the SF model proposed in this thesis will be discussed. According to Warren, Jagodinzski's nomenclature of the stacking sequence [ABC] can be alternatively described by introducing a "*k*" or "*h*" transition term.[6] A transition is a label attributed to the third

layer using, as a reference, the nature (in A,B,C terms) of the previous two. If the third layer is eclipsed with respect to the first one (as in ABA), the transition is called hexagonal (*h*), otherwise (*i.e.*, if the layer is staggered), the transition is cubic (*k*). No other sequences are possible for closed packed crystals, all equally dense, though no periodicity is ever assumed.

Three types of staking faults are known, easily recognized by the transition sequence (or stacking sequence):[17,18]

- Growth (or Twin) Fault (TF or GF) …*kk**h**kk*… (ABCBA);
- Intrinsic (or Deformation) Fault (ISF or DF) …*kk**hh**kk*… (ABCBCA);
- Extrinsic (or Double Deformation) Fault (ESF or DDF) …*kk**h**k**h**kk*… (ABCBABC).

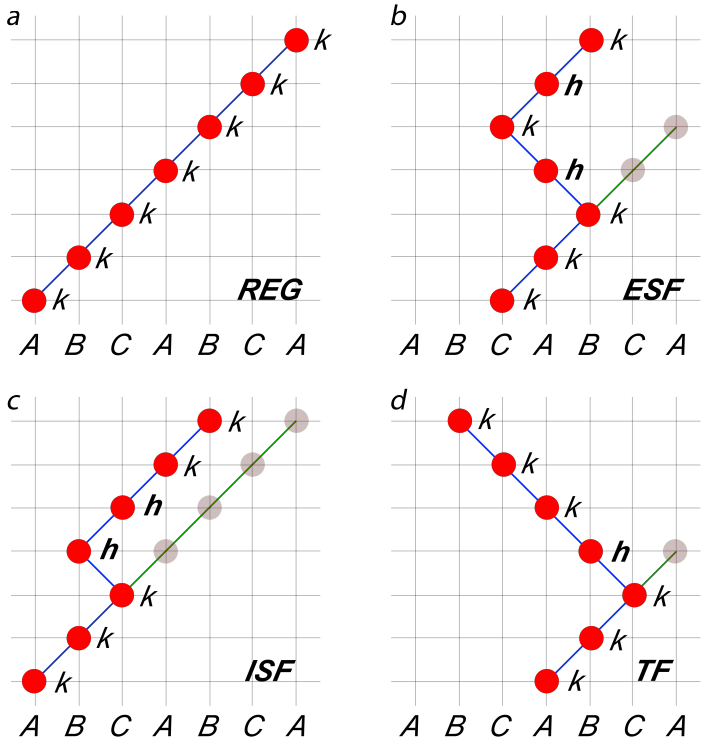

Figure 4.5. *Schematics of different types of stacking. a) regular cubic stacking built by a periodic repetition of ABC layers, represented by k transitions only. b) ESF is generated produced by alternating k and h transitions. c) ISF is produced by the presence of two consecutive hexagonal transitions within an overall cubic environment. d) TF generated by the presence of a single and isolated h transition, mirroring the sequences about the defect position.*

hkl	Pure *fcc*	**u**, **b**	ISF shift	ESF shift	TF shift
111	8	2 (u)	no	no	no
		6 (b)	▷	◁	no
200	6	6 (b)	◁	▷	no
…	…	…	…	…	…
311	24	12 (u)	no	no	no
		6 (b)	▷	◁	no
		6 (b)	◁	▷	no
…	…	…	…	…	…

Table 4.3. *The table includes the "shift" behaviors of Bragg reflections of elemental fcc crystals when affected by different types of stacking faults. The **u**nbroadened reflections (when H-K=3n, see Figure 4) are not shifted being never affected by the SF phenomenon. The **b**roadened reflections (when H-K≠3n, see Figure 4) are shifted (or not) depending on the planar defect type.*
Legend: no = not shifted; ▷ shifted to the right; ◁ shifted to the left

From now on, growth, intrinsic and extrinsic SF terms will be used with the exception of twin fault, term peculiarly dedicated to elemental metals.
Figure 4.5 pictorially shows the nature of the different stacking fault types and their labeling, in comparison with an ideally periodic *fcc* sequence (upper left panel).
The insertion of planar defects of these types typically leads to modifications of the XRPD peaks (shifts and broadening), which depend on the *hkl* indices but follow complex rules.[16]
According to diffraction theory, each observable peak in the XRD trace of a polycrystalline (powdered) material contains the contribution of all its "symmetry equivalent" reflections. For example, in an ideal and fully periodic *fcc* structure, the 111 peak is composed by *eight* equal reflections, each of the same integrated intensity (neglecting anomalous scattering effects), position, width and shape (the number of symmetry equivalents may vary depending on peak indices, parity and Laue class); however, the introduction of a planar defect orthogonal to the [111]

direction breaks their equivalence by separating them in two classes:

- Two reflections (*H-K = 3n*, n = 1,2,3...) are not affected by SF (see Figure 4.2 for the indices transformation from *hkl* to *HKL*) (u type, for **u**nbroadened);
- 6 reflections (*H-K* $\neq$ *3n*, n = 1,2,3...) affected by SF (b type, for **b**roadened);

each of them exhibiting a specified peak broadening and angular shift. Table 4.3 contains a summary of these feature, which depend on *hkl* type and parity.

Table 4.4 and recent simulations also show that the introduction of a planar defect along the [111] direction, does not break the symmetry of the six equivalent reflections of *h00* peaks, producing a symmetric peak with a well-defined 2ϑ shift with a monotonic behavior (in terms of shift and broadening) with the stacking fault probability.[18] Depending on the *hkl* reflection indices and the type of defects as summarized in Table 4.4, the resulting peak may be shifted and/or partially skewed. In 2002, Ustinov[18] reported, for the simple case of *fcc* metals, how and how much the full width at half maximum (FWHM) of the peaks is affected by reflection inequivalence; significantly, the FWHM *vs.* the stacking fault probability trends were

hkl	Intrinsic SF		Extrinsic SF		Growth SF	
	shift	asymmetry	shift	asymmetry	shift	asymmetry
111	no	◣	no	◢	no	▲
200	▷	▲	◁	▲	no	▲
220	no	▲	no	▲	no	▲
311	no	◢	no	◣	no	▲
222	no	◢	no	◣	no	▲
400	◁	▲	▷	▲	no	▲

Table 4.4. *The table reports the impact on Bragg peak shape and broadening of elemental fcc crystals when affected by different types of stacking faults. The symbols in table highlight that the co-presence of broadened and unbroadened reflections (e.g. 111 ones) that constitute the same Bragg peak produces asymmetric peak traces. Contrarily, the presence of broadened reflections only (e.g. 200 peak), contributes to the shift of the peak maximum about which the peak trace is symmetric.*

Legend:

no = not shifted; ▷ shifted to the right; ◁ shifted to the left

▲ symmetric; ◣ asymmetric with tails to the right; ◢ asymmetric with tails to the left

found to be non-monotonic for all peaks, except the *h00* family. For this reason, determination of the SF probability would be easy if peaks of this class only were used, enabling the SF type to be evaluated by the peak broadening and shift (if only one of these planar defects was present). However, the simultaneous presence of two or more SF types may generate peak broadening and asymmetries that are not easily interpretable; to give an example, the co-presence of ISF and ESF can be interpreted as a large number of TF.[18] Indeed, each *hkl* reflection contributes to the peak shape with its own broadening and angular shift, determining the total, observable, peak shape and location.

The classic method proposed in Warren's book[16] provides an estimation of the ISF probability, α_W, based on the experimental evaluation of the 2θ angular shifts, as follows:[16]

$$\Delta(2\vartheta) = \frac{90\sqrt{3}\alpha_W \tan\vartheta}{\pi^2 h_0^2 (u+b)} \sum_b (\pm) L_0$$

$Eq.\,4.1$

where:

α_W : ISF probability

$h_0^2 = h^2 + k^2 + l^2$

$(u+b)$: (broadened and unbroadened) reflection multiplicity

$L_0 = h + k + l$

$(\pm) : L_0 = 3n \rightarrow 0,\ L_0 = 3n-1 \rightarrow -1,\ L_0 = 3n+1 \rightarrow +1,\ n \in Z$

$(\pm) = -1, 0, +1$

Thanks to Equation 4.1, peak shifts of an ideal *fcc* packing of spheres may be calculated using the numerical terms reported in Table 4.5.

The ideal Bragg angle of the *hkl* reflection of a *cubic* crystal is easily calculated as follows:

$$2\vartheta_{hkl} = 2\sin^{-1}\left(\frac{\lambda\sqrt{h^2+k^2+l^2}}{2a_k}\right)$$

$Eq.\,4.2$

where λ is the operational wavelength and a_k is the cubic lattice parameter.

hkl	h_0^2	$\sum_b (\pm) L_0$	$(u+b)$	$\frac{1}{h_0^2(u+b)} \sum_b (\pm) L_0$
111	3	6	8	$1/4$
200	4	-12	6	$-1/2$
220	8	24	12	$1/4$
311	11	-24	24	$-1/11$
222	12	-12	8	$-1/8$
400	16	24	6	$1/4$
331	19	24	24	$1/19$
420	20	-24	24	$-1/20$
422	36	36	24	$1/24$
511	27	-18	24	$1/36$

Table 4.5. *The table reports all the values required to compute Equation 4.1. Legend and description of the parameters in table are discussed right after Equation 4.1.*

As the experimental peak shifts from ideal values can be estimated (provided that the instrumental resolution is adequate), Equations 4.1 and 4.2 enable the estimation of the α_W parameter; however, peak shifts can also appear as a consequence of lattice strain or instrumental errors. To avoid these annoying effects, combining two Equations of the 4.1 type, provide a robust method for evaluating the ISF probability value α_W. If the 111 and 200 couple is used (which are intense peaks in *fcc* metals), Warren's formula reduces to:[16]

$$\Delta(\Delta 2\vartheta_{200} - \Delta 2\vartheta_{111}) = \frac{-90\sqrt{3}\alpha_W}{\pi^2}\left(\frac{\tan\vartheta_{200}}{2} + \frac{\tan\vartheta_{111}}{4}\right) \qquad Eq.\,4.3$$

An example of this approach will be reported in the experimental section on CdSe, which, however, is not a simple case, as a number of additional peak broadening and shifting effects are present, on top on the poorly defined position of the 200 peak (weak for intrinsic structural reasons).

All the previous considerations are valid when the extension of the crystal domain can be considered infinite. Since, in nanomaterials, this approximation vanishes, the evaluation of the SF probability using classical methods can only be applied in a qualitative way, mainly by detecting the presence of planar defects by observing experimental peak shifts. Another issue linked to nanomaterials, and related to their limited size, is the non-uniform extension of "atomic" planes. Indeed size, morphology and crystal orientation change, within the same QD, the area of the crystal sections normal to [111] and, as a consequence, also the absolute SFE (SFE $\times$ area), with measurable effects on the XRPD trace. For sake of simplicity, this aspect has been evaluated on elemental nanoparticles (*fcc* Pt clusters, discussed at the end of this PhD thesis), simulating the XRPD traces on platinum nanocrystals with different shapes.[19] This study showed the effects of TF and ISF (with probabilities ranging from 0 to 2.5%) in nanocrystals with different morphologies, namely, spherical and cylindrical, the latter oriented with the [111] axis. The study revealed that peak shift and broadening heavily depend on the nanoparticle shape, or, in other terms, they are the trace of the finite, and very small domain size of the defective planes. The evaluation of a randomly positioned stacking fault within spherical NP confirms a monotonic peak broadening for the introduction of a TF and a monotonic peak broadening and shift introducing an ISF. This study also aimed at the evaluation of the observable peak shifts as function of the crystal shape. As depicted in Figure 4.6, depending on the different extension of the crystal domain, the effects on the XRPD pattern are not in line with Warren's theory. This theory, derived for bulk materials, can in principle quantitatively predict the probability of an ISF; for a spherical nanoparticle, the entity of the peak shift of the 111 peak is more or less half of that of the 200 peak (see Figure 4.6b), in agreement with what proposed by Equation 4.1: *i.e.* shifts agree in absolute value and direction. If, however, a cylindrical cluster is considered, the relative shifts (shown in Figure 4.6 d,e) cannot be calculated by Warren's method. Since the extension of the planar defect depends of the crystal shape and location (central *vs.* peripheral), several simulations were performed for both morphologies. As expected, modifying the location of an ISF in a cylindrical cluster (where the area of all the transversal sections is equivalent), does not provide dramatic differences on the simulated diffraction trace. At variance, in spherical clusters, positioning the planar defect in

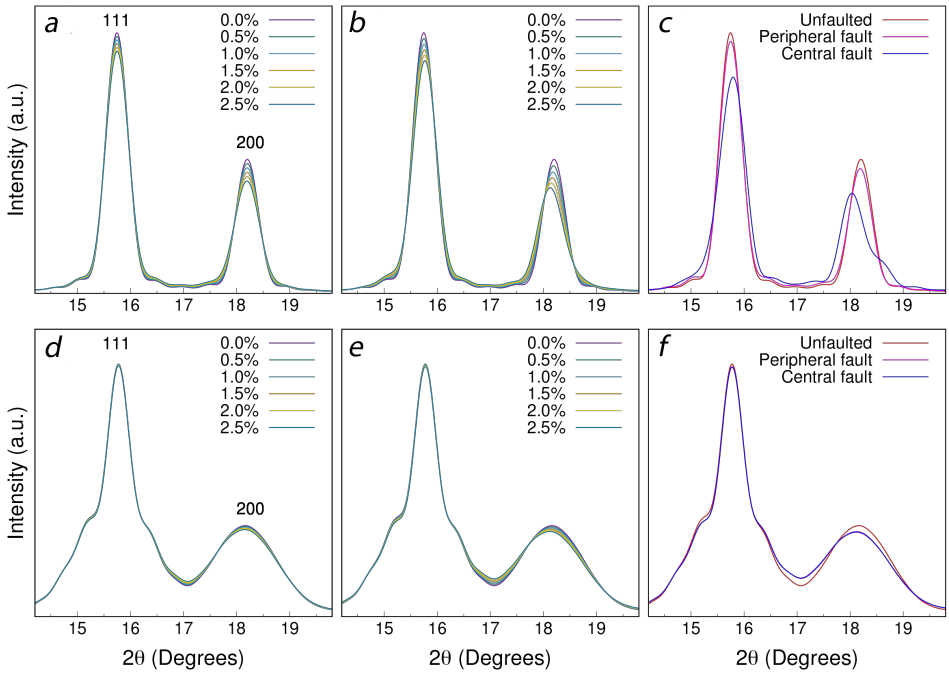

Figure 4.6. *Effect on the XRPD pattern (111 and 200 peaks) of Pt nanoclusters with different morphologies. The simulations on top are performed on a spherical cluster with a diameter of 8.0 nm, while those at the bottom refer to cylindrical clusters (with base diameter of 2.0 nm and axial length of 10.0 nm). The first column shows the effects of different TF percentages (TF randomly located in the cluster), while the second one shows the effects of an ISF (TF and ISF randomly located in the cluster). The last column shows the effect of the localization of the SF in the two different morphologies, particularly evident in the spherical case.*

the nanoparticle center produces vivid differences, if compared with the effects generated from a fault located in the periphery of the cluster (see Figure 4.6 c,f).

Summarizing, these considerations sanctioned the need of defining new, and advanced, SF models, developed specifically for nanomaterials, and to be numerically treated within a unified data analysis protocol, *i.e.* that implemented in the Debussy suite, where the Debye Scattering Equation is actively used.[19]

In the recent past, alternative studies aiming at evaluating the SF probability in nanomaterials have been performed using WAXTS techniques (PDF[20–22] and DSE[19,23,24]). In these works, WAXTS methods showed their enormous potential in characterizing stacking sequences and fault probabilities, but, due to high SF

percentages, the concomitant presence of strain and the extremely reduced size, their full characterization is still a challenging task. The use of **configurational** DSE, implemented by us in the Debussy suite, not only enabled the evaluation of all these aspects (including SF probability in the different morphologies and preferential localization of faults), but also allowed localized distortions and surface stoichiometry to be detected and fully quantified.

4.2 Surface Aspects

As introduced in Chapter 1, in very small nanoparticles, the surface plays a fundamental role starting from the synthetic aspects, to the stabilization of the particles crystal phase, and ending up with the material functional properties.[25–28] Central to the work of this Ph. D. thesis is the development of a method which can maximize the structural information that can be extracted via X-ray diffraction methods, using advanced WAXTS techniques. In this short section, I will briefly discuss a number of surface-related aspects, neglecting, for the moment, relevant issues related to ion vacancies and connectivity (briefly explained in Chapter 1 while presenting different aspects on the synthesis and material properties). In particular, I will draw the reader's attention to surface disorder and other morphological aspects, like particles faceting.

Semiconducting nanoparticles of the II-VI type are generally synthetized with a bottom-up approach, as this approach can guarantee a high degree of monodispersity.[29] As anticipated in Chapter 1, the colloidal synthesis relies on the addition of different ligands that (apparently) boost the preferential formation of distinct phases and nanocrystal shapes. Ligands and, in general, the entire chemical environment during nanomaterials synthesis can have different effects on the nanoparticle structure (Figure 4.7) and stability and, consequently, on its properties. This is more than true in ultra-small nanoparticles, possessing a relatively large fraction of atoms on the surface, or shallowly buried below it. For example, uncharged metallic nanoparticles, lacking surfactants, possess exposed atoms with low-coordinated environments, which tend to preferentially bind to the metal core

(than to outer vacuum) and induce a visible surface contraction. At variance, as also found in oxidic materials, semiconducting colloidal NPs, often stabilized by a crown of charged ligands, result in non-stoichiometric nanocrystals,[30,31] with ligand-dependent contraction or expansion phenomena.

The physical quantity that controls these effects is the surface free Gibbs energy that, in case of crystalline solids, is tensorial[32] (*i.e.* it can vary as function of the crystallographic direction); its surface density (the surface tension γ) is defined as the quantity of energy required to generate a unitary surface area at given conditions (V, T and n constant) during an elastic process (see Equation 4.4).[32]

$$\gamma = \frac{dG}{dA} \qquad Eq.\,4.4$$

where:

dG : Gibbs energy variation

dA : incremental surface area

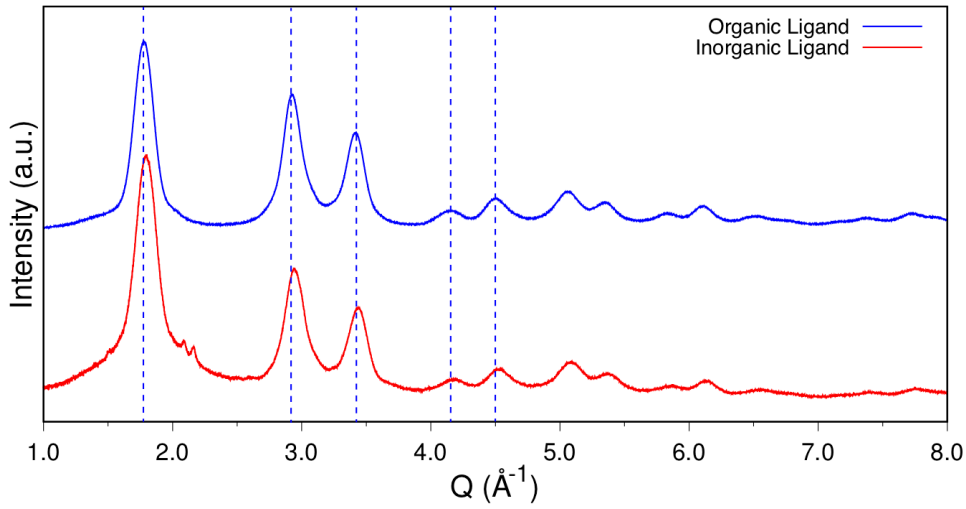

Figure 4.7. *Experimental patterns of CdSe QDs with average diameter of 4.1 nm with different ligands at the surface. The solid blue line is referred to a sample with oleic acid at the surface. The solid red line is referred to the same sample after a ligand exchange with K_2S. The two patterns are equivalent except for a contraction effect applied by the inorganic ligand layer.*

With the aim of evaluating surface effects in isotropic nanoparticles and with the aid of homogeneous elastic deformation theory, a new parameter g (surface stress) is introduced, expressed as a first order expansion of γ in dA as follows:[32]

$$g = \gamma + A\frac{d\gamma}{dA}$$

$Eq.\,4.5$

From g, it is finally possible to quantify the induced deformation in homogenous spherical particles expressed as cell contraction $\Delta a/a$, as function of the material compressibility k and its radius R (T constant).[32]

$$\frac{\Delta a}{a} = -\frac{2}{3}\frac{gk}{R}$$

$Eq.\,4.6$

where:

$$k = -\frac{1}{V}\frac{dV}{dP}$$

Equation 4.6 highlights the fundamental point of this mathematical analysis, revealing that the cell compression/expansion is always size dependent and has a maximum effect when $R \rightarrow size\ of\ an\ atom/molecule$, while tends to fade when $R \rightarrow large\ (bulk)$. If the crystal size controls the extent of the cell parameter variation, g, since generally $k > 0$, enforces the contractive or expansive nature of the distortion. In metals, g is positive and produces a contraction,[33–35] while, in other ionic binary systems, g can be negative, leading to a surface expansion.[36]

In nanoparticles with anisotropic shapes, the occurrence of crystal faces, edges and vertices force to treat, as explained before, the surface tension quantity in a tensorial description.

An alternative more complex model was proposed in 2005 by Qi and Wang[33] for non-spherical metallic particles. In this work, it was estimated that a shape contribution accounts for *ca.* 10% of the resulting cell contraction/expansion

parameter with respect to the ideal spherical case.

All these relaxation effects originate from changes of the interatomic distances within the sample and can be detected, and quantified, by WAXTS techniques if appropriate models are built. Unfortunately, the extent of this deformation is small and often hidden by the presence of polydisperse samples or of crystals with additional source of strain or defects. However, since the wide-angle region of X-ray scattering data, even on polydisperse samples, provides accurate "mass-averaged" cell parameters, small surface relaxation effects can be estimated using, for each NP, a crystal lattice distortion which follows a specific size-dependent law. One of these cases will be presented and explained in detail in Chapter 7, where highly polydisperse samples of Pt NCs were analyzed. For monodisperse samples, such as CdSe, where the XRPD pattern is the result of only a very limited number of clusters, this size dependent law can be detected evaluating the average cell expansion as a function of the crystal size. This approach enables the fruitful comparison of the results from different samples (of the same composition and synthetized with the same recipe), each possessing a different *average* crystal size.

Another fundamental aspect of NPs surface is the tendency to form faceted clusters: this occurs because, during the synthesis, crystal growth is much faster on specific directions and reduction of the excess surface energy is at work. In the absence of externally morphology-directing agents (vessel surfaces, laminar flow, etc.), crystal symmetry imposes the final crystal shape, though a variety of morphology may belong to the same crystal class. For example, in a pure zinc blende CdSe (with cubic m-3m point group symmetry), low-indices facets belong to the 100, 110 and 111 families. When 100 facets only (or 110 or 111) are exposed, platonic solids (cube, rhombododecahedron and octahedron) are formed, all highly isotropic. Other equally sized polyhedra can be formed, for example by merging 111 and 100 families of facets. Depending the different surface extension of these faces, regular, or less ideal cuboctahedra can be formed.

However, when kinetic effects or, more importantly, the presence of defects break the point symmetry of fully ordered systems, then elongated crystal may form, with unexpected size dependent faceting and mismatching morphological/structural symmetry. Chapter 6, where SAXS methods will be discussed, will report on such important finding in our samples of nominal cubic CdSe symmetry.

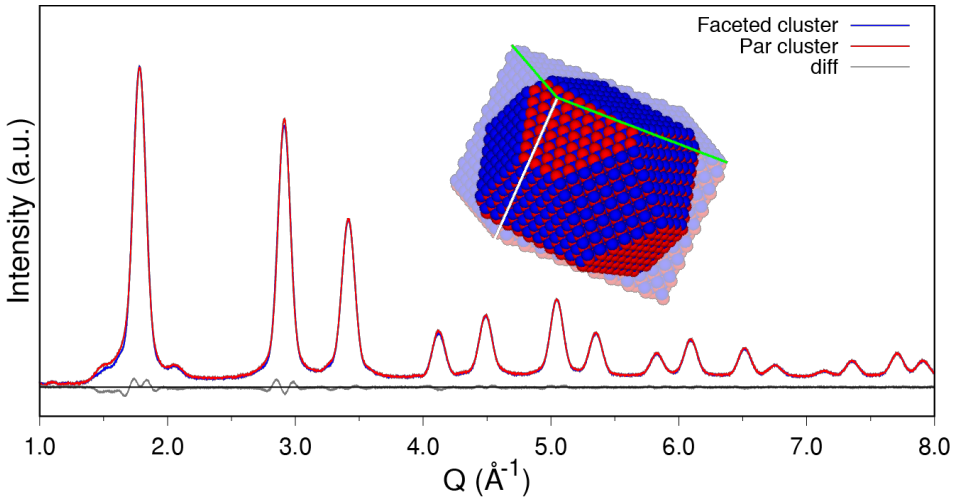

Figure 4.8. *DSE simulations of CdSe NCs populations, with a Gaussian noise < 1% added. The two traces (blue for faceted NCs, red for the regular prism) refer to the morphologies shown in the inset and present nearly identical features in the wide-angle region. Accordingly, only SAXS in the Porod region enabled the detection and quantification of the crystal faceting (discussed in Chapter 6).*

Contrary to the surface relaxation, that can be estimated from the wide-angle region, this portion of scattering data is very marginally affected by faceting, its effect being barely visible for DSE-base simulations of single clusters and fading even for highly monodispersed (bur real) populations (see Figure 4.8).

Despite the wide-angle region, for real samples, is blind to second-order morphological descriptors (here, faceting), by suitably positioning the beam-stop during a WAXTS acquisition, for monodisperse and very small nanoparticles the *Porod* section of the small angle scattering region becomes accessible. This part of synchrotron scattering data can be crucial for the determination of faceting since, even in dedicated laboratory SAXS instrument, the Porod region of the SAXS data may be rather noisy. Additionally, since DSE simulations are not restricted to any specific portion of the 2θ range, it was used, to our knowledge, for the first time, to simulate the *Porod* region of the entire XRPD pattern using a population of faceted cluster.

Conclusions

II-VI semiconducting materials and, in general, nanoparticles of any type may present a structural defectiveness that can be detected and quantified using the DSE approach. Starting from the classical theories on planar defects, we built atomistic model of nanosized clusters to assess the features made visible by DSE-based simulations and foresaw how to extract information on nanocrystal defectiveness from WAXTS data. Even if the WAXTS pattern ideally contains information from each nanocrystal in the ensemble, DSE derives statistically averaged values, but can also provide size-dependent information about stoichiometry, surface strain and, through the innovative characterization of the Porod region in the SAXS regime, on nanocrystal faceting. Given the enormous potential of the DSE in characterizing small (crystalline) nanoparticles, next Chapter will focus on the mathematical / geometrical / statistical construction of structural & microstructural models containing size, shape, strain, stacking fault and ion vacancy effects in a unified frame.

References

(1) Gao, Y.; Peng, X. Crystal Structure Control of CdSe Nanocrystals in Growth and Nucleation: Dominating Effects of Surface versus Interior Structure. *J. Am. Chem. Soc.* **2014**, *136* (18), 6724–6732.

(2) Wei, S.-H.; Zhang, S. B. Structure Stability and Carrier Localization in CdX (X=S, Se, Te) Semiconductors. *Phys. Rev,* **2000**, 62 (11), 6944-6947.

(3) Hughes, S. M.; Alivisatos, A. P. Anisotropic Formation and Distribution of Stacking Faults in II-VI Semiconductor Nanorods. *Nano Lett* **2013**, *13* (1), 106–110.

(4) Huang, J.; Kovalenko, M. V.; Talapin, D. V. Alkyl Chains of Surface Ligands Affect Polytypism of CdSe Nanocrystals and Play an Important Role in the Synthesis of Anisotropic Nanoheterostructures. *J. Am. Chem. Soc.* **2010**, *132* (45), 15866–15868.

(5) C. B. Murray; C. R. Kagan. Synthesis and Characterization of Monodisperse Nanocrystals and Close-Packed Nanocrystals Assemblies. *Annu. Rev. Mater. Sci.* **2000**, *30*, 545–610.

(6) Jagodzinski, H. Polytypism in SiC Crystals. *Acta Cryst.* **1954**, *7* (3), 300–300.

(7) Gallagher, P. C. J. The Influence of Alloying, Temperature, and Related Effects on the Stacking Fault Energy. *Metall. Trans.* **1967**, 1, 2429-2461.

(8) Li, R.; Lu, S.; Kim, D.; Schönecker, S.; Zhao, J.; Kwon, S. K.; Vitos, L. Stacking Fault Energy of Face-Centered Cubic Metals: Thermodynamic and *Ab Initio* Approaches. *J. Phys. Condens. Mat.* **2016**, *28* (39), 395001.

(9) Takeuchi, S.; Suzuki, K.; Maeda, K.; Iwanaga, H. Stacking-Fault Energy of II–VI Compounds. *Philos. Mag. A* **2006**, *50* (2), 171–178.

(10) Rosengaard, N. M.; Skriver, H. L. Calculated Stacking-Fault Energies of Elemental Metals. *Phys. Rev.* **1993**, *47* (19), 12865–12873.

(11) Takeuchi, S.; Suzuki, K. Stacking Fault Energies of Tetrahedrally Coordinated Crystals. *Phys. Stutus Solidi C* **1999**, *171* (1), 99–103.

(12) *Bond and Bands in Semiconductors*; Academic Press, **1973**.

(13) Ashrafi, A. B. M. A.; Ueta, A.; Avramescu, A.; Kumano, H.; Suemune, I.; Ok, Y.-W.; Seong, T.-Y. Growth and Characterization of Hypothetical Zinc-Blende ZnO Films on GaAs(001) Substrates with ZnS Buffer Layers. *Appl. Phys. Lett.* **2000**, *76* (5), 550–552.

(14) Van Swygenhoven, H.; Derlet, P. M.; Frøseth, A. G. Stacking Fault Energies and Slip in

Nanocrystalline Metals. *Nat. Mater.* **2004**, *3* (6), 399–403.

(15) Jo, M.; Koo, Y. M.; Lee, B.-J.; Johansson, B.; Vitos, L.; Kwon, S. K. Theory for Plasticity of Face-Centered Cubic Metals. *Proc. Natl. Acad. Sci. U S A* **2014**, *111* (18), 6560–6565.

(16) B. E. Warren. *X-Ray Diffraction*; Dover Publications, I. N. C., Series Ed.; Dover Books in Physiscs; New York, **1990**.

(17) Kakinoki, J. Diffraction by a One-Dimensionally Disordered Crystal. II. Close-Packed Structures. *Acta Cryst.* **1967**, *23* (6), 875–885.

(18) Ustinov, A. I.; Budarina, N. M. Influence of Planar Defects on Powder Diffractograms of Fcc Metals. *Powder Diff.* **2002**, *17* (04), 270–277.

(19) Bertolotti, F.; Moscheni, D.; Migliori, A.; Zacchini, S.; Cervellino, A.; Guagliardi, A.; Masciocchi, N. A Total Scattering Debye Function Analysis Study of Faulted Pt Nanocrystals Embedded in a Porous Matrix. *Acta Crystallogr. A* **2016**, *72*, 632–644.

(20) Masadeh, A. S.; Bozin, E.; Farrow, C. L.; Paglia, G.; Juhas, P.; Karkamkar, A.; Kanatzidis, M. G.; Billinge, S. J. L. Quantitative Size-Dependent Structure and Strain Determination of CdSe Nanoparticles Using Atomic Pair Distribution Function Analysis. *Phys. Rev. B* **2007**, *76* (11).

(21) Yang, X.; Masadeh, A. S.; McBride, J. R.; Božin, E. S.; Rosenthal, S. J.; Billinge, S. J. L. Confirmation of Disordered Structure of Ultrasmall CdSe Nanoparticles from X-Ray Atomic Pair Distribution Function Analysis. *Phys. Chem.* **2013**, *15* (22), 8480.

(22) Kumpf, C.; Neder, R. B.; Niederdraenk, F.; Luczak, P.; Stahl, A.; Scheuermann, M.; Joshi, S.; Kulkarni, S. K.; Barglik-Chory, C.; Heske, C.; et al. Structure Determination of CdS and ZnS Nanoparticles: Direct Modeling of Synchrotron-Radiation Diffraction Data. *J. Chem. Phys.* **2005**, *123* (22), 224707.

(23) Longo, A.; Martorana, A. Distorted f.c.c. Arrangement of Gold Nanoclusters: A Model of Spherical Particles with Microstrains and Stacking Faults. *J. Appl. Cryst.* **2008**, *41* (2), 446–455.

(24) Longo, A.; Sciortino, L.; Giannici, F.; Martorana, A. Crossing the Boundary between Face-Centred Cubic and Hexagonal Close Packed: The Structure of Nanosized Cobalt Is Unraveled by a Model Accounting for Shape, Size Distribution and Stacking Faults, Allowing Simulation of XRD, XANES and EXAFS. *J. Appl. Cryst.* **2014**, *47* (5), 1562–1568.

(25) Azpiroz, J. M.; De Angelis, F. Ligand Induced Spectral Changes in CdSe Quantum Dots. *ACS Appl. Mater. Interfaces* **2015**, *7* (35), 19736–19745.

(26) Voznyy, O.; Thon, S. M.; Ip, A. H.; Sargent, E. H. Dynamic Trap Formation and Elimination in Colloidal Quantum Dots. *J. Phys. Chem. Lett.* **2013**, *4* (6), 987–992.

(27) Jang, Y.; Shapiro, A.; Isarov, M.; Rubin-Brusilovski, A.; Safran, A.; Budniak, A. K.; Horani, F.; Dehnel, J.; Sashchiuk, A.; Lifshitz, E. Interface Control of Electronic and Optical Properties in IV-VI and II-VI Core/Shell Colloidal Quantum Dots: A Review. *Chem. Comm.* **2017**, *53* (6), 1002–1024.

(28) Giansante, C.; Infante, I. Surface Traps in Colloidal Quantum Dots: A Combined Experimental and Theoretical Perspective. *J. Phys. Chem. Lett.* **2017**, *8* (20), 5209–5215.

(29) Kwon, S. G.; Hyeon, T. Formation Mechanisms of Uniform Nanocrystals via Hot-Injection and Heat-Up Methods. *Small* **2011**, *7* (19), 2685–2702.

(30) Piveteau, L.; Ong, T.-C.; Rossini, A. J.; Emsley, L.; Copéret, C.; Kovalenko, M. V. Structure of Colloidal Quantum Dots from Dynamic Nuclear Polarization Surface Enhanced NMR Spectroscopy. *J. Am. Chem. Soc.* **2015**, *137* (43), 13964–13971.

(31) Piveteau, L.; Ong, T.-C.; Walder, B. J.; Dirin, D. N.; Moscheni, D.; Schneider, B.; Bär, J.; Protesescu, L.; Masciocchi, N.; Guagliardi, A.; et al. Resolving the Core and the Surface of CdSe Quantum Dots and Nanoplatelets Using Dynamic Nuclear Polarization Enhanced PASS–PIETA NMR Spectroscopy. *ACS Cent. Sci.* **2018**, 4, 1113-1125.

(32) Solliard, C.; Flueli, M. Surface Stress and Size Effects on the Lattice Parameters of Particles of Gold and Platinum. *Surf. Sci.* **1985**, 156, 487-494.

(33) Qi, W. H.; Wang, M. P. Size and Shape Dependent Lattice Parameters of Metallic Nanoparticles. *J. Nanopart. Res.* **2005**, *7* (1), 51–57.

(34) Qi, W. H.; Wang, M. P.; Su, Y. C. Size Effect on the Lattice Parameters of Nanoparticles. *J. Mater. Sci.* **2002**, 21, 877-878.

(35) Wasserman, H. J.; Vermaak, J. S. On the Determination of the Surface Stress of Copper and Platinum. *Surf. Sci.* **1972**, *32* (1), 168–174.

(36) Diehm, P. M.; Agoston, P.; Albe, K. Size-Dependent Lattice Expansion in Nanoparticles: Reality or Anomaly? *Chem. Phys. Chem.* **2012**, *13* (10), 2443–2454.

5

Atomistic Models of Stacking Faults in II-VI Nanocrystals for WAXTS-DSE Characterization

With DSE it is possible to treat models both in the configuration space (operating at the atomistic coordinate model level), and in the correlation space (operating at the atomic pair interatomic distance level). The high flexibility of configurational models in DSE analysis, permits the development of strategies for building nanoparticle models introducing, when desired, different kinds of defects breaking the symmetry along one or more crystallographic directions. This Chapter will be focused on the elaboration of a new DSE-based model, implemented in the DebUsSy program suite, for planar defects of the stacking fault type and developed, for binary II-VI and III-V nanoparticles, in the configuration space. Starting from known probabilistic approaches of the sequence generation of atomic planes in closed-packed crystal structures, the main steps for model building are detailed; moreover, a procedure for the optimization of the SF model is presented, based on reasonable assumptions which are valid for the real case of colloidal CdSe QDs.

5.1 Generation of Faulted NCs

Due to the presence of a surface ligand shell, cubic (Zinc blende) CdSe nanoparticles are non-stoichiometric and, as they possess a relatively low SFE,[1] are prone to internal defectiveness by the presence of "hexagonally" stacked layers in an overall cubic sequence. In addition, size and shape effects concur to distort the ideal WAXTS patterns of ZB CdSe NPs, as they can be presently synthetized using specific and tailored routes, with different morphologies[2–4] and size/shape dispersion. Therefore, the study of this purportedly simple, but extremely complex system,[5–7] requires a high degree of flexibility, which a non-periodic crystal scattering theory only can tackle.

Chapter 4 highlighted the possible occurrence, in several *fcc* or *hcp* metals and even in II-VI semiconductors, of planar defects, their different types and labeling and, particularly, their non-negligible effects on the XRD pattern.[8] Since different stacking sequences produce different effects on the X-ray diffraction pattern, the individuation of a robust, efficient, fast and flexible strategy for sequence and nanocrystal generation is a crucial point for the atomistic model construction used in the DSE analysis. Synthetic processes, material composition and the presence of defects in nanostructured samples can slightly or drastically influence the particle morphology and its faceting. They can also induce isotropic or anisotropic strains, at a level which cannot be easily detected by conventional, or even high-resolution, microscopy techniques. It is worth of note that any model of defectiveness which can be introduced to cope with the experimental data is *material dependent* and a different, even if similar, treatment has to be considered for other nanoscale systems, even with the same composition. Accordingly, no standard or universal approaches, as those built in conventional whole-pattern profile programs (say, in the Le Bail, Pawley or Rietveld modes), can be normally employed.

As previously mentioned, the DSE approach is used in:

- the correlation space: operating at the atomic pair interatomic distances level;
- the configuration space: acting at the atomic coordinates level.

Modeling in each of the two spaces offers specific pros and cons; the major

differences may be expected concerning:

- the CPU time;
- the implementation of specific effects in the model;
- differences in the refinement strategy.

Directly working on the set of interatomic distances allows the SF information to be directly implemented in the Debye equation,[9,10] making the stacking disorder (of a faulted structure representing the average over all the probabilistic configurations) a refinable feature within a reasonable CPU time. On the other hand, using the configuration approach offers a more intuitive and easier way to manage models on a chemical basis but different probabilistic configurations need to be managed. The configuration approach has been preferred over the correlation one in this work; however, a deeper analysis of pros and cons of each the two ways of using the DSE method would be fruitful.

The DSE-based model here reported for the construction of faulted CdSe NCs is the result of a progressive improvement via a direct, mutual and cyclic interaction between the model and the WAXTS experimental data. Briefly, starting from a population of spherical clusters with a pure ZB structure, data misfits were gradually interpreted and minimized by improving the (progressively more complex) models, including effects produced by:

- Stacking disorder and its nature;
- Shape and crystal structure relative orientation;
- Local or average anisotropic strain;
- Stoichiometry;
- Surface composition.

The application of various models and the most important results will be presented in Chapter 6, fully dedicated to the characterization of ZB CdSe QDs and their size-dependent structural properties. In this Chapter, the crystallographic and mathematical aspects of the NC model here developed will be presented. The construction of the faulted model is structured in five steps, to be iteratively repeated for every NC with different size and different stacking disorder sequence/entity, as follows:

1. Step 1: Input required and coordinate transformation;
2. Step 2: Sequence generation;

3. Step 3: Generation of a faulted lattice of nodes;
4. Step 4: 3D windowing of a faulted lattice with the NC shape;
5. Step 5: Dressing the lattice nodes with CdSe units.

5.1.1 Step 1: Input and Coordinate Transformation

Since we aim building a model of planar defects in ZB CdSe NCs, a minimal set of information is necessary, to generate, and compute, a large set of *atomistic configurations* for a population of NCs of increasing size and selected morphology. These are later suitably "merged" into single sets of interatomic distances/multiplicities representing, in a statistical manner, the real sample configurations. Information includes:

- *a,* the lattice parameter of the pristine cubic cell; [Ideal periodicity]
- Crystal chemical composition; [Stoichiometry]
- Stacking disorder parameters; [Defectiveness]
- Number of sequences to be generated;
- Crystal morphology; [Shape]
- Growth directions for anisotropic shapes;
- The maximum particle extension (one parameter for isotropic or two parameters for anisotropic or core-shell morphologies) [Size].

In order to start the construction of faulted nanocrystals, the F-centered structure of ZB is transformed into a primitive trigonal cell, and fractional coordinates are mapped into Cartesian coordinates. This enable the generation of three distinct translation vectors, used for the construction of an aperiodic set of nodes (along z), not anymore representing a 3D lattice in the crystallographic sense.
As shown in the Figure 5.1, the *fcc* cell of nodes with $a_k = b_k = c_k$ and $\alpha = \beta = \gamma = 90°$, can be easily transformed into a primitive trigonal cell defined by:

$$\boldsymbol{a_t} = -\boldsymbol{a_k}/2 + \boldsymbol{b_k}/2 + 0 \qquad Eq.\,5.1a$$

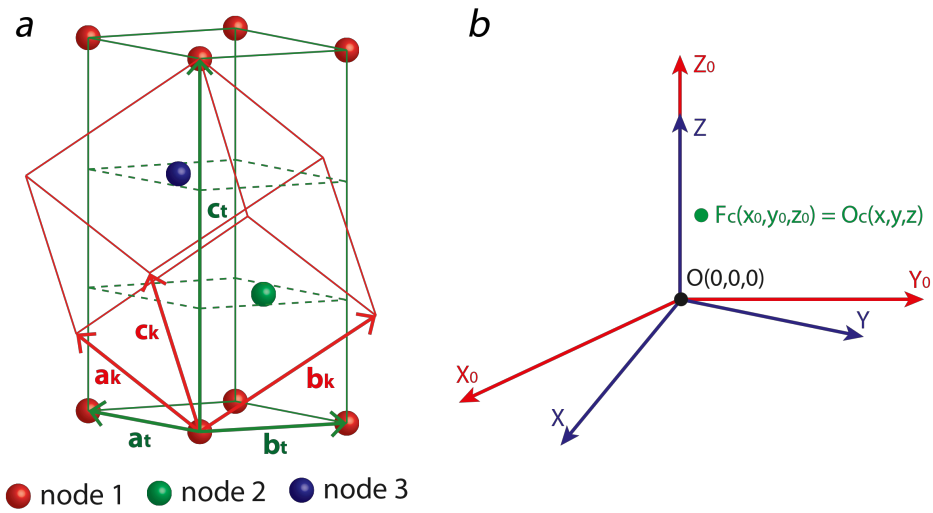

Figure 5.1. *a) cell transformation from the F-centred cubic cell (in red) to the primitive trigonal cell (in green). Red, green and blue spheres represent the three nodes describing the shift of the A, B and C atomic planes along the plane perpendicular to the [111] stacking direction of the cubic cell. b) reference system conversion from the fractional coordinates (red axes) to Cartesian ones (blue axes) (general case).*

$$\boldsymbol{b_t} = 0 - \boldsymbol{b_k}/2 + \boldsymbol{c_k}/2$$

$Eq.\,5.1b$

$$\boldsymbol{c_t} = \boldsymbol{a_k} + \boldsymbol{b_k} + \boldsymbol{c_k}$$

$Eq.\,5.1c$

or:

$$a_t = b_t = \frac{\sqrt{2}}{2} a_k \;; c_t = \sqrt{3} a_k; \;\; \alpha = \beta = 90°; \gamma = 120°$$

The fractional coordinates (x_0, y_0, z_0) of any atom of a crystalline material can be transformed into Cartesian coordinates (x, y, z) by multiplying the vector $\boldsymbol{F_c} = (x_0, y_0, z_0)$ by the orthogonalization matrix $\boldsymbol{A}$, in order to obtain a vector with orthogonal coordinates $\boldsymbol{O_c} = (x, y, z)$ as follows:[11]

$$\boldsymbol{O_c} = \boldsymbol{A F_c}$$

$Eq.\,5.2a$

$$\begin{pmatrix} x \\ y \\ z \end{pmatrix} = \begin{pmatrix} a\sin\beta & b\cos\gamma^*\sin\alpha & 0 \\ 0 & 1/b^* & 0 \\ a\cos\beta & b\cos\alpha & c \end{pmatrix} \begin{pmatrix} x_0 \\ y_0 \\ z_0 \end{pmatrix}$$

$Eq.\,5.2b$

where:

$$\cos\gamma^* = \frac{\cos\alpha\cos\beta - \cos\gamma}{\sin\alpha\sin\beta}$$

$$b^* = \frac{ac\sin\beta}{V}$$

$$V = abc\sqrt{1 - \cos\alpha^2 - \cos\beta^2 - \cos\gamma^2 + 2\cos\alpha\cos\beta\cos\gamma}$$

where $a,\ b,\ c$ and α, β, γ are the cell parameters in the real space, while b^*, γ^* are the cell parameters in the reciprocal space.
In this case, since the setting of the trigonal unit cell is hexagonal, the operation can be simplified as follows (see Figure 5.1b):

$$\begin{pmatrix} x \\ y \\ z \end{pmatrix} = \begin{pmatrix} a_t & b_t/2 & 0 \\ 0 & b_t\sqrt{3}/2 & 0 \\ 0 & 0 & c_t \end{pmatrix} \begin{pmatrix} x_0 \\ y_0 \\ z_0 \end{pmatrix}$$

$Eq.\,5.2c$

From the matrix $\boldsymbol{A}$ in Equation 5.2c (adapted to a dimensionless cubic cell with edge lengths = 1) and its operation on the three versors of the X_0, Y_0, Z_0 reference frame, three dimensionless translation vectors $\Delta\boldsymbol{x}, \Delta\boldsymbol{y}, \Delta\boldsymbol{z}$.

$$\Delta\boldsymbol{x} = \begin{pmatrix} \sqrt{2}/2 \\ 0 \\ 0 \end{pmatrix};\ \Delta\boldsymbol{y} = \begin{pmatrix} \sqrt{2}/4 \\ \sqrt{6}/4 \\ 0 \end{pmatrix};\ \Delta\boldsymbol{z} = \begin{pmatrix} 0 \\ 0 \\ \sqrt{3} \end{pmatrix}$$

$Eq.\,5.3.\,a; b; c$

and three dimensionless vectors defining the position of the three different types of planes (x_i, y_i) at nodes 1, 2 and 3 in Figure 5.1 are obtained, from a generic cubic

(x, y) Cartesian coordinates of node 1	
$\begin{pmatrix} x_1 \\ y_1 \end{pmatrix} = \begin{pmatrix} a_t & b_t/2 \\ 0 & b_t\sqrt{3}/2 \end{pmatrix} \begin{pmatrix} 0 \\ 0 \end{pmatrix} = \begin{pmatrix} 0 \\ 0 \end{pmatrix}$	Dimensionless $\begin{pmatrix} 0 \\ 0 \end{pmatrix}$
(x, y) Cartesian coordinates of node 2	
$\begin{pmatrix} x_2 \\ y_2 \end{pmatrix} = \begin{pmatrix} a_t & b_t/2 \\ 0 & b_t\sqrt{3}/2 \end{pmatrix} \begin{pmatrix} 1/3 \\ 2/3 \end{pmatrix} = \begin{pmatrix} a_t/3 + b_t/3 \\ b_t\sqrt{3}/3 \end{pmatrix}$	Dimensionless $\begin{pmatrix} \sqrt{2}/3 \\ \sqrt{6}/6 \end{pmatrix}$
(x, y) Cartesian coordinates of node 3	
$\begin{pmatrix} x_3 \\ y_3 \end{pmatrix} = \begin{pmatrix} a_t & b_t/2 \\ 0 & b_t\sqrt{3}/2 \end{pmatrix} \begin{pmatrix} 2/3 \\ 1/3 \end{pmatrix} = \begin{pmatrix} 2a_t/3 + b_t/6 \\ b_t\sqrt{3}/6 \end{pmatrix}$	Dimensionless $\begin{pmatrix} 5\sqrt{2}/12 \\ \sqrt{6}/12 \end{pmatrix}$

Table 5.1. *Cartesian coordinates of the nodes used to define the relative disposition of A, B and C planes in the trigonal system (a_t, b_t, c_t). The rightmost columns are derived from the dimensionless cubic lattice with ($a_k = b_k = c_k = 1$).*

cell with $a_k = b_k = c_k$ and a specific dimensionless unit cell with $a_k = b_k = c_k = 1$, as reported in Table 5.1.

Once these vectors are obtained, it is possible to build a 3D lattice of stacked planes along the [111] crystallographic direction of the pristine cubic unit cell (the [001] direction of the trigonal setting). Before starting the process of lattice construction, the fundamental information about the stacking sequence is required. Accordingly, a sequence generation is implemented in the program that is treated in the next paragraph.

5.1.2 Step 2: Sequence Generation

During the second half of the XIX century, in pioneering works, several authors, such as Jagodzinski (1949-1954),[12,13] Paterson (1952),[14] Gevers (1954),[15] Warren (1959),[16] Willis (1959)[17] and Johnson (1963),[18] developed methods for *random sequences* generation to deal with a wide range of planar defects. In 1965, Kakinoki[19,20] introduced an innovative and unifying method for the generation of any type of planar defect previously reported in the literature using a probability matrix. This method is able to produce *correlated* faulted sequences using probability

coefficients based on $l = 3(2^{s-1})$ building blocks with a variable number of previous layer extension *s* (*s* =1,2,3,4…). In simple words, *s* is the memory buffer influencing the occurrence of a defined probability upon stacking the *s+1* layer. Using the Jagodzinski's nomenclature of layers A, B and C, as presented in Chapter 4, the simplest combination cases (*s* =1,2,3) of Kakinoki's method are illustrated:

e.g.: $\boldsymbol{s = 1}$ $\boldsymbol{l = 3}$

1) A 2) B 3) C

e.g.: $\boldsymbol{s = 2}$ $\boldsymbol{l = 6}$

1) CA 3) BA 5) AB
2) CB 4) BC 6) AC

e.g.: $\boldsymbol{s = 3}$ $\boldsymbol{l = 12}$

1) $BCA \equiv k$ 5) $CAB \equiv k$ 9) $ABC \equiv k$
2) $ACA \equiv h$ 6) $BAB \equiv h$ 10) $CBC \equiv h$
3) $ABA \equiv h$ 7) $BCB \equiv h$ 11) $CAC \equiv h$
4) $CBA \equiv k$ 8) $ABC \equiv k$ 12) $BAC \equiv k$

etc…

where k and h are cubic and hexagonal sequences.

The $l \times l$ probability matrix, is constituted by l^2 elements called p_{ij} defining the probability of a transition from the *i-th* to the *j-th* block for the case s = 3 as follows:

	$\boldsymbol{BC}A$	$\boldsymbol{AC}A$	$\boldsymbol{AB}A$	$\boldsymbol{CB}A$	$\boldsymbol{CA}B$	$\boldsymbol{BA}B$	$\boldsymbol{BC}B$	$\boldsymbol{AC}B$	$\boldsymbol{ABC}$	$\boldsymbol{CBC}$	$\boldsymbol{CAC}$	$\boldsymbol{BAC}$
$\boldsymbol{BCA}$	0	0	0	0	α	0	0	0	0	0	$1-\alpha$	0
$\boldsymbol{ACA}$	0	0	0	0	β	0	0	0	0	0	$1-\beta$	0
$\boldsymbol{ABA}$	0	0	0	0	0	$1-\beta$	0	0	0	0	0	β
$\boldsymbol{CBA}$	0	0	0	0	0	$1-\alpha$	0	0	0	0	0	α
$\boldsymbol{CAB}$	0	0	$1-\alpha$	0	0	0	0	0	α	0	0	0
$\boldsymbol{BAB}$	0	0	$1-\beta$	0	0	0	0	0	β	0	0	0
$\boldsymbol{BCB}$	0	0	0	β	0	0	0	0	0	$1-\beta$	0	0
$\boldsymbol{ACB}$	0	0	0	α	0	0	0	0	0	$1-\alpha$	0	0
$\boldsymbol{ABC}$	α	0	0	0	0	0	$1-\alpha$	0	0	0	0	0
$\boldsymbol{CBC}$	β	0	0	0	0	0	$1-\beta$	0	0	0	0	0
$\boldsymbol{CAC}$	0	$1-\beta$	0	0	0	0	0	β	0	0	0	0
$\boldsymbol{BAC}$	0	$1-\alpha$	0	0	0	0	0	α	0	0	0	0

or, in a contracted form:

	k	h
k	α	$1-\alpha$
h	β	$1-\beta$

Where:

α : probability of the transition $k \rightarrow k$

$1-\alpha$: probability of the transition $k \rightarrow h$

β : probability of the transition $h \rightarrow k$

$1-\beta$: probability of the transition $h \rightarrow h$

$p_{ij} = 0$ means that the transition is not permitted whereas $p_{ij} \neq 0$ means that transitions from cubic (*k*) to cubic or hexagonal (*h*) and from *h* to *h* or *k* are permitted (*e.g*: $p_{1,4}$ corresponds to the not permitted transition $B\boldsymbol{CA} \rightarrow \boldsymbol{CB}A$; $p_{1,5}$ corresponds to the permitted transition $B\boldsymbol{CA} \rightarrow \boldsymbol{CA}B$). This model can be expanded for $s = 4$ or adapted in order to model one or more stacking faults type at the same time, increasing the number of possible transitions (from 4 to 8) of the different configurations of equal-size NCs.

Following Kakinoki, four parameters (α, β, γ, δ) associated with specific transitions can be defined (Table 5.2).

This method has been used in DSE analyses of *fcc* and *hcp* metals[9,10] and implemented at the correlational level with α, β, γ and δ adjustable parameters.

Kakinoki's method is intrinsically best applied in combination with the DSE in the correlation mode. This can be found in a recent paper by Longo *et. al.*[10], where the

SF probability	transition	SF probability	transition
α	$kk \rightarrow k$	$1-\alpha$	$kk \rightarrow h$
β	$hk \rightarrow k$	$1-\beta$	$hk \rightarrow h$
γ	$hh \rightarrow k$	$1-\gamma$	$hh \rightarrow h$
δ	$kh \rightarrow k$	$1-\delta$	$kh \rightarrow h$

Table 5.2. *SF probability parameters of Kakinoki's s = 4 model and related cubic (k) ↔ hexagonal (h).*

authors introduced a frequency $f_i = \sum_j f_j p_{ij}$ of occurrence of the *i-th* block in the formalism of the Debye equation describing the faulted structure of nanosized Co particles, and provided the formulas relating the (refined) α, β, γ, δ parameters to the frequencies of different types of transitions (for s = 3 and s = 4).

In this Ph.D. work, the Kakinoki's approach has been adapted to be used for generating (a finite number of) independent sequences of layers during the atomistic model construction of NCs, which enabled the treatment of different types of faulting (GF, ISF, ESF, IG) at the configuration level. Nevertheless, the α, β, γ, δ parameters are expected to describe comparable faulted structures.

The implementation of this approach at the configurational level was developed as the best compromise between the complexity of the model and the CPU time.

Indeed, one of the main problems associated with the use of DSE is related to the extensive computational time. Therefore, the introduction of a large number of variable parameters (for $s > 3$), despite of their theoretical efficiency, is not recommended.

As explained in Chapter 3, multiple computational strategies are used in Debussy to decrease the CPU time for the calculation of the interatomic distances and of their multiplicities. Nevertheless, for non-periodic structures, this CPU time drastically increases, especially when dealing with large clusters.[21] Contrarily to the DSE approach working in the correlation space, that directly generates a "hybrid" structure containing different combinations of PDs, the approach working in the configuration space needs that a large enough number of clusters are generated, each of them with a well-defined sequence, and that the sampled interatomic distances are calculated for each of them. Taking advantage of the equi-spacing of the interatomic distances provided by the gaussian sampling algorithm,[22] after the generation of the sequences, the pseudo-multiplicities of the different configurations of equally-sized NCs are linearly combined into a single "hybrid" set to be used by the Debussy suite.

In constructing the atomistic models of faulted sequences, the Kakinoki's approach was adopted. However, for relatively large particles, this probabilistic approach is massively time consuming. In one of the materials object of this thesis (Pt NPs; Chapter 7) it was proved that, when the SFE is high and the probability of SF is low, *i.e.* within a few percent level (thus, reasonably, a nanocluster does not contain

multiple faults; see Chapter 7), the number of possible sequences can be drastically reduced by $\sim 1/4$ by adopting some simplifying assumptions during the model construction.[23] Unfortunately, for II-VI semiconductors, much larger SF probabilities (up to 30-40%) are reported in the literature, making such as simplified sequence generation protocol completely inappropriate. Accordingly, the use of the random approach becomes unavoidable.

Inspired by Kakinoki, a finite number of sequences with a well-defined number of transitions is here generated using an iterative method (calling the right p_{ij} when a specific *i-th* bloch is considered) and dealing with the different probability coefficients on the previous four layers (s = 4).

According to Warren's theory (see Chapter 4) and following the systematic analysis of the effects of the different faults proposed by Ustinov and Budarina (2002), it is possible to highlight the predominance of *intrinsic* (ISF) or *extrinsic (ESF)* fault by carefully analyzing the experimental data. As an example, our CdSe WAXTS traces emphasized the predominant presence of ISF. This is corroborated by the discussion presented in Chapter 6. Moreover, HRTEM images collected on 3.8 nm CdSe NCs shows also the occasional presence of growth faults. Accordingly, the "random" stacking sequence generation for CdSe materials has been developed in order to preferentially introduce ISFs and GFs, playing with the appropriate combination of

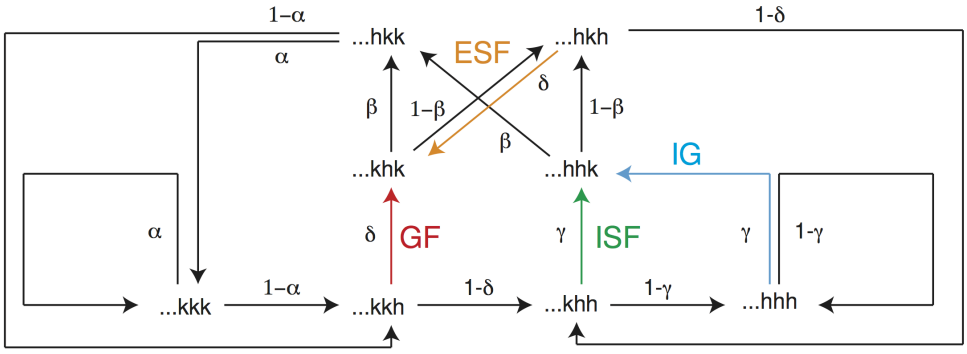

Figure 5.2. *Flowchart of the sequence generation using α, β, γ and δ parameters. The strategy of fixing $\gamma = 1$ limits the presence of IG that are reduced to zero, forcing the preferential formation of ISF, GF and a small statistical fraction of ESF. The algorithm used keeps anyway the possibility to introduce even IG in order to test eventual presence of a slight number of it in real samples.*

the SF probability parameters presented in Table 5.2.

For s = 4, the sequence generation can be produced using the scheme in Figure 5.2. Let's consider a sequence where the *i+1-th* layer or transition has to be classified at given α, β, γ and δ. As a practical example, taking as reference Figure 5.2, if the sequence of the *i-th* block is of the "ABCA" ("*kk*") type, the probability α (given in input) is called and the subsequent layer is added as B (defining a *k* transition) or C (defining a *h* transition) according to the fact that $\alpha \geq r$ or $\alpha < r$ respectively, where $0 \leq r \leq 1$ is a random number. If a h transition is introduced, the new block is of the "BCAC" ("*kh*") type; then the probability δ (given in input) is called and the subsequent layer is added as B (defining a *k* transition) or A (defining a *h* transition), according to the fact that $\delta \geq r$ or $\delta < r$ respectively, and so on. As a practical example, hereafter a single sequence of 15 layers is generated for $\alpha = 0.5$, $\beta = 1.0$, $\gamma = 0.8$ and $\delta = 0.5$:

"A B C A C A B C A C B A C A C"

corresponding to following sequence in the Jagodzinsky formalism:

"*k k h h k k k h k k k h h*".

Growth Fault				
$kk \overset{1-\alpha}{\longrightarrow} h$	$kkh \overset{\delta}{\rightarrow} k$		$kkhk \overset{\beta}{\rightarrow} k$	
$GF_p = (1-\alpha)\,\delta\,\beta$				
Intrinsic Stacking Fault				
$kk \overset{1-\alpha}{\longrightarrow} h$	$kkh \overset{1-\delta}{\longrightarrow} h$	$kkhh \overset{\gamma}{\rightarrow} k$	$kkhhk \overset{\beta}{\rightarrow} k$	
$ISF_p = (1-\alpha)\,(1-\delta)\,\beta$ if $\gamma = 1$				
Extrinsic Stacking Fault				
$kk \overset{1-\alpha}{\longrightarrow} h$	$kkh \overset{\delta}{\rightarrow} k$	$kkhk \overset{1-\beta}{\longrightarrow} h$	$kkhkh \overset{\delta}{\rightarrow} k$	$kkhkhk \overset{\beta}{\rightarrow} k$
$ESF_p = (1-\alpha)\,\delta^2\,\beta(1-\beta)$				

Table 5.3. *This table reports the calculation of the growth, intrinsic and extrinsic stacking faults probabilities within a stacking sequence generated with the SF parameters shown in Table 5.2. Based on these calculations, it is possible to drive the sequences generation aiming at introducing a preferential stacking fault type.*

In order to produce a stacking sequence with the simultaneous presence of GF and ISF, while avoiding the presence of IG and reducing that of ESF, it is necessary to fix $\gamma = 1$ and to combine the remaining probability coefficients as schematized in Table 5.3.

From the analysis and formulae shown in Table 5.3, one can derive that the presence of intergrowth (i.e. extended *h* layers) is null if $\gamma = 1$; in such condition, the ratio between GF and ISF probabilities is equal to:

$$\frac{GF_p}{ISF_p} = \frac{(1-\alpha)\,\delta\,\beta}{(1-\alpha)\,(1-\delta)\,\beta} = \frac{\delta}{(1-\delta)}$$

$Eq.5.4$

Equation 5.4 also shows that δ plays a fundamental role in preferentially introducing a GF or an ISF, as shown in Figure 5.3.

Concerning the formation of ESFs, despite the fact that their presence cannot be completely avoided, their relative presence to GF and ISF is small and defined by:

$$\frac{ESF_p}{GF_p} = \frac{\delta(1-\beta)}{1}$$

$Eq.5.5a$

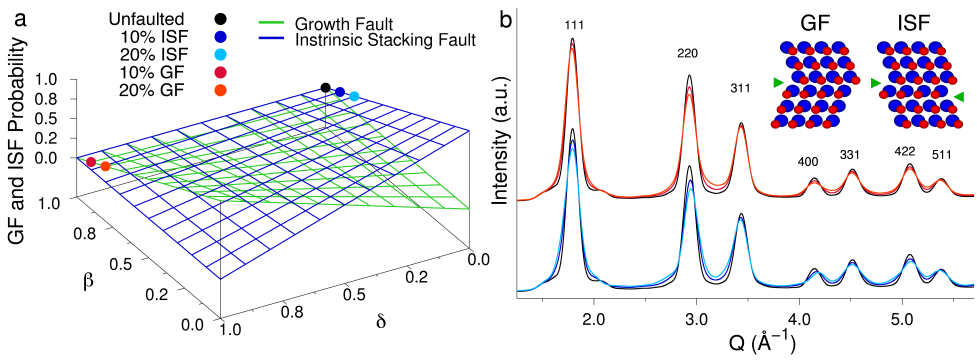

Figure 5.3. *(a) GF and ISF probability as function of β and δ parameters; colored dots correspond to the β and δ values in the legend. (b) Simulated patterns of ZB CdSe NCs containing planar defects; the colors of the solid lines correspond to the β and δ coefficients of dots with the same color in a. Simulations are obtained by merging 50 sequences generated random; the black solid traces correspond to the unfaulted case.*

In a practical example, using the results obtained in this PhD project, if $\beta \cong 0.75$ and $\delta \cong 0.60$, the ratio is:

$$\frac{ESF_p}{GF_p} \approx 0.150$$

$Eq. 5.5b$

Thanks to these considerations, two predominant fault types can be taken into account in order to turn the complex problem of determining four parameters into the case of two probability variables, by forcing $\gamma = 1$ and fixing $\alpha = \beta$. It is worth of note that, with this approximation, the stacking fault type ratios do not change and, at the same time, the presence of ESF, here treated as two consecutive GF, is not completely suppressed.

At this point, taking the β and δ as independent and "optimizable" variables ranging between 0 and 1, a $(n_{seq} \times n_{lay})$ matrix of n_{seq} rows and n_{lay} columns is generated for each NC size. n_{lay} is equivalent to the number of stacked layers while n_{seq} is relative to the number of sequences and both these integers are predefined and used as input. Every cell of this matrix contains, in the *ij-th* position the layer type (A, B or C) and therefore, information at the transition, as later explained within this section.

The number of stacked layers n_{lay} is further calibrated to account for the NC size, as follows:

$$n_{lay} = \frac{L_{111}}{d_{111}}; \quad d_{111} = \frac{c_t}{3}$$

$Eq. 5.6a; 5.6b$

where:

L_{111}: size of the NC along the 111 direction

d_{111}: interlayer distance along the 111 direction

The $n_{seq} \times n_{lay}$ matrix is generated any time the number of stacking layers along [111] is changed, *i.e.* for each NC size.

The output of this step is finalized to the production of two matrices:

- Matrix of layers $n_{seq} \times n_{lay}$

$$\begin{matrix} & n_{lay} \\ n_{seq} & \begin{pmatrix} A & B & C & \dots & A \\ A & C & A & \dots & B \\ A & C & B & \dots & C \\ A & B & A & \dots & A \\ A & B & C & \dots & A \end{pmatrix} \end{matrix}$$

- Matrix of transitions $n_{seq} \times (n_{lay} - 2)$

$$\begin{matrix} & n_{lay} - 2 \\ n_{seq} & \begin{pmatrix} k & \dots & k \\ h & \dots & k \\ k & \cdots & h \\ h & \cdots & k \\ k & \cdots & h \end{pmatrix} \end{matrix}$$

The matrix of layers is used to construct a disordered lattice of nodes each of which will be dressed with the CdSe unit, while the matrix of transitions is used for the rapid identification of the transition at different levels within the NC.

The nature of SF and the definition of the SFE suggest that a lower energy is required to introduce a planar defect in the structure when the section/area of faulted layer is small. In nanoparticles, the extension of the faulted plane may change as a function of the layer position and the NC morphology. For this reason, one might expect that the probability of introducing a SF is not homogeneous within the same cluster leading to a preferential concentration of faults in a portion of the NC. In order to manage this condition, the four SF probability parameters can be used to further restrict the defect to a specific location within the particle and to a specific extension. As explained in Chapter 4, since the effect of the SF probability has to be evaluated in terms of area of the faulted planes, this suggests that the localization of defects on planes with a restricted extension does not suffice to account for a high density of faults.

5.1.3 Step 3: Generation of a "faulted" Lattice of Nodes

Once the information on the stacking disorder and translation vectors along the three cartesian directions for each plane type (A, B or C) is available, a faulted lattice of nodes (*i.e.* an aperiodic, but non-random, 3D disposition of points) can be built. The dimensionless translation vectors from Equations 5.3a-5.3c are firstly converted into physical translation vectors by multiplying them for the cubic cell parameter a.

$$\Delta \boldsymbol{X} = a\Delta \boldsymbol{x}; \quad \Delta \boldsymbol{Y} = a\Delta \boldsymbol{y}; \quad \Delta \boldsymbol{Z} = a\frac{\Delta \boldsymbol{z}}{\boldsymbol{3}}$$

$$Eq.\,5.7a; 5.7b; 5.7c$$

$$\Delta \boldsymbol{X} = \begin{pmatrix} a\sqrt{2}/2 \\ 0 \\ 0 \end{pmatrix}; \qquad \Delta \boldsymbol{Y} = \begin{pmatrix} a\sqrt{2}/4 \\ a\sqrt{6}/4 \\ 0 \end{pmatrix}; \qquad \Delta \boldsymbol{Z} = \begin{pmatrix} 0 \\ 0 \\ a\sqrt{3}/3 \end{pmatrix}$$

$$Eq.\,5.8a; 5.7b; 5.7c$$

ΔZ, the interplanar distance, is divided by 3 because the trigonal unit cell contains 3 layers of nodes in the [001] direction (see Figure 5.1a).

A final required information involves the definition of the (x_j, y_j) coordinates of the initial nodes for the A, B and C planes of the material, which are obtained by multiplying the x_i, y_i coordinates of nodes in Table 5.1 by the cubic cell parameter a of the material, as done in Table 5.4.

By combing the translation vectors in Equations 5.8a-5.8c and the initial nodes position of A, B and C planes by fixing the starting nodes, a 3D disposition of nodes is generated through an iterative procedure where the position (x_i, y_i, z_i) of the *i-th* node is obtained as follows:

$$\begin{pmatrix} x_i \\ y_i \\ z_i \end{pmatrix} = n_x\Delta \boldsymbol{X} + n_y\Delta \boldsymbol{Y} + n_z\Delta \boldsymbol{Z_c} + \boldsymbol{S_{A,B,C}}$$

$$Eq.\,5.9$$

where:

$\boldsymbol{S_{A,B,C}}$: appropriate bi-dimensional position of starting nodes for the different plane types

n_x, n_y, n_z: integer number of repetitions along x, y and z direction

Cartesian x, y position of layer A
$\begin{pmatrix} x_A \\ y_A \end{pmatrix} = a \begin{pmatrix} x_1 \\ y_1 \end{pmatrix} \rightarrow \boldsymbol{S_A} = \begin{pmatrix} x_A \\ y_A \\ 0 \end{pmatrix} = \begin{pmatrix} 0 \\ 0 \\ 0 \end{pmatrix}$
Cartesian x, y position of layer B
$\begin{pmatrix} x_B \\ y_B \end{pmatrix} = a \begin{pmatrix} x_2 \\ y_2 \end{pmatrix} \rightarrow \boldsymbol{S_B} = \begin{pmatrix} x_B \\ y_B \\ 0 \end{pmatrix} = \begin{pmatrix} a\sqrt{2}/3 \\ a\sqrt{6}/6 \\ 0 \end{pmatrix}$
Cartesian x, y position of layer C
$\begin{pmatrix} x_C \\ y_C \end{pmatrix} = a \begin{pmatrix} x_3 \\ y_3 \end{pmatrix} \rightarrow \boldsymbol{S_C} = \begin{pmatrix} x_C \\ y_C \\ 0 \end{pmatrix} = \begin{pmatrix} 5a\sqrt{2}/12 \\ a\sqrt{6}/12 \\ 0 \end{pmatrix}$

Table 5.4. *Cartesian coordinates of the nodes used as relative position of A, B and C planes derived for the material having cubic lattice parameter a.*

As described in Chapter 4, the presence of eclipsed or staggered conformations in binary compounds of the wurtzite/zinc-blende structure may involve a modulation of the interplanar distance of few tens of pm along z.[1] This modulation is introduced in our model either as an average expansion/contraction effect (δc) or as a local effect at the $k \leftrightarrow h$ transition (δZ). For this reason, three distinct interplanar vectors were considered: $\Delta \boldsymbol{Z_u} = \Delta \boldsymbol{Z}$, $\Delta \boldsymbol{Z_c}$ and $\Delta \boldsymbol{Z_f}$ (**u** and **f** stand for *unfaulted* and *faulted* spacings, respectively), as follows:

$$\Delta \boldsymbol{Z_c} = \begin{pmatrix} 0 \\ 0 \\ \left(a\sqrt{3} + \delta c\right)/3 \end{pmatrix} \qquad Eq.\,5.10$$

$$\Delta \boldsymbol{Z_f} = \begin{pmatrix} 0 \\ 0 \\ a\sqrt{3}/3 + \delta Z \end{pmatrix} \qquad Eq.\,5.11$$

As for Equation 5.9, two new Equations (5.12 and 5.13) are written permitting to consider the extra spacings generated by the vectors $\Delta \boldsymbol{Z_c}$ and $\Delta \boldsymbol{Z_f}$.

a) In case of a homogeneous strain along [111] of the cubic cell:

$$\begin{pmatrix} x_i \\ y_i \\ z_i \end{pmatrix} = n_x \Delta \boldsymbol{X} + n_y \Delta \boldsymbol{Y} + n_z \Delta \boldsymbol{Z_c} + \boldsymbol{S_{A,B,C}}$$

$Eq.\,5.12$

b) In case of an anisotropic strain localized at the $k \leftrightarrow h$ transitions along the [111] of the cubic cell:

$$\begin{pmatrix} x_i \\ y_i \\ z_i \end{pmatrix} = n_x \Delta \boldsymbol{X} + n_y \Delta \boldsymbol{Y} + n_z (f(n_z) \Delta \boldsymbol{Z_f} + (1 - f(n_z)) \Delta \boldsymbol{Z_u}) + \boldsymbol{S_{A,B,C}}$$

$Eq.\,5.13$

where:

$f(n_z)$: fraction of faulted layers up to a specific level n_z, $(n_z = 1, \dots, N)$, n_z being the positive integer addressing the layer position within the entire sequence of N (faulted and unfaulted) layers

Atomic planes along Z axis are stacked following the stacking rules proposed in Paragraph 5.1.2.

5.1.4 Step 4: 3D windowing of Faulted Lattice with the NC Shape

Once the entire set of nodes is completed, in order to reproduce the desired NC shape, a "cut" of the network of lattice nodes with a shape function becomes necessary. In Bragg's theory, for a powder diffraction experiment, a diffraction peak is measured at a given $2\theta_{Bragg}$, and contains the sum of all the symmetry-related contributions with (crystal-system and/or Laue Group-dependent) exchange or permutation of the *hkl* indices; accordingly, the crystal anisotropy, as well as the relative crystallographic axes orientation to the crystal shape, produce detectable differences, particularly in the case of highly monodispersed NCs and high intensity/high resolution WAXTS experiments.

For CdSe NCs, two different morphologies have been considered, spherical and prismatic. The spherical morphology does not require any re-orientation of the lattice of nodes with respect to the shape function. In contrast, in the case of prisms exhibiting {100} cubic faces, an appropriate re-orientation of the lattice nodes before the 3D windowing has to be managed.

Indeed, the lattice of nodes is built by stacking the A, B and C layers along the [111] *crystallographic* cubic axis that is oriented parallel to the z-axis of the *Cartesian* reference system, to which the node coordinates refer to. However, to proceed with excising a prismatic shape out from the set of nodes it is convenient that the {100} are normal to the Cartesian axes of a rotated reference frame.

This operation is performed by applying to the entire set of nodes two rotation matrices, before the shape cut and after setting the origin at their centre of mass. The geometrical transformation implies a rotation $\varphi = -\pi/4$ around the z-axis and a rotation $\vartheta = -arcos(1/\sqrt{3})$ around the x-axis of the Cartesian reference system, where φ and ϑ are the angles of a spherical coordinate system having z as the polar axis.

In matrix notation:

$$\begin{pmatrix} x_i \\ y_i \\ z_i \end{pmatrix}_{z=001} = \boldsymbol{R_z R_x} \begin{pmatrix} x_i \\ y_i \\ z_i \end{pmatrix}_{z=111} \qquad Eq.\,5.14a$$

$$\boldsymbol{R_z} = \begin{pmatrix} \cos(\varphi) & -\sin(\varphi) & 0 \\ \sin(\varphi) & \cos(\varphi) & 0 \\ 0 & 0 & 1 \end{pmatrix}; \qquad \boldsymbol{R_x} = \begin{pmatrix} 1 & 0 & 0 \\ 0 & \cos(\vartheta) & -\sin(\vartheta) \\ 0 & \sin(\vartheta) & \cos(\vartheta) \end{pmatrix} \qquad Eq.\,5.14b; 5.14c$$

After fixing the shape function S (S = 1 within the surface boundary, S = 0 outside), the new crystallographic orientation can be now cut. As we do not care of the absolute orientation of each nanocrystal in lab space (random orientation is inherent in the DSE modelling), only the crystal axes vs. the morphological descriptors are used, which simplifies the final model construction.

Other aspects to be considered in the atomistic model are possible surface strain

and compositional variation, which can be heavily influenced by surface reconstruction (in naked clusters) of by disordering/dynamic effects brought about by the presence of external ligands or by specific synthetic conditions. Synthesis can presently control the formation of engineered systems with different compositions in the core and in the surface.[24] For these reasons, slightly different windowing approaches can be used, in order to account for:

- Homo Core-Shell Spherical NCs;
- Homo, Core-Shell, Core-Crown, Sandwich prismatic NCs (including nPL).

The parameters used for the shape cut will be duly discussed in Paragraph 5.1.6, since their actual values depend on the discretization of sizes and, therefore, on the NC growth step used for the population generation.

Concerning surface strain phenomena, it is well-known that surfaces are heavily influenced by the different physico-chemical environment and, in some cases, by synthetic conditions. As more deeply described in Paragraph 4.2, in metallic systems several studies revealed that bare surface nanoparticles manifest a detectable contraction of the average unit cell upon decreasing the size, being this effect attributed to the presence of "dangling bonds", well counterparted by stronger (and shorter) interatomic interactions between surface atoms and shallowly buried atoms within the nanoparticle.[25] In colloidal semiconductors, where different types of ligands may be present at the surface, the average unit cell parameter is often found to increase upon decreasing size.[24] This finding can be modeled by introducing expansion (or even contraction) of interatomic distances at the surface layers. To manage this distortion in our model, a coefficient of "surface" strain was defined as S_s and applied to the nodes lying on the outer shell of NCs:

$$S_s = \frac{l_{s,uCdSe}}{l_{c,u,CdSe}} \qquad eq.\,5.15$$

where:

$l_{s,u,CdSe}$: strained CdSe bond length at the surface

$l_{c,u,CdSe}$: unstrained CdSe bond length in the inner core

which requires an arbitrary criterium for defining the core/shell separation.

5.1.5 Step 5: Dressing the Lattice of Nodes with CdSe Units

At this stage, the shape-cut set of nodes has to be expanded into an atomistic model containing specific atomic species at their "true atomic locations". To do so, the nodes are simply "dressed" with the desired motif, here a suitably oriented CdSe dumbbell. The *i-th* node at the position defined by the vector $\boldsymbol{n_i}$ of coordinates x_i, y_i and z_i is dressed by putting the Cd atom in the $\boldsymbol{n_i}$ position and the Se atom by subtracting the l_{CdSe} bond distance along the cubic [111] direction from the x_i, y_i and z_i Cartesian coordinates. Since nodes lie on faulted and unfaulted planes, and may undergo additional strain, within each biatomic CdSe unit, the appropriate internuclear distance l_{CdSe} changes for the different conditions.

a) for faulted NCs without any additional strain along the [111] direction:
   - for "buried" core nodes (c):

$$l_{c,u,CdSe} = \frac{c_t}{4}; \quad l_{c,f,CdSe} = l_{c,u,CdSe} \qquad Eq.\,5.16a; 5.16b$$

   - for surface nodes (s):

$$l_{s,u,CdSe} = l_{c,u,CdSe}S_s;\ l_{s,f,CdSe} = l_{c,f,CdSe}S_s \qquad Eq.\,5.16c; 5.16d$$

b) for NCs with homogeneous strain along [111]:
   - for "buried" core nodes (c):

$$l_{c,CdSe} = \frac{c_t + \delta c}{4} \qquad Eq.\,5.17a$$

   - for surface nodes (s):

$$l_{s,CdSe} = l_{c,CdSe}S_s \qquad Eq.\,5.17b$$

c) for NCs with strain along the [111] localized at the $k \leftrightarrow h$ transition:

- for "buried" core nodes (c):

$$l_{c,u,CdSe} = \frac{c_t}{4}; \quad l_{c,f,CdSe} = l_{c,u,CdSe} + \delta z$$

$$Eq. 5.18a; 5.18b$$

where $\delta z = 3\,\delta Z/4$

- for surface nodes (s):

$$l_{s,u,CdSe} = l_{c,u,CdSe} S_s;\ l_{s,f,CdSe} = l_{c,f,CdSe} S_s$$

$$Eq. 5.18c; 5.18d$$

where subscripts for l stand for:
c: core, s: surface, f: faulted, u: unfaulted

δz refers to the faulted-associated strain applied to the Cd-Se bond distance along the [111] direction.
The final NC is now generated and ready for the calculation of the interatomic distances.

5.1.6 Discretization of NCs Size for Mono- and Bi-variate Populations

Simulating the XRD pattern for a single cluster with a well-defined size and using a single sequence is clearly not enough to describe the scattering trace measured for a real sample. The latter, indeed, may contain clusters of different sizes, each with its own number or mass fraction, and faults positioned in a statistical, or even preferential or correlated manner. To manage a population of faulted NCs, a 3D array was used to account different sizes, shapes and planar stacking ordering. In this 3D matrix, the i, j, k cell addresses two mutually orthogonal size parameters (for the i, j terms) and one "disordering" parameter (the k term). To better understand the strategy, the overall process is hereafter summarized, starting from the simplest case of an unfaulted population, when the k term is neglected, two situations can

be envisaged:

- for isotropic shapes, such as variably-sized spheres or cubes (or even the unlikely set of prisms of fixed axial ratio or any shape replicated by a simple scaling factor), mono-variate populations can be encoded in a 1D matrix (a vector) of clusters, where the sequence addresses terms of progressively increasing size.
- for shapes requiring bivariate populations (in the simplest cases, tetragonal or hexagonal prisms, or cylinders), a 2D array is required to describe the existence of two different (ideally independent) growth directions. The use of 2D arrays inevitably causes a large increase of the CPU time, which, in our experience, in database building may be tenfold or more.

For the 1D case, the construction of a population of variably-sized clusters requires the definition of a "step", related to the difference in size between clusters *i* and *i+1* in the overall sequence. We have adopted numerical protocols to compute "optimal" steps, the definition of which, however, may be morphologically dependent. In the simplest case of primitive cubic cells, the step along the three directions is equal to the length of the cube edge. If, instead, the cell is body or face-centered, the step is calculated according to the volume of the primitive cell, of trigonal symmetry, which is two, or four, times smaller, respectively. If, instead, spheres are used, then the diameter ($d_{sph} = 2r_{sph}$) of the sphere of equivalent volume of the cubic cell (of volume V_c) is used. The following equations summarize the underlying algebra:

$$V_c = V_{sph} = \frac{4}{3}\pi r_{sph}^3$$

$Eq.\,5.19$

Which, by rearranging, gives:

$$d_{sph} = 2r_{sph} = (d_{i+1} - d_i) = 2\sqrt[3]{\frac{3V_c}{4\pi}} = \sqrt[3]{\frac{6V_c}{\pi}}$$

$Eq.\,5.20$

where:

d_{i+1}: diameter of the *(i+1)-th* spherical NC

d_i: diameter of the *i-th* spherical NC

For a bivariate population, two distinct directions require two independent growth parameters, one in the basal plane (*ab*) of a tetragonal or hexagonal prism (with *a=b*) and the other along $\boldsymbol{c}$, where $\boldsymbol{c}$ is aligned with $\boldsymbol{a} \times \boldsymbol{b}$. A similar approach can be used for cylinders, where the growth step in *ab* is commensurate with the radius of the basal circle. In the present case, CdSe NCs were built as tetragonal prisms limited by cubic {100} faces, with steps determined according to the cubic rather than the trigonal unit cell. Therefore, the step in the *ab* plane is calculated according to Equation 5.20 (~ 6.82 Å) and the step along c is equal to the cubic parameter (~ 6.08 Å). When a population of faulted NCs is built, the third dimension (k) in the 3D array refers to the stacking sequences, generated for equally sized and shaped NCs (thus with the same number of atoms). The set of distances of each member of this population are then linearly merged and used to compute a single set of sampled interatomic distances. Indeed, the properties of Fourier transforms include linearity, *i.e.* invariancy with respect to sum and multiplication operators. As a consequence, the XRPD pattern obtained by averaging those independently calculated for a set of *n* faulted clusters (with different stacking sequences) is mathematically equivalent to that calculated using a "hybrid", "unphysical" cluster, where all the sequences used for the generation of the *n* clusters are ideally encoded. Thus, the pseudo multiplicities vector of the "equi-spaced" sampled interatomic distances of a *hybrid* structure are averaged before calculating the DSE pattern, enabling the fast calculation of a single XRPD trace at each i, j cell, avoiding summation of multiple patterns, one per each i, j, k atomic configuration.

During the population building process, the actual stacking fault density, $p_{SF_{ij}}$ of each "hybrid" *ij-th* NC, (see Equation 5.21), is calculated as follows:

$$p_{SF_{ij}} = \frac{n_{h_{ij}}}{n_{k_{ij}} + n_{h_{ij}}} = \frac{A_{h_{ij}}}{A_{k_{ij}} + A_{h_{ij}}} \qquad Eq.\,5.21$$

where:

$n_{h_{ij}}$: number of atoms of the NC ij at the hexagonal transitions

$n_{k_{ij}}$: number of atoms of the NC ij at the cubic transitions

$A_{h_{ij}}$: total surface extension of layers at the hexagonal transition of the NC ij

$A_{k_{ij}}$: total surface extension of layers at the cubic transition of the NC ij

and stored in a ($i_{max} \times j_{max}$) matrix $\boldsymbol{M_{SF}}$, where i_{max} and j_{max} are related to the size extention of the Nc in the ab and c directions, respectively (which are not necessarily equal).

In a practical example, using the results obtained in this Ph. D. project, the $\boldsymbol{M_{SF}}$ matrix (where $i_{max} = 9$, $j_{max} = 6$, $\beta = 0.65$ and $\delta = 0.70$) of 54 $p_{SF_{ij}}$ elements generated for the ZB CdSe QDs sample with nominal size 3.0 nm for a random stacking sequence and 50 different configurations is:

$$\boldsymbol{M'_{SF}} = \begin{array}{c|ccccccccc} & i=1 & \cdots & & & & & & & i_{max} \\ j=1 & 0.000 & 0.000 & 0.000 & 0.000 & 0.000 & 0.000 & 0.000 & 0.000 & 0.000 \\ \vdots & 0.252 & 0.252 & 0.261 & 0.272 & 0.297 & 0.286 & 0.292 & 0.306 & 0.305 \\ & 0.301 & 0.301 & 0.291 & 0.284 & 0.281 & 0.280 & 0.281 & 0.282 & 0.283 \\ & 0.289 & 0.289 & 0.291 & 0.295 & 0.288 & 0.301 & 0.303 & 0.302 & 0.302 \\ & 0.333 & 0.333 & 0.331 & 0.328 & 0.327 & 0.326 & 0.325 & 0.324 & 0.324 \\ j_{max} & 0.312 & 0.316 & 0.318 & 0.317 & 0.317 & 0.317 & 0.316 & 0.315 & 0.314 \end{array}$$

considering the cluster with thickness in c of 0.6 nm unfaulted. For a better graphical layout, the transposed matrix $\boldsymbol{M'_{SF}}$ ($i_{max} \times j_{max}$) is proposed above.

In this particular case, all $p_{SF_{ij}}$ entries are somewhat similar, given that the sequence generation in random mode smears out the stacking fault probabilities across the entire NC. If, instead, a localized fault model (giving priority to central layers; $\beta = 0.40$ and $\delta = 0.50$) is assumed, a different $\boldsymbol{M'_{SF}}$ matrix is obtained (as shown hereafter) where a definite trend of variations is observed.

$$\boldsymbol{M'_{SF}} = \begin{array}{c|ccccccccc} & i=1 & \cdots & & & & & & & i_{max} \\ j=1 & 0.000 & 0.000 & 0.000 & 0.000 & 0.000 & 0.000 & 0.000 & 0.000 & 0.000 \\ \vdots & 0.403 & 0.403 & 0.394 & 0.365 & 0.328 & 0.293 & 0.263 & 0.239 & 0.217 \\ & 0.430 & 0.430 & 0.403 & 0.367 & 0.331 & 0.296 & 0.269 & 0.242 & 0.221 \\ & 0.377 & 0.389 & 0.355 & 0.327 & 0.297 & 0.270 & 0.245 & 0.223 & 0.203 \\ & 0.433 & 0.433 & 0.408 & 0.379 & 0.348 & 0.318 & 0.289 & 0.234 & 0.243 \\ j_{max} & 0.372 & 0.373 & 0.351 & 0.328 & 0.303 & 0.280 & 0.257 & 0.237 & 0.218 \end{array}$$

This information allows the calculation of the final probability of defects p_{SF} taking in to account the weighted contribution of each NC as presented in the next paragraph (see Equation 5.23 of this Chapter).

5.2 Strategy for Model Optimization of NCs with Stacking Faults

The sampled interatomic distances (SIDs) of the "hybrid" database are used by the Debussy program for the calculation of a simulated XRPD pattern. As described in Chapter 3, Debussy is able to refine morphological, structural and microstructural parameters by standard χ^2 minimization (Equation 5.22).

$$\chi^2 = \frac{\sum_{i=1}^{N} \left(\frac{(I_{oi} - I_{ci})}{\sigma_{oi}} \right)^2}{(N - P + C)} \qquad Eq. 5.22$$

Where:

I_{oi} and I_{ci}: observed and calculated pattern intensities at the *i-th* angular step

σ_{oi}: estimated standard deviation of the measured intensity

N: number of observation points

P: number of refined variables

C: number of constrains

In the standard approach, the refinement process is typically performed by using the encoded SID database. However, when non-uniform strain or disorder effects (like SF parameters) need to be refined, a new set of SID has to be calculated at each refinement cycle, at the cost of a larger CPU time. For faulted NCs, since each DB results from the averaging of several SF configurations, a much longer CPU time is required in calculating SID databases of hybrid structures having new SF parameters or strained Cd-Se distances. Each DB calculation is particularly slow (about 20 min for 3nm particles and 2h for 6nm particles), therefore it was necessary to define an alternative strategy for parameters optimization.

Besides the extremely time-consuming calculation due to the large number of parameters, also large correlations among them have to be taken into account. A step by step refinement procedure was adopted, mainly suggested by the several tests performed on CdSe QDs which guided us to a reasonable and robust strategy for characterizing samples containing NCs with planar defects and other related

effects. The main refinement steps are summarized hereafter.

a) Determination of size, size dispersion, faceting and shape by SAXS data

A first point consisted in discriminating size effects from peak broadening generated by the planar defects. As portrayed in Chapter 2, SAXS is one of the most suitable tools to extract information about NP shapes, faceting, size and size dispersion, being the small angle scattering region unaffected by atomic-scale structural features. The determination of the average crystal size, size dispersion and shape by SAXS is fundamental, since the presence of morphologically anisotropic particles can selectively widen diffraction peaks hiding the real information on defectiveness. A strong advantage of using SAXS techniques in combination with DSE analysis is that size and shape model parameters from SAXS can be used as constraints during the refinement of morphology by DSE in the WAXTS range.

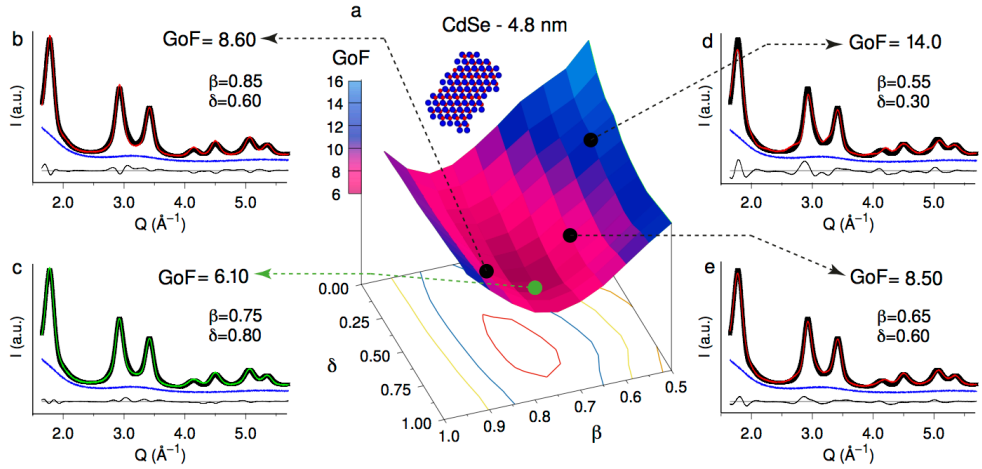

Figure 5.4. *Stacking faults parameter optimization. Different combinations of β and δ are explored via χ^2 minimization. The GoF=$\sqrt{\chi^2}$ surface in a) represents the obtained goodness of fits for different β and δ values by fixing all the remaining model parameters. A minimum was found at β=0.75 and δ=0.80 corresponding to the best fit (green curve) in c). (b-d) DSE simulations of representative cases picked from the surface and showing different degrees of matching to the WAXTS data (black dots).*

Figure 5.4 reprinted with permission from (ACS Nano, **2018**, *12* (12), pp 12558–12570*)*

b) Stacking fault investigation

Once the information on size and shape has been retrieved, a population of faulted ZB NCs and their corresponding SID databases for different SF parameters is generated, aiming at exploring the space of β and δ SF parameters, as shown in Figure 5.4 and discussed in Paragraph 5.1.2. Initial values of the SF parameters and their range of variability are guessed from the analysis of peak shifts and broadening of WAXTS data. During this exploration, all the other refinable structural parameters (such as *s.o.f.*, thermal parameters and isotropic lattice strains) and microstructural parameters (size and shape) were kept fixed.

c) Final optimization

Once all the parameters defining size, shape and fault probability of the NCs are defined within a good level of accuracy, a final refinement is carried out to relax: size and shape (that is, refined within limits) to SAXS values, *s.o.f.*s and thermal parameters and additional deformation of the CdSe bond distance, depending on the model adopted. Once the convergence is reached, the sample stacking fault probability p_{SF} is calculated as follows:

$$p_{SF} = \sum_{i=1}^{i_{max}} \sum_{j=1}^{j_{max}} \chi_{ij} p_{SF_{ij}} \qquad Eq.5.23$$

where:

i_{max}*:* maximum index of NC size in the ab plane of the cubic ZB structure

j_{max}*:* maximum index of NC along the c axis

$p_{SF_{ij}}$*:* stacking fault probability of the ij-th NC

χ_{ij}*:* refined mass fraction of the ij-th NC

This permits to obtain precise information about the stacking faults effects, in particular in models where the SF is localized and the stacking fault probability cannot be easily estimated analytically.

Conclusions

In this Chapter, a method to build atomistic models of ZB CdSe NCs with planar defects of the stacking fault type has been presented. Multiple configurations of faulted sequences are combined into a single set of sampled interatomic distances for each NC size of a population of NCs. This approach allows the computational tricks of the Debussy suite to be used and extended to the case of faulted NCs.
The stacking fault parameters β and δ are optimized prior to other structural parameters and after a robust size and shape model is available from SAXS data.
In this work, a strategy based on the step-by-step refinement was adopted to explore different stacking fault parameters combinations, based on a grid-search.
In next Chapter, the application of this protocol to real samples of CdSe QDs will be presented.

References

(1) Takeuchi, S.; Suzuki, K. Stacking Fault Energies of Tetrahedrally Coordinated Crystals. *Phys. Stutus Solidi C* **1999**, *171* (1), 99–103.

(2) Ithurria, S.; Dubertret, B. Quasi 2D Colloidal CdSe Platelets with Thicknesses Controlled at the Atomic Level. *J. Am. Chem. Soc.* **2008**, *130* (49), 16504–16505.

(3) Lim, J.; Bae, W. K.; Park, K. U.; zur Borg, L.; Zentel, R.; Lee, S.; Char, K. Controlled Synthesis of CdSe Tetrapods with High Morphological Uniformity by the Persistent Kinetic Growth and the Halide-Mediated Phase Transformation. *Chem. Mater.* **2013**, *25* (8), 1443–1449.

(4) Chen, O.; Chen, X.; Yang, Y.; Lynch, J.; Wu, H.; Zhuang, J.; Cao, Y. C. Synthesis of Metal-Selenide Nanocrystals Using Selenium Dioxide as the Selenium Precursor. *Angew. Chem.* **2008**, *47* (45), 8638–8641.

(5) B. O. Dabbousi; J. Rodriguez-Viejo; F. V. Mikulec; J. R. Heine; H. Mattoussi; R. Ober; K. F. Jensen; M. G. Bawendi. (CdSe)ZnS Core-Shell Quantum Dots: Synthesis and Characterization of a Size Series of Highly Luminescent Nanocrystallites. *J. Phys. Chem. B* **1997**, *101*, 9463–9475.

(6) Chen, O.; Zhao, J.; Chauhan, V. P.; Cui, J.; Wong, C.; Harris, D. K.; Wei, H.; Han, H. S.; Fukumura, D.; Jain, R. K.; et al. Compact High-Quality CdSe-CdS Core-Shell Nanocrystals with Narrow Emission Linewidths and Suppressed Blinking. *Nat. Mater.* **2013**, *12* (5), 445–451.

(7) Jang, Y.; Shapiro, A.; Isarov, M.; Rubin-Brusilovski, A.; Safran, A.; Budniak, A. K.; Horani, F.; Dehnel, J.; Sashchiuk, A.; Lifshitz, E. Interface Control of Electronic and Optical Properties in IV-VI and II-VI Core/Shell Colloidal Quantum Dots: A Review. *Chem. Comm.* **2017**, *53* (6), 1002–1024.

(8) Ustinov, A. I.; Budarina, N. M. Influence of Planar Defects on Powder Diffractograms of Fcc Metals. *Powder Diff.* **2002**, *17* (04), 270–277.

(9) Longo, A.; Martorana, A. Distorted f.c.c. Arrangement of Gold Nanoclusters: A Model of Spherical Particles with Microstrains and Stacking Faults. *J. Appl. Cryst.* **2008**, *41* (2), 446–455.

(10) Longo, A.; Sciortino, L.; Giannici, F.; Martorana, A. Crossing the Boundary between Face-Centred Cubic and Hexagonal Close Packed: The Structure of Nanosized Cobalt Is Unraveled by a Model Accounting for Shape, Size Distribution and Stacking Faults, Allowing Simulation of XRD, XANES and EXAFS. *J. Appl. Cryst.* **2014**, *47* (5), 1562–1568.

(11) A. Immirzi. *La Diffrazione Dei Cristalli*, 2nd edition.; Cooperativa universitaria Athena,

2010.

(12) Jagodzinski, H. Polytypism in SiC Crystals. *Acta Cryst.* **1954**, *7* (3), 300–300.

(13) H. Jagodzinski. Eindimensionale Fhlordnung in Kristallen Und Ihr Einfluss Auf Die Rontgeninterferenzen. III. Vergleich Der Berechnungen Mit Experimentellen Ergebnissen. *Acta. Cryst.* **1949**, pp 298–304.

(14) Paterson, M. S. X-Ray Diffraction by Face-Centered Cubic Crystals with Deformation Faults. *J. Appl. Phys.* **1952**, *23* (8), 805–811.

(15) Gevers, R. The Diffraction of X-Rays by Close-Packed Crystals Containing Both `growth Stacking Faults' and `deformation or Transformation Stacking Faults'. *Acta Cryst.* **1954**, *7* (4), 337–343.

(16) Warren, B. E. X-Ray Studies of Deformed Metals. *Prog. Mater. Phys.* **1959**, *8*, 147–202.

(17) Willis, B. T. M. The Effect of Segregation on the Diffraction from a Face-Centred Cubic Alloy with Deformation Faults. *Acta Cryst.* **1959**, *12* (9), 683–689.

(18) C. Johnson. Diffraction by Face-Centered Cubic Crystals Containing Extrinsic Stacking Faults. *Acta Cryst.* **1963**, pp 490–497.

(19) Kakinoki, J.; Komura, Y. Diffraction by a One-Dimensionally Disordered Crystal. I. The Intensity Equation. *Acta Cryst.* **1965**, *19* (1), 137–147.

(20) Kakinoki, J. Diffraction by a One-Dimensionally Disordered Crystal. II. Close-Packed Structures. *Acta Cryst.* **1967**, *23* (6), 875–885.

(21) Debye Function Analysis: Theoretical and Experimental Aspects. In *Crystallography for Health and Biosciences*; A. Cervellino, A. Guagliardi, R. Frison, G. Cernuto, Eds.; Insubria University Press, **2012**; pp 177–186.

(22) Cervellino, A.; Giannini, C.; Guagliardi, A. On the Efficient Evaluation of Fourier Patterns for Nanoparticles and Clusters. *J. Comput. Chem.* **2006**, *27* (9), 995–1008.

(23) Bertolotti, F.; Moscheni, D.; Migliori, A.; Zacchini, S.; Cervellino, A.; Guagliardi, A.; Masciocchi, N. A Total Scattering Debye Function Analysis Study of Faulted Pt Nanocrystals Embedded in a Porous Matrix. *Acta Crystallogr. A* **2016**, *72*, 632–644.

(24) Diehm, P. M.; Agoston, P.; Albe, K. Size-Dependent Lattice Expansion in Nanoparticles: Reality or Anomaly? *Chem. Phys. Chem.* **2012**, *13* (10), 2443–2454.

(25) Qi, W. H.; Wang, M. P.; Su, Y. C. Size Effect on the Lattice Parameters of Nanoparticles. *J. Nanopart. Res.* **2005**, *7* (1), 51–57.

6

Characterization of Organic Ligand-Capped Zinc Blende CdSe QDs

Adapted with permission from (ACS Nano, **2018**, *12* (12), pp 12558–12570*)*

This Chapter is fully dedicated to the analysis of WAXTS and SAXS data collected on organic ligand capped Cadmium Selenide QDs in colloidal form possessing a nominal pure ZB structure. This Chapter intends to present and discuss the results of the structural characterization based on the models of faulted NCs and methods described in the previous ones; the entire scientific path undertaken during these three years of Ph.D. studies will be also highlighted. Indeed, together with the synthesis of CdSe colloids and their optical and surface characterization performed at ETH Zürich (Switzerland), I have focused my work on their complete structural and microstructural characterization, by developing ad hoc DSE-based models and algorithms, at the University of Insubria and To.Sca.Lab (Como, Italy).

6.1 Experimental

6.1.1 Synthesis

As described in Chapter 1, pure CdSe-based nanomaterials show interesting optical properties when the crystalline domain of these particles fall in the 2-6 nm range. Four samples in this size window were synthetized using as guideline the heat-up recipe proposed by Chen et al.[1] for the preparation of nominally pure CdSe ZB NCs.[1] During the four syntheses, the environment conditions were kept unchanged for all the samples to increase the reproducibility. This means that even the heating mantel, the thermocouple, the stirrer and the three neck-flask used remained the same to avoid misalignment with the calibration of the thermocouple and changes of the local concentration of the precursors (due to a slightly different shape of the reactor or the different speed of the stirrer).

The first step in the synthesis consisted in the preparation of the cadmium precursor and its dispersion in the high boiling solvent (1-octadecene, ODE). The values in the following are given for the preparation of CdSe NCs of ~ 5nm. 0,115g (1mmol) of CdO were added to a three-neck-flask with 1,5 mL (4 mmol) oleic acid (OA) and 32mL of ODE. Since water and moisture can interfere with the reaction, the flask was connected to a Schlenk line and its content stirred under lab vacuum at RT. After changing channel from vacuum to argon, the mixture was heated to 240 °C for 1h until the CdO was completely dissolved and the solution changed from reddish to transparent. In this step, the Cd-Oleate precursor for the NCs synthesis is formed. Since the reaction produces water, the solution was cooled down to 50 °C and the channel changed from the argon to the lab vacuum pump for 30 min.

0.1g (1 mmol) of SeO_2 were added to the solution and the whole mixture was heated to 240 °C ramping up at the rate of 20 °C /min. Once the reaction temperature was reached (slightly below 240 °C) under continuous stirring, CdSe NCs rapidly form and grow. This is manifested by the changing of color of the reaction mixture, turning from yellow to orange-red (within ca. 2 min) to brown (after 5 min), as shown in Figure 6.1. Worth of note, the color due to the electronic band gap is highly temperature dependent; the reaction was carried out at 240 °C but after stopping

the reaction, the NCs color loses the reddish hue.[2] The NCs growth was stopped by rapidly cooling down the suspension using compressed air and cold water. Subsequently, the reaction mixture was washed to eliminate the ODE excess, the remaining precursors and smaller undesired clusters using a solvent/antisolvent procedure, with toluene as apolar solvent (10 mL) and ethanol as polar solvent. The amount of ethanol is not fixed because NCs with different size have a different solubility in the apolar matrix and a different amount of antisolvent is required. The ethanol volume is decided by the operator that manually drops the antisolvent in the apolar suspension until it becomes turbid, highlighting the precipitation of the largest fraction of NCs. At the very end, after three washing cycles, the nanocrystalline CdSe precipitate was dissolved in only 1 mL of toluene in order to obtain a highly concentrated sample, suitable for the WAXTS measurements.

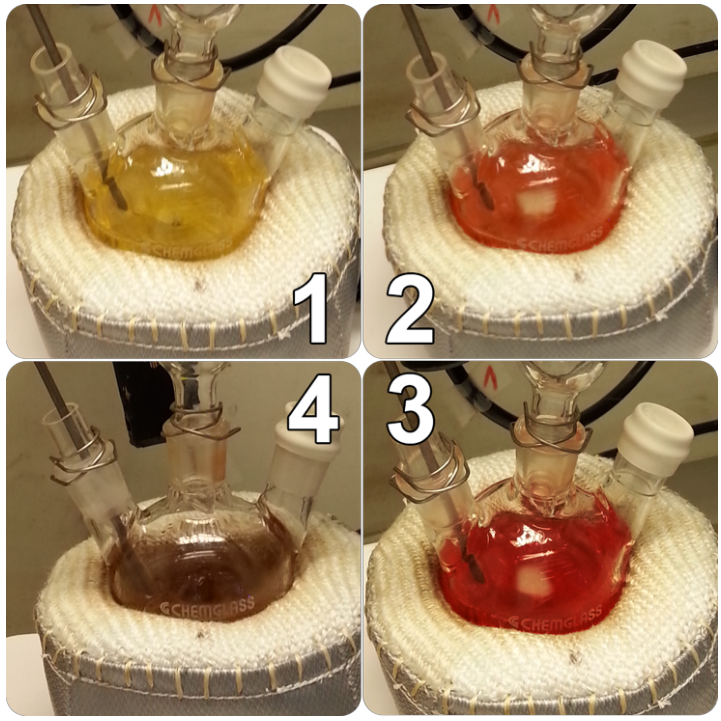

Figure 6.1. *Synthesis of CdSe NCs described in Paragraph 6.1.1. Four pictures of the reactor were taken at different times. The figure intends to show the increasing average size of the NCs with time.*

6.1.2 Conventional Spectroscopic Characterization

Immediately after the synthesis, a series of routine analyses were performed in order to control the morphology of the nanoparticles (via Transmission Electron Microscopy), the average crystal size (using the Uv-Vis absorption spectroscopy and calibration curves based on TEM) and the crystal phase purity (using XRPD) as shown in Figure 6.2. All the four samples show a "spherical-like" morphology and an apparently pure cubic phase (XRPD).

The most used analytical technique that indirectly provides information about the average NPs size is the absorption spectroscopy and the calibration curve correlating the position of the absorption peak maximum to the NC size. Every sample was diluted in toluene until a first absorption peak of absorbance *ca.* 0.1 was

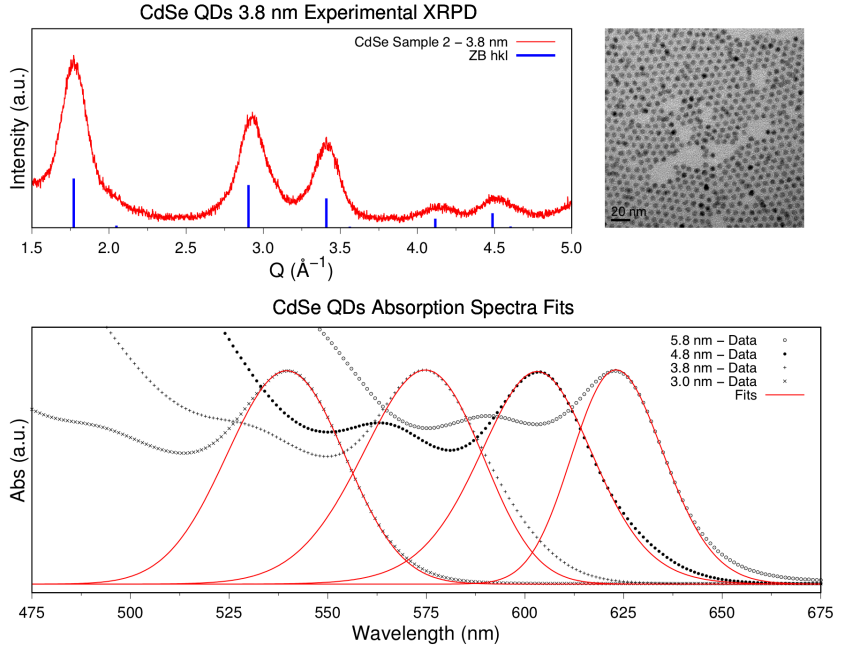

Figure 6.2. *Post-synthetic characterization of CdSe NCs. TEM images of* $CdSe\ QDs - 3.8\ nm$ *showing a spherical-like shape (top right) and the XRPD pattern (top left) acquired on the same dried sample, from which the cubic ZB symmetry with apparently no WZ features is observed. At the bottom, the first absorption peak for the four samples in the legend (dots) and the simulated signals (solid red curves) obtained by using spherical NPs with sizes distributed according to a log-normal law and a size dispersion below 15%.*

obtained; the measurements were performed in a quartz cell with 10 mm optical path. This experimental procedure reduces multiple absorption and other undesired effects such as oversaturation of the signal.

The four absorbance signals, as expected, are shifted to the red for samples with a longer reaction time, meaning that the largest particles gradually appear darker or bluish. A "preliminary" size estimation can be extracted in two different ways. The first, and the easiest, consists in fitting the first absorption peak with a PseudoVoigt[3] function, extracting the position of its maximum and deriving the NPs size from the Jasieniak's calibration curve (Equation 2.2).[4] The second option, described in Paragraph 2.1.2, consists in the simulation of the 1st absorption peak by considering a complete distribution of NP sizes (in our case, according to a log-normal function). Comparable results on these approaches are reported in Table 6.1. The slight and expected misfits between the two methods highlight the limitation of considering a single size for this type of characterization, which can be slightly misleading as the size dependent band gap it is not linear.[5] Worth of note, the highest misfit between the fitting and simulation approaches in determining the average particles diameters are attributed to the samples with the higher estimated size dispersion. From now on, the four samples will be labelled as: $CdSe\ QDs - 3.0nm$, $CdSe\ QDs - 3.8nm$, $CdSe\ QDs - 4.8nm$ and $CdSe\ QDs - 5.8nm$.

Sample	Jasieniak's calibration		Simulation	
	Abs_{max} (nm)	$< D >_A$ (nm)	$< D >_S$ (nm)	$\sigma_s / < D >_S$
$CdSe\ QDs - 3.0nm$	540	3.0	2.9	0.08
$CdSe\ QDs - 3.8nm$	575	3.8	3.6	0.10
$CdSe\ QDs - 4.8nm$	604	4.8	4.6	0.13
$CdSe\ QDs - 5.8nm$	624	5.8	5.8	0.08

Table 6.1. *Jasieniak's calibration refers to the average NPs diameters calculation using Equation 2.2.*
The simulation refers to the average size and size distribution of the NPs obtained using Equation 2.4.
$< D >_A$: average NCs diameter extracted from the first absorption peak maximum Abs_{max}
$< D >_S$ and σ_S: average NCs diameter and relative distribution obtained from the simulation of the entire first absorption peak.

6.1.3 Synchrotron X-ray Scattering Data Collection

The colloidal suspensions in toluene of the four samples, were loaded into borosilicate capillaries with certified composition (Hilgemberg GmbH 0500), 0.8 mm in diameter and 0.01 mm of wall thickness. WAXTS data of these samples were collected using a wavelength of 0.56548 Å (22keV) at the Material Science Beamline (X04SA-MS4) at the Paul Scherrer Institut (Villigen, CH) with the procedure described in Paragraph 3.3. For the accurate determination of the beam energy and the correction of sample offsets, a silicon powder standard (NIST 640d, with a_0= 0.543123(8) nm at 22.5 °C) was used. Data were collected in the 0.5° - 120° range with eight repetitions and acquisition time of 20 seconds each. The data reduction procedure was applied as described in Paragraph 3.3.
WAXTS data after reduction of the four experimental patterns, shown in Figure 6.3, confirm the absence of peaks from the WZ phase and a detectable progressive peak broadening upon decreasing the nominal size.

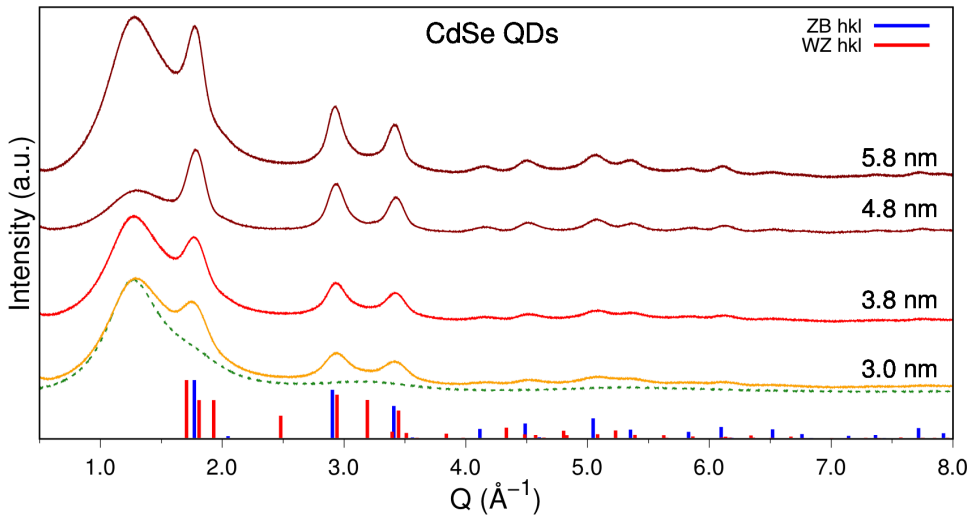

Figure 6.3. *Experimental WAXTS data collected on $CdSe\ QDs - 3.0nm$ (yellow solid line), $CdSe\ QDs - 3.8nm$ (light red solid line), $CdSe\ QDs - 4.8nm$ (red solid line), $CdSe\ QDs - 5.8nm$ (dark red solid line) and $toluene$ (green dashed line). The picture confirms the prevalent ZB features of the XRPD patterns and the high S/N with respect to the lab data. The progressive narrowing of the FWHM of Bragg peaks upon increasing the nominal average crystal size is clearly visible.*

6.2 Preliminary Characterization

6.2.1 The Detection of Stacking Faults in "Apparently" Pure ZB CdSe cQDs

As described in Chapter 4, the presence of planar defects perpendicular to the cubic [111] direction, such as GF, ISF and ESF, strongly affects the peak width and, in the case of ISF and ESF, also the position of Bragg peaks. The peak displacement follows complex ,but well-known, selection rules (Warren, 1990),[6] presented and discussed in Chapter 4. Starting from these considerations, a preliminary DFA analysis was performed on each of the four samples, using the Debussy program suite.[7] Databases of sampled interatomic distances were generated for unfaulted NCs with spherical shape; the unit cell parameter from bulk value was adopted (a = 6.077Å)[8]. Initial simulations were performed using the nominal size and the size distribution extracted from the UV-Vis absorption spectroscopy and Jasieniak's calibration;[4] this leaded to a remarkable difference in terms of peak broadening and position with respect to the experimental data (simulation as orange solid line in Figure 6.4). A second test (red solid line in Figure 6.4) was carried out by refining the NCs size and size distribution, in order to evaluate their deviation from nominal values, and by relaxing the ZB cell parameter (refined value *a* = 6.083 Å). The best match provided an average diameter of 2.4 nm (to be compared with the nominal value of 4.8 nm) and a dispersion of 38% (instead of 13%) for the $CdSe\ QDs - 4.8nm$ sample.
We than extracted the peak position (Q_{exp}: the peak maximum in Q scale) from the WAXTS data shown in Figure 6.4; starting from Equation 4.2 we calculated the ideal position of Bragg peaks Q_{cal} for the refined ZB cell (a = 6.083 Å) as follows:

$$Q_{cal} = \frac{4\pi \sin \vartheta_{hkl}}{\lambda} \qquad Eq.6.1$$

and consequently, the experimental shift ΔQ_{exp} defined as $Q_{exp} - Q_{cal}$.
Following Warren's theory and subsequent modifications, [9,10] diffraction peak shifts due to planar defects are not always linear when increasing the SF density.

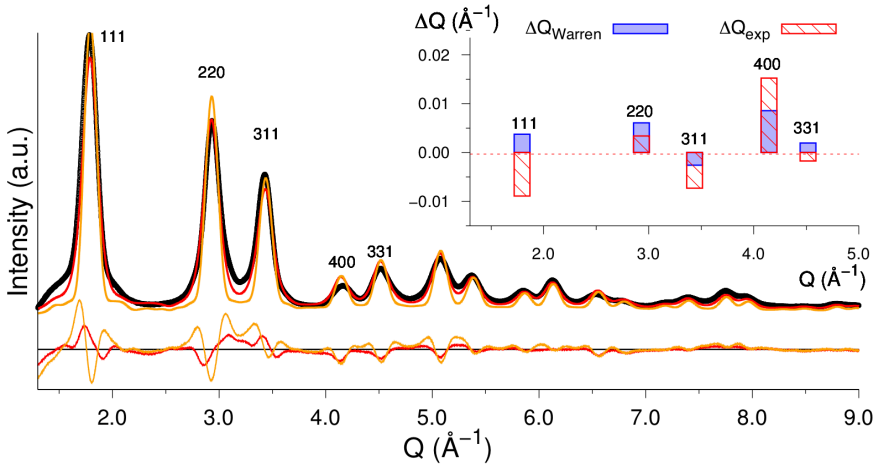

Figure 6.4. *WAXTS data of the $CdSe\ QDs - 4.8nm$ sample (black dots) and Debussy fits. The orange solid line represents the pattern simulation of a defect-free ZB structure in spherical NCs having an average size of 4.8 nm and a size dispersion of 13%. The red solid line describes the simulation obtained by relaxing the parameters of the log normal size distribution, resulting in $< D >$ = 2.4 nm and $\sigma/< D >$ = 39%. The inset compares the deviation of the experimental positions of selected peaks from the calculated ones (ΔQ_{exp}), corresponding to a = 6.083 Å vs the calculated peak shift from Warren theory[6] (ΔQ_W) using an α_W= 0.035 (the description and meaning of α_W are reported in Chapter 4).*

Equation 4.1, describing the peak shift $\Delta(2\vartheta)_W$ due to ISF, was here converted into ΔQ_W as follows:

$$\Delta Q_W = \left(\frac{4\pi \sin\left(\vartheta_{hkl} + \Delta\vartheta_{W_{hkl}}\right)}{\lambda}\right) - Q_{cal} \qquad Eq.\,6.2$$

and used to extract the ISF density α_W for the $CdSe\ QDs - 4.8nm$ sample. The α_W value of 0.035 was obtained by using the GRG (Generalized Reduced Gradient) algorithm by minimizing the square differences between ΔQ_{exp} and ΔQ_W. All the Q and ΔQ values are listed in Table 6.2; ΔQ_{exp} and ΔQ_W are also graphically shown as the inset of Figure 6.4 and show the major deviations on 111 and 331 peaks where opposite signs are found. These deviations suggest that effects are due not only to the presence of ISF, but also to the presence of differently strained CdSe bond

hkl	Peak positions (Å^{-1})		Peak shifts (Å^{-1})	
	Q_{exp}	Q_{cal}	ΔQ_{exp}	ΔQ_W
111	1.7983	1.7946	-0.00890	0.00374
220	2.9367	2.9306	0.00339	0.00608
311	3.4338	3.4364	-0.00730	-0.00258
400	4.1530	4.1444	0.0152	0.008553
331	4.5183	4.5163	-0.00173	0.00196

Table 6.2. *The table shows the experimental (Q_{exp}) and calculated (Q_{cal}) peak positions of hkl peaks together with their experimental (ΔQ_{exp}) and calculated (ΔQ_W) position shifts. The calculated shifts obtained using an α_W = 0.035 do not match the experimental ones in terms of entity and, more significantly, of direction, revealing the presence of addition sources of peak shifts.*

distances along the different crystallographic directions, as will be explained in Paragraph 6.4.

Since the presence of this "anisotropic" strain of CdSe is unexpected in ideal cubic structures, we associated this effect to the presence of WZ transitions in the crystals.

6.2.2 PDF Analysis on "Apparently" Pure ZB CdSe cQDs

In addition to the DSE analysis, thanks to the courtesy of Prof. S. J. Billinge and Dr. F. Bertolotti, WAXTS data for PDF analysis were collected at the Brookhaven National Laboratory (BNL) synchrotron using a beam energy of 67 keV ($\lambda = 0.1834$ Å) up to Q = 25 Å^{-1}, for $CdSe\ QDs - 3.0nm$, $CdSe\ QDs - 3.8nm$ *and* $CdSe\ QDs - 4.8nm$ QDs. Using the PDFgetX3 program, these data were Fourier transformed into the experimental G(r).

Using the "small box model" approach implemented in the PDFgui software, the structural and microstructural analyses of CdSe particles with ZB structure were performed minimizing the mismatch between the experimental and calculated G(r) functions in terms of χ^2. The refined parameters are: cell parameter, size, atomic thermal displacement parameters and Se site occupancy factors. Results of these

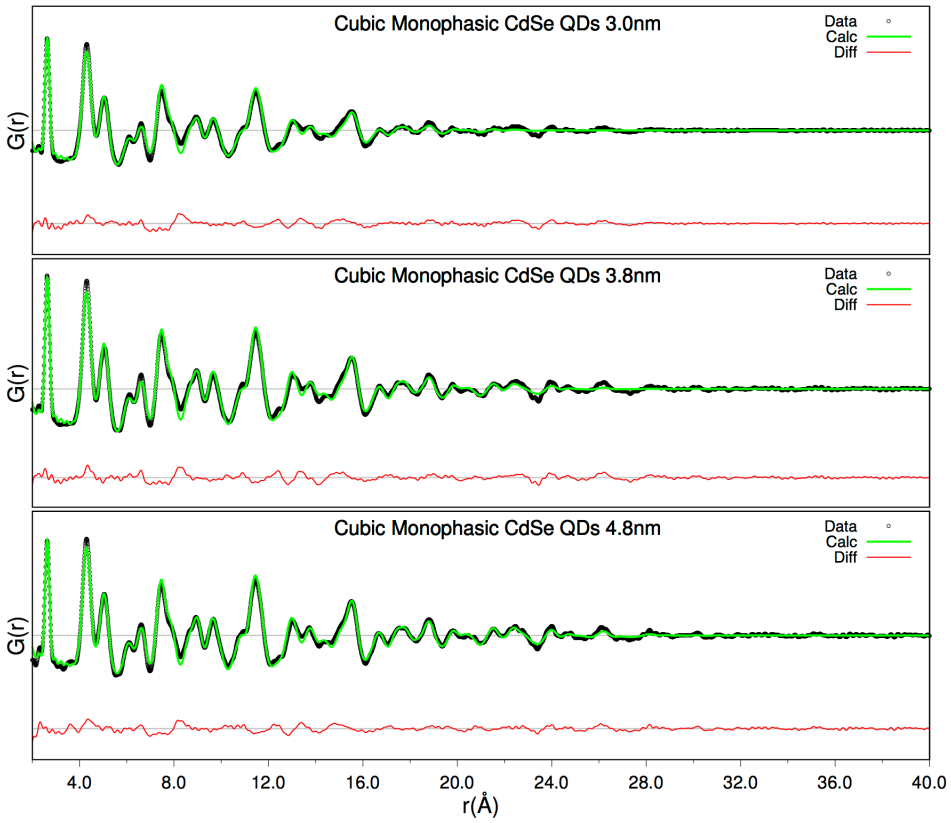

Figure 6.5. *PDF fits (green solid lines) of the $CdSe\ QDs - 3.0nm$, $CdSe\ QDs - 3.8nm$ and $CdSe\ QDs - 4.8nm$ samples vs the experimental G(r)s (black dots) obtained by monophasic ZB spherical particles.*

minimizations are reported in Figure 6.5 and Table 6.3.

Table 6.3 shows a systematic underestimation of NCs size, in agreement with what was obtained by the DSE analysis, and a small lattice expansion for low sizes. This fact confirms that a defect-free ZB structure phase is not sufficient to properly describe the wide angle X-ray diffraction pattern of these QDs, neither in the reciprocal or the real space. Stacking defects need to be introduced for a deeper comprehension of the system.

As reported in Chapter 3, PDF analysis can be analytically performed by direct fitting, providing the peak positions, widths, shape and intensities, enabling the estimation of possible deviations from the expected structure. The first five peaks of the experimental G(r) functions were individually fitted with Gaussian functions after

PDF refinement				
Sample	a_k(Å)	$< D >$ (nm)	$Cd:Se$	R_{wP}
$CdSe\ QDs - 3.0nm$	6.0927	2.51	1.33	0.169
$CdSe\ QDs - 3.8nm$	6.0894	2.96	1.24	0.157
$CdSe\ QDs - 4.8nm$	6.0845	3.36	1.30	0.154

Table 6.3. *The table shows the refined: ZB cell parameter a_k, the average NCs diameters $< D >$, the NCs $Cd:Se$ stoichiometry and the weighted R_{wP} factor of the three CdSe QDs samples. The three PDF refinements highlight an average expansion of the cubic lattice and an underestimation of the average NC diameters, in full agreement with the preliminary DSE analysis. The analysis of the G(r) also shows the presence of a Cd excess attributable to the presence of the external layer of capping ligands.*

the subtraction of a linear baseline. Results of this analysis in terms of bond distances $dist$ and FWHM of G(r) peaks are reported in Table 6.4.

The average interatomic distance values (dis) match those of the bulk ZB CdSe structure within 0.01 Å; in contrast, a high variability is observed in the FWHM of the different peaks. This evidence suggests a structural anisotropy, in agreement with what was found from WAXTS data by Warren's theory.

The interpretation and quantification of this anisotropy, together with the detail on the SF effects, required the development of detailed atomistic models of ZB NCs with planar defects and of a protocol of analysis (described in Chapter 5). This will be specifically discussed in the following sections.

	Bulk ZB	3.0 nm		3.8 nm		4.8 nm	
Distance	$dist$, Å	$dist$, Å	FWHM, Å	dis, Å	FWHM, Å	$dist$, Å	FWHM, Å
Cd-Se	2.63	2.63	0.49	2.63	0.62	2.63	0.20
Cd-Cd / Se-Se	4.30	4.30	1.06	4.30	1.28	4.30	1.09
Cd-Se	5.04	5.05	0.53	5.04	0.70	5.04	0.69
Cd-Cd / Se-Se	6.08	6.08	0.22	6.09	0.30	6.06	0.31
Cd-Se	6.62	6.61	0.45	6.60	0.53	6.61	0.47

Table 6.4. *The table includes the average Cd-Se, Cd-Cd and Se-Se interatomic distance ($dist$) and relative distribution (FWHM) values extracted from the direct PDF analysis using Gaussian functions.*

6.3 Morphological and Surface Investigation of ZB CdSe NCs

As presented in Chapter 4, the effects of stacking faults on the measured scattering trace are partially hidden by morphological (size and shape) features. Indeed, since particles with a high density of planar defects do not maintain a cubic symmetry, their shapes may be non-perfectly isotropic.
In order to investigate the actual morphology of the four CdSe samples, we resorted to SAXS experiments and data analyses. In addition, a brief paragraph is included for DNP-NMR experiments performed on the $CdSe\ QDs - 3.8nm$ sample. This innovative spectroscopic method was used to corroborate the information on crystal surface and to extract a qualitative information on core and surface disorder.

6.3.1 Small Angle X-Ray Scattering Experiments and DSE-Based Modeling

SAXS measurements on the set of CdSe samples investigated in this Ph.D. project were performed at the iNano center of the Aarhus University, thanks to the courtesy of Prof. J. S. Pedersen and Dr. F. Bertolotti (Aarhus Institute of Advanced Studies). The experiments were performed on the same solutions used for the X-ray synchrotron data collection at SLS (1:1 diluted with toluene), using an X-ray gallium source (λ=1.340 Å) on a Bruker AXS NanoSTAR instrument equipped with homebuilt scatterless slits.[11,12] The suspensions were injected and guided into a quartz capillary inside a high vacuum chamber; data were subtracted from the capillary and solvent contribution of scattering before the analysis. As described in Chapter 2, the DSE can be used with atomistic models of appropriate size and morphology[7] to reproduce the small angle scattering signal of particles. Beyond the DSE approach, SAXS data were also fitted using analytical form factor models (by Prof. J. S. Pedersen).[13] In this paragraph, only the results obtained with the DSE (that agree with those obtained using the form factor model) will be discussed. Best fits from analytical form factor for spherical and prismatic models are shown in Figure 6.6. The main advantages of using the DSE for fitting SAXS data are here summarized in

three points:

a) the population of NCs has the same discretization for SAXS and WAXTS;
b) the same size-distribution law (taken as log normal, Equation 3.30) can be used for SAXS and WAXTS data analysis;
c) the atomistic models used for fitting SAXS data and their validation in the WAXTS region jointly permit to determine the orientation of the crystal structure with respect to the exposed facets.

Despite that anisotropic shapes are often reported for the most studied WZ NCs, justified by the point group of the hexagonal structure,[14,15] deviations from isotropic shapes in ZB CdSe NCs are usually investigated in nPLs and nRDs but less frequently reported in QDs.[16] Starting from these considerations, SAXS data were initially analyzed considering NPs with spherical shape; later, a more complex model was introduced by considering NPs with prismatic morphology exhibiting two long (equally sized $L_1 = L_2$) and one short (L_3) edges.

To this goal, bivariate populations of atomistic models with different faceting were built in order to detect:

a) size and shape anisotropy;
b) size dependent faceting.

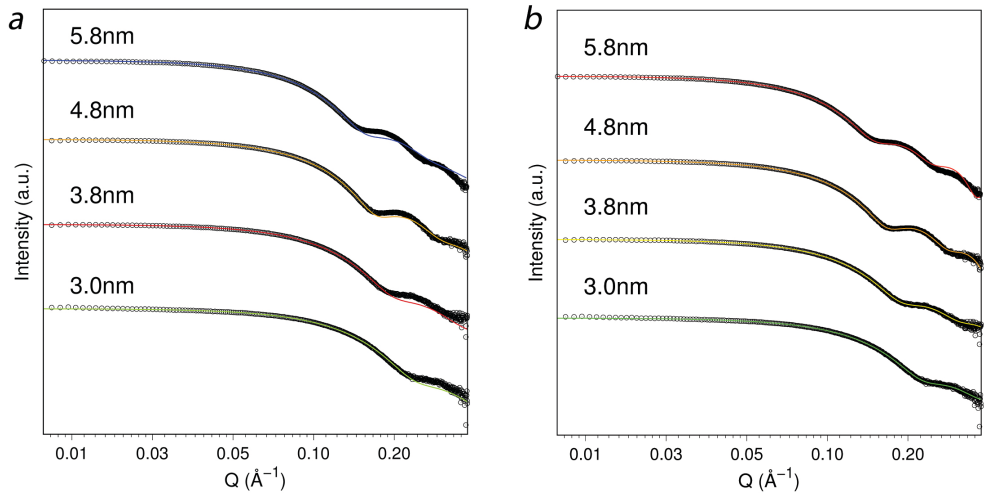

Figure 6.6. *Log-Log plot of SAXS data and best fits on $CdSe\ QDs - 3.0nm$, $CdSe\ QDs - 3.8nm$ and $CdSe\ QDs - 4.8nm$ samples using the analytical form factors describing a sphere (a) and a prism (b).*

The investigated morphologies are summarized in the scheme below, where the conditions for the different faceting are also quoted:

	Prismatic exposing facets		Faceting conditions
1)	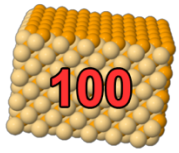	{100}	$\|x\| \leq a;\ \|y\| \leq a;\ \|z\| \leq c$
2)	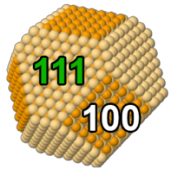	{111}	$\|x\| + \|y\| + \|z\| \leq d$
3)	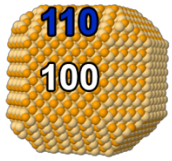	{110}	$\|x\| + \|y\| \leq e$ $\|x\| + \|z\| \leq e$ $\|y\| + \|z\| \leq e$

Where:

a, c, d, e: thresholds for faceting; only atoms satisfying the conditions set above belong to the NC

$|x|, |y|, |z|$: atomic Cartesian coordinates referred to the centre of mass

The three described morphologies were tested on CdSe QDs of increasing size. For $CdSe\ QDs - 3.0nm$ and $CdSe\ QDs - 3.8nm$ the best fit was obtained using a prismatic shape with only {100}, exposed facets and aspect ratios L_3/L_1 *ca*. 0.7. Upon increasing the size, the same morphological model leaded to a progressively increasing misfit for $CdSe\ QDs - 4.8nm$ and $CdSe\ QDs - 5.8nm$ samples. In these cases, different morphologies including new facets ({111} and {110}) and constant ratio $A_{\{100\}}/A_{\{111\}}$ or $A_{\{100\}}/A_{\{110\}}$ did not provide convincing results, as shown in Figure 6.7 for $CdSe\ QDs - 5.8nm$. This figure also highlights that only a suitable

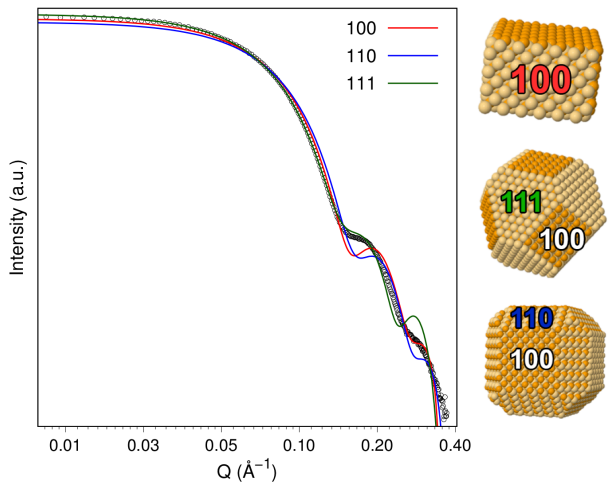

Figure 6.7. *Log-Log plot of SAXS data and fits on* $CdSe\ QDs - 5.8nm$ *QDs using 1, 2, 3 morphologies with constant areal ratio* $Area_{\{111\}}/Area_{\{100\}}$ *for morphology 2 and* $Area_{\{110\}}/Area_{\{100\}}$ *for morphology 3.*

combination of morphologies 1 and 2 significantly improves the fit at larger sizes. Since the idea of NPs with the same size and same faceting is only an approximation, the need of introducing additional faceting when increasing size suggested us to build populations of prismatic NCs with increasing edges, but constant threshold d = 2.5 nm cuts. This inevitably produces NCs with {100} facets only for NPs of equivalent diameter smaller than ~ 4 nm. This strategy enabled to a satisfactory match of both the SAXS signal and the Porod region of the WAXTS pattern of the four samples (see Figure 6.10). The results of these refinements are reported in Table 6.5.

From the values reported in Table 6.5, considering their size distribution, one can derive that the 10% of NCs of the $CdSe\ QDs - 3.8nm$ sample are truncated. For $CdSe\ QDs - 5.8nm$, the number of truncated NCs drastically increases to 92%, with {111} facets accounting the 20% of the total surface area in the most frequent NC and about 75% in the largest. Despite this huge number of truncated NCs, in the wide-angle region, the precise information on faceting is lost (see Figure 4.8), being hidden by size dispersion and faulting effects. Accordingly, the structural and microstructural analysis in the wide angle region was performed using the prismatic morphology exposing {100} facets only.

Sample	$L_1 = L_2$ (nm)	σ_1/L_1	L_3 (nm)	σ_3/L_3	*AR*
$CdSe\ QDs - 3.0nm$	3.34	9.4%	2.42	11%	0.724
$CdSe\ QDs - 3.8nm$	4.08	8.5%	2.92	10%	0.716
$CdSe\ QDs - 4.8nm$	4.64	7.1%	3.48	10%	0.750
$CdSe\ QDs - 5.8nm$	5.20	10%	3.76	22%	0.724

Table 6.5. *The table includes the refined values of $L_1 = L_2$, L_3 edges and relative dispersions (σ_1 and σ_3) of the CdSe QDs samples described in the DSE simulations by truncated prisms with d=2.5 nm (see texts). The NCs aspect ratio (AR), defined as L_3/L_1, is reported in the last column.*

6.3.2 DNP-PASS-PIETA-NMR studies on ^{113}Cd nuclei

DNP-PASS-PIETA-NMR was here used to investigate surface and core modification of the chemical environment[17,18] in a preliminary, still exploratory study; to this purpose, the $CdSe\ QDs - 3.8nm$ sample was analyzed by this method. As described in Paragraph 2.2.3, this analysis requires a specific sample preparation in order to maximize the signal enhancement. 15μL of a saturated colloidal suspension of NPs in toluene were mixed with 7.5μL of TEKPol (50mM) in TCE (1,1,2,2 tetrachloroethane) and mixed with a low amount of standard mesoporous silica, with certified pore diameter of 15nm. The grainy (solid) phase is later packed in a certified sapphire rotor (3.2 mm of diameter) and subjected to measurement. A comprehensive understanding of DNP-NMR method, pulse scheme, strategy and experimental parameters is out of the scope of this Ph. D. project; the interested reader can refer to the available literature.[18]

Since this ^{113}Cd NMR analysis was performed to compare signals detected on clusters with similar composition but different shape and crystal phase, here, the DNP-PASS-PIETA signals of the $CdSe\ QDs - 3.8nm$ and of a CdSe nanoplatelets from a different synthesis (nPLs 1.5 nm thick and 15-20 nm wide) are compared. For both samples, two signals are detected:

a) Core Cd atoms: Cd is tetrahedrally coordinated to four Se atoms,
b) Surface Cd atoms: Cd is coordinated to *n*Se atoms and *m*Oleate residues (*n*+*m*=4),

that well describe the different chemical environment of the Cd core (buried into the NP), if compared to the surface Cd atoms. An interesting feature of the raw data is the different broadening of the two signals. With reference to Figure 6.8, the broadening of the core signals of quasi-spherical QDs and flat nPLs seems to be comparable. Differently, the surface peak of QDs, with respect to that of the nPLs, is significantly broader, skewed and shifted to lower ^{113}Cd isotropic chemical shifts.

It is known from the literature that ZB CdSe nPLs expose {100} facets only[19] while the ZB CdSe QDs are considered roughly spherical, and expose both {111} and {100} facets.[20] For this reason, the broadening and shift for the ^{113}Cd signal of the surface Cd peak was attributed to the different faceting of the two systems (QDs possessing a higher "surface versability"). However, the SAXS analysis reported in a previous paragraph revealed a negligible amount of exposed {111} facets in $CdSe\ QDs - 3.8nm$ sample; consequently, the hypothesis of a broader peak due to the different faceting vanishes, corroborating the hypothesis of a larger structural disorder at the surface of QDs compared to the nPLs.

The hypothesis a surface disorder in QDs can be attributed to the high density of SF,

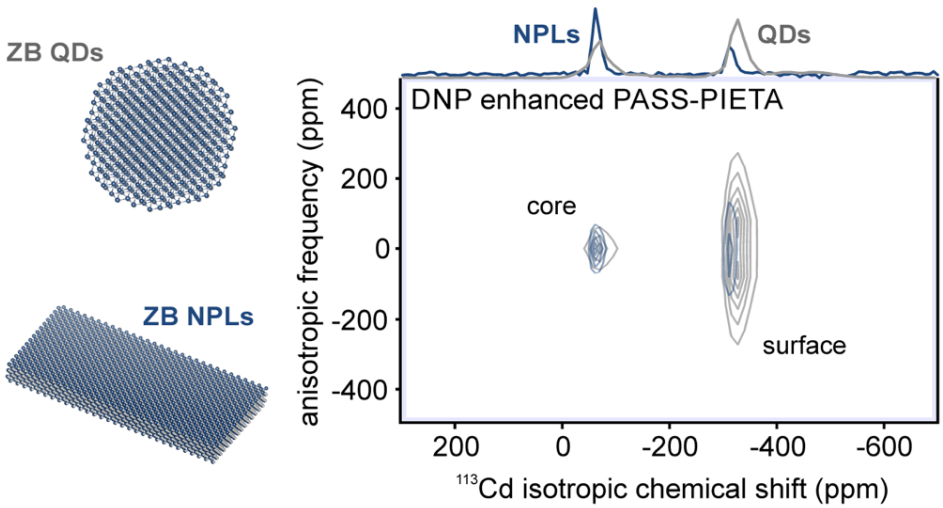

Figure 6.8. *Overlaid ^{113}Cd DNP-PASS-PIETA-NMR on $CdSe\ QDs - 3.8nm$ and CdSe nPL (1.5 nm thick). The solid grey lines refer to the QDs NCs while the blue one to the nPLs. The broad peak tail in QDs at -311 ppm suggests a surface disorder attributed to the presence of discontinuous surfaces generated by the SF (work still in progress for nPLs).*

generating a structural diversity of Cd atoms at the surface. The chemical environment of the buried Cd in faulted NCs should not significantly change (even in the presence of strain, not easily detectable by NMR), while, at the local level, surface Cd atoms may show displacements which cause the NMR to broaden. Whether this hypothesis is viable, can only be proven after the DSE complete analysis of SF in CdSe nPLs (work in progress).

6.4 Structural and Strain Analysis of faulted ZB CdSe NCs

6.4.1 Random vs Localized stacking fault model

Once the SAXS region of the diffraction pattern was explored and precious information about the crystal-size and morphology obtained, the second step of the *refinement strategy* reported in Paragraph 5.2 was performed, the goal of which is disentangling size from fault effects in WAXTS data. When faults or other deformations occur at the nanoscale, their effects on the diffraction pattern strongly depend on the defect location or orientation with respect to the NCs structure and morphology.[21] Therefore, two distinct models of planar defects distribution were examined:

a) *A random model:* with an equiprobable density of SF along the [111] cubic direction of the NCs, regardless of the fault localization in the sequence;
b) *A localized model*: with preferential occurrence of hexagonally faulted layers within a limited number of planes (five in this case), localized in the central portion of the NCs.

The case in which the faulted layers are preferentially localized in the peripheral regions of the colloidal CdSe QDs was not considered here, since their effects on the powder diffraction pattern is by far too weak, as also demonstrated elsewhere,[21] due to the limited extension on these planes and not in line with the remarkable peak shifts and broadening observed in the CdSe experimental data.

The optimization conditions for the two models are summarized below, their construction being extensively reported in Chapter 5.

Random model (RND)

For each NCs size a fixed number of sequences (50), characterized by a different stacking of layers along the [111] cubic direction of the ZB structure, has been generated for all samples. This number was estimated as the best compromise between the computational time and the minimum number of repetitions necessary to minimize the differences in the calculated DSE patterns, upon changing the sequence of planes for constant SF probability and length of the sequences.
This number was obtained by evaluating the agreement factor R_P of the average DSE simulation (I_x) against an ideal reference one (I_{999}), computed using a very large number of sequences (999, threshold $R_P \sim 10^{-2}$), as shown in Figure 6.9:

$$R_P = \sqrt{\frac{\sum_i (I_{i,x} - I_{i,999})^2}{\sum_i (I_{i,999})^2}} \qquad Eq.\,6.3$$

Where:
$I_{i,999}$: intensity at the *i-th* 2θ angle of the simulated pattern of a faulted NC using 999 sequences (reference)
$I_{i,x}$: intensity at the *i-th* 2θ angle of the simulated pattern of a faulted NC using x sequences.

The α, β, γ and δ parameters, introduced and discussed in Chapter 5, were used as input for the sequence generation. These parameters can vary from 0 to 1 and describe the probability of the different types of transitions within the CdSe ZB layers stacked along [111]. According to some preliminary analysis of the experimental data, the presence of *intergrowths* of WZ in ZB (*i.e.* a number of more than two consecutive *h* layers within a single sequence) was initially excluded, due to the absence of peaks belonging to the WZ structure in the CdSe synchrotron X-ray data. For this reason, jointly to the need of reducing the hyperspace of all the possible quadruplets (in other terms, the CPU time), the γ value, that describes the probability of finding a "regular" *k* layer after two *h* transitions ($hh \rightarrow k$), was set equal to 1 in the sequence generation step.

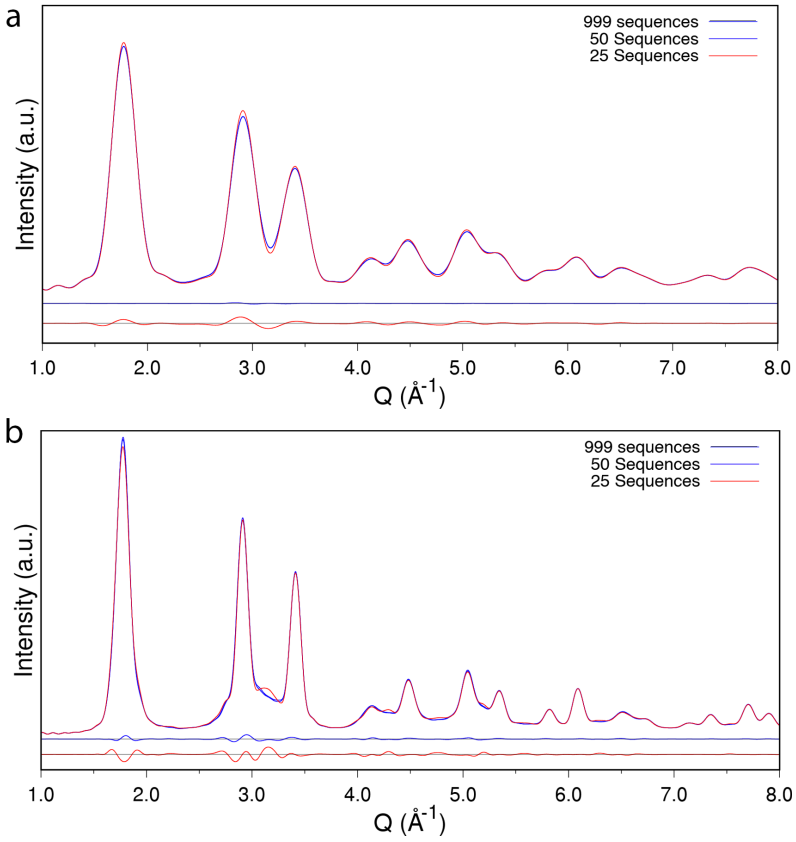

Figure 6.9. *The figures report the DSE simulations generated by merging 999 (black traces), 50 (blue traces) and 25 (red traces) sequences of layers for spherical CdSe NCs of 2.7 nm (a) and 6.1 nm (b). The two plots intend to graphically show, for a small and a larger NC, the misfits between the "ideal" trace generated by averaging 999 sequences vs the ones generated merging 50 and 25 sequences in a RND sequence generation case.*

Additional tests demonstrated that by relaxing γ below 0.7 in our DSE simulations produces indeed inconsistent results with the experimental data. For sake of simplicity, in the search of the best SF probability, another constraint ($\alpha = \beta$) was used, meaning that the probability of introducing a hexagonal transition is not dependent on the configurations of the two previous transitions but only on the preceding one. A 2D map of the GoF parameters in the β and δ coordinates was explored, following a grid search strategy, in the range $0.5 < \beta < 1.0$ and $0.0 < \delta < 1.0$, with a step of ±0.05, as shown in Figure 5.4 of Chapter 5.

Localized model (LOC)

Restraining the localization of the *h* faulted planes, within the regular ...*kkk*... ZB sequence, in the central part of the CdSe clusters maximizes their effects in the corresponding DSE pattern.[21] For this reason, the number of sequences for the *localized model* has been increased to 100 with respect to the *random model* where the defect effects were "diluted" throughout the whole NCs volume; again, this number was identified as the minimum number of repetitions necessary to have negligible differences ($R_P \sim 10^{-2}$) between the averaged DSE pattern of a single size NC with 100 different sequences, given the same SF probability and number of layers.

Within the five layers centered at $N_{lay}/2$ (where N_{lay} is the total number of layers of each NC of the bivariate population), the strategy followed to generate 100 sequences for each NC size is the same described for the *random model*, in terms of SF probability parameters (α, β, γ, δ) and constraints applied to the model.

In this case, the ranges of SF input parameters eventually explored for optimizing the SF % for each sample were: $0.25 < \beta < 0.45$ and $0.40 < \delta < 0.60$, with a step of ±0.05.

The final best β and δ values of all samples for both the RND and LOC models are quoted in Table 6.6. The δ values from the RND model suggest that the majority of planar defects in our CdSe NCs are of the GF type and that there are no significant differences among the different samples in terms of amount of GF and ISF. The β

Sample	RND		LOC	
	β	δ	β	δ
$CdSe\ QDs - 3.0nm$	0.65	0.70	0.40	0.50
$CdSe\ QDs - 3.8nm$	0.70	0.80	0.35	0.50
$CdSe\ QDs - 4.8nm$	0.75	0.80	0.40	0.50
$CdSe\ QDs - 5.8nm$	0.75	0.60	0.30	0.50

Table 6.6. *The table includes the β and δ values that minimize the GoF values of each sample upon exploration of the SF parameters hypersurface, as shown in Figure 5.4.*

and δ values of the LOC model, referred to the 5 central planes, are numerically different and not directly comparable to the RND ones. In both cases, in our construction they are not influenced by the layer extensions, which indeed have a significant influence on the effect on the diffraction peaks. In order to quantify the total amount of planar defects also accounting for the plane extension, the total fault percentages ($SF\% = p_{SF} \times 100$) was computed for all CdSe samples as follows:

$$SF\% = \sum_{i=1}^{i_{max}} \sum_{j=1}^{j_{max}} \chi_{ij} \left(\frac{A_h}{A_h + A_k} \right)_{ij} \times 100$$

$Eq.\,6.4$

Where:
χ_{ij} is the final mass fraction of each *ij-th* NC for a population of $i \times j$ NCs;
A_h and A_k, are the areas of the *h* and *k* planes within the *ij-th* NC.

The SF% values for the localized model are reported in Table 6.7; they indicate that larger SF% are found at smaller sizes. This finding will be later discussed.
For both the *random* and *localized* SF models, the Simplex algorithm[22] was used to optimize the initial structural and microstructural model parameters against the experimental data, after the exploration of the SF probability hyperspace. The information derived from Small Angle X-ray Scattering was used to restrain the NCs shape and the average sizes (L_a and L_c) and standard deviations (σ_a and σ_c) of the bivariate lognormal size-distributions. The final best fits are shown in Figure 6.10 and Figure 6.11.

Ligands coverage

A list of additional structural refined parameters includes: i) the Isotropic Debye-Waller factors were refined for four independent "atomic" species (Cd_{core}, Cd_{shell}, Se_{core}, Se_{shell}); ii) the site occupancy factor (*s.o.f.*) of Se atoms located on the shell at the NCs surfaces and of Cd_{core} atoms.

Sample	GoF		Cd:Se	Coverage (nm^{-2})	*SF%*
	LOC	RND			
$CdSe\ QDs - 3.0nm$	2.44	2.66	1.29	4.0	31.9
$CdSe\ QDs - 3.8nm$	2.99	3.19	1.13	2.7	28.3
$CdSe\ QDs - 4.8nm$	6.20	7.08	1.17	3.9	25.3
$CdSe\ QDs - 5.8nm$	2.80	2.89	1.15	4.0	24.5

Table 6.7. *The table includes the GoFs relative to the DSE refinement using the localized (LOC) and random (RND) models. In orange, the stoichiometry and ligand coverage values.*

For the $CdSe\ QDs - 3.0nm$ sample a value Cd_{core} = 0.86 was found suggesting the presence of Cd vacancies in the core. Metal vacancies in chalcogenides QDs are not new and has been reported in many papers; their occurrence is often invoked in the description of cation exchange reaction mechanisms.[23]

In our analysis, the presence of Se_{shell} and Cd_{core} vacancies enabled the estimation of the average stoichiometry, given as an overall Cd:Se ratio in Table 6.7 and, more importantly, a physically-sound ligand coverage values $\langle c \rangle$, also reported in Table 6.7. The values are computed according to charge balance considerations involving the total number of Cd^{2+} and Se^{2-} of each NC within the population and the presence of oleate ligands at their surface (see ref.[24] for further details), as follows:

$$c_{ij} = \frac{2N_{Cd,ij} - 2N_{Se,ij}}{A_{surf,ij}} \qquad Eq.6.5a$$

$$\langle c \rangle = \sum_{i=1}^{i_{max}} \sum_{j=1}^{j_{max}} c_{ij}\chi_{ij} \qquad Eq.6.5b$$

Where

c_{ij}: coverage of the *ij-th* NC

χ_{ij}: Number fraction of the *ij-th* NC

$N_{Cd,ij}$: number of Cd atoms of the *ij-th* NC

$N_{Se,ij}$: number of Se atoms of the *ij-th* NC

$A_{surf,ij}$: Surface area of the *ij-th* NC

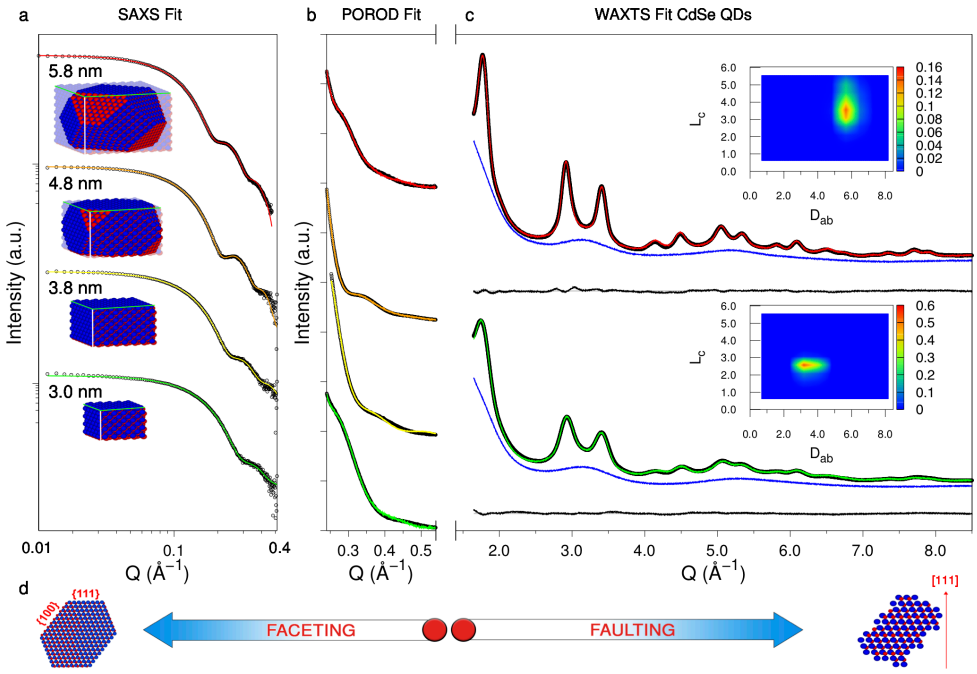

Figure 6.10. *a) SAXS data collected on the four samples here investigated, and best fits obtained using our DSE based approach. The insets represent the most representative NC of the population showing the size dependent faceting appearing over 5nm of crystal extension. b) Simulation of the Porod region of the WAXTS pattern using the same morphology used for fits in "a)", showing the excellent agreement of the same models on two different portions of scattering data. c) DSE-based best fits of the* $CdSe\ QDs - 3.0nm$ *(green solid line) and* $CdSe\ QDs - 5.8nm$ *(red solid line). d) Graphical representation of the information retrieved from SAXS and WAXTS data.*

6.4.2 CdSe Bond Distance Strain

Despite the introduction of a large density of planar defects into the atomistic model, the new calculated positions of the peaks, shown in Table 6.2, (especially for the 111, 311 and 331 peaks) do not perfectly match those in the experimental traces, as shown in Figure 6.12.

This finding of a persistent, size-dependent, misfit was interpreted as due to an additional relaxation of the Cd-Se bond distance along the stacking axis. To manage this relaxation in our atomistic CdSe model, an additional strain (δz) was applied

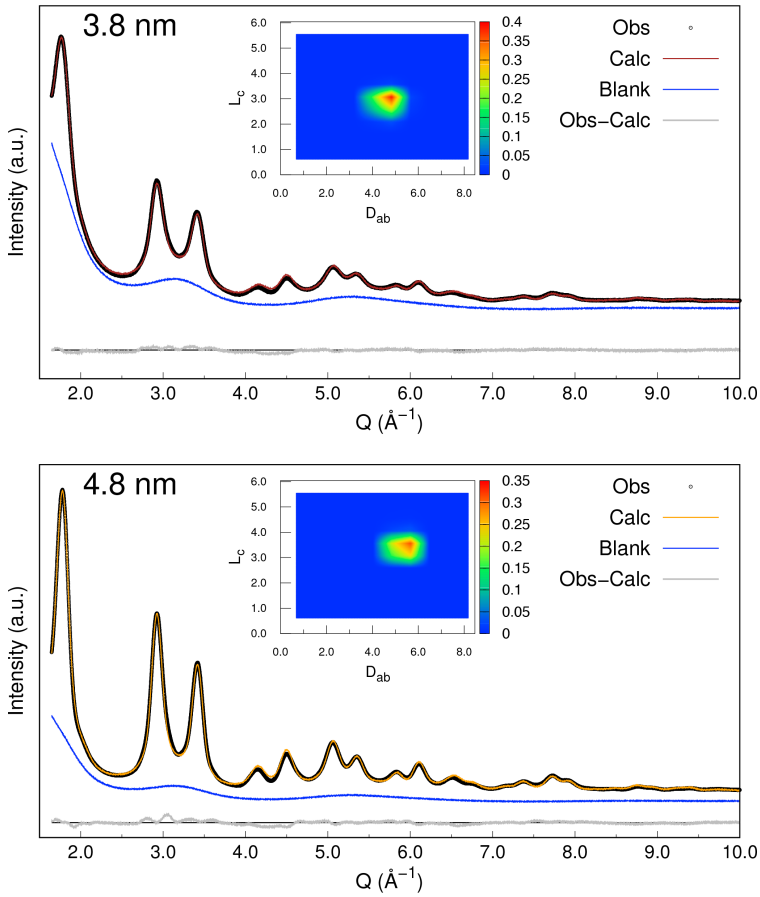

Figure 6.11. *DSE-based best fits and 2D size distribution maps of $CdSe\ QDs - 3.8nm$ (red solid line) and $CdSe\ QDs - 4.8nm$ (orange solid line) versus the WAXTS experimental pattern (black dots).*

along the [111]-cubic direction. δz was applied to the interlayer distances, when transitions of the $k \rightarrow h$ and $h \rightarrow k$ types occur (Figure 6.12). The option of locating this strain at the h transition only was tested and excluded, since it provided too large unphysical CdSe bond distances of 2.84 Å.

The δz strain was tested on both localized (LOC) and random (RND) models, leading, in both cases, to a better agreement of the DSE simulations to the experimental data. The GoF values are given in Table 6.8 for all samples. Worth of note, the strain is always positive and size-dependent for both models (see Figure 6.12b).

The DSE analysis reveals that for the localized (random) model, upon increasing the NCs size, a progressively smaller axial Cd-Se interatomic distance at the $k \rightarrow h$ and $h \rightarrow k$ transitions is found, from 2.71 Å [3%] (2.74 Å [4%]) for the $CdSe\ QDs - 3.0nm$ down to 2.67 Å [1.6%] (2.68 Å [2%]) for the $CdSe\ QDs - 5.8nm$. The numbers in square brackets refer to the relative changes with respect to the bulk reference CdSe value of 2.63 Å.[8] To go deeply into the comprehension of this anisotropic strain, an additional test was performed, consisting in refining independently the *a* and *c* parameters of the trigonal lattice by assuming the

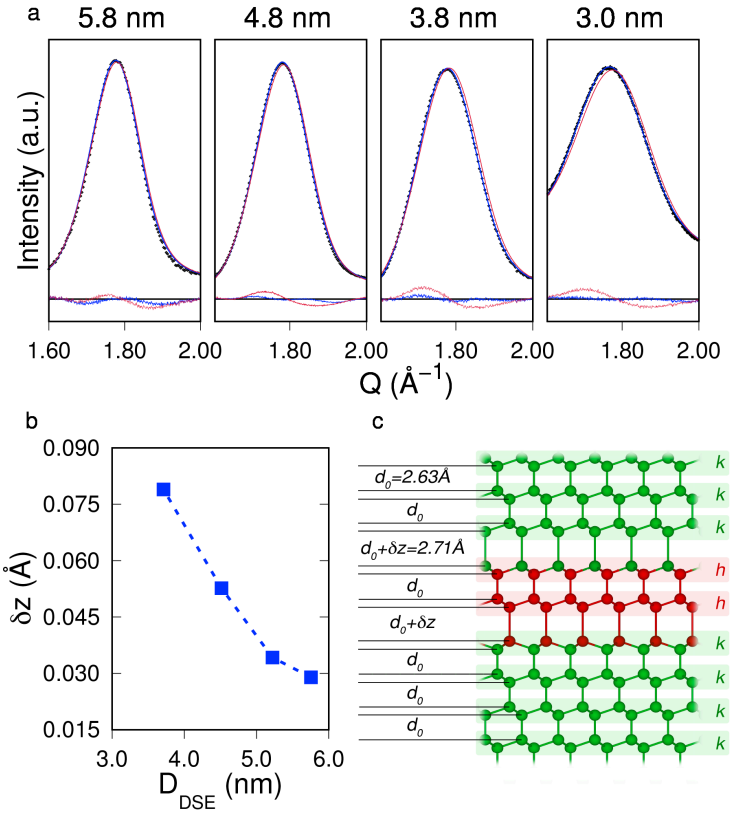

Figure 6.12. *a) Experimental 111 diffraction peak of the four samples (black dots) and best DSE fits obtained without (red difference curves) and with (blue difference curves) the use of the additional anisotropic strain of the Cd-Se bond distance along the stacking direction. b) Size-dependent anisotropic strain (δz) modelled at the $k \rightarrow h$ and $h \rightarrow k$ transitions for the localized model. c) Graphical representation of the local relaxation of the Cd-Se bond distance along the [111] cubic direction applied to the $CdSe\ QDs - 3.0nm$ (exaggerated for better rendering).*

breaking of the cubic symmetry in faulted ZB NCs. A relaxation along c of 1% was obtained, in line with a previous article published by Wu et al.[25] data in which, using EXAFS, the authors report an evident axial expansion of the c axis in WZ CdSe QDs. The GoF values are comparable to the localized models. Despite that our result matches the description of Wu, we consider the presence of an isotropic strain within the cubic system less probable than the anisotropic one, since it implies relaxation also far away from the transition planes. Therefore, despite WAXTS is not able to discriminate between a homogeneous strain or a localized one (in proximity of the planar defects), the localized strain model is here preferred. The treatment of Wu on WZ CdSe QDs also highlights the presence of a compressive strain normal to the stacking direction. In our data, this compression was not detected, and Cd-Se distances do not show significative changes of the initial bulk value.

Sample	GoF		Cd-Se distance (Å)	
	RND	LOC	$[110]$, $[111]_u$	$[111]_f$
$CdSe\ QDs - 3.0nm$	2.39	2.24	2.633	2.711
$CdSe\ QDs - 3.8nm$	2.95	2.89	2.633	2.686
$CdSe\ QDs - 4.8nm$	6.11	5.90	2.633	2.666
$CdSe\ QDs - 5.8nm$	2.68	2.70	2.632	2.662

Table 6.8. *The table includes the GoF values and the refined Cd-Se atomic distances of the best LOC model. Cd-Se interatomic distances along the [111] at the $k \rightarrow h$ and $h \rightarrow k$ transitions are labelled as $[111]_f$, while the others (at the $k \rightarrow k$ and $h \rightarrow h$ transitions along the [111] and [110]) are labelled as [110], $[111]_u$.*

Table 6.8 shows a systematic, even if small, GoF improvement of the LOC model for samples with smaller average sizes and values converging to those of the RND model for larger sizes. These results can be interpreted considering the relative values of SFE and the uSFE. As explained in Paragraph 4.1, the SFE represents the energy difference between a stable unfaulted crystal and a stable faulted system, whereas while uSFE represents the energy barrier (uSFE>>SFE) to be overcome to heal the fault (in this case the h transition). A recent study on *fcc* metals revealed that the

uSFE is nearly independent from the material composition.[26,27] In analogy with this finding, a large uSFE is expected for CdSe materials and would explain (using Eyring's equation) their faulted structural stability (at the atomic level) over years, despite the fact that they possess a very low SFE value of ca. 14mJ/m^2.[28] Since the actual uSFE is strongly dependent on the faulted plane area, we infer that the peripheral layers of smaller clusters (*ca.*5 layers for the $CdSe\ QDs - 3.0nm$) self-heal with a minimal energy contribution, explaining why the LOC model prevails on the RND one in reproducing the experimental data at smaller sizes.

Another important information extracted from the DSE analysis is shown in Figure 6.13 and refers to the size dependent SF probability that well correlates with the anisotropic strain δz.

In order to better understand the driving force of this strain, a size-dependent contribution from surface stress was considered. Inspired by what presented on PbS QDs in ref,[24,29] we correlate the average cubic lattice parameter of the four QDs samples with NCs diameter D, using Equation 6.6.

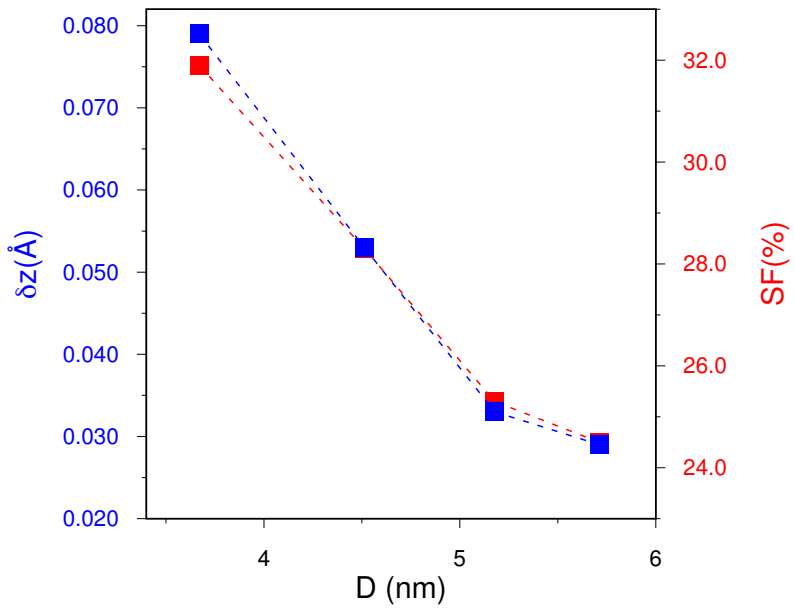

Figure 6.13. *SF% and anisotropic strain (δz) applied in the [111] cubic stacking direction, as function of the average crystal diameter D. The reduction of the SF% upon decreasing the average size and the same trend for δz suggest the incisive role of the SF in generating this strain.*

$$a_{QDs} = a_0\left(1 - \frac{\Omega}{D}\right)$$

$Eq.6.6$

Where:

a_0: bulk CdSe ZB lattice parameter [$a_0 = 6.066(3)$Å]

$\Omega = 4\gamma/3B$: depends on the surface tension γ and the bulk modulus B.

As shown in Figure 6.14, a negative surface tension γ=-4.86 eV nm^{-2} was found (for the bulk modulus of 53 GPa).[30,31] The isotropic relaxation generated from the surface tension thus corresponds only to the 0.3% of the bulk CdSe distance for the $CdSe\ QDs - 3.0nm$ sample and confirms that the high strain detected (3%, ten times larger than that calculated as surface contribution) is driven by stacking fault defectiveness.

Eventually, the LOC model produced the high-quality fits displayed in Figure 6.10 and 6.11. Additionally, the sizes of NCs agree with the size and size dispersion values derived by SAXS within $\pm 0.1\ nm$ (see Figure 6.15a). Despite the evolution of the

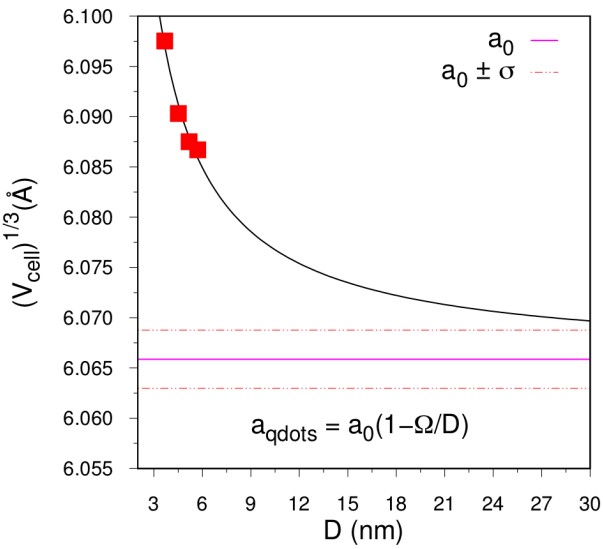

Figure 6.14. *Size dependence of the "pseudo"-cubic cell parameter calculated from the cell volume obtained refining a and c independently. The red points were fitted using a size dependent law*[7] *where Ω=-0.019(2) and a_0=6.066(3)Å (γ=-4.86 eV/nm^2 ; B=53 GPa).*[30,31]

crystal faceting upon increasing the average NCs size, the aspect ratio remains practically unchanged. By deriving the average size and size dispersion of "spherical equivalent" populations ($\langle D_{eq} \rangle$), these diameters were compared with those extracted by Jasieniak's formula.[4] All size values are given in Table 6.9.

In order to account for an additional (uniform, regardless the *hkl* indexes) 2ϑ-dependence of the peak broadening, an isotropic microstrain distribution parameter ($\varepsilon_{hkl} = (d_{hkl} - d_{0,hkl})/d_{0,hkl}$), describing the modulation of the lattice spacings, d_{hkl}, with respect to the reference value, $d_{0,hkl}$, as a probable consequence of the local strain distribution) was introduced in the reciprocal space to the final DSE model pattern, following a $\tan(\vartheta)$ dependence of the Gaussian peaks broadening[32] and optimized in the final models of faulted NCs. The best value has been identified as $\varepsilon = 0.6\%$ for all the samples, independent from the NCs size.

6.4.3 Size and Morphology by Considering SAXS and WAXTS Analysis

Figure 6.15b shows how the average crystal size estimation proposed by the TEM/UV-Vis absorption calibration by Jasieniak,[4] underestimates the size extracted by scattering techniques for NCs smaller than 5 nm.[33] This can be attributed to different factors such as:

a) The difficulty of TEM to analyse ultra-small particles, since their surfaces are not well defined;
b) The inaccurate size estimation by UV, which strongly depends on the size distribution (as shown in Table 6.1); indeed, both E_g and ε values are size-dependent and markedly non-linear.

Physically reasonable values are also found for the Isotropic Debye Waller factors B_{iso} (reported in Table 6.10). The Cd and Se values inside the core remain nearly constant, while refined values for the shell atoms are higher. This is in line with the expected higher mobility at the surface and occasional substitution of surface atoms by the organic ligands.

The esd of the refined parameters have not been provided because the refinement strategy of CdSe QDs was based on the application of restraints to morphological parameters; this case is not currently treated in the Debussy routine implemented

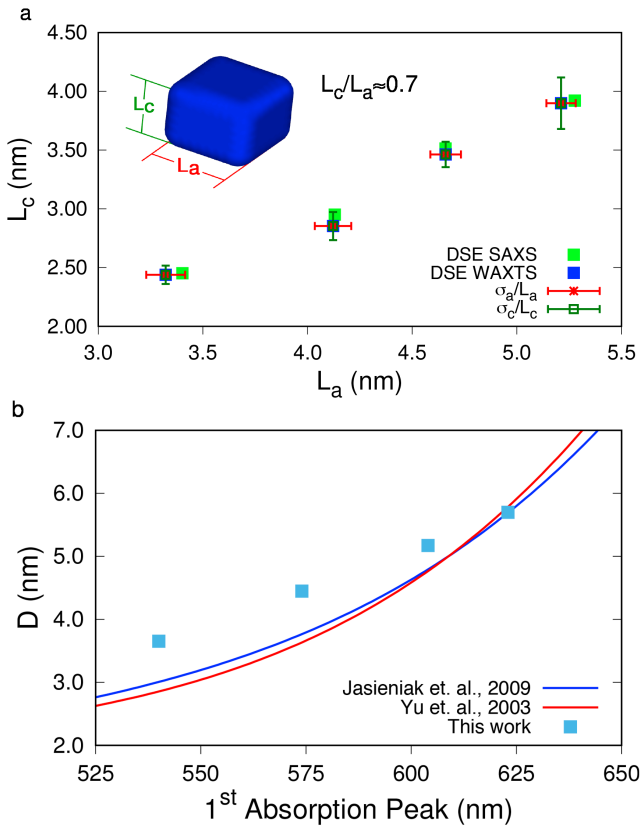

Figure 6.15. *a) average sizes of the prismatic NCs refined in the small angle region (green dots) and in the wide-angle region (blue dots) and relative size dispersion. b) Diameters of NCs from this work (blue dots) are compared with the sizing curves proposed by Jasieniak (blue solid line) and Yu (red solid line).*

for the calculation of the esd's and the available program code is not able to provide physically-sound values. Future work in this direction is planned. Moreover, the information on the parameters provided with this work is not accessible by alternative programs with or without their uncertainties. This sentence does not intend to decline their importance but contrarily to admit that a strategy to calculate them in different cases and capture their meaning within this approach is still a challenging task.

The uncertainties of SF% values are not computable since the SF parameters were not refined but optimized using a grid search; therefore, the full determination of the curvature of the hypersurface about the minimum cannot be performed. On the

Sample	$L_1 = L_2$ (nm)	σ_1/L_1	L_3 (nm)	σ_3/L_3	*AR*
$CdSe\ QDs - 3.0nm$	3.260	9.3%	2.42	9.1%	0.74
$CdSe\ QDs - 3.8nm$	4.010	6.8%	2.82	11.7%	0.69
$CdSe\ QDs - 4.8nm$	4.610	7.1%	3.420	10.6%	0.74
$CdSe\ QDs - 5.8nm$	5.16	7.0%	3.71	21.9%	0.72
Sample	$\langle D_{eq} \rangle$ (nm)	$\sigma/\langle D_{eq} \rangle$	*Deviation from Jasieniak* (nm)		
$CdSe\ QDs - 3.0nm$	3.65	6.8%	0.65		
$CdSe\ QDs - 3.8nm$	4.47	6.1%	0.67		
$CdSe\ QDs - 4.8nm$	5.17	5.9%	0.37		
$CdSe\ QDs - 5.8nm$	5.70	8.7%	0.10		

Table 6.9. *The table includes the final refined values of size and size dispersion of the four samples. All the samples are composed by cuboid NCs with an aspect ratio of ca. 0.7 nm. In green, the "spherical equivalent" sizes and size distributions to be compared with those extracted from the TEM/UV-Vis absorption calibration curve proposed by Jasieniak.*[4]

other hand, the grid search highlights the visible quality change of the fit varying the SF parameters with a step of ±0.05 during the sequence generation, meaning that the method can quantify SF with acceptable precision.

Sample	B_{iso} surface (Å^2)		B_{iso} core (Å^2)		*s.o.f.* $_{surf}$
	Cd	Se	Cd	Se	Se
$CdSe\ QDs - 3.0nm$	3.50	-	1.20	1.16	0.00
$CdSe\ QDs - 3.8nm$	1.60	2.51	1.10	1.20	0.50
$CdSe\ QDs - 4.8nm$	2.00	2.40	1.10	1.11	0.30
$CdSe\ QDs - 5.8nm$	2.00	2.47	1.14	1.10	0.27

Table 6.10. *The table reports the final refined values of thermal parameters and site occupancy factors of the four samples. In orange, the thermal parameters referred to the atoms buried into the crystal core; in blue, the ones at the surface that justify surface mobility phenomena and different chemical environment.*

Conclusions

As discussed in the Chapter 5 and here demonstrated in Paragraphs 6.1 and 6.2, conventional X-ray diffraction methods of analysis are not sufficient to characterize nanosized materials and, in particular, systems with a high density of defects, like CdSe QDs. Despite the fact that WAXTS patterns encode information about crystal structure, size, shape and defects, retrieving robust information from the high Q region (1-8 $Å^{-1}$) only may be a challenging task, since size and size distribution effects strongly correlate with those due to the presence of defects. The key point in characterizing nanosized systems, especially the one here presented, is the use of combined techniques that facilitate to discriminate size and defects contributions in the WAXTS pattern. To achieve this goal, a unified model of NCs can be used to reproduce both the low Q region of the diffraction pattern (that is insensitive to the atomic-scale structure) and the high Q region. The information about size and morphology retrieved from SAXS analysis is used as restraints to optimize the model in the high Q region, containing details about defects type and their density. This approach enabled us to unveil unpredicted features of CdSe NCs of nominally pure ZB phase. The analysis of the SAXS pattern revealed a non-isotropic prismatic morphology and a size dependent faceting. The use of this precious information made it possible to quantify the SF density and their localization; the presence of an anisotropic strain along the stacking direction (cubic [111]) was also obtained. As explained in Chapter 1, the characterization of the surface chemistry and the structural defectiveness represent the key point in understanding and improving optical properties of CdSe QDs. Since the optical properties and the band gaps strongly depend on the bond strength, detecting strain relaxation of the Cd-Se bond distance (as done here) may be of high impact to improve the optoelectronic properties and to inspire new synthetic procedures by modulating and controlling strains and defects.

Another remarkable aspect highlighted in this Chapter is the successful use of the DSE versus the simpler PDF approaches available in the literature. In this respect, we note that the analysis in the reciprocal space gives to the analyst robust and immediate "directional" information about the NCs shape (particularly when markedly anisotropic) and/or bond-distance strain on the diffraction trace owing to

the relation between crystallographic directions and diffraction peaks. Shape and bond-distance strain information are contained in the PDF as well, as PDF results from the Fourier transform of the reciprocal space diffraction pattern, but the precise interpretation of these features in PDF signal is more difficult owing to the loss of information about crystallographic directions. This aspect was the key-point for the introduction into the DSE model of the additional and anisotropic strain along the [111] direction. Moreover, compared to state-of-art treatment of faulted structures by PDF analysis, the model of stacking faults here treated by the DSE method allowed different types of faults (mainly GF and ISF, as discussed in Chapters 4 and 5), to be considered, stacked and localized within the single NC model, leading to a highly detailed characterization of SF in CdSe QDs, not to mention the possibility to perform a study using a population of NCs with different morphologies.

Last but not least, the model here developed for CdSe faulted NCs will be further used, once improved and adapted to characterize engineered nanomaterials of the II-VI (CdSe@CdSe core shells, etc.) and III-V semiconductors (GaN, InP) classes aiming at extending the comprehension of the role of defects on their optical properties.

References

(1) Chen, O.; Chen, X.; Yang, Y.; Lynch, J.; Wu, H.; Zhuang, J.; Cao, Y. C. Synthesis of Metal-Selenide Nanocrystals Using Selenium Dioxide as the Selenium Precursor. *Angew. Chem.* **2008**, *47* (45), 8638–8641.

(2) Dai, Q.; Song, Y.; Li, D.; Chen, H.; Kan, S.; Zou, B.; Wang, Y.; Deng, Y.; Hou, Y.; Yu, S.; et al. Temperature Dependence of Band Gap in CdSe Nanocrystals. *Chem. Phys. Lett.* **2007**, *439* (1–3), 65–68.

(3) Sánchez-Bajo, F.; Cumbrera, F. L. The Use of the Pseudo-Voigt Function in the Variance Method of X-Ray Line-Broadening Analysis. *J. Appl. Cryst.* **1997**, *30* (4), 427–430.

(4) Jasieniak, J.; Smith, L.; van Embden, J.; Mulvaney, P.; Califano, M. Re-Examination of the Size-Dependent Absorption Properties of CdSe Quantum Dots. *J. Phys. Chem. C* **2009**, *113* (45), 19468–19474.

(5) Brus, L. Electronic Wave Functions in Semiconductor Clusters: Experiment and Theory. *J. Phys. Chem.* **1986**, *90* (12), 2555–2560.

(6) B. E. Warren. *X-Ray Diffraction*; Dover Publications, I. N. C., Series Ed.; Dover Books in Physiscs; New York, **1990**.

(7) Cervellino, A.; Frison, R.; Bertolotti, F.; Guagliardi, A. DEBUSSY 2.0: The New Release of a Debye User System for Nanocrystalline and/or Disordered Materials. *J. Appl. Cryst.* **2015**, *48* (6), 2026–2032.

(8) O. Madelung; U. Rössler; M. Schulz. Cadmium Selenide (CdSe) Lattice Parameters, Thermal Expansion. In *II-VI and I-VII Compounds; Semimagnetic Compounds*; Springer, Heidelberg: Berlin, Germany; Vol. 41B, pp 1–4.

(9) Ustinov, A. I.; Budarina, N. M. Influence of Planar Defects on Powder Diffractograms of Fcc Metals. *Powder Diff.* **2002**, *17* (04), 270–277.

(10) Estevez-Rams, E.; Leoni, M.; Scardi, P.; Aragon-Fernandez, B.; Fuess, H. On the Powder Diffraction Pattern of Crystals with Stacking Faults. *Philos. Mag. A* **2003**, *83* (36), 4045–4057.

(11) Li, Y.; Beck, R.; Huang, T.; Choi, M. C.; Divinagracia, M. Scatterless Hybrid Metal–Single-Crystal Slit for Small-Angle X-Ray Scattering and High-Resolution X-Ray Diffraction. *J. Appl. Cryst.* **2008**, *41* (6), 1134–1139.

(12) Schwamberger, A.; De Roo, B.; Jacob, D.; Dillemans, L.; Bruegemann, L.; Seo, J. W.; Locquet, J. P. Combining SAXS and DLS for Simultaneous Measurements and Time-Resolved Monitoring of Nanoparticle Synthesis. *Nuclear Instruments and Methods in*

Physics Research Section B: Beam Interactions with Materials and Atoms **2015**, *343*, 116–122.

(13) Analysis of Small-Angle Scattering Data from Colloids and Polymer Solutions: Modeling and Least-Squares Fitting. *Advances in Colloid and Interface Science*. 70th ed. **1997**, pp 171–210.

(14) C. B. Murray; C. R. Kagan. Synthesis and Characterization of Monodisperse Nanocrystals and Close-Packed Nanocrystals Assemblies. *Annu. Rev. Mater. Sci.* **2000**, *30*, 545–610.

(15) Korsounski, V. I.; Neder, R. B.; Hradil, K.; Barglik-Chory, C.; Müller, G.; Neuefeind, J. Investigation of Nanocrystalline CdS–Glutathione Particles by Radial Distribution Function. *J. Appl. Cryst.* **2003**, *36* (6), 1389–1396.

(16) Smith, A. M.; Mohs, A. M.; Nie, S. Tuning the Optical and Electronic Properties of Colloidal Nanocrystals by Lattice Strain. *Nat. Nanotechnol.* **2009**, *4* (1), 56–63.

(17) Piveteau, L.; Ong, T.-C.; Rossini, A. J.; Emsley, L.; Copéret, C.; Kovalenko, M. V. Structure of Colloidal Quantum Dots from Dynamic Nuclear Polarization Surface Enhanced NMR Spectroscopy. *J. Am. Chem. Soc.* **2015**, *137* (43), 13964–13971.

(18) Piveteau, L.; Ong, T.-C.; Walder, B. J.; Dirin, D. N.; Moscheni, D.; Schneider, B.; Bär, J.; Protesescu, L.; Masciocchi, N.; Guagliardi, A.; et al. Resolving the Core and the Surface of CdSe Quantum Dots and Nanoplatelets Using Dynamic Nuclear Polarization Enhanced PASS–PIETA NMR Spectroscopy. *ACS Cent. Sci.* **2018**, 4, 1113-1125.

(19) Ithurria, S.; Dubertret, B. Quasi 2D Colloidal CdSe Platelets with Thicknesses Controlled at the Atomic Level. *J. Am. Chem. Soc.* **2008**, *130* (49), 16504–16505.

(20) Lim, J.; Bae, W. K.; Park, K. U.; zur Borg, L.; Zentel, R.; Lee, S.; Char, K. Controlled Synthesis of CdSe Tetrapods with High Morphological Uniformity by the Persistent Kinetic Growth and the Halide-Mediated Phase Transformation. *Chem. Mater.* **2013**, *25* (8), 1443–1449.

(21) Bertolotti, F.; Moscheni, D.; Migliori, A.; Zacchini, S.; Cervellino, A.; Guagliardi, A.; Masciocchi, N. A Total Scattering Debye Function Analysis Study of Faulted Pt Nanocrystals Embedded in a Porous Matrix. *Acta Crystallogr. A* **2016**, *72*, 632–644.

(22) J. A. Nelder; R. Mead. A Simplex Method for Function Minimization. *Comput. J.* **1965**, *27*, 308–313.

(23) Casavola, M.; van Huis, M. A.; Bals, S.; Lambert, K.; Hens, Z.; Vanmaekelbergh, D. Anisotropic Cation Exchange in PbSe/CdSe Core/Shell Nanocrystals of Different Geometry. *Chem. Mater.* **2012**, *24* (2), 294–302.

(24) Bertolotti, F.; Dirin, D. N.; Ibáñez, M.; Krumeich, F.; Cervellino, A.; Frison, R.; Voznyy,

O.; Sargent, E. H.; Kovalenko, M. V.; Guagliardi, A.; et al. Crystal Symmetry Breaking and Vacancies in Colloidal Lead Chalcogenide Quantum Dots. *Nat. Mater.* **2016**, *15* (9), 987–994.

(25) Wu, P.-J.; Stetsko, Y. P.; Tsuei, K.-D.; Dronyak, R.; Liang, K. S. Size Dependence of Tetrahedral Bond Lengths in CdSe Nanocrystals. *Appl. Phys. Lett.* **2007**, *90* (16), 161911.

(26) Jo, M.; Koo, Y. M.; Lee, B.-J.; Johansson, B.; Vitos, L.; Kwon, S. K. Theory for Plasticity of Face-Centered Cubic Metals. *Proc. Natl. Acad. Sci. U S A* **2014**, *111* (18), 6560–6565.

(27) Van Swygenhoven, H.; Derlet, P. M.; Frøseth, A. G. Stacking Fault Energies and Slip in Nanocrystalline Metals. *Nat. Mater.* **2004**, *3* (6), 399–403.

(28) Takeuchi, S.; Suzuki, K. Stacking Fault Energies of Tetrahedrally Coordinated Crystals. *Phys. Stutus Solidi C* **1999**, *171* (1), 99–103.

(29) Cervellino, A.; Frison, R.; Cernuto, G.; Guagliardi, A.; Masciocchi, N. Lattice Parameters and Site Occupancy Factors of Magnetite–Maghemite Core–Shell Nanoparticles. A Critical Study. *J. Appl. Cryst.* **2014**, *47* (5), 1755–1761.

(30) Alivisatos, A. P.; Harris, T. D.; Brus, L. E.; Jayaraman, A. Resonance Raman Scattering and Optical Absorption Studies of CdSe Microclusters at High Pressure. *J. Phys. Chem. C* **1988**, *89* (10), 5979–5982.

(31) Yeh, C.-Y.; Lu, Z. W.; Froyen, S.; Zunger, A. Zinc-Blende–Wurtzite Polytypism in Semiconductors. *Phys. Rev. B* **1992**, *46* (16), 10086–10097.

(32) Leineweber, A. Understanding Anisotropic Microstrain Broadening in Rietveld Refinement. *Z Kristallogr.* **2011**, *226* (12), 905–923.

(33) Maes, J.; Castro, N.; De Nolf, K.; Walravens, W.; Abécassis, B.; Hens, Z. Size and Concentration Determination of Colloidal Nanocrystals by Small-Angle X-Ray Scattering. *Chem. Mater.* **2018**, *30* (12), 3952–3962.

7

Stacking Faults Modeling in Elemental Solids: An Example for an Alternative Strategy

Despite advanced experimental and data analysis methods for a complete microstructural characterization of metal chalcogenide nanocrystals have enabled us to extract outstanding results on CdSe based samples, the use of this approach for the characterization of planar defects in larger NPs is extremely time consuming. Indeed, the need to build, and analyze, a much larger number of faulted nanocrystals where the number of independent sequences exponentially grows with size, makes the Debye Scattering Equation-based method previously describe highly inappropriate. However, materials possessing relatively high Stacking Fault Energies are characterized by a low SF density and, thus, only a limited number of planar defects, within the same nanocrystal, is statistically possible. This is particularly true for metals showing SFE's higher than 100 mJ m^{-2}, a value 6 to 10 times higher than for CdSe nanocrystals. Accordingly, we developed an alternative method for the computation of sampled interatomic distance databases of faulted metals, and considerably reduced the number of the to-be-generated sequences, shifting from a random sequences generation approach to a controlled one.

This method was applied in the study of platinum nanocrystals embedded in a mesoporous silica matrix, a particularly complex system due to the simultaneous presence of a practically amorphous material and of a multimodal population of nanocrystalline Pt. In this case, robust complementary information on size and shape of the nanocrystalline portion from other techniques (SAXS, UV-Abs) was not available, or of limited usage (TEM, HRTEM).

In this Chapter, several aspects and approximations in the sequence generation protocol will be discussed and results on experimentally measured WAXTS data from tailored syntheses of Pt nanocrystals performed at variable temperatures.

This study is part of a larger research project entitled "Metal-Organic based Nanoparticles Arrays with Large Induced Shape Anisotropy (MONALISA)", co-funded by Fondazione CARIPLO (Project No. 20110289), shared by University of Insubria, the Italian CNR and the University of Bologna. Here, the mesosized channels of the SiO_2 matrix, organized in parallel bundles, were taken as 1D nano-reactors. In such a way, we aimed at growing metallic nanoparticles with a large shape anisotropy, with a potential increase of the properties linked to their 2D ordering, supplemented by a possible collective effect.[1,2] However, despite the geometrical constraints imposed by the silica mesopores, metallic nanoparticles can also form at the surface of the porous matrix. In the absence of this templating effect, more isotropic NPs can be formed, likely (also) with sizes well above the diameter of the pervious silica channels. Under this hypothesis, and on the basis of the direct analysis of our WAXTS data, the need of studying much larger (than CdSe) nanoparticles became soon evident. However, since the calculation of the SID of non-periodic (*i.e.* defective or faulted) NCs severely increases with its diameter D (up to D^6 for truly amorphous NCs), the generation of databases suitable for our WAXTS analysis, with two independent growth directions and using a random approach, turns into several days, or even weeks, of CPU time on our available UNIX servers.[3] For this reason, a strategy for reducing the calculation time was sought and is hereafter proposed.

7.1 An Alternative Approach to SF Treatment in DSE Analysis

As anticipated in Chapter 3 and in the preceding paragraph, the calculation of the SID of defective NPs more-than-linearly increases with the particle diameter. Why this occurs, it is easy to understand: particularly in the database calculation step, but, to some extent, also in the Debussy refinement), these computations strictly depend on the number of atoms (proportional di D^3) present in the nanoparticles. For example, in the model construction of CdSe, four *different* chemical species

were introduced, Cd and Se, each split for “core” and “surface” location, thus enabling the use of separate structural parameters (say, *s.o.f.*s and Debye Waller factors) to address their different stereochemical environments. This differentiation, however, does not affect the length of the SID database construction; indeed, partitioning of the entire set of interatomic distances of an ideal elemental NP into a summation of the sets of interatomic distances for each couple of atoms does not change the overall number of distances to be computed. However, the occurrence of elemental NPs (described by a single atomic species) slightly reduces the CPU time in the DSE-refinement step, as the number of refined parameters is reduced. Such a small CPU-time, is, anyway, barely significant, as the rate determining step of the whole analysis still resides within the construction of the entire SID database. This said, we found that the clue to significantly reducing the CPU time is limiting the number of sequences required in order to obtain, after merging, a hybrid configuration representative of a real sample. To better illustrate our approach, the following section presents an alternative strategy for SID database generation for the investigation of planar defects in large(r) metallic nanoparticles with low SF probabilities.

7.1.1 A Controlled Strategy to SID Database Generation

When the probability of SF is as low as a few percent, as typically found in several metallic NPs,[4–7] a new strategy for sequence generation can be used, which successfully replaces the random generation mode with a controlled one. Assuming that only one fault is present per NC at most, a pre-defined SF probability can be obtained weighing faulted (*f*) and unfaulted (*u*) sequences. Despite this assumption can appear severe for real samples, the probability to find a NC with more than one planar defect becomes significant only in large-enough NCs, that is with more than 50 layers (*ca.* 12.5 nm) for *fcc* platinum NCs with a SF probability of 2%, and with more than 100 layers (*ca.* 25 nm) for a SF probability of 1%. Thus, for smaller NCs, this assumption becomes even more valid. Once, within this assumption, the pseudo-multiplicities of the interatomic distances of all possible sequences are obtained, a hybrid set can be derived by combining them linearly and producing a

set of SID representative of the "average" faulted structure. A further advantage intrinsic in this approach is the reduction of the number of independent sequences, if symmetry considerations are included. The following paragraphs explicit in algebraic form our new overall protocol of SID construction.

Given a NP with N layers stacked along the [111] direction of a cubic structure, it is possible to allocate a planar defect in position m in a region defined between 3 and N (in a general case, a planar defect needs at least 4 layers to be identified). With a simple C_2 rotation operation, passing through the center of the crystal and normal to [111], it is possible to obtain the same crystal where the defect is located at the $N - m + 1$ position. Therefore, the number of sequences to be generated decreases from $N - 3$ to n, a number significantly lower than those used in Chapter 6 for CdSe (typically, 50 to 100 sequences).

$$n = \frac{N - 6 + t}{2} + 1 \qquad Eq.\,7.1$$

where:

N : number of layers

$t = mod(N, 2)$

It goes without saying that, within this treatment, NPs with $N < 6$ *must* be considered unfaulted. While this may not be necessarily true, we are here considering very tiny nanoparticles (with [111] column length near 1 nm) which contribute very little to the overall scattering. Equation 7.1 reveals how in the largest particles examined in this study ($N = 50$) the number of sequences is only 23 per defect type (*e.g.*: ISF). Of higher relevance, different databases, each representing a different SF probability, do not need to be (re)-calculated by generating new sets of nanoparticles. Indeed, they can be easily obtained by linearly combining the already-generated sequences (diluting, using unfaulted configurations, the contribution of faulted ones).

In the present case, a statistically robust information on (TEM-based) particle size distribution, on which the preferential "geometrical" location of the defects within the NP can be effectively tested by analyzing the experimental WAXTS pattern, was

absent. Therefore, not being possible to derive such information from our intrinsically complex scattering data, the (reasonable) choice of *equally probable* configurations was made. This approximation is apparently in disagreement with what discussed in a previous Chapter; as presented therein, the SFE differently acts in differently-sized sections of finite (non-cylindrical) NPs. As SFEs need to be multiplied by the extension of the displaced atomic layer), SF are (thermodynamically) more favored for peripheral layers with smaller sections (particularly for large SFEs). Additionally, and at variance with the previously discussed CdSe QDs, our nanocrystalline Pt samples have been subjected to high-temperature annealing for prolonged time, possibly overcoming the activation energy (uSFE) necessary for a faulted NC to heal some "wounds". This aspect is corroborated with the results of this study, later discussed, that show a moderate decrease of the SF probability upon the thermal treatment.

Using unlocalized faults and the validity of equiprobability assumption, and in order to compute SID databases with a well-defined SF probability, the pseudo-multiplicities of the n faulted sequences have been weighed with those of a precise number of unfaulted NCs, using the approach described below.

For sake of simplicity, we considered that each fault type (TF or ISF) represents a *single* defect, a feature attributed to *one* layer only, even if the deformation fault is the result (of the mismatch) of two consecutive layers in hexagonal transitions. This simplification does not change the use and the interpretation of the stacking fault probability term, but simply enables its use in a general way, *i.e.* by addressing the occurrence of a planar defect, independently of its nature.

Let the ISF or (TF) probability within an ordered *fcc* elemental crystal along the [111] direction be defined by p. Since this probability can be modulated (*i.e. lowered*) in a SID database by combining faulted with unfaulted nanocrystals, *when only faulted NPs are merged* its maximum value, *i.e.* p, is obtained. Additionally, the assumption of introducing a single defect only per NP, at a given p, intrinsically sets a limit to the its maximum size, D_{max}. For example, if p_{ISF} is the probability of a deformation fault, then:

$$D_{max} = \frac{d_{111}}{p_{ISF}} \qquad Eq.7.2$$

where d_{111} is the interlayer distance along the [111] direction (0.24 nm for elemental platinum). Thus, values of p_{ISF} near 1% provide an upper limit of D_{max} = *ca.* 24 nm. [*Worth of note, for CdSe ZB QDs, typically possessing p values in the 0.2-0.3 range[8,9] and an interlayer distance of 0.34 nm[10], the only well-represented particles would be those with d < 2.0 nm, making this approach wholly unsuitable to ultra-small, highly defective NPs*].

In the following, a set of faulted (F: the number of faulted NPs) and unfaulted (U: the number of unfaulted NPs) nanoparticles, with N layers each, will be considered. Thus, independently of their nature, they are all equally sized and contain the same quantity of Pt atoms. According to its definition, p_{ISF} can be taken as the ratio between faulted layers and the total number of layers (N_{tot}), as in Equation 7.3.

$$p_{ISF} = \frac{N_f}{N_{tot}} = \frac{N_f}{N_f + N_u}$$

$Eq.\,7.3$

where:

N_f : number of faulted layers

N_{tot} : total number of layers

N_u : number of unfaulted layers

Since unfaulted layers are also present in faulted structures, the total number of layers unaffected by faulting, N_u, is given by the sum of the N layers of unfaulted NPs and the number of unfaulted layers in faulted ones ($N_u = N_{u_u} + N_{u_f}$). Therefore, rearranging Equation 7.3 it is possible to obtain Equation 7.4.

$$N_f = p_{ISF} N_{u_u} + p_{ISF} N_{u_f} + p_{ISF} N_f$$

$Eq.\,7.4$

where:

N_{u_u} : number of unfaulted layers in unfaulted NCs

N_{u_f} : number of unfaulted layers in faulted NCs

N_f : number of faulted layers in faulted NCs

After dividing each term per N, Equation 7.4 can be rewritten into Equation 7.5.

$$\frac{N_f}{N} = \frac{p_{ISF} N_{u_u} + p_{ISF} N_{u_f} + p_{ISF} N_f}{N}$$

$Eq.7.5$

Since: *i)* the number of unfaulted layers derived by the set of faulted NPs is N_{u_f}, with $N_{u_f} = F(N-1)$; and *ii)* the number of unfaulted layers derived by the set of unfaulted NPs is $N_{u_{u'}}$ with $N_{u_u} = UN$, Equation 7.5 can be rearranged into Equation 7.6.

$$\frac{N_f}{N} = p_{ISF} U + \frac{F(N-1)}{N} + p_{ISF} \frac{N_f}{N}$$

$Eq.7.6$

As the number of defective NPs is equal to the total number of stacking faults ($N_f = F$), from Equation 7.6 one derives that:

$$U = \frac{N_f}{p_{ISF} N} (1 - p_{ISF} N)$$

$Eq.7.7$

Considering that at least 3 layers on each side of the NP are necessary to define the presence of a SF, Equation 7.7 is finally transformed into Equation 7.8, which provided U, *i.e.* the number of unfaulted NPs to be merged with the faulted ones.

$$U = \frac{(N-6)}{p_{ISF} N} (1 - p_{ISF} N)$$

$Eq.7.8$

Using Equation 7.8, a software program merging all the possible faulted configurations for a defined p and size N, was written, and following Equation 7.9, provided the sampled interatomic distances dataset for each p and N values.

$$SID_m = \frac{\sum_{i=1}^{n_f} SID_i + U(SID_u)}{U + F}$$

$Eq.\,7.9$

where:

SID_m : SID merged and representative of the SF% p

n_f : number of faulted configurations

Once all the SID databases are obtained, the DebUsSy program has been used as presented in a following paragraph.

7.2 Experimental Section

7.2.1 Synthesis, Microscopy and Synchrotron X-ray Data Collection.

The synthesis of the silica-platinum nanocomposites prepared for the MONALISA project were performed at the University of Insubria and University of Bologna. Mesoporous silica of the MCM-41 type was prepared according to the literature (Zukalsa et al. 2007)[11] using simple aqueous or hydro-alcoholic solutions. These materials, prepared as fluffy powders, were characterized by BET porosimetry and conventional powder diffraction analysis. These analyses (gathered in Figure 7.1) provided an average size of the pores of 3.7 ± 0.2 nm (BET), set in parallel bundles with a periodicity of ca. 4.2 nm (XRPD). The small difference between these values is in agreement with the relatively this size of the silica walls, separating the, so far empty, channels.

After testing their successful preparation, the silica powders were impregnated for 12 h with a highly concentrated acetone solution of high nuclearity platinum carbonyl clusters of the Chini type[12], namely $[NBu_4]_2[Pt_{12}(CO)_{24}]$. The solvent was removed under mild vacuum and the resulting solids were heated in order to remove the carbonylic fraction from the precursors and to promote their aggregation into Pt nanoparticles with high shape anisotropy (Figure 7.2).

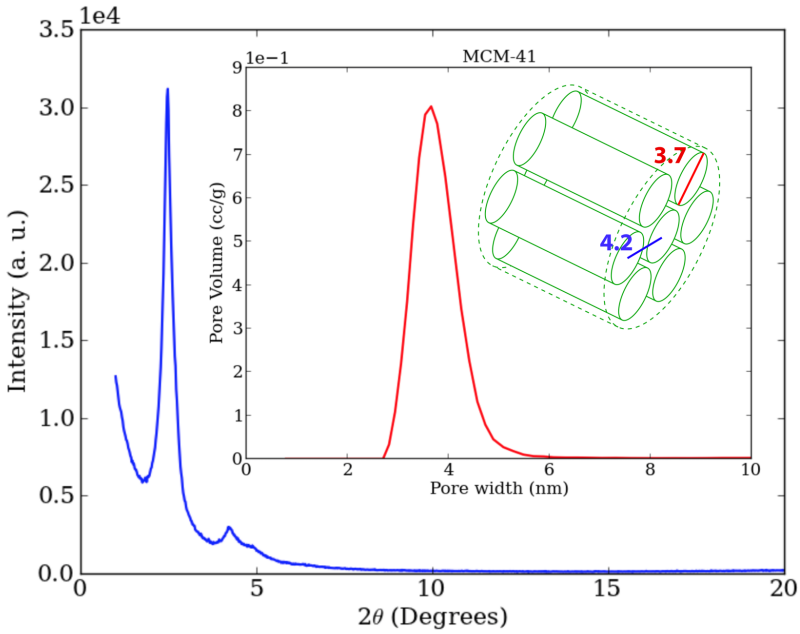

Figure 7.1. *The solid blue line represents the experimental XRPD pattern of the mesoporous silica MCM-41 (data collected in the lab with a Bruker D8 Advance diffractometer). Three peaks can be easily distinguished, attributed to the 10, 11 and 20 reflections of a planar hexagonal lattice with a = 4.2 nm. The solid red line represents the pore width distribution of the SiO_2 estimated via BET porosimetry.*

In order to monitor the possible differential crystal growth due to distinct thermal treatments, three different annealing conditions (8h) were used: 423 K, 473 K and 523 K. From here on, the three samples grown under different temperature conditions will be labelled with $Pt@SiO_2 - 423K$, $Pt@SiO_2 - 473K$ and $Pt@SiO_2 - 523K$.

Thanks to the high contrast between silica and platinum-rich materials, TEM images, collected the IMM Institute of the Italian CNR in Bologna by Dr. A. Migliori, showed, in all samples, the presence of both spherical and elongated metal NPs (Figure 7.3). However, these TEM images were devoid of any type of structural information and, most importantly, no statistically robust information about size, size-distribution and mass fraction of the two different populations (labelled hereafter as “small” and “large” ones) could be obtained, also because the silica matrix limits the attainable

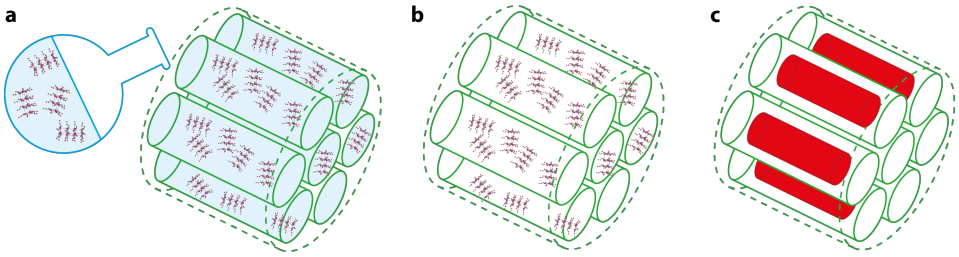

Figure 7.2. *The three steps of Platinum NP synthesis. The mesoporous silica MCM-41 was impregnated with the acetone solution of Pt precursor (a). After the impregnation, the solvent was removed under mild vacuum, in order to eliminate the solvent and to deposit the Pt precursors within the amorphous matrix before the thermal treatment and to avoid undesired violent boiling phenomena that may potentially expel the metallic NPs from the silica matrix (b). The thermal treatment removes the carbonyl component of the precursor and favors the aggregation and growth of anisotropic NPs inside the channels (c).*

spatial resolution in TEM analyses.

The three thermally-treated powdered nanocomposites and the pristine silica matrix were measured by synchrotron X-ray diffraction methods at the material science beamline of the SLS-PSI facility, using the protocol described in Chapter 3.

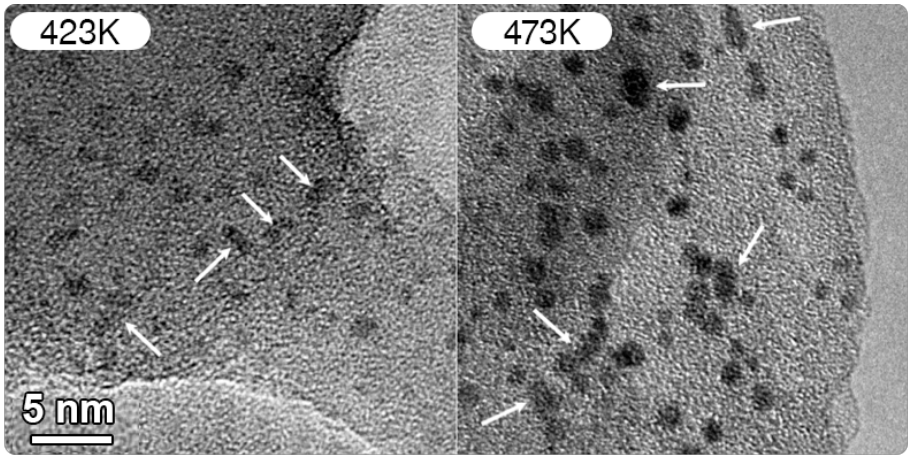

Figure 7.3. *TEM pictures of* $Pt@SiO_2 - 423K$ *and* $Pt@SiO_2 - 473K$*. Both pictures suggest the presence of elongated, or 1D-aggregated, particles inside the amorphous matrix (shown by arrows). The low definition of the pictures is a consequence of the attenuation of the beam caused by the silica matrix.*

Thanks to the high scattering power of platinum nanoparticles, thin capillaries (with a bore of 0.3 mm only and a nominal wall thickness of 0.01 mm) of G50 glass were used as sample holders. The beam energy used was set to $20\ keV$ (0.62049 Å) and data were collected in the entire 5-120° (2ϑ) range (see Figure 7.4). To properly account for the silica matrix contribution in our DSE analysis, the scattering trace of the pristine, untreated MCM-41 silica was added to the signal modeled by the DebUsSy program.[13,14] The data analyses of the platinum NPs were then performed directly on the nanocomposite WAXTS patterns, without subtracting a (suitably scaled) amorphous silica component.

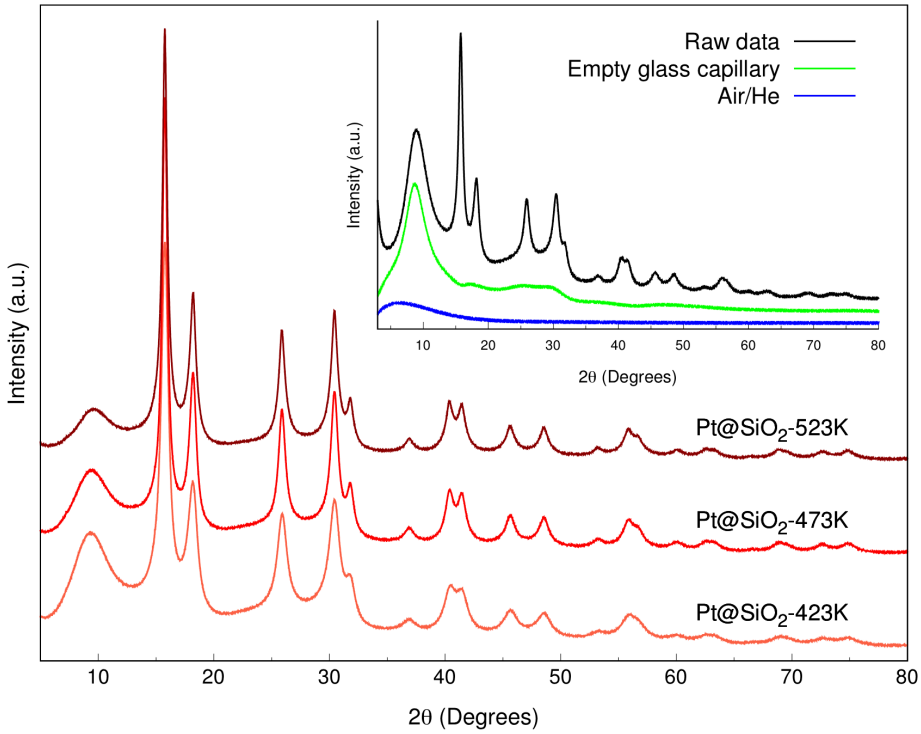

Figure 7.4. *"Reduced" experimental WAXTS patterns of the three silica/Pt nanocomposites prepared with the different thermal treatments described in the text. The peak separation in these plots, easily attributed to their different widths and shapes, makes it possible to appreciate the differential growth of the nanoparticles: the higher the temperature, the larger the NPs. In the inset, the raw signals of the* $Pt@SiO_2 - 423K$ *sample, of the capillary and of the sample environment contributions, necessary for the data reduction, are shown.*

7.2.2 The Need of a Tailored Data Analysis Protocol for the $Pt@SiO_2$ Nanocomposites

As described in Paragraph 7.1, the characterization of faulted elemental nanoparticles is not straightforward, and requires the sequential introduction of models of increasing complexity to fully account for evidences of mismatch between the observed and calculated patterns. After several test performed on simple(r) models, the final one used to fully match the experimental WAXTS patterns of these samples included:

1) The definition of multiple (isotropic or anisotropic – in this case, *cylindrical*) populations;
2) The need of introducing an additional contribution to scattering, modeled by a Chebyshev polynomial, and accounting for the presence of a further (unknown) amorphous component;

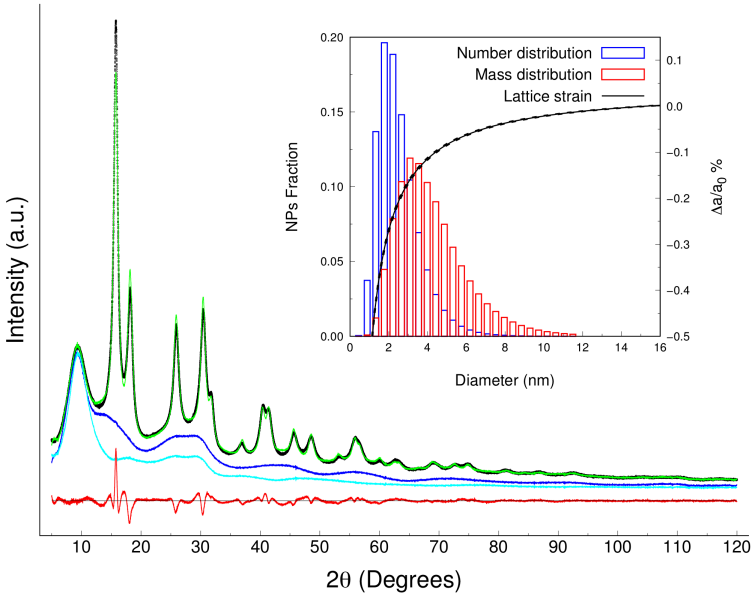

Figure 7.5. *DSE simulation of a monovariate population of faulted spherical NPs. The presence of an excess of intensity at the 200 peak and the additional evident mismatch of the 111 peak suggested us to introduce anisotropic NPs shapes, elongated along the [111] direction (possibly driven by the stacking sequence of triangular Pt_3 units within the Chini type precursor).*

3) A size dependent law for the cubic cell parameter of spherical NPs, known to vary with size, which becomes particularly relevant for polydisperse systems;
4) The optimization of the ISF probability term, p_{ISF}.

Starting from simulations grounded on SID databases calculated for faulted spherical Pt NCs *only* and observing a clear misfit in the 200 and 111 peaks (see Figure 7.5), in line with TEM observations and with the goal of the Pt NPs syntheses, we initially resorted to the introduction of an additional population of morphologically anisotropic metal NPs.

In this case, since the shape anisotropy is likely directed by the templating agent, the bivariate databases do not require equal extensions in two normal growth directions (as normally done for truly bivariate, and polydisperse, populations), but they can be limited, in the cylindrical approximation, to base values equal, or similar, to the diameter of the channels of the mesoporous silica.

Despite the introduction of the two populations, this fit required an additional, and very wavy, background component, modeled by a Chebyshev polynomial with 30 coefficients. Whether this component bears any significant value, and is physically interpretable, a d-PDF (differential PDF) analysis[15] was performed on the different spectral components, using PDFgetX3 program.[16] Accordingly, the sample, the total background, the MCM-41 silica matrix traces and the additional amorphous contribution, described phenomenologically by a polynomial approximation function (shown in Figure 7.6a) were converted into PDF signals (shown in Figure 7.6b). These calculations are mathematically legitimate as the Fourier transform integral is a linear operator, transparent to adding and scaling the different components.

Taking advantage from the separation in the reciprocal space of these four signals, we interpreted each d-PDF curve by correlating their peak positions with the (set of) interatomic distances present in the different components. The low-*r* peak (falling near 1.6 Å), present in the first three traces, is easily assigned to the Si-O distances of the silica amorphous matrix, whereas the intense peak at 2.7 Å (absent in the silica component) well matches the typical intermetallic distance found in bulk Pt and in the Pt precursors as well. The clear presence of this 2.7 Å peak in the PDF calculated from the phenomenologically-derived trace of an additional amorphous

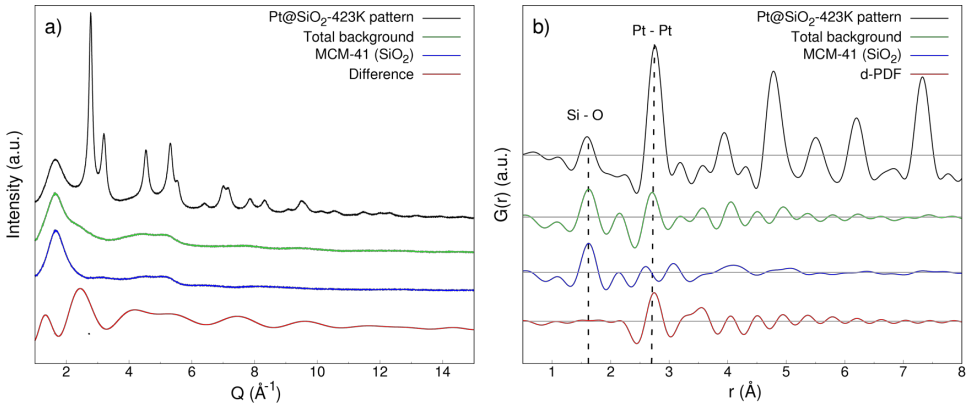

Figure 7.6. *WAXTS scattering patterns in reciprocal space (a) and its sin-Fourier transformed PDFs (b) (423K sample). The black lines represent the experimental traces of the entire sample. From the PDF curves, two low-r predominant peaks can be highlighted (corresponding to the Si – O distance of the silica matrix and to the Pt – Pt one of the nanocrystalline fraction). The green lines represent the total background calculated during the DSE refinement. The d-PDF trace contains the same two peaks, highlighting the presence in the amorphous portion of both the metallic and silica components. The solid line in panel a is the experimental trace measured on a pure silica matrix. As expected, its analysis in real space confirms the presence of the Si-O peak at 1.6 Å and the absence of the Pt component. The red line in panel a is the calculated Chebyshev polynomial (rescaled for a better graphical representation). Its d-PDF on the right shows a clear peak at 2.7 Å, revealing the presence of an additional Pt fraction, attributable to the incomplete decomposition of the Pt precursor.*

component (see red curves in Figure 7a,b) can then be attributed to the presence of sub-nanometer Pt clusters, apparently trapped in the smallest pores of the amorphous silica. This hypothesis is further corroborated by the fact that all the three samples clearly manifest the occurrence of this fraction and a polynomial "correction" with the same shape and structure is needed for obtaining a satisfactory match.

As explained in Chapter 4, the reduced size of the NPs under study can produce surface strain effects that differently affect the cell parameters of the NCs within the same population. In this work this strain was modeled, for the isotropic (spherical) fraction, by a size dependent law (*vide infra*); at variance, for the anisotropic population, since more complex (and unknown) strain effects may be at

work, a simplified model with a representative average cell parameter was used for all nanoparticles. Equation 7.10[13] shows the functional dependence of the strain model implemented in the DebUsSy suite for the size-dependent law for the cubic cell parameter a_k of spherical NCs, where factorization into two distinct terms enables the evaluation of two different (possibly countercorrelated) physico-chemical effects.

$$a_k = (1 + \sigma_1)\left(1 - \frac{\sigma_2}{D + \sigma_2}\right)$$

$Eq.\,7.10$

Indeed, the two refinable parameters, σ_1 and σ_2, can be easily interpreted by studying the limits of the function a_k at $D \to 0$ and $D \to \infty$, hereafter reported:

$$\lim_{D\to\infty} a_k = (1 + \sigma_1)$$

$Eq.\,7.11$

$$\lim_{D\to 0} a_k = 0 \text{ if } \sigma_2 \neq 0$$

$Eq.\,7.12$

Shortly, σ_1 represents the deviation from the reference cell parameter encoded in the database in correctly reproducing the cell parameter of the bulk structure. This acts only as an overall scaling factor, *e.g.* for experimental artifacts or differential temperature conditions. At variance, σ_2 plays the most important role since its sign determines the compressive ($\sigma_2 > 0$) or expansive ($\sigma_2 < 0$) nature of the strain of the NPs upon reducing the particle size since:

$$\frac{\partial}{\partial D} a_k = \frac{\sigma_2(\sigma_1 + 1)}{(D + \sigma_2)^2}$$

$Eq.\,7.13$

or, neglecting the small difference between D and $D + \sigma_2$:

$$\frac{\partial}{\partial D} a_k = \frac{\sigma_2(\sigma_1 + 1)}{D^2}$$

$Eq.\,7.14$

Typically, metal NPs contract by lowering their sizes in order to saturate their surface dangling bonds or in other terms, by surface tension effects;[17–19] on the contrary, in binary systems (oxides, sulfides, etc.), the presence of ligands or of hydrogen atoms saturating surface sites, typically induces a slight expansion.[20]

The DSE analysis confirms that, upon lowering the crystal size, platinum NPs contract (numerical results are synoptically collected in next paragraph, dedicated to the comparative analyses of the three samples – see Table 7.1).

Worth of note, the SF probability cannot be automatically minimized by the DebUsSy suite within an iterative algorithm; a sampling strategy which actively uses SID databased generated with different SF probabilities was therefore used. This strategy is somewhat similar to that presented for the CdSe samples, where the minimization of the goodness of fit parameter was achieved upon varying the β and δ coefficients within restricted, but physical meaningful, numerical boundaries. Several parallel refinements, each with a different ISF probability, were performed with a 0.25% step, aiming at identifying the best agreement between the simulated trace and the experimental data.

As later witnessed (see Table 7.1), we here anticipate that the SF probabilities of the different samples fell in the 1.5 - 2.0 % range, with a minimal dependence at different annealing conditions. As we have cannot distinguish different SF probability values in spherical and cylindrical NCs, identical values were assigned to the two populations. This choice is further motivating by the following analysis.

Indeed, we found that, beyond issues related to the exploration of the parameter hyperspace and convergence efficiency, attributing the entire SF percentage to one population (and not to the other) makes the initial approximation of having only one fault per nanoparticle unsustainable. This is clearly exemplified by the $Pt@SiO_2 - 423K$ case, which provides a “best” fit with a 2.0% SF probability. If, in an ideal example, a 50:50 (weight percent) of NPs from the isotropic and cylindrical population was present, attributing the entire SF percentage to one class only, would indeed raise the effective SF probability value to 4%, limiting a maximum size to 25 (and not to 50) layers (i.e. to 6, and not 12 nm). The consequence of this approach would make many, if not most, of the NPs (those larger than this limit) unsuitable for the set approximation.

7.2.3 Comparative Structural and Microstructural Analysis

This paragraph presents in a synoptic manner the results obtained from the structural and microstructural characterization of three Pt@SiO_2 samples, prepared from the same original batch, and annealed in different conditions to probe their behavior under different thermal stimuli. With reference to the parameters introduced in Paragraph 7.2.2 and quoting numerical values from unfaulted NPs as starting point, graphical outputs are shown in Figures 7.7, 7.8 and 7.9, while numerical results are listed in Table 7.1.

Figure 7.7 shows, for the $Pt@SiO_2 - 423K$ sample, the co-presence of the two populations and their contribution to the total pattern (see Panel a). Therein, panels b and c portray the two populations used for the best fit. The confined size of cylindrical NCs in the basal plane, perpendicular to the [111] direction, produces significantly broader traces that strongly contribute to the peak tails. This contribution is very similar to the broadening effect generated by the presence of planar defects and is magnified, in case of unfaulted models, by decreasing the effective spherical fraction weight percentage. This can be easily observed by comparing the pertinent size values collected in Table 7.1 for the faulted/unfaulted models, where the latter are systematically smaller. Thus, correctly treating the SF model significantly influences the determination of the average crystal size.

The analysis of the parameter evolution in parallel refinements also indicated that the weight percentage and the average size of the spherical fraction are heavily correlated, and that the size underestimation in the faulted model of $Pt@SiO_2 - 523K$ (see last column un Table 7.1) can be attributed to such effect.

Analyzing the average crystal sizes of the two distinct populations suggests that, for all three samples: *i)* the spherical crystals were grown outside the templating matrix; *ii)* the cylindrical fraction, the basal crystal sizes of which ($\langle D_{ab} \rangle_{M,cyl}$) perfectly match the size of pores of the nanoreactors, is likely grown inside the silica channels.

The comparative analysis shows that the higher temperature treatment favors the formation of larger spherical crystalline domains (Figure 7.8.a). For anisotropic crystals, one can appreciate the preferential crystal growth along the **c** axis (with a large distribution of lengths) with the **ab** bases of more or less constant size (see Figure 7.8.b).

Sample	$Pt@SiO_2 - 423K$	$Pt@SiO_2 - 473K$	$Pt@SiO_2 - 523K$
		Unfaulted model	
GoF	3.41	3.05	3.06
$\langle a_k \rangle_{sph}$(nm)	0.3916(3)	0.3921 (4)	0.3921 (1)
$\langle a_k \rangle_{cyl}$(nm)	0.3919 (-)	0.3920 (-)	0.3919 (-)
$\langle D \rangle_{M,sph}, \sigma_{M,sph}$ (nm)	5.29 (2), 1.5 (1)	7.82 (2), 2.5 (1)	9.33 (2), 3.22 (9)
$\langle D_{ab} \rangle_{M,cyl}, \sigma_{ab,M,cyl}$ (nm)	1.5 (1), 0.6 (4)	2.1 (3), 1.1 (4)	2.2 (3), 1.1 (3)
$\langle L_c \rangle_{M,sph}, \sigma_{c,M,cyl}$ (nm)	5.70 (2), 3.08 (5)	6.99 (1), 2.41 (8)	6.70 (1), 2.94 (6)
$\langle L_c \rangle_{M,cyl} / \langle D_{ab} \rangle_{M,cyl}$	3.75	3.34	3.06
$\%w_{sph}$	39.1	32.0	27.4
		Faulted Model	
GoF	2.76	2.62	2.57
$\langle a_k \rangle_{sph}$(nm)	0.3918 (2)	0.3919 (1)	0.39195 (7)
$\langle a_k \rangle_{cyl}$(nm)†	0.3919 (-)	0.3920 (-)	0.3919 (-)
p_{ISF}	2.0	1.5	1.5
$\langle D \rangle_{M,sph}, \sigma_{M,sph}$ (nm)	5.79 (2), 1.5 (1)	8.08 (2), 2.0 (1)	9.03 (2), 3.56 (7)
$\langle D_{ab} \rangle_{M,cyl}, \sigma_{ab,M,cyl}$ (nm)	1.7 (1), 0.6 (3)	2.2 (2), 1.0 (3)	2.2 (2), 1.1 (2)
$\langle L_c \rangle_{M,sph}, \sigma_{c,M,cyl}$ (nm)	5.16 (2), 3.18 (5)	6.49 (1), 3.22 (6)	5.73 (1), 3.01 (5)
$\langle L_c \rangle_{M,cyl} / \langle D_{ab} \rangle_{M,cyl}$	3.0	2.9	2.6
$\%w_{sph}$	43.3	39.4	38.3

Table 7.1. *The table presents relevant structural and microstructural features derived from the Debye Function Analysis for samples $Pt@SiO_2 - 423K$, $Pt@SiO_2 - 473K$ and $Pt@SiO_2 - 523K$.*

Uncertainties of the refined variables are derived using the curvature of the χ^2 hypersurface about the minimum.

$\langle a_k \rangle$: refined average cubic cell parameter (Å)

$\langle D \rangle$: refined average diameter

$\langle D_{ab} \rangle$ and $\langle L_c \rangle$: refined average size parameters in ab and along c

σ_x: refined diameter/length variance

Subscripts "sph" and "cyl" refer to the shape of the nanocrystals, while M to mass based distribution.

† *Unrealistic uncertainty values likely due to the severe correlations and unsuitability of the constant-strain model for anisotropic shapes.*

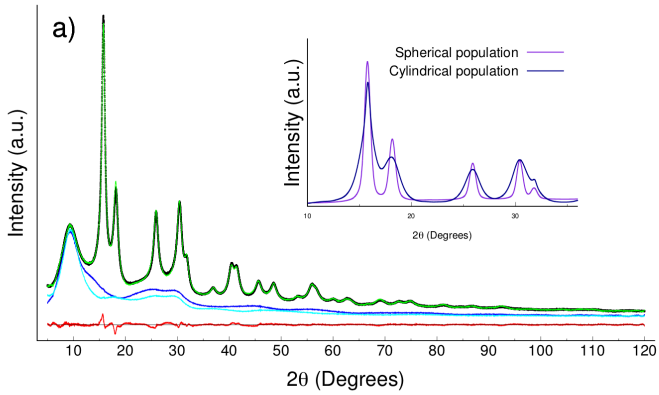
a)
Intensity (a.u.)
2θ (Degrees)
Spherical population
Cylindrical population

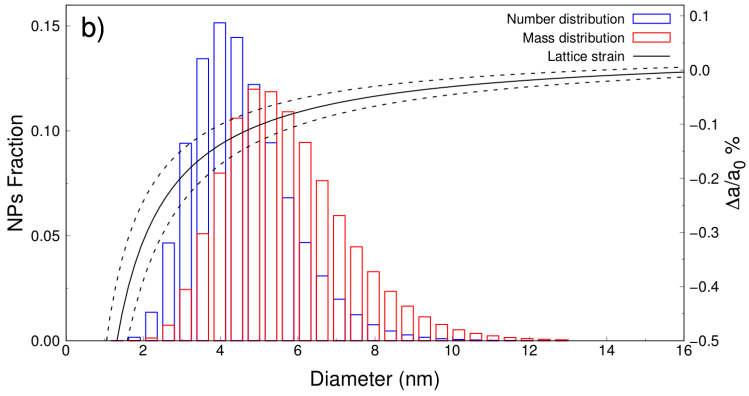
b)
NPs Fraction
Diameter (nm)
Number distribution
Mass distribution
Lattice strain
Δa/a0 %

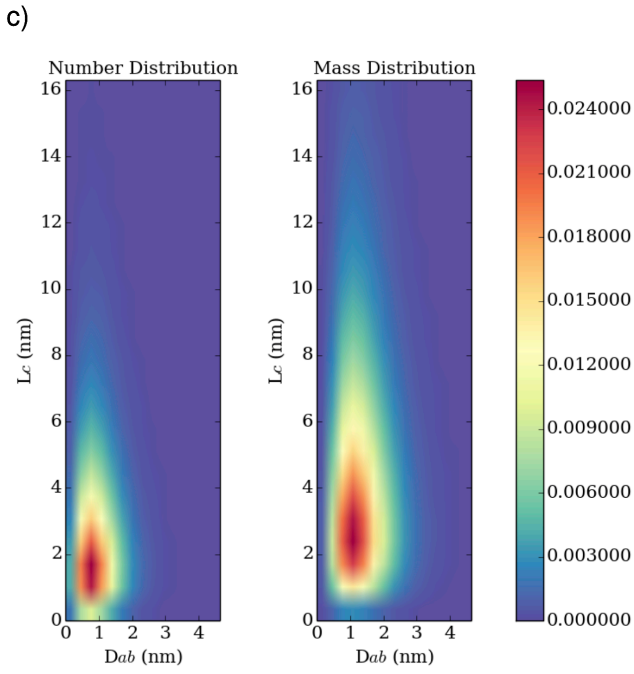
c)
Number Distribution
Mass Distribution
Lc (nm)
Dab (nm)

Figure 7.7. *Graphical outputs of the Debussy program related to* $Pt@SiO_2 - 423K$ *sample. a) Best fit (green solid line),* $Pt@SiO_2 - 423K$ *experimental data (black dots), MCM-41 silica experimental data (light blue solid line), calculated background (dark blue solid line) and difference profile between calculated and experimental data (solid red line). The inset shows the individual contributions of the spherical (purple solid line) and cylindrical (blue solid line) population used to simulate the XRPD trace. b) Number (blue) and mass (red) size distribution of the spherical population. The black solid line refers to the size-dependent lattice strain calculated on the basis of eq. 7.11. The black dashed lines represent the standard deviation from the refined size dependent curve. c) Number and mass size distributions of the cylindrical fraction. The plot highlights the presence of elongated NCs with sizes of the basal plane that fit with the pore size of the host.*

The DSE analysis reveals also that a thermal treatment with higher temperature not only promotes the formation of anisotropic crystals with higher aspect ratio (AR), but it is also able to increase the weight fraction of anisotropic *vs.* spherical NPs. This observation is counterintuitive, as this would mean "surface" NCs entering the pores. An alternative option, more in line with what observed before, would be the additional aggregation/sintering of residual (still isolated, as per the d-PDF results) fragments, attaching themselves to the anisotropic NPs preformed (in the silica channels) at lower temperature.

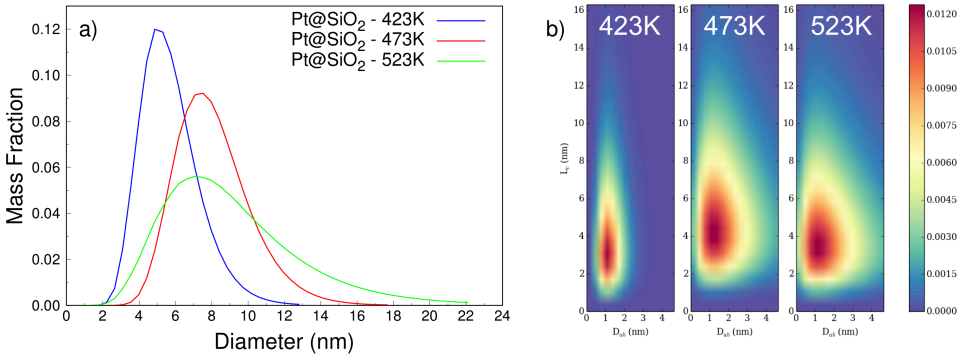

Figure 7.8. *Mass fraction distributions of the three* $Pt@SiO_2$ *samples, extracted from the DSE-refinements. On the left (a), the spherical distribution and on the right (b), the cylindrical distribution plotted as a 2D colored map (with* D_{ab} *and* L_c *coordinates). The picture shows the increase of the average crystal size of SPH NPs grown outside the templating agent and the formation of an anisotropic component that does not significantly change the aspect ratio upon the thermal treatment.*

Another fundamental aspect is described in Figure 7.7.b, where the size dependence law of the isotropic lattice strain (Equation 7.10) is presented (for $Pt@SiO_2 - 423K$ $\sigma_1 = 0.184 \cdot 10^{-5}$ and $\sigma_2 = 0.521 \cdot 10^{-2}$). [A similar analysis was performed on all three samples]. The σ_1 value does not significantly change the literature cell parameter reported for metallic Pt [3.9236(6) Å][21], while the effect of σ_2 is particularly noticeable for spherical NCs with $D < 10$nm. Since, for $Pt@SiO_2 - 423K$, the polydispersity of the spherical fraction ranges from 4 to 8 nm, the average cell parameter $\langle a_k \rangle_{sph}$ must be calculated following a mass-weighted formula, as in Equation 7.15:

$$\langle a_k \rangle_{sph} = \sum_{i=1}^{D_{max}} \chi_{M,i}\, a_{k,i} \qquad Eq.\,7.15$$

Where:

$\chi_{M,i}$: mass fraction of the *i-th* NC

$a_{k,i}$: cubic cell parameter of the *i-th* NC (Å)

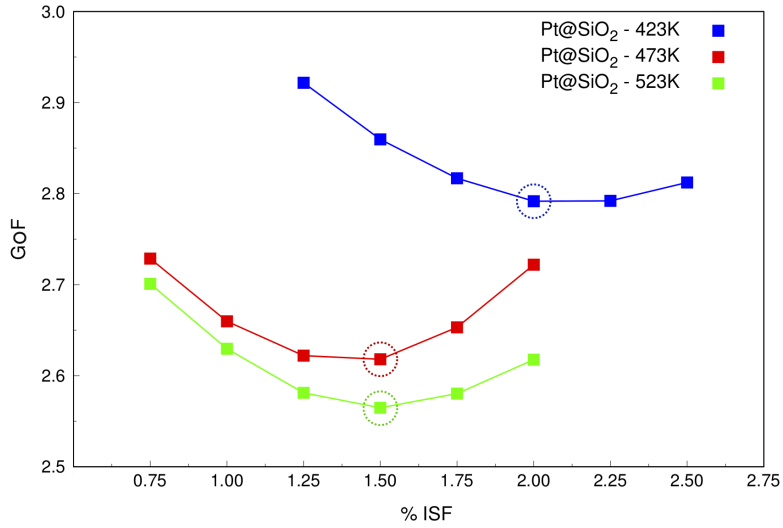

Figure 7.9. *Plot of the Goodness of fit values of the best fits for the three $Pt@SiO_2$ nanocomposites, obtained at different (fixed) stacking fault probability values. These points quantitatively represent the match between the experimental and calculated patterns upon increasing the deformation fault percentage (% ISF in the abscissa) in 0.25% steps. The minima of the curves indicate the most probable % ISF value, which decreases upon annealing at 473 K and 523 K.*

In the three samples, the deformation fault probability, plotted in Figure 7.9, was estimated as described in section 7.2.2. The trend of the GoF indicators *vs.* the stacking faults probability values shows evident minima with a reasonable sensitivity of 0.25%. Figure 7.9 also quantitatively shows how the increased annealing temperature slightly reduces the SF probability from 2.0 % for the 423K sample to lower values (1.5 %) for the $Pt@SiO_2 - 423K$ and $Pt@SiO_2 - 523K$ ones. Increasing the annealing temperature can provide the energy required to restore, in defective systems, the thermodynamically stable form (the ideally periodic crystal) or, alternatively, promote the formation of a structure with a lower percentage of planar defects. Whether one or the other process occurs (or both), cannot be derived from our analysis.

Conclusions

Despite the presence of: i) a complex hybrid system, ii) the unavailability of experimental techniques providing robust complementary information that can assist the DSE analysis and iii) the large average size of the nanocrystalline fractions, WAXTS techniques can still provide meaningful structural and microstructural information on nanosized metal samples. The quantitative derivation of the stacking fault probabilities and of the surface relaxation parameters was made possible by introducing physically-sound assumptions and approximations. This approach is justified by the necessity of reducing the CPU time to reasonable values, without significantly altering the results of our analysis. The use of a controlled stacking fault generation approach enabled the derivation of structural and microstructural parameters during of crystal growth of Pt NPs under different thermal annealing conditions. Combining DSE analysis with PDF calculations (and particularly the d-PDF on the wavy "background trace") provided unambiguous evidence that the additional amorphous fraction must be attributed to incomplete Pt atoms aggregation, due to partial decomposition of the precursor, a high-nuclearity carbonyl cluster.

References

(1) Moon, H. R.; Lim, D.-W.; Suh, M. P. Fabrication of Metal Nanoparticles in Metal–Organic Frameworks. *Chem. Soc. Rev.* **2013**, *42* (4), 1807–1824.

(2) Volosskiy, B.; Niwa, K.; Chen, Y.; Zhao, Z.; Weiss, N. O.; Zhong, X.; Ding, M.; Lee, C.; Huang, Y.; Duan, X. Metal-Organic Framework Templated Synthesis of Ultrathin, Well-Aligned Metallic Nanowires. *ACS Nano* **2015**, *9* (3), 3044–3049.

(3) Bertolotti, F.; Moscheni, D.; Migliori, A.; Zacchini, S.; Cervellino, A.; Guagliardi, A.; Masciocchi, N. A Total Scattering Debye Function Analysis Study of Faulted Pt Nanocrystals Embedded in a Porous Matrix. *Acta Crystallogr. A* **2016**, *72*, 632–644.

(4) Beyerlein, K. R.; Leoni, M.; Snyder, R. L.; Scardi, P. On Faulting in Nanocrystallites of FCC Metals. *Mater. Sci.* **2011**, *681*, 13–18.

(5) Li, R.; Lu, S.; Kim, D.; Schönecker, S.; Zhao, J.; Kwon, S. K.; Vitos, L. Stacking Fault Energy of Face-Centered Cubic Metals: Thermodynamic and *Ab Initio* Approaches. *J. Phys. Condens. Mat.* **2016**, *28* (39), 395001.

(6) Jo, M.; Koo, Y. M.; Lee, B.-J.; Johansson, B.; Vitos, L.; Kwon, S. K. Theory for Plasticity of Face-Centered Cubic Metals. *Proc. Natl. Acad. Sci. U S A* **2014**, *111* (18), 6560–6565.

(7) Gallagher, P. C. J. The Influence of Alloying, Temperature, and Related Effects on the Stacking Fault Energy. *Metall. Trans.* **1967**, 33.

(8) Masadeh, A. S.; Bozin, E.; Farrow, C. L.; Paglia, G.; Juhas, P.; Karkamkar, A.; Kanatzidis, M. G.; Billinge, S. J. L. Quantitative Size-Dependent Structure and Strain Determination of CdSe Nanoparticles Using Atomic Pair Distribution Function Analysis. *Phys. Rev. B* **2007**, *76* (11).

(9) Yang, X.; Masadeh, A. S.; McBride, J. R.; Božin, E. S.; Rosenthal, S. J.; Billinge, S. J. L. Confirmation of Disordered Structure of Ultrasmall CdSe Nanoparticles from X-Ray Atomic Pair Distribution Function Analysis. *Phys. Chem.* **2013**, *15* (22), 8480.

(10) O. Madelung; U. Rössler; M. Schulz. Cadmium Selenide (CdSe) Lattice Parameters, Thermal Expansion. In *II-VI and I-VII Compounds; Semimagnetic Compounds*; Springer, Heidelberg: Berlin, Germany; Vol. 41B, pp 1–4.

(11) Zukal, A.; Thommes, M.; Čejka, J. Synthesis of Highly Ordered MCM-41 Silica with Spherical Particles. *Micropor. Mesopor. Mat.* **2007**, *104* (1–3), 52–58.

(12) Femoni, C.; Iapalucci, M. C.; Longoni, G.; Lovato, T.; Stagni, S.; Zacchini, S. Self-Assembly of $[Pt_{3n}(CO)_{6n}]^{2-}$(n=4−8) Carbonyl Clusters: From Molecules to Conducting Molecular Metal Wires. *Inorg. Chem.* **2010**, *49* (13), 5992–6004.

(13) Cervellino, A.; Frison, R.; Bertolotti, F.; Guagliardi, A. DEBUSSY 2.0: The New Release of a Debye User System for Nanocrystalline and/or Disordered Materials. *J. Appl. Cryst.* **2015**, *48* (6), 2026–2032.

(14) Cervellino, A.; Giannini, C.; Guagliardi, A. DEBUSSY: A Debye User System for Nanocrystalline Materials. *J. Appl. Cryst.* **2010**, *43* (6), 1543–1547.

(15) Mirijam Zobel; Reinhard B. Neder; Simon A. J. Kimber. Universal Solvent Restructuring Induced by Colloidal Nanoparticles. *Science* **2015**, *347*, 292–294.

(16) Juhás, P.; Davis, T.; Farrow, C. L.; Billinge, S. J. L. A Rapid and Highly Automatable Program for Processing Powder Diffraction Data into Total Scattering Pair Distribution Functions. *J. Appl. Cryst.* **2013**, *46* (2), 560–566.

(17) Wasserman, H. J.; Vermaak, J. S. On the Determination of the Surface Stress of Copper and Platinum. *Surf. Sci.* **1972**, *32* (1), 168–174.

(18) Qi, W. H.; Wang, M. P.; Su, Y. C. Size Effect on the Lattice Parameters of Nanoparticles. *J. Mater. Sci.* **2002**, 21, 877-878.

(19) Qi, W. H.; Wang, M. P. Size and Shape Dependent Lattice Parameters of Metallic Nanoparticles. *J. Nanopart. Res.* **2005**, *7* (1), 51–57.

(20) Diehm, P. M.; Agoston, P.; Albe, K. Size-Dependent Lattice Expansion in Nanoparticles: Reality or Anomaly? *Chem. Phys. Chem.* **2012**, *13* (10), 2443–2454.

(21) Arblaster, J. W. Crystallographic Properties of Platinum. *Platinum Met. Rev.* **2006**, *50* (3), 118–119.

General Conclusions

The work presented in this thesis successfully reached the objectives prefixed in Chapter 1. This three years long experience permitted to increase my knowledge on II-VI semiconductors, in particular on CdSe-based materials. The period spent abroad, among ETH in Zurich, permitted to improve my skills on colloidal synthesis and to understand the importance of kinetic and thermodynamic effects in guiding the crystal phases (ZB or WZ) and shape. Furthermore, I had also the opportunity to be involved in NMR projects on CdSe materials permitting to explore new advanced techniques for surface characterization on nanomaterials. The need of high-quality data for the Debye Function Analysis contributes to the increase of my knowledge on synchrotron radiation and WAXTS measurements on colloidal solutions. This experience has been maturated in two beamtimes dedicated to luminescent materials at the MS beamline of the PSI.

A model of NCs with planar defects to be implemented in the Debussy suite has been developed and used to characterize a set of CdSe-based samples of increasing size. This model was conceived to have a high degree of flexibility, permitting to generate atomistic models of NCs with different stacking fault probabilities. Since the stacking fault behavior in nanostructures is size, material and phase dependent, a further degree of flexibility has been introduced into the atomistic model in order to manage fault-induced isotropic and/or local anisotropic strains together with surface vacancies and thermal disorder. Despite the potentiality of the WAXTS DSE-based model, the fit of SAXS data has been integrated, in order to disentangle the size-induced peaks broadening from the defects-induced ones. The synergic use of the complex atomistic model into atomic-scale structure sensitive and insensitive region of the X-ray scattering data, permitted to unveil, within reasonable computational time, new features on morphology, surface and core defects of CdSe samples.

An investigation on stacking fault probability for metallic material has been proposed as well. The larger particle sizes, together with the lower probability of stacking faults in these samples, pushed to the development and use of an alternative simplified method for planar defects characterization. In this case, the

complementary use of the Debye Scattering equation and the differential PDF, permitted the understanding of the system by and large.

Both cases of application of the DSE here presented remarked the need of using complementary techniques in nano-system characterization, since the complexity of the analyzed system and the information extracted with the DFA method may be not robust enough and lead to weaker results.

Moreover, this thesis permitted to develop a protocol to investigate CdSe-based NCs. As explained in Chapter 1, the importance in understanding the morphology and faceting, together with atomi-scale structural and microstructural features represent a key point to understand physical phenomena and improve the optical efficiency of II-VI semiconductors.

Future work will be addressed to the study of more complex engineered CdSe-based systems with higher potential for applications. A first step will be done towards the understanding of CdSe NCs which underwent a ligand exchange process from organic (Oleate) to inorganic ligands (K_2S, K_4SnS_4, $K_6Sn_2S_7$). In particular, the study will be addressed to the role of the ligand in modifying the surface structure and how this can affect the stacking fault percentage and the strain by them induced. Further steps will be moved towards more efficient heterosystems, such as core-shells, in order to understand the role of the shell on the photoluminescence properties.

List of Publications

(1) Bertolotti, F.; **Moscheni, D.**; Migliori, A.; Zacchini, S.; Cervellino, A.; Guagliardi, A.; Masciocchi, N. A Total Scattering Debye Function Analysis Study of Faulted Pt Nanocrystals Embedded in a Porous Matrix. *Acta Crystallogr. A* **2016**, *72*, 632–644.

(2) Piveteau, L.; Ong, T.-C.; Walder, B. J.; Dirin, D. N.; **Moscheni, D.**; Schneider, B.; Bär, J.; Protesescu, L.; Masciocchi, N.; Guagliardi, A.; et al. Resolving the Core and the Surface of CdSe Quantum Dots and Nanoplatelets Using Dynamic Nuclear Polarization Enhanced PASS–PIETA NMR Spectroscopy. *ACS Central Science* **2018**, *4* (9), 1113–1125.

(3) Bertolotti, F.; **Moscheni, D.**; Guagliardi, A.; Masciocchi, N. When Crystals Go Nano - The Role of Advanced X-Ray Total Scattering Methods in Nanotechnology: When Crystals Go Nano - The Role of Advanced X-Ray Total Scattering Methods in Nanotechnology. *Eur. J. Inorg. Chem.* **2018**, *2018* (34), 3789–3803.

(4) **Moscheni, D.**; Bertolotti, F.; Piveteau, L.; Protesescu, L.; Dirin, D. N.; Kovalenko, M. V.; Cervellino, A.; Pedersen, J. S.; Masciocchi, N.; Guagliardi, A. Size-Dependent Fault-Driven Relaxation and Faceting in Zincblende CdSe Colloidal Quantum Dots. *ACS Nano* **2018**, *12* (12), 12558–12570.

Notes